August 30, 2011
EWI Project No. 50854GTH

Enhanced Defect Detection and Sizing Accuracy Using Matrix Phased Array Ultrasonic Tools

Other Transaction Agreement No. DTPH56-08-T-000002

Final Project Report

May 2008 through July 2011

DISTRIBUTION STATEMENT. Distribution authorized to U.S. Government agencies only to protect information protected by a contractor's "limited rights" statement, or received with the understanding that it will not be routinely transmitted outside the U.S. Government. Other requests for this document are to be referred to the Technical Manager.

Government Purpose Rights

Submitted to:

U.S. Department of Transportation
Pipeline and Hazardous Materials Safety Administration
Pipeline of Transportation Safety
Washington, DC

Final Report

Project No. 50854GTH

Other Transaction Agreement No. DTPH56-08-T-000002

on

Enhanced Defect Detection and Sizing Accuracy Using Matrix Phased Array Ultrasonic Tools

to

U.S. Department of Transportation
Pipeline and Hazardous Materials Safety Administration
Office of Pipeline Safety
Washington, DC

Government Purpose Rights

August 30, 2011

Roger Spencer, Evgueni Todorov, Perry White, and Nancy Porter (EWI)
Mark Lozev (BP)

Abstract

The overall objective this research program was to enhance detection and sizing accuracy of crack-like and planar imperfections created during pipeline fabrication and service using matrix phased array (MPA) ultrasonics tools with the goal of improving the predicted reliability of pipelines during early design stage and service life. The technical objectives of the program were to: develop concepts for MPA ultrasonic probe modules for outside diameter (OD) or inside diameter (ID) pipe inspection; define and optimize detection and sizing capabilities of the MPA modules via modeling and simulation; design and fabricate two probes modules (one for OD and one for ID inspection); and to determine and demonstrate the detection and sizing performance of the MPA probe modules. The following four MPA probe concepts were developed:

- Concept 1 – Girth Weld Inspection from OD Surface
- Concept 2 – Inspection of Pipe Wall Damage from OD Surface
- Concept 3 – Inspection of Pipe Wall Damage from ID of Pipe
- Concept 4 – Stationary Probe for Monitoring Pipe Wall.

In general, all four MPA concepts demonstrated good potential for pipeline inspection. Concept 1 proved challenging, as the different MPA tilt and skew channels produce a large amount of data. Despite this challenge, probability of detection (POD) values and flaw sizing accuracy obtained for MPA of girth welds were similar to those obtained for linear phased array (LPA). Given that MPA is an emerging technology for girth weld inspection, the overall results were encouraging. Concept 2 demonstrated good results on material approximately 25 mm in thickness where longitudinal and refracted longitudinal beams could be used to detect reflectors on the opposite (back) surface. A possible application for the probe would be to detect ID corrosion damage when inspecting from the OD pipe surface. Concept 3 performed well; however, a method for transporting multiple probe segments through a fluid-filled pipe is needed. Concept 4 worked well as a 2-axis stationary C-Scan for health monitoring. Unlike single-element probes, this 2D MPA probe provided A-Scan data for each point on the C-Scan, thus allowing multiple measurements to be made over the entire probe footprint. Concept 4 could be deployed provided a means for probe attachment to the pipe is addressed. Modeling and simulations agreed well with the experimental results and proved valuable for probe design and predicting detection capabilities. It is recommended that future work concentrate on MPA procedures and software that will provide quick and reliable analysis of MPA data. This should involve the selection of beam tilt and skew angles that are most advantageous, as well as, flaw sizing protocols for tilted and skewed flaws.

Acknowledgements

This research program consisted of a large international project team with multiple funding sources. Funding was provided by the U.S. Department of Transportation Pipeline and Hazardous Materials Safety Administration (DOT PHMSA), ConocoPhillips, and Edison Welding Institute (EWI). In kind contributions were provided by BP, TransCanada, BAM, ConocoPhillips, UT Quality, ExxonMobil, and EWI.

Although large, the project team was quite active and provided contributions that exceeded our expectations. The EWI project team wishes to acknowledge the extraordinary efforts of the following individuals and their organizations:

- **Jim Merritt** (DOT PHMSA), who attended numerous project meetings and provided guidance and insight throughout the project.
- **Mark Lozev** (BP America), who started out as the Principal Investigator at EWI, then moved to BP where he continued to provide oversight and direction for the program.
- **Joe Kiefer** (ConocoPhillips), who attended numerous project meetings, provided feedback, support, guidance, and funding.
- **Kevin Hodgins** (UT Quality), who provided field trial support.
- **Evan Vokes** (TransCanada), who organized and facilitated the field trials on the Keystone Project in Canada.
- **David Hodgkinson** (TransCanada-retired), who helped design the program and continued to be involved in the project after his retirement from TransCanada.
- **Joshua Sleigh** (ExxonMobil), who provided funding for ApplusRTD to scan blind samples.

Disclaimer

U.S. Department of Transportation
Pipeline and Hazardous Materials Safety Administration
Pipeline Safety Research and Development Program

This research was funded in part under the Department of Transportation, Pipeline and Hazardous Materials Safety Administration's Pipeline Safety Research and Development Program. The view and conclusions contained in this document are those of the authors and should not be interpreted as representing the official policies, either expressed or implied, of the Pipeline and Hazardous Materials Safety Administration, or the U.S. Government.

Executive Summary

The need for developing more accurate detection and assessment tools and to improve size and depth measurement accuracy of crack-like and planar imperfections is becoming more apparent in the pipeline industry.[1] Cracking and planar imperfections are one of the most difficult defects to size and assess. Cracking is involved in hydrogen-induced damage, stress-corrosion cracking (SCC) failures, mechanical damage failures, and many weld failures. Phased array (PA) ultrasonic testing (UT) technology using linear phased array (LPA) probes has proven to be superior to conventional automated ultrasonic testing (AUT) equipment in its capability to detect and size defects.[2-5] An enhancement of defect detection and sizing accuracy and improvement of predicted pipeline reliabilities can be achieved by using the next generation of matrix phased array (MPA) ultrasonic techniques.

The overall objective of the program was to enhance detection and sizing accuracy of crack-like and planar imperfections created during pipeline fabrication and service using MPA ultrasonic tools with the goal of improving the predicted reliability of pipelines during early stage design.

The technical objectives of the program can be summarized as follows:

- Develop a concept for MPA ultrasonic probe modules applicable for either outside diameter (OD) or inside diameter (ID) pipe inspection and carried by different inspection systems.
- Define and optimize detection and sizing capabilities of the modules via modeling and simulation.
- Design and fabricate two probe modules: one for OD and one for ID inspection.
- Determine and demonstrate the detection and sizing performance of the probe modules.

Although ultrasonic inspection technology and tools has improved significantly, there is still a need for more reliable detection and accurate sizing of crack-like and planar defects, cracks in dents, and detection of secondary features within deformed pipe.[1] MPA UT technology has the potential to provide the needed inspection improvements. At the time the project was funded, it was recognized that additional work was needed to evaluate MPA technology to meet these challenges. To address the issues, the project concentrated on the following topics:

- Inspection of complex defects using optimized MPA probe modules to electronically focus, steer, and scan in multiple directions.

- The use of improved resolution, imaging, defect quantification, and characterization to optimize detection sizing accuracy in pipeline inspections.

- The use of advanced signal analysis to combine information from multiple incidence angles to infer the mechanical damage/corrosion-induced roughness and wall thickness (WT) in difficult to detect and size complex defects.

- Fabrication of prototypes of MPA probe modules and determination of detection and sizing performance in laboratory and field conditions.

In the early stages of this project, the following four concepts were selected by industry partners to address areas where MPA could improve inspection capabilities:

- Concept 1 – Girth Weld Inspection from OD Surface
- Concept 2 – Inspection of Pipe Wall Damage from OD Surface
- Concept 3 – Inspection of Pipe Wall Damage from ID of Pipe
- Concept 4 – Stationary Flexible Array Monitoring of Pipe Wall.

Concept 1 – In the past 5 to 10 years, LPA has gained in popularity for girth weld inspection, because the electronic steering and focusing capability of LPA provides good zonal coverage with only two probes as compared to 12 or more conventional probes. However, one disadvantage of LPA is the fact that the beam can only be focused and steered I n one direction (i.e., the primary probe axis). This generally results in an elliptical-shaped beam. Because MPA probes have elements in a 2D pattern, the ultrasonic beam can be steered and focused in two directions. This can help produce a spherical beam and add other advantages such as, beam steering and beam focusing in both the primary and secondary probe axis. With better control of the beam, it should be possible to improve flaw detection and sizing capabilities.

Evaluation of Concept 1 was conducted using six girth weld samples containing implanted flaws. The samples were designed with different flaw types and orientations. All designed flaws were planar flaws such as cracks, inadequate penetration, lack of side wall fusion, and inter-bead lack of fusion. Some of these flaws were intentionally tilted and skewed relative to the weld bevel and some flaws were in close proximity to each other. These flaws provided an opportunity to evaluate the capabilities of MPA, especially since the same six samples were also scanned by five LPA systems. This provided a good basis for comparing MPA performance to LPA performance.

Two MPA systems were used for the evaluations. One system was used during an open trial inspection where the flaw locations were known. The other system was used during a blind trial inspection where the operators had no knowledge of the flaw locations. The MPA open trial was a non zonal technique that was used as a supplemental fingerprinting technique. The MPA blind trial was a zonal inspection technique similar to the techniques commonly used for pipeline girth weld inspection. The MPA blind trial instrumentation and software were part of a new product that is still being tested and evaluated. While it was not a finished product, this project provided a

good opportunity for the developers to test their system and it also provided valuable information for benchmarking MPA technology for a girth weld inspection scenario.

Performance evaluations of Concept 1 demonstrated that MPA data can be difficult to handle, because of the large quantity of data available through multiple beam tilt and skew channels. In addition, it was noted that flaw detection and sizing routines that are typically used for conventional and LPA do not necessarily apply to MPA. For example, the decision as to which beam tilt or skew channel to use for flaw evaluation and sizing was not necessarily the channel displaying the highest signal amplitude like it would be for LPA. Consequently, data analysis protocols for MPA should be developed to exploit unique MPA capabilities. Despite data analysis challenges, the probability of detection (POD) values for MPA were similar to those obtained for LPA. Given that MPA is an emerging technology for girth weld inspection, the overall results were encouraging.

This phase of the project also provided an opportunity to evaluate the use of Tomographic Computer Aided Radiology (TomoCAR) radiography to locate and size flaws in lieu of destructive verification that is often used to obtain actual flaw sizes for POD and sizing studies. Two girth weld samples were scanned by TomoCAR at the Federal Institute for Materials Research and Testing (BAM) in Berlin, Germany. Selected flaws were later cross-sectioned and compared to the TomoCAR results. While the comparisons were not extensive, the comparisons were very good and typically were within 0.5 mm in depth and height. While TomoCAR has limitations, it has potential as an alternative to destructive verification.

Concept 2 – This concept consisted of a flexible MPA probe to inspect for pipe damage by scanning from the OD surface. During the project, flexible MPA probe parameters were evaluated using UT modeling and simulations. A flexible probe was then built Imasonic and evaluated at EWI. The flexible probe used linear variable displacement transducers (LVDT) to obtain the shape of the probe as it conformed to the pipe surface. LVDT data was constantly fed back to the MPA software to compensate for changes in surface profile. The MPA software then adjusted the focal laws to electronically steer the beam in order to maintain the specified beam angle and focal depth.

Performance evaluations of Concept 2 demonstrated that the probe and software were able to provide real-time beam steering and focusing compensation. However, current manufacturing technology for the probe limited the probe frequency and element pitch to parameters that were better suited for material approximately 25 mm in thickness or greater. The pipe available for the evaluations was approximately 7 mm in thickness; consequently, the probe was not optimal for the pipe samples tested. Additional scans conducted on thicker plate material demonstrated that the ultrasonic characteristics of the probe were good. One drawback of the probe design was the dependability of the LVDTs. During the evaluations, one or more of the LVDT plungers

malfunctioned resulting in failure to calibrate the displacement. A more robust LVDT design is needed for field deployment of the technology.

Concept 3 – Using modeling and simulation software, an ID MPA probe was designed for use in a liquid-filled pipe with an ID of approximately 150 mm. The probe was a non-contact immersion probe with a water path distance of approximately 40 mm between the probe face and the pipe ID surface. The probe was designed to inspect for pipe damage such as corrosion pitting and cracking primarily on the OD surface of the pipe. The probe design allowed for electronic beam steering in the circumferential and axial directions, and electronic scanning in the circumferential direction. The electronic steering and scanning was combined with a mechanical line scan along the pipe length.

Using flat-bottom holes (FBH) and electric discharge machined (EDM) notches, performance evaluations of the Concept 3 probe demonstrated that wall thinning as small as 0.5 mm could be detected and sized. In addition, EDM notches measuring 0.5 mm in through wall height on the OD surface were detectable. With the use of electronic beam steering in the circumferential and axial directions, detection was also demonstrated when notches were tilted and skewed by as much as 20 degrees from the axial and circumferential planes.

Concept 4 – This concept looked at the use of MPA probes for pipe wall health monitoring applications. The general idea was to generate stationary C-Scans of the area defined by the footprint of the probe. This provides the advantage of being able to scan an area rather than acquiring only a single point measurement.

With existing MPA probes, the concept was evaluated using tapered and FBH reflectors, as well as, a square notch. At selected electronic beam angles and focal depths, electronic scanning was used to scan across the entire footprint of the probe. Results showed that a 2-mm diameter FBH at a depth of 6.3 mm could be accurately imaged and sized. In addition, lateral resolution was sufficient to distinguish 3.7-mm-diameter taper bottom holes that were within 1.2-mm edge to edge in a 13.2-mm-thick sample.

In general, all four MPA concepts developed during this project showed good potential for pipeline inspection. Concept 4 (health monitoring) could be deployed provided a means for probe attachment to the pipe is addressed. As explained below, the other three concepts need additional work to make them field ready.

When using MPA for girth weld inspection, it was a challenge to manage the large amount of data available through the different MPA tilt and skew channels. It appears that flaw evaluation and sizing algorithms currently used for conventional and LPA may not be sufficient for MPA. For example, algorithms need to address which channel(s) should be used for determining flaw size. Despite the challenge of large amounts of data, POD values and flaw sizing accuracy obtained

for MPA of girth welds were similar to those obtained for LPA. Given that MPA is an emerging technology for girth weld inspection, the overall results were encouraging.

The flexible MPA probe used on this project provided good results on material approximately 25 mm in thickness, where longitudinal and refracted longitudinal beams could be used to detect reflectors on the opposite (back) surface. A possible application for the probe would be to detect ID corrosion damage when inspecting from the OD pipe surface.

While the ultrasonic part of the flexible MPA probe functioned well, problems were experienced with the LVDT pistons used for surface contour measurements. In three different instances, an LVDT piston stopped functioning resulting in the inability to use the real-time focal law feedback. For field applications, a more robust probe is required.

Ultrasonic performance of the ID MPA probe was good; however; a method for transporting the multiple probe segments through a fluid filled pipe is needed. For optimal performance, the transporting mechanism needs to maintain probe alignment and constant radial distance from the pipe ID surface.

Modeling and simulation results obtained during this project agreed well with the experimental results and proved valuable data for probe design and detection prediction capabilities. This was especially evident from modeling and experimental data for the ID MPA probe.

MPA probes worked well to provide a 2-axis stationary C-Scan for health monitoring. Unlike single-element probes, the 2D MPA probe provided A-Scan data for each point on the C-Scan. This allowed multiple measurements to be made over the entire probe footprint and provided a more comprehensive understanding of test component characteristics.

TomoCAR radiography results compared well to destructive verification measurements for flaw height and depth. The comparisons were very good and measurements were typically within 0.5 mm. While TomoCAR has limitations, it does present itself as a potential alternative to destructive verification for POD and sizing accuracy studies.

MPA of girth welds will require further development of data handling and analysis routines in order to fully use the capabilities of MPA technology. It is recommended that future work concentrate on MPA procedures and software that provide quick and reliable analysis of MPA data. This should involve the selection of beam tilt and skew angles that are most advantageous, as well as, flaw sizing protocols for tilted and skewed flaws.

It is recommended that the TomoCAR technology be further developed as a substitute alternate for destructive measurements made during qualification/quantification programs to determine

POD and sizing accuracy. The use of this technology could reduce the cost of such programs and allow the validation samples to be re-used.

It is recommended that flexible MPA technology be further evaluated for inspection of components greater than 15 mm in thickness. In addition, LVDT plungers should be evaluated to improve robustness for field applications.

While the ID probe segment had good ultrasonic characteristics, additional work should be performed to design a system for transporting the probe through the ID bore. The transporting device needs to maintain good probe alignment and be self contained with power supplies and data-acquisition capabilities.

Abbreviated Terms

AUT	automated ultrasonic testing
BAA	broad agency announcement
BAM	Federal Institute for Materials Research and Testing
BW	backwall
CEA	Commissariat à l'Energie Atomique
CR	computed radiography
DDA	digital detector array
DS	downstream
DT	destructive testing
EDM	electric discharge machined
EMDC	ExxonMobil Development Company
EWI	Edison Welding Institute
FBH	flat-bottom holes
FD	focal depths
FMPA	flexible matrix phased array
HAZ	heat-affected zone
HIC	hydrogen-induced cracking
HSBH	hemi-spherical bottom holes
ID	inside diameter
IGSCC	inter-granular stress corrosion cracking
LIST	Laboratory for Integration of Systems and Technologies
LPA	linear phased array
LVDT	linear variable displacement transducers
LW	longitudinal wave
MPA	matrix phased array
MT	magnetic particle testing
OD	outside diameter
PA	phased array
PE	pulse-echo
POD	probability of detection
PT	penetrant testing
RT	radiography testing
SCC	stress-corrosion cracking
SDH	side-drilled holes
TCPL	TransCanada Pipelines
TOFD	time-of-flight diffraction
TomoCAR	Tomographic Computer Aided Radiology
TRA	Terms of the Relationship Agreement
U.S. DOT PHMSA	Department of Transportation Pipeline and Hazardous Materials Safety Administration
US	upstream
UT	ultrasonic testing
UTQ	UT Quality
VT	visual testing
WT	wall thickness

Contents

Page

Abstract i

Acknowledgements ii

Disclaimer iii

Executive Summary iv

Abbreviated Terms x

1.0 Introduction 1

2.0 Task 1 – Development of MPA Concepts 4

3.0 Tasks 2 and 3 – Virtual Optimization 9
3.1 MPA Optimization and Modeling 9
3.1.1 Comparison of LPA and MPA Performance for Flaw Detection, Sizing, and Resolution 9
3.1.1.1 Resolution 10
3.1.1.2 Sizing 11
3.1.1.3 Detection of Skewed Flaws 13
3.1.2 Flexible Array for Inspection from OD and in Dents (Concept 2) 15
3.1.2.1 Near Field Depth Verification 15
3.1.2.2 Optimization of Array Layout Element Size and Gap 20
3.1.2.3 Verification of Beam Focusing for Dent Inspection from OD 26
3.1.2.4 Simulation of Pipe Wall Thinning Detection 32
3.1.2.5 Crack Detection on Round and Elongated Dent ID with Longitudinal Waves 35
3.2 Rigid Array for Inspection from ID (Concept 3) 40
3.2.1 Initial Shear Wave (SW) Optimization 42
3.2.2 Initial Longitudinal Wave (LW) Optimization 47
3.2.2.1 Investigation of LW Refracted Angle and Circumferential Coverage 49
3.2.2.2 Investigation of Reduced Aperture Size (12×4) 55
3.2.2.3 Summary Optimization Plots for Sx, Gx, and Number of Active Elements 58
3.2.2.4 Optimization of Secondary Probe Axis Element Size (Sy) and Inter-Element Gap (Gy) 62
3.2.2.5 Optimized Probe Steering and Focal Capabilities 68
3.2.2.6 Specifications of Optimized Probe 79
3.2.2.7 Flaw Interaction of Optimized Probe with Flat-Bottom Holes (FBH) and Hemi-Spherical Bottom Holes (HSBH) 80
3.2.2.8 Interaction of Optimized Probe with Planar Flaws Connected to the OD 85
3.2.2.9 Interaction of Optimized Probe with SCC Flaws Connected to OD 91
3.3 Rigid and Flexible Arrays for Continuous Localized Monitoring from OD (Concept 4) 98
3.3.1 Illustration of Scanning Patterns and Techniques for Corrosion Detection 99
3.3.2 Optimization of Beam Forming and Steering for Permanently Mounted (Dry Couplant) Probe 101
3.3.3 Health Monitoring Flaw Interaction Simulations 109
3.3.4 Task Observations and Conclusions 114
3.4 Task 4 – Fabrication of MPA Probes 114

Contents (Continued)

Page

3.5 Girth Weld Inspection from OD (Concept 1) 117
3.5.1 Design and Fabrication of Test Welds 118
3.5.1.1 Fingerprinting 119
3.5.1.2 TomoCAR Fingerprinting 119
3.5.2 MPA AUT Scanning 122
3.5.3 MPA Open Trial Setup 123
3.5.4 MPA Blind Trial Setup 124
3.5.4.1 MPA Blind Trial Data Evaluation 126
3.5.4.2 Limitations to MPA Data Interpretation for Blind Trial Welds 127
3.5.5 Destructive Evaluation 129
3.5.6 Task Conclusions and Significance 138
3.6 Inspection of Pipe Wall Damage from OD Pipe Surface (Concept 2) 140
3.6.1 Task Observations and Conclusions 144
3.7 Inspection of Pipe Wall Damage from ID Pipe Surface (Concept 3) 145
3.7.1 Task Observations and Conclusions 159
3.8 Stationary 2D Array Monitoring of Pipe Wall from OD Pipe Surface Concept 4 160
3.8.1 Task Observations and Conclusions 171

4.0 Field Trials 172
4.1 Field Trial Location 172
4.2 Inspection Procedure 174
4.3 Calibration Blocks 174
4.4 Task Observations and Conclusions 183

5.0 Advanced NDE Training 184

6.0 Technology Demonstration Workshop 185
6.1 Workshop Participants 185
6.2 Workshop Agenda 187
6.3 Workshop Presentations 188
6.4 Workshop Demonstrations 188
6.5 Workshop Survey 190

7.0 Pipeline Conference Presentation 191

8.0 Final Financial Section 191
8.1 Government Funding 191
8.2 Team Cost-Share Funding 192
8.2.1 Planned Cost-Sharing (As Quantified in the Original Proposal) 193
8.2.1.1 Planned Cash Cost-Share 193
8.2.1.2 Planned In-Kind Support 194
8.2.2 Additional Cost-Sharing (NOT Quantified in the Original Proposal) 196
8.2.2.1 Additional Cash Cost-Share 196
8.2.2.2 Additional In-Kind Support 197
8.2.2.3 Other Support 198
8.3 Subcontracts 200

9.0 Conclusions 200

Contents (Continued)

Page

10.0 Recommendations 201

11.0 References 202

Appendices

Appendix A Concept 4 – Health Monitoring (Beam Modeling Results)

Appendix B Concept 4 – Health Monitoring Modeling Simulations (Beam-to-Flaw Interactions)

Appendix C Field Trial – MPA Procedure

Appendix D Field Trial – UTQ Calibration Block Drawings

Appendix E EWI Calibration Block Drawings

Appendix F Field Trial – Daily Activity Log

Appendix G Workshop Presentations

Appendix H Workshop Survey Results

Appendix I Rio Conference Presentation

Appendix J Rio Conference Paper

Tables

Table 1. Verification of Near Field Depth at Various Apertures and Refracted Angles 17

Table 2. Optimization of FMPA on Pipe (Normal Beam, Full Array) 22

Table 3. Optimization of FMPA on Plate (Normal Beam, Full Array) 23

Table 4. Beam Focusing in Dent (FMPA at Various Angles and Probe Orientation) 30

Table 5. Beam Steering in Dent (Comparison of FMPA Desired and Actual Refracted Angles) 30

Table 6. Beam Focusing in Dent (Transversely Oriented FMPA at Various Angles. Reduced Active Group 8×5) 30

Table 7. Variable WP, FD, and Gx (ID MPA 5 MHz, 16×4 Active Aperture, 45-degrees SW)45

Table 8. Variable Frequency, WP, Sx, Gx, Gy, and Active Aperture (ID MPA 5 MHz, 45-degrees SW) 46

Table 9. Variable WP, FD and Gx (ID MPA 5 MHz, 16×4 Active Aperture, 1-degrees LW). 48

Contents (Continued)

Page

Table 10. Variable Refracted Angle and Gx (ID MPA 5 MHz, 16×4 Active Aperture, 40-mm WP, 25-mm FD) 50

Table 11. Reduced Active Aperture (ID MPA 5 MHz, 1-mm Sx, 1-mm Sy, 0.6-mm Gy, 40-mm WP, 25-degrees LW) 53

Table 12. Variable Aperture, FD, Sx, and Gx (ID MPA 5 MHz, 40-mm WP, 25-degrees LW) 53

Table 13. Variable FD and Refracted Angle (ID MPA 5 MHz, 12×4 Active Aperture, 40-mm WP, Sx = Sy = 0.5 mm, Gx = Gy = 0.6 mm) 56

Table 14. Secondary Direction - Variables FD, Sy, and Gy (ID MPA 5 MHz, 16×4 Active Aperture, 40-mm WP, 15-degrees LW, 0.5-mm Sx, 0.6-mm Gx) 64

Table 15. Secondary Direction - Variables FD, Sy, and Gy (ID MPA 5 MHz, 16×4 Active Aperture, 30-degrees LW, 0.5-mm Sx, 0.6-mm Gx) 65

Table 16. Summary Table (Optimized ID MPA 5 MHz, 16×4 Active Aperture, LW) 70

Table 17. Summary Table (Condition Monitoring, Rigid MPA 5 MHz, 4×4 Active Aperture, LW) 106

Table 18. Summary Table (Condition Monitoring, Rigid MPA 5 MHz, 8×4 Active Aperture, LW) 107

Table 19. Summary Table (Condition Monitoring, Rigid MPA 5 MHz, 12×6 Active Aperture, LW) 108

Table 20. Detectability Summary Rigid MPA 5 MHz, 4×4 Active Aperture, WT 12 mm 113

Table 21. Detectability Summary Rigid MPA 5 MHz, 8×4 Active Aperture, WT 12 mm 113

Table 22. Detectability Summary Rigid MPA 5 MHz, 8×4 Active Aperture, WT 25 mm 113

Table 23. MPA Probe Parameters 128

Table 24. MPA Scan Setups 128

Table 25. Breakdown of MPA Blind Trial Setups 129

Table 26. Summary of Linear PA AUT Setups 129

Table 27. Number of Metallographic Cross-Sections for Non-Skewed Flaws 130

Table 28. POD Summary for LPA and MPA Trials 137

Table 29. Summary of LPA and MPA Sizing Accuracy for All Flaws 137

Contents (Continued)

Page

Table 30. Summary of LPA and MPA Sizing Accuracy for Tilted and Skewed Flaws Only .. 138

Table 31. Probe Parameters 161

Table 32. Workshop Participants 186

Table 33. Average Score for Each Workshop Presentation 190

Table 34. Summary of Actual Project Funding 191

Table 35. Total Team Cost Share Funding 193

Table 36. Status of Planned Cash Cost-Share 194

Table 37. Status of Planned In-Kind Support 195

Table 38. Status of Additional Cash Cost-Share 197

Table 39. Status of Additional In-Kind Support 197

Table 40. Status of Other Support 199

Figures

Figure 1. OD Girth Weld Inspection Using 2D MPA Probes 5

Figure 2. OD Inspection Using Flexible 2D MPA Probe 6

Figure 3. Internal Inspection Using 2D MPA Probe Modules 7

Figure 4. Stationary 2D MPA Probe for Continuous Monitoring 8

Figure 5. Example of Stationary Thickness Monitoring Using Flexible MPA Probe 8

Figure 6. Layout of LPA (16 Elements) and MPA (16 × 8 Elements) Probes with Identical Length, Pitch, Number, and Size of Elements in Primary Direction – X and Total Width in Secondary Direction – Y 10

Figure 7. Comparison of LPA and MPA Capabilities to Resolve 3-mm Gap between Flaws at -6 dB Level 11

Figure 8. Comparison of LPA and MPA Capabilities to Size the Length of Two Flaws: 5- and 15-mm Long 12

Figure 9. Generation of Acoustical Beam with MPA Skewed in Secondary Direction for Improved Detection and Sizing of Skewed Flaws 14

Contents (Continued)

Page

Figure 10. Comparison of LPA and MPA Capabilities to Detect Skewed Flaws 14

Figure 11. Flexible Matrix Probe Design Layout (Original Layout 1, Elements – 12 × 5) (Element size - S_x = 1 mm and S_y = 2 mm, Gaps - G_x = 0.5 mm and G_y = 1 mm) 15

Figure 12. Near Field Depth (H) with Original Flexible Matrix Probe Layout 1 (Elements 12×5, Primary and Secondary Direction, 3 MHz, Longitudinal Wave) 18

Figure 13. Near Field Depth (H) with Original Flexible Matrix Probe Layout 1 (Elements 12×5, Primary and Secondary Direction, 3 MHz, Longitudinal Wave, Reduced Size S_y = 1 mm and Reduced Gap G_y = 0.5 mm)..... 19

Figure 14. Near Field Depth (H) with Modified Flexible Matrix Probe Design (Elements 12×5 and Variable Aperture, Primary and Secondary Directions, 3 MHz, Longitudinal Wave)..... 20

Figure 15. Layout Optimization – Longitudinal Wave Normal Beam Focusing at 25-, 16-, and 8-mm Depth with Layout 1 of FMPA (Elements - 12×5, Pipe Specimen, S_x = 1 mm, S_y = 2 mm, G_x = 0.5 mm and G_y = 1 mm) 24

Figure 16. Layout Optimization – Longitudinal Wave Normal Beam Focusing at 25-, 16-, and 8-mm Depth with Design 4 of FMPA (Elements - 10×6, Plate Specimen, S_x = 1 mm, Reduced S_y = 1.5 mm, G_x = 0.5 mm and G_y = 1 mm)..... 25

Figure 17. Layout Optimization – Longitudinal Wave Normal Beam Focusing at 25-, 16-, and 8-mm Depth with Layout 1 of FMPA (Elements - 12×5, Plate Specimen, Sx = 1 mm, Sy = 2 mm, Gx = 0.5 mm and Gy = 1 mm)..... 26

Figure 18. Pipe Dent Geometry 27

Figure 19. Probe Longitudinal and Transverse Orientation in the Dent 28

Figure 20. Focusing and Beam Steering at 25- and 16-mm Focal Depth with Full-Array Aperture..... 31

Figure 21. Focusing and Beam Steering at 8-mm Focal Depth with Full-Array Aperture..... 32

Figure 22. Focusing and Beam Steering at 8-mm Focal Depth with Reduced FMPA Aperture 8×5..... 32

Figure 23. Pipe Wall Thinning (Four Spots at 0.1- and 0.2-mm Increment) Simulation with FMPA at 3 MHz 34

Figure 24. Pipe Wall Thinning (Four Spots) Simulation with FMPA at 7 MHz at 0.1-mm Increment 35

Figure 25. Flaws in Dent (Elbow) (FMPA 3 MHz, LW, C-Scan and Echo Dynamics) 36

Contents (Continued)

Page

Figure 26. Flaws in Dent (Elbow) (FMPA 3 MHz, LW, Calibration Notch and ID Signals) ... 37

Figure 27. Flaws in Dent (Elbow) (FMPA 3 MHz, LW, 10- × 1.0- and 10- × 1.5-mm Notch Signals) ... 37

Figure 28. Flaws in Dent (Groove) (FMPA 3 MHz, LW, C-Scan and Echo Dynamics) ... 38

Figure 29. Flaws in Dent (Groove) (FMPA 3 MHz, LW, Calibration Notch and ID Signals) . 39

Figure 30. Flaws in Dent (Groove), FMPA 3 MHz, LW, 10- × 1.0- and 10- × 2.0-mm Notch Signals) ... 39

Figure 31. Position of MPA Probe for Pipe Inspection from the ID ... 40

Figure 32. Variable FD and Gx - Gx 0.1 mm (Top) and Gx 0.3 mm (Bottom) (ID MPA 5 MHz, Active Aperture 16×4, WP 10 mm, SW 45 degrees) ... 42

Figure 33. Variable FD and Gx – Gx 0.1 mm (Top) and Gx 0.3 mm (Bottom) (ID MPA 5 MHz, Active Aperture 16×4, WP 5 mm, SW 45 degrees) ... 43

Figure 34. Variable FD and Gx – Gx 0.1 mm (Top) and Gx 0.3 mm (Bottom) (ID MPA 5 MHz, Active Aperture 16×4, WP 0.1 mm, SW 45 degrees) ... 43

Figure 35. Variable Large Sx (ID MPA 5 MHz, Active Aperture 16×4, FD 25 mm, WP 10 mm, SW 45 Degrees, Sy – 0.5 mm, Gx – 0.3 mm, Gy – 0.1 mm) ... 44

Figure 36. Higher Frequency (ID MPA 10 MHz, Active Aperture 16×4, FD 25 mm, WP 10 mm, SW 45 Degrees, Sy – 0.5 mm, Gx – 0.3 mm, Gy – 0.1 mm) ... 44

Figure 37. Large WP 25.4 mm and Small ID Inch (ID MPA 5 MHz, Active Aperture 16×4, FD 25 mm, SW 45 Degrees, Sx and Sy – 0.5 mm, Gx and Gy – 0.1 mm) ... 45

Figure 38. Variable Refracted Angle and Gx – Gx 0.6 mm (Top) and Gx 1.2 mm (Bottom) (ID MPA 5 MHz, Active Aperture 16×4, FD 25 mm, WP 40 mm, Sx and Sy 0.5 mm, Gy 0.3 mm) ... 51

Figure 39. Variable Refracted Angle, Large Sx and Gx – Gx 0.6 mm (Top) and Gx 1.2 mm (Bottom) (ID MPA 5 MHz, Active Aperture 16×4, FD 25 mm, WP 40 mm, Sx and Sy 1 mm, Gy 0.6 mm) ... 51

Figure 40. Reduced Active Aperture, Variable FD and Gx – Gx 0.6 mm (Top) and Gx 1.2 mm (Bottom) (ID MPA 5 MHz, WP 40 mm, LW 25 degrees, Sx 1 mm, Sy 1 mm, Gy 0.6 mm) ... 54

Figure 41. Variable Element Size and Gap – Increased Sx and Gx (ID MPA 5 MHz, Active Aperture 16×4, FD 25 mm, WP 40 mm, LW 25 degrees) ... 54

Contents (Continued)

Page

Figure 42. Variable Aperture and FD – Increased Sx – 0.75 mm and Gx – 0.6 mm (ID MPA 5 MHz, WP 40 mm, LW 25 degrees) 55

Figure 43. Variable Angle and FD – Top - Requested Refracted Angle 15 Degrees, Actual 7-13 degrees, Bottom – Requested Refracted Angle 25 Degrees, Actual 11-20 Degrees (ID MPA 5 MHz, Active Aperture 12×4, WP 40 mm, Sx and Sy 0.5 mm, Gx and Gy 0.6 mm) 57

Figure 44. Variable Angle and FD – Top - Requested Refracted Angle 35 Degrees, Actual 16-28 Degrees, Bottom – Requested Refracted Angle 45 Degrees, Actual 24-36 Degrees (ID MPA 5 MHz, Active Aperture 12×4, WP 40 mm, Sx and Sy 0.5 mm, Gx and Gy 0.6 mm) 57

Figure 46. Primary Steering Error vs. WP, FD, and Gx (ID MPA 5 MHz, Active Aperture 16×4, LW 15 Degrees) 58

Figure 47. Primary Focal Size and Steering Error vs. Refracted Angle and Gx (ID MPA 5 MHz, Active Aperture 16×4, FD 25 mm, WP 40 mm) 58

Figure 48. Primary Focal Size and Steering Error vs. Refracted Angle and FD (ID MPA 5 MHz, Active Aperture 12×4, WP 40 mm) 59

Figure 49. Primary Focal Size vs. Active Aperture, Sx, and Gx (ID MPA 5 MHz, FD 25 mm, WP 40 mm, LW 25 Degrees) 59

Figure 50. Primary Steering Error vs. Active Aperture, Sx, and Gx (ID MPA 5 MHz, FD 25 mm, WP 40 mm, LW 25 Degrees) 60

Figure 51. Primary Coverage vs. Active Aperture, Sx, and Gx (ID MPA 5 MHz, FD 25 mm, WP 40 mm, LW 25 Degree) 60

Figure 52. Variable Gy and FD (ID MPA 5 MHz, Active Aperture 16×4, WP 40 mm, LW 15 Degrees, Sx 0.5 mm, Gx 0.6 mm, Sy 1 mm) 66

Figure 53. Variable Gy and FD (ID MPA 5 MHz, Active Aperture 16×4, WP 40 mm, LW 30 Degrees, Sx 0.5 mm, Gx 0.6 mm, Sy 1 mm) 66

Figure 54. Secondary Focal Size vs. FD, Sy, and Gy (ID MPA 5 MHz, Active Aperture 16×4, WP 40 mm, LW 15 Degrees, Sx 0.5 mm, Gx 0.6 mm) 67

Figure 55. Secondary Steering Error vs. FD, Sy, and Gy (ID MPA 5 MHz, Active Aperture 16×4, LW 15 Degrees, Sx 0.5 mm, Gx 0.6 mm) 67

Figure 56. Secondary Focal Size vs. FD, Sy, and Gy (ID MPA 5 MHz, Active Aperture 16×4, WP 40 mm, LW 30 Degrees, Sx 0.5 mm, Gx 0.6 mm) 68

Figure 57. Secondary Steering Error vs. FD, Sy, and Gy (ID MPA 5 MHz, Active Aperture 16×4, LW 30 Degrees, Sx 0.5 mm, Gx 0.6 mm) 68

Contents (Continued)

Page

Figure 58. Normal Beam (Optimized ID MPA 5 MHz, Active Aperture 16×4, FD 25 mm, WP 40 mm) 72

Figure 59. Normal Beam (Optimized ID MPA 5 MHz, Active Aperture 16×4, FD 12 mm, WP 40 mm) 73

Figure 60. Normal Beam (Optimized ID MPA 5 MHz, Active Aperture 16×4, FD 3 mm, WP 40 mm) 74

Figure 61. Optimized ID MPA 5 MHz, Active Aperture 16×4, FD 25 mm, WP 40 mm, Top – Primary 45 Degrees, Secondary 0 Degrees, Bottom – Primary 0 Degrees, Secondary 30 Degrees 75

Figure 62. Optimized ID MPA 5 MHz, Active Aperture 16×4, FD 12 mm, WP 40 mm, Top – Primary 45 Degrees, Secondary 0 Degrees, Bottom – Primary 0 Degrees, Secondary 30 Degrees 75

Figure 63. Optimized ID MPA 5 MHz, Active Aperture 16×4, FD 3 mm, WP 40 mm, Top – Primary 45 Degrees, Secondary 0 Degrees, Bottom – Primary 0 Degrees, Secondary 30 Degrees 76

Figure 64. Optimized ID MPA 5 MHz, Active Aperture 16×4, FD 25 mm, WP 0.1 mm, Top – Primary 45 Degrees, Secondary 0 Degrees, Bottom – Primary 0 Degrees, Secondary 30 Degrees 76

Figure 65. Optimized ID MPA 5 MHz, Active Aperture 16×4, FD 12 mm, WP 0.1 mm, Top – Primary 45 Degrees, Secondary 0 Degrees, Bottom – Primimary 0 Degrees, Secondary 30 Degrees 77

Figure 66. Optimized ID MPA 5 MHz, Active Aperture 16×4, FD 3 mm, WP 0.1 mm, Top – Primary 45 Degrees, Secondary 0 Degrees, Bottom – Primary 0 Degrees, Secondary 30 Degrees 77

Figure 67. Primary and Secondary Focal Size vs. FD and WP – Optimized ID MPA 5 MHz, Active Aperture 16×4, Normal Beam 78

Figure 68. Primary and Secondary Focal Size vs. FD and WP – Optimized ID MPA 5 MHz, Active Aperture 16×4, Primary 45 Degrees, Secondary 0 Degrees 78

Figure 69. Primary and Secondary Focal Size vs. FD and WP (Optimized ID MPA 5 MHz, Active Aperture 16×4, Primary 0 Degrees, Secondary 30 Degrees) 79

Figure 70. Primary and Secondary Steering Error vs. FD and WP (Optimized ID MPA 5 MHz, Active Aperture 16×4, Left – Primary 45-Degrees, Secondary 0 Degrees, Right – Primary 0 Degrees, Secondary 30 Degrees) 79

Contents (Continued)

Page

Figure 71. FBH (Variable Diameter) Interaction at 3 mm from ID, B-Scan, and Echo Dynamics (ID MPA 5 MHz, Active Aperture16×4, FD 3 mm, WP 40 mm, Normal Beam) 81

Figure 72. HSBH (Variable Diameter) Interaction at 3 mm from ID, B-Scan, and Echo Dynamics (ID MPA 5 MHz, Active Aperture16×4, FD 3 mm, WP 40 mm, Normal Beam) 81

Figure 73. FBH (2-mm Diameter) Interaction at Variable Distance from OD, B-Scans, FD 6, 12, and 25 mm (ID MPA 5 MHz, Active Aperture16×4, WP 40 mm, Normal Beam) 82

Figure 74. Signal Strength, FBH (2-mm Diameter) Interaction at Variable Distance from OD, FD 6, 12, and 25 mm (ID MPA 5 MHz, Active Aperture16×4, WP 40 mm, Normal Beam) 83

Figure 75. Mid-Wall FBH and HSBH (Variable Diameter) Interaction, Typical Echo Dynamics at 12 mm from ID (ID MPA 5 MHz, Active Aperture16×4, FD 12 mm, WP 40 mm, Normal Beam)..... 84

Figure 76. Signal Strength, FBH and HSBH Interaction, Variable Diameter and Distance from ID, FD 3, 12, and 25 mm (ID MPA 5 MHz, Active Aperture16×4, WP 40 mm, Normal Beam) 84

Figure 77. OD Connected Notch Interaction, Variable Height, and WT, B-Scans (ID MPA 5 MHz, Active Aperture 16×4, FD 6, 12, and 25 mm, WP 40 mm, Primary 45 Degrees, Secondary 0 Degrees)..... 86

Figure 78. OD Connected Notch Interaction, Variable Height, and WT, Echodynamics (ID MPA 5 MHz, Active Aperture 16×4, FD 6, 12 and 25 mm, WP 40 mm, Primary 45 Degrees, Secondary 0 Degrees)..... 87

Figure 79. OD Connected Notch Interaction, Variable Height, and WT, B-Scans (ID MPA 5 MHz, Active Aperture 16×4, FD 6, 12, and 25 mm, WP 20 mm, Primary 45 Degrees, Secondary 0 Degrees)..... 88

Figure 80. OD Connected Notch Interaction, Variable Height, and WT, Echodynamics (ID MPA 5 MHz, Active Aperture 16×4, FD 6, 12 and 25 mm, WP 20 mm, Primary 45 Degrees, Secondary 0 Degrees)..... 89

Figure 81. OD Connected Notch Interaction, Variable Height, and WT, B-Scans (ID MPA 5 MHz, Active Aperture 16×4, FD 6, 12, and 25 mm, WP 0.1 mm, Primary 45 Degrees, Secondary 0 Degrees) 90

Figure 82. OD Connected Notch Interaction, Variable Height, and WT, Echodynamics (ID MPA 5 MHz, Active Aperture 16×4, FD 6, 12, and 25 mm, WP 0.1 mm, Primary 45 Degrees, Secondary 0 Degrees)..... 91

Contents (Continued)

Page

Figure 83. MPA Beam Spatial Steering and Definitions 92

Figure 84. Setup for SCC Detection, 3D Steering 93

Figure 85. ID MPA 5 MHz, 16×4, 3D Steering, Variable Branch Angle, C-Scans 94

Figure 86. ID MPA 5 MHz, 16×4, 3D Steering, Variable Branch Angle, B-Scans 95

Figure 87. ID MPA 5 MHz, 16×4, 3D Steering, SCC Height Sizing on Simulated B-Scans . 96

Figure 88. ID MPA 5 MHz, 16×4, 3D Steering, SCC Length Sizing on Simulated Skew-Enhanced Sectorial Scan in Secondary Direction S2s-Scans 97

Figure 89. ID MPA 5 MHz, 16×4 (Comparison of SCC and planar flaws) 98

Figure 90. Permanently Mounted FMPA 24×12 for Health Monitoring 100

Figure 91. Health Monitoring Scanning and Signals 101

Figure 92 Normal Beam, Rigid MPA 5 MHz, Active Aperture 4×4, FD 6 mm (L), FD 12 mm (R), Dry Couplant 103

Figure 93. Normal Beam, Rigid MPA 5 MHz, Active Aperture 8×4, FD 6 mm (L), FD 12 mm (R), Dry Couplant..... 103

Figure 94. Normal Beam, Rigid MPA 5 MHz, Active Aperture 12×6, FD 6 mm (L), FD 12 mm (R), Dry Couplant..... 104

Figure 95. Beam Steering 10 Degrees, Rigid MPA 5 MHz, Active Aperture 8×4, FD 3 mm, Dry Couplant..... 104

Figure 96. Beam Steering 10 Degrees, Rigid MPA 5 MHz, Active Aperture 12×6, FD 25 mm, Dry Couplant..... 105

Figure 97. Detection of FBH Reflectors in a 12-mm WT Using a MPA 5-MHz Probe with a 4×4 Active Aperture and a 0-Degree Beam Angle (C-Scan Views)..... 110

Figure 98. Detection of FBH Reflectors in a 12-mm WT Using a MPA 5-MHz Probe with a 4×4 Active Aperture, 12-mm FD, and a 0-Degree Beam Angle 110

Figure 99. Detection of FBH Reflectors in a 12-mm WT Using a MPA 5-MHz Probe with a 4×4 Active Aperture, 3-mm FD, and a 0-Degree Beam Angle 111

Figure 100. Detection of FBH Reflectors in a 12-mm WT Using a MPA 5-MHz Probe with a 4×4 Active Aperture, 12-mm FD, and a 10-Degree Beam Angle 112

Figure 101. Concept 2; 2D Flexible Array Probe Fabricated During the Project 115

Figure 102. Concept 3; ID MPA Probe Fabricated During the Project 116

Contents (Continued)

Page

Figure 103. Existing 5-MHz, 16×8 Element MPA Probe 116

Figure 104. Existing 5-MHz, 64×8 Element MPA Probe 117

Figure 105. Existing 15-MHz, 11×11 Element MPA Probe 117

Figure 106. TomoCAR Setup 120

Figure 107. TomoCAR Images from Implanted Flaw Sample 1, Location 1610-1618 121

Figure 108. Location 108: Comparison of TomoCAR (L) and Metallographic Cross-Section (R) 121

Figure 109. Location 856: Comparison of TomoCAR (L) and Metallographic Cross-Section (R) 122

Figure 110. Location 978: Comparison of TomoCAR (L) and Metallographic Cross-Section (R) 122

Figure 111. MPA Open Trial Scan 123

Figure 112. Screen Output Display for Open Trial Scans 124

Figure 113. MPA Blind Trial Scan 125

Figure 114. MPA Electronics and Scanner 125

Figure 115. Example of Saw Cut Segment 130

Figure 117. Example of CR on Un-Polished Water Jet Cut Samples 132

Figure 118. Polished and Etched Weld Cross-Section Showing Typical Measurements 132

Figure 119. Example of Difficulty in Viewing Tight Flaws at 5× 133

Figure 120. POD Curve for MPA Blind Trial 135

Figure 121. POD Curve for MPA Open Trial 135

Figure 122. Combined Blind Trial POD Curve for all Five LPA AUT Systems 136

Figure 123. POD Curve for Best LPA Blind Trial 136

Figure 124. Example of Flexible 2D MPA Probe in Dent 140

Figure 125. Simulation Example of Beam Compensation for Surface Contour 141

Figure 126. Screen Display of LVDT Surface Contour 141

Contents (Continued)

Page

Figure 127. 2D Flexible Array Probe Used for Experimental Trials 142

Figure 128. Flexible MPA Probe Scanning Carriage and Instrumentation 143

Figure 129. Flexible MPA Scan of OD Notches in Dent Location..... 143

Figure 130. Flexible MPA Scan of Through-Wall Crack in Dent Location 144

Figure 131. Scan of Notches in 25-mm-Thick Sample 144

Figure 132. ID MPA Probe..... 145

Figure 133. Sketch of Hole Sample 146

Figure 134. Sketch of Notch Sample 146

Figure 135. Machined Reference Samples 147

Figure 136. Initial Evaluation Setup for ID MPA Probe..... 148

Figure 137. Hole Sample Using 4×4 Element Aperture at Focal Depths of 5 and 10 mm ... 149

Figure 138. Hole Sample Using 6×4 Element Aperture at Focal Depths of 5 and 10 mm ... 149

Figure 139. Hole Sample Using 8×4 Element Aperture at Focal Depths of 5 and 10 mm ... 150

Figure 140. Hole Sample Using 12×4 Element Aperture at FD of 5 and 10 mm..... 150

Figure 141. Noise Level Between Front Surface and First Back Wall Reflection..... 151

Figure 142. Comparison of Modeling Simulation and Actual Results of 2-mm FBH Using 6×4 Element Aperture and 5-mm FD 152

Figure 143. Detection of Round Bottom Holes Using Loss of Back Surface Signal..... 153

Figure 144. Detection of Axial and Circumferential Notches in Reference Sample..... 154

Figure 145. Detection of Circumferential Notches Using 0-Degree L-Wave with a 6×4 Element Aperture 154

Figure 146. Original Pipe Demonstration Loop 155

Figure 147. Original Probe Carrier 155

Figure 148. Tethered Probe Carrier in 6-in.-Diameter Pipe..... 156

Figure 149. Modified Probe Carrier with Motor..... 157

Figure 150. Modified Demonstration Pipe with Bore Scanner..... 157

Contents (Continued)

Page

Figure 151. 0-Degree Longitudinal Scan of Hole Sample in Demonstration Pipe 158

Figure 152. Scan of Notch Sample in Demonstration Pipe Showing Circumferential and Axial Notches 158

Figure 153. 0-Degree Longitudinal Scan of Notch Sample in Demonstration Pipe Showing Circumferential and Axial Notches..... 159

Figure 154. 2D MPA Probe; 5 MHz (16×8 Elements)..... 161

Figure 155. Health Monitoring Demo Sample..... 162

Figure 156. Stationary Electronic Scan Data of 1.2-mm-Deep Notch Using 5-MHz Probe with 6×4 Element Aperture 163

Figure 157. Stationary Electronic Scan Data of Unflawed Base Metal Adjacent to Notch Using 5-MHz Probe with 6×4 Element Aperture..... 163

Figure 158. Stationary Electronic Scan Data of Hole Group 1 Using 5-MHz Probe with 4×4 Element Aperture 164

Figure 159. Stationary Electronic Scan Data of Hole Group 1 Using 15-MHz Probe with 3×3 Element Aperture 164

Figure 160. Stationary Electronic Scan Data of Hole Group 3 Using 5-MHz Probe with 4×4 Element Aperture 165

Figure 161. Stationary Electronic Scan Data of Hole Group 3 Using 15-MHz Probe with 3×3 Element Aperture 165

Figure 162. Stationary Electronic Scan Data of 2-mm-Diameter FBH, 6.3-mm Deep Using 5-MHz Probe with 4×4 Element Aperture..... 166

Figure 163. Stationary Electronic Scan Data of 2-mm-Diameter FBH, 6.3-mm Deep Using 5-MHz Probe with 6×4 Element Aperture..... 167

Figure 164. Stationary Electronic Scan Data of 2-mm-Diameter FBH, 6.3-mm Deep Using 15-MHz Probe with 3×3 Element Aperture..... 167

Figure 165. Stationary Electronic Scan Data of 2-mm-Diameter FBH, 12.7-mm Deep Using 5-MHz Probe with 4×4 Element Aperture and 12 mm FD 168

Figure 166. Stationary Electronic Scan Data of 2-mm-Diameter FBH, 19.1-mm Deep Using 5-MHz Probe with 4×4 Element Aperture and 19 mm FD 168

Figure 167. Stationary Electronic Scan Data of 2-mm-Diameter FBH, 19.1-mm Deep Using 5-MHz Probe with 6×4 Element Aperture and 25 mm FD 169

Contents (Continued)

Page

Figure 168. Magnetic Particle Results of SCC in Pipe Sample 170

Figure 169. 5-MHz MPA Probe Mounted on Shear Wave Wedge 170

Figure 170. MPA Results of SCC 171

Figure 171. Field Trial Site 173

Figure 172. Map of Keystone Pipeline Project 173

Figure 173. MPA 2-Axis Scanner 175

Figure 174. Output Display of MPA Data..... 175

Figure 175. U-Groove Joint for UTQ Calibration Block..... 176

Figure 176. UTQ Calibration Drum and 9.8-mm Calibration Sample 177

Figure 177. Field Trial Weld Joint Geometry 178

Figure 178. EWI Truck Following UTQ Truck Performing AUT Scans for TCPL..... 178

Figure 179. Weld MLA 4681 - UTQ Scan Screen Capture..... 179

Figure 180. Weld MLA 4681 - EWI MPA Scan Screen Captures (Various Angles) 180

Figure 181. Weld MLA 4681 - EWI MPA Scan Screen Captures (0 Degree Only) 180

Figure 182. Weld MLA 4925 - UTQ Scan Screen Capture..... 181

Figure 183. Weld MLA 4925 - EWI MPA Scan Screen Captures (Various Angles) 182

Figure 184. Weld MLA 4925 - EWI MPA Scan Screen Captures (0 Degree Only) 182

Figure 185. Dr. Todorov Presenting Modeling and Inspection Simulations Data 188

Figure 186. MPA Probe Concept 1 Demonstration Equipment 189

Figure 187. MPA Concept 3 Probe Mounted in Carrier 189

Figure 188. Survey Responses to Question 1 190

Figure 189. Quarterly Payable Milestones/Invoices - DTPH56-08-T-000002..... 192

1.0 Introduction

This program was specifically designed to address Topic Area 3, Defect Detection/Characterization of broad agency announcement (BAA) DTPH56-07-BAA-000002 as identified by the Defect Detection/Characterization Technical Track Session workgroup during the Government/Industry Pipeline R&D Forum, held in New Orleans, LA, February 7-8, 2007 (i.e., Develop More Accurate Detection and Assessment Tools that Improve Size and Depth Detection Accuracy from Either Outside or Inside the Pipe, the Assessment Detection/Discrimination of Secondary Features, and the Calculations of Defect Growth Rates).

The need for developing more accurate detection and assessment tools and to improve size and depth measurement accuracy of crack-like and planar imperfections is becoming more apparent in the pipeline industry.[1] Cracking and planar imperfections are some of the most difficult defects to size and assess. Cracking is involved in hydrogen-induced damage, stress-corrosion cracking (SCC) failures, mechanical damage failures, and many weld failures. Phased array (PA) ultrasonic testing (UT) technology using linear phased array (LPA) probes is proven to be superior to conventional automated ultrasonic testing (AUT) equipment in its capability to detect and size defects.[2-5] An enhancement of defect detection and sizing accuracy and improvement of predicted pipeline reliabilities may be possible using the next generation of matrix phased array (MPA) ultrasonic techniques.

The overall objective of the program was to enhance detection and sizing accuracy of crack-like and planar imperfections created during pipeline fabrication and service using MPA ultrasonic tools with the goal of improving the predicted reliability of pipelines during early stage design. The technical objectives of the program were to:

- Develop a concept for MPA ultrasonic probe modules applicable for either outside diameter (OD) or inside diameter (ID) pipe inspection and carried by different inspection systems.
- Define and optimize detection and sizing capabilities of the modules via modeling and simulation.
- Design and fabricate two probe modules: one for OD and one for ID inspection.
- Determine and demonstrate the detection and sizing performance of the probe modules.

Although ultrasonic inspection technology and tools has improved significantly, there is still a need for more reliable detection and accurate sizing of crack-like and planar defects, cracks in dents, and detection of secondary features within deformed pipe.[1] MPA UT technology has the potential to provide the needed inspection improvements. At the time the project was funded, it was recognized that additional work was needed to evaluate MPA technology to meet these challenges. To address the issues, the project concentrated on the following topics:

- Inspection of complex defects using optimized MPA probe modules to electronically focus, steer, and scan in multiple directions.

- The use of improved resolution, imaging, defect quantification, and characterization to optimize detection sizing accuracy in pipeline inspections.

- The use of advanced signal analysis to combine information from multiple incidence angles to infer the mechanical damage/corrosion-induced roughness and wall thickness (WT) in difficult to detect and size complex defects.

- Fabrication of prototypes of MPA probe modules and determination of detection and sizing performance in laboratory and field conditions.

The program was executed with cash and in-kind cost share contributions from various organizations. The majority of funding was provided by the U.S. Department of Transportation Pipeline and Hazardous Materials Safety Administration (DOT PHMSA). Remaining cash and in-kind cost share contributions were provided by Edison Welding Institute (EWI), ConocoPhillips, BP, TransCanada Pipeline (TCPL), ExxonMobil, Commissariat à l'Energie Atomique (CEA) division of the Laboratory for Integration of Systems and Technologies (LIST), Imasonic, Zetec, itRobotics, and UT Technology.

The technical approach was executed and transferred to industry via eight tasks described below.

- Task 1 – Develop a Concept (Funding Source: EWI)
  - Developed and coordinated concept for a MPA modules applicable for either outside or inside inspection of the pipe and carried by different inspection tools and platforms.

- Task 2 – Perform Virtual Optimization (Funding Source: DOT, EWI, Industry In-kind)
  - Developed improved 3D modeling, simulation, design approach and tools for detection and virtual visualization of fabrication cracks, in-service developed SCC and dents with cracks in carbon steel pipes and welds using rigid and flexible MPA modules.
  - Defined and optimized detection and sizing capabilities of the proposed modules using the improved 3D modeling, design, and simulation approach.
  - EWI worked jointly with CEA/LIST to develop improved CIVA tools. EWI investigated MPA beam interaction with complex flaws and virtual visualization optimization using improved CIVA tools. CEA/LIST provided in-kind contribution of engineering direct labor to develop the improved CIVA tools.

- Task 3 – Design of Matrix PA Modules (Funding Source: EWI)
  - EWI designed and fabricated two representative MPA modules - one flexible for outside and one rigid circumferential for inside inspection of the pipe. EWI designed the MPA modules using improved CIVA tools developed during Task 2.

- Task 4 – Fabrication of Matrix PA Modules (Funding Source: EWI, Industry In-kind)
  - Imasonic fabricated representative MPA modules and provided an in-kind contribution of engineering direct labor and materials.

- Task 5 – Laboratory Performance Determination (Funding Source: DOT, Industry Direct and In-kind)
  - Determined the performance and capabilities of the MPA modules in laboratory conditions using the equipment and tools provided by EWI and project partners.
  - EWI developed a methodology for open and blind trials. EWI then performed fingerprinting of the specimens. EWI conducted destructive validation and statistical analysis to determine the performance of MPA modules under laboratory conditions.
  - With funding provided by ExxonMobil, EWI conducted an extensive performance determination of ExxonMobil/ApplusRTD MPA system under laboratory conditions.
  - CEA/LIST and Zetec provided MPA equipment and engineering direct labor throughout project duration. itRobotics designed and provided a probe cart for the Concept 3 probe.
  - BAM provided TomoCar computed radiography services for fingerprinting weld specimens. ConocoPhillips provided $200K in cash cost sharing.

- Task 6 – Field Test and Field Pipes Initial Trial (Funding Source: DOT, Industry In-kind)
  - Performed a field test to define robustness of MPA prototypes. TCPL coordinated field testing comparison of MPA and LPA systems for girth weld inspection using zonal LPA (supplied by TCPL) and non zonal MPA (supplied by EWI) approaches. EWI developed a field test methodology, defined robustness of EWI MPA system in field conditions.
  - TCPL provided access to the Keystone pipeline construction site in Hardisty, Alberta (Canada) for field trials, the results from one UT system used to inspect the pipe during field trials, and engineering time. UT Technology also provided a truck for field trial execution and engineering direct labor.
  - EWI also performed several smaller trials on selected field pipes at Battelle Memorial Institute facilities in West Jefferson, Ohio.

- Task 7 – Industry/Government Training and Workshop (Funding Source: DOT, Industry In-kind)
  - A 1-week training class was provided at EWI for ExxonMobil staff.

- A 1-day workshop was conducted at EWI for DOT, pipeline operators, service providers to transfer project results to the industry.
- For the workshop, Zetec and Olympus NDT provided MPA equipment and engineering direct labor.

- Task 8 – Progress Meetings, Pipeline Conference, Annual Panel Peer Review, Reporting, and Program Management (Funding Source: DOT, Industry In-kind)
  - Conducted kick-off, progress and final meetings, published/presented papers, participated in DOT peer review meetings; prepared and submitted monthly and quarterly status reports, and the draft final project report.

This is the final technical report that contains the results of the research program.

2.0 Task 1 – Development of MPA Concepts

The versatility of 2D MPA makes it possible to electronically steer and focus an ultrasonic beam in three dimensions. With this versatility, it was surmised that MPA technology should provide more accurate detection and sizing of flaws and mechanical damage with less dependence on probe orientation. The objective of Task 1 was to develop initial draft concepts for pipeline inspection using 2D ultrasonic MPA technology. These initial concepts were then shared with industry partners who provided feedback for development of the final draft concepts. Based on the interests of industry partners, the following four concepts were formulated for investigation during this project:

- Concept 1 – Girth Weld Inspection from OD Surface
- Concept 2 – Inspection of Pipe Wall Damage from OD Surface
- Concept 3 – Inspection of Pipe Wall Damage from ID of Pipe
- Concept 4 – Stationary Flexible Array Monitoring of Pipe Wall.

These four concepts, as developed, are explained further in the following paragraphs.

Concept 1 – Girth Weld Inspection from OD Surface: This concept provides a means for inspecting pipeline girth welds using two rigid 2D MPA probes mounted on plastic wedges. The purpose of the scan is to detect weld fabrication flaws. Electronic beam steering, focusing, and scanning will produce full inspection coverage of the weld. The 2D array will also allow electronic skewing of the beam to detect off angle flaws, or to compensate for unintentional probe skewing caused by mechanical misalignment. A variation of this technique could possibly allow detection of flaws that are transverse to the weld axis without the need for additional probes. The use of 2D MPA probes may also provide improvement in time-of-flight diffraction (TOFD) scans that are currently performed using LPA probes and/or dedicated TOFD probes. If the TOFD quality is adequate, dedicated TOFD probes could also be eliminated. Ideally, it is

envisioned that girth weld inspection will be performed in a single circumferential mechanical scan using only two MPA probes. Concept 1 is represented in Figure 1.

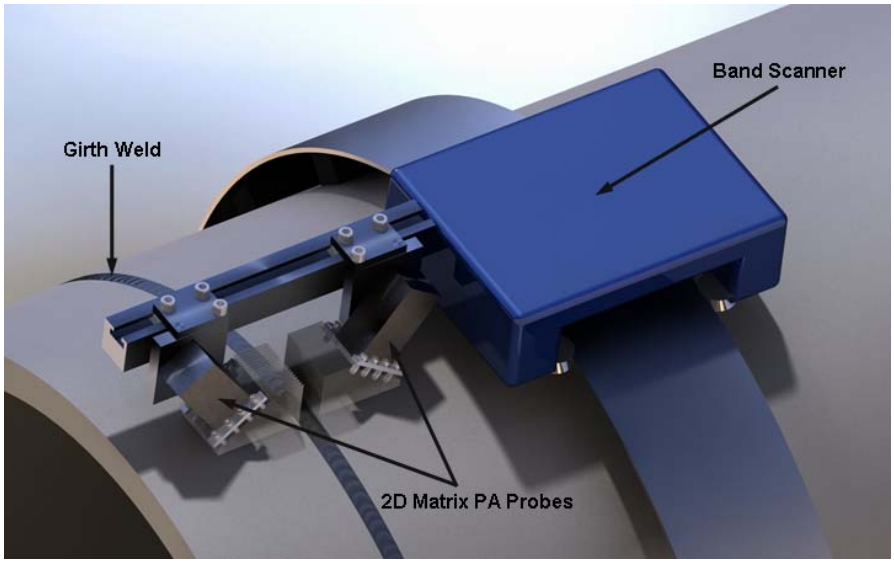

Figure 1. OD Girth Weld Inspection Using 2D MPA Probes

Concept 2 – Inspection of Pipe Wall Damage from OD Surface: This concept uses a flexible 2D MPA probe to inspect localized damaged areas of pipelines. The damage could be caused by corrosion pitting with associated inter-granular stress corrosion cracking (IGSCC), or from dents in the OD surface. The flexible array should be capable of mapping the general surface profile through a combination of ultrasonic data and displacement data from linear variable displacement transducers (LVDT). Electronic beam steering, focusing, and scanning will be used to ultrasonically measure the remaining pipe WT and detect any cracking associated with the surface damage. Concept 2 is represented in Figure 2.

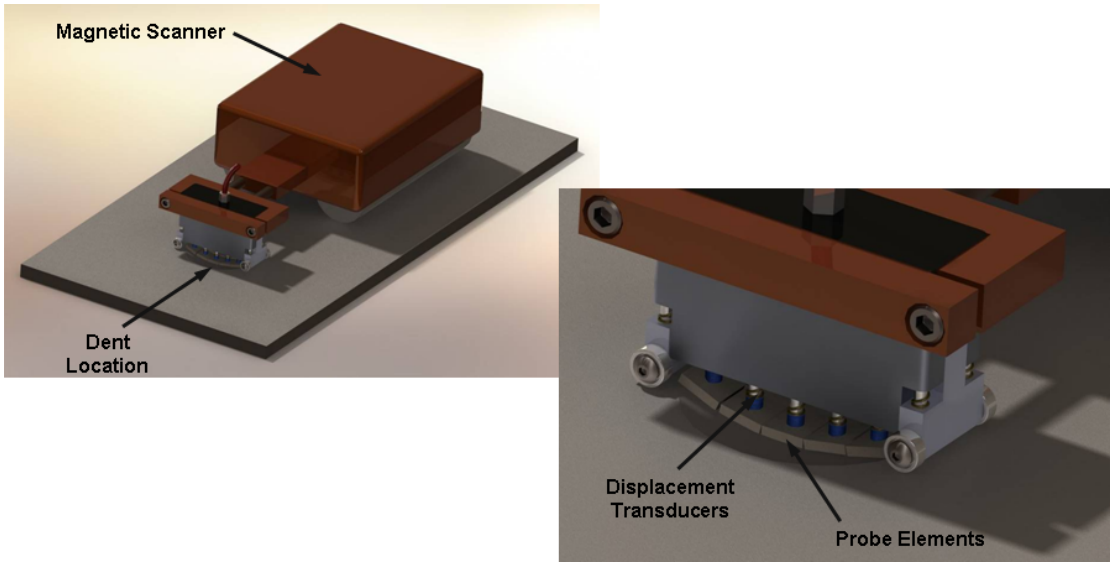

Figure 2. OD Inspection Using Flexible 2D MPA Probe

Concept 3 – Inspection of Pipe Wall Damage from ID of Pipe: This concept uses rigid 2D MPA probe module(s) to inspect localized damaged areas of pipes having diameters in the range of 4 to 8 in. The pipe damage could be caused by corrosion pitting with associated IGSCC, or from dents, or other mechanical damage. This inspection concept could be used in instances where access to the pipe is not possible due to insulation or other obstructions. It is envisioned that this inspection will use a robot or crawler to transport the probe module(s) to the area of interest. During inspection, the pipe will be filled with water which will provide a coupling medium for the ultrasound. Consequently, the MPA probe module(s) will need to be capable of operating fully immersed in water. The probe module(s) will not contact the ID surface of the pipe, but instead, stand off from the ID surface approximately 10 to 25 mm. The robot should be un-tethered and capable of storing or transmitting the inspection data for analysis by the operator. Electronic beam steering, focusing, and scanning will be used to ultrasonically measure the remaining pipe WT and detect any cracking associated with the surface damage. Concept 3 is represented in Figure 3.

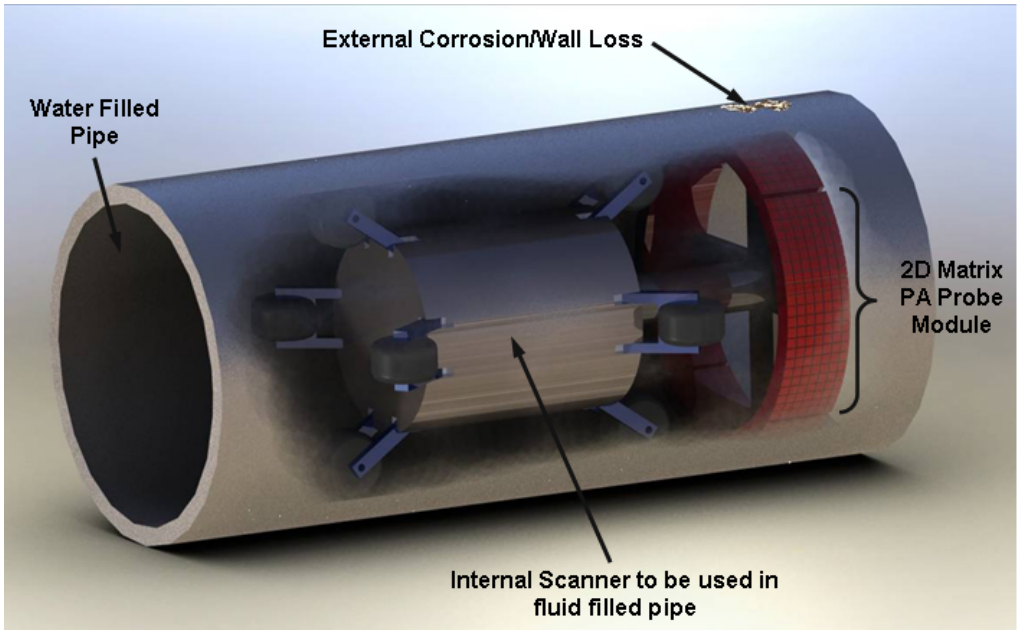

Figure 3. Internal Inspection Using 2D MPA Probe Modules

Concept 4 – Stationary Flexible Array Monitoring of Pipe Wall: This concept will use a flexible 2D MPA probe without LVDTs. In this arrangement a flexible array will be permanently or semi-permanently attached to the OD surface to monitor characteristics such as wall thinning, corrosion mapping, or flaw propagation over an extended time period. This concept could be used for in-service monitoring or for corrosion and crack growth studies. Electronic beam steering, focusing, and scanning will be used to ultrasonically measure the remaining pipe WT and to monitor flaw propagation at the probe location. Concept 4 is represented in Figure 4. Figure 5 shows a possible output for this concept.

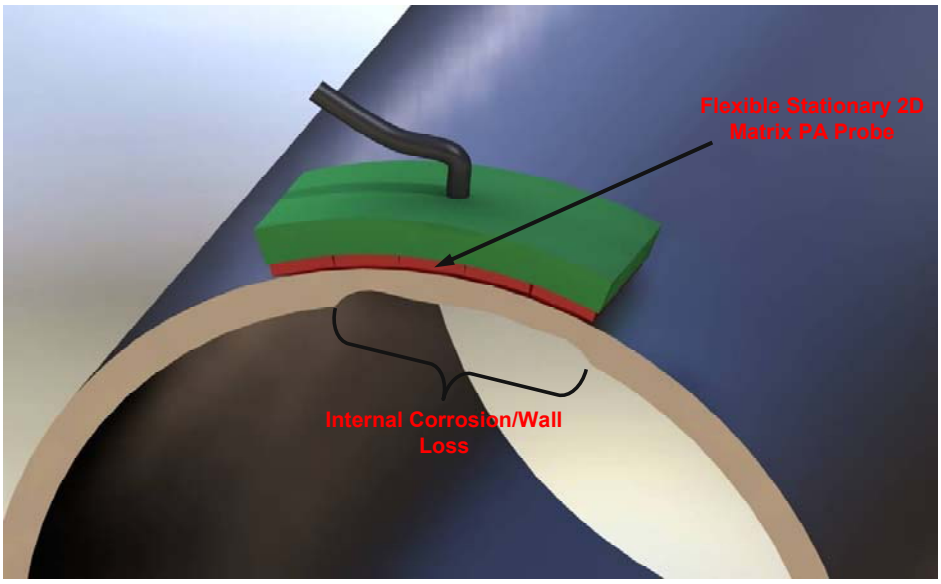

Figure 4. Stationary 2D MPA Probe for Continuous Monitoring

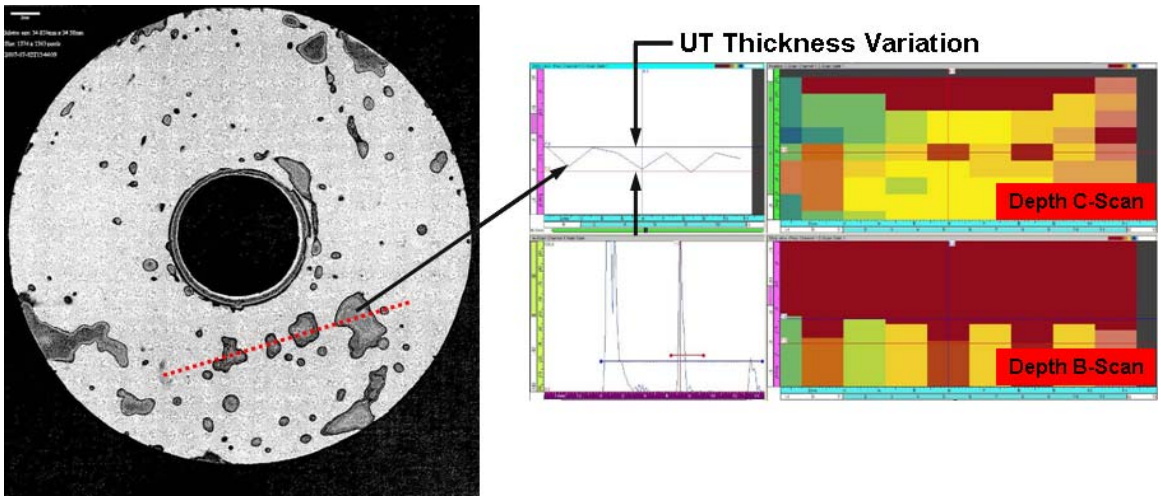

Figure 5. Example of Stationary Thickness Monitoring Using Flexible MPA Probe

After development of the four concepts, work was begun to investigate the advantages and disadvantages of each. For Concepts 2 and 3 prototype probes were designed and built to allow the technology to be investigated for pipeline applications. The remaining two concepts used probes and equipment provided by EWI and industry partners.

3.0 Tasks 2 and 3 – Virtual Optimization

3.1 MPA Optimization and Modeling

3.1.1 Comparison of LPA and MPA Performance for Flaw Detection, Sizing, and Resolution

In contrast to the conventional ultrasonic testing (UT) method, phased array (PA) UT technology uses a probe with many piezoelectric elements that are pulsed using programmed delay times. LPA UT uses an array of elements arranged in a line pattern that are pulsed with different delays. The acoustical beam can be formed by selecting a group (called an active group) of array elements. The acoustical beam can then be focused at a certain depth, steered to various refracted angles, then electronically scanned or moved to avoid the mechanical movement of the entire probe to and from the area of interest. Another significant advantage of the array probe is that several active groups can be simultaneously defined to perform pulse-echo (PE) (where one group transmits and receives the signals) and tandem, a.k.a., pitch-catch, (where one group transmits and another group receives the signals). While the capabilities of LPA to manipulate the acoustical beam in one direction (referred to as primary) are excellent, the acoustical beam cannot be manipulated into another or secondary direction. Recent developments in PA UT include the use of a MPA probe that has an active area divided into two dimensions. The division can be in the form of a 2D checker board or sectored rings. MPA probes have the potential for steering and focusing the acoustical beam in 3D space allowing the possibility of focusing at different depths and skew angles using the same wedge. New studies have reported the development and introduction of flexible, conformable matrix PA UT probes that improve inspection of complex shapes and joints as will be discussed further.

Two typical linear (16 elements) and matrix (16 × 8 elements) PA were selected and modeled to demonstrate the advantages of MPA over LPA in terms of flaw detection, sizing, and resolution. These probes are typical of probes that could be used for girth weld inspection (Concept 1). As shown in Figure 6, the two probes have identical length, pitch, number, and element dimensions along the primary direction (X). Eight elements were formed along the width of the MPA with a total width equal to the width of the LPA along the secondary (Y) direction. Further, the arrays were pulsed at the same frequency of 5 MHz and generated a shear wave at a 55-degree refracted angle with a wedge providing 38-degree incident angle. The shear wave beam was focused 8-mm deep in a typical 8-mm-thick steel plate specimen.

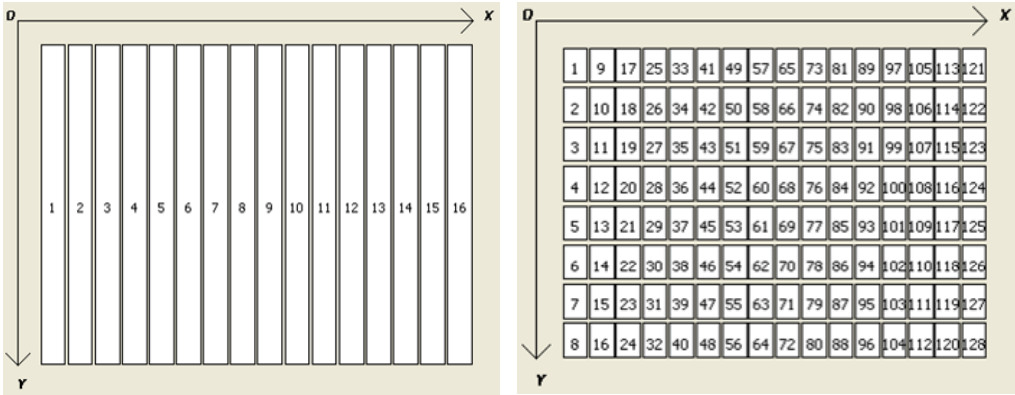

Linear Phased Array (LPA) Layout

Matrix Phased Array (MPA) Layout

Figure 6. Layout of LPA (16 Elements) and MPA (16 × 8 Elements) Probes with Identical Length, Pitch, Number, and Size of Elements in Primary Direction – X and Total Width in Secondary Direction – Y

To compare detection, resolution, and sizing capabilities of the LPA and MPA probes, notches were used simulating planar flaws connected to the back wall with lengths smaller and larger than the beam at the inspection area.

3.1.1.1 Resolution

The first models were built to demonstrate LPA and MPA capabilities in resolving flaws with small separation. Two notches 15-mm long × 1-mm high were separated by 3 mm and positioned on the back wall as shown in Figure 7. Each of the notches was selected to be larger than the beam of both the LPA and MPA to eliminate notch length as a factor that could possibly interfere with the resolution estimates. For each probe, the simulated C-Scan and echo dynamics are illustrated in Figure 7. It is clearly seen that the two notches are impossible to separate with the LPA down to -6 dB and will be reported as one flaw. The two notches are perfectly separated with the MPA probe down to -28.5 dB, which is more than 2 times smaller than the commonly accepted noise level of -20 dB.

Significantly better resolution is achievable with the MPA probe as compared to the LPA probe under equal conditions previously discussed. With MPA, the model allowed measurement of a 3.04-mm flaw separation at a level of -6 dB, which is very close to the actual model of 3 mm.

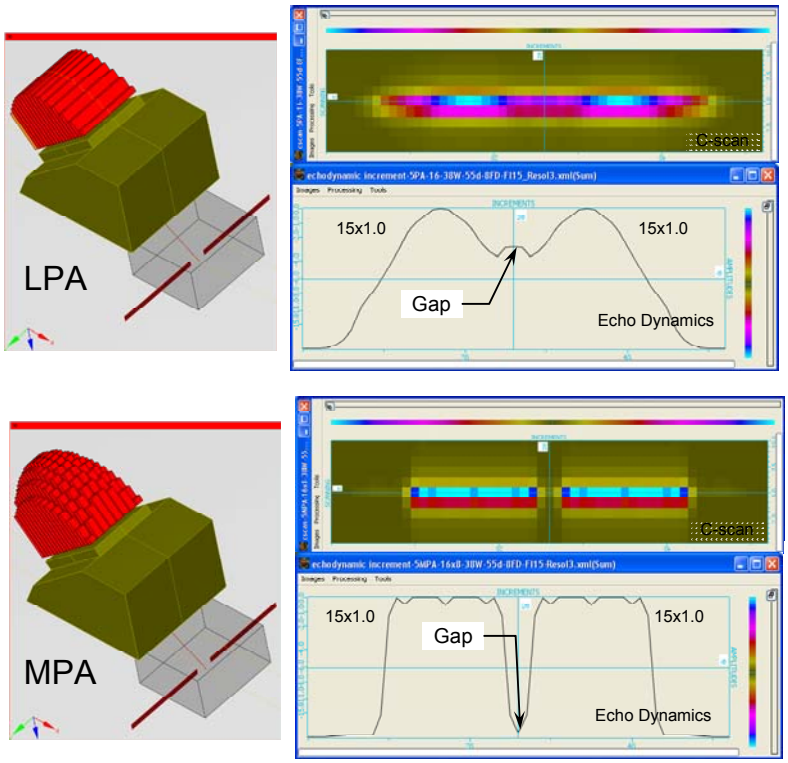

Figure 7. Comparison of LPA and MPA Capabilities to Resolve 3-mm Gap between Flaws at -6 dB Level

3.1.1.2 Sizing

The models, built to obtain and compare the sizing capabilities of LPA and MPA probes, used two notches with lengths smaller (5 mm) and larger (15 mm) than the anticipated lateral (secondary) axis beam size (~12 mm) of the LPA probe at the inspection area. The notches had identical height (1 mm) and sufficient separation (20 mm) to eliminate the height and separation effects on sizing estimates. For each probe, the simulated C-Scan and echo dynamics are shown in Figure 8. A table with length measurements and relative error for each probe is also incorporated in Figure 8. As expected, the LPA probe significantly oversized (114% error) the short notch. The short-notch LPA-estimated size was close to the expected beam size (~12 mm) at this area. On the contrary, the MPA length size estimate of 5 mm was very accurate (0% error). The error in length size estimates of -2% and 0.7% for the LPA and MPA probes was not that different for the large notch with a length of 15 mm. This confirmed the expectation that the notch or the flaw will be sized accurately regardless of the probe type, provided the flaws are longer than the beam size along the notch.

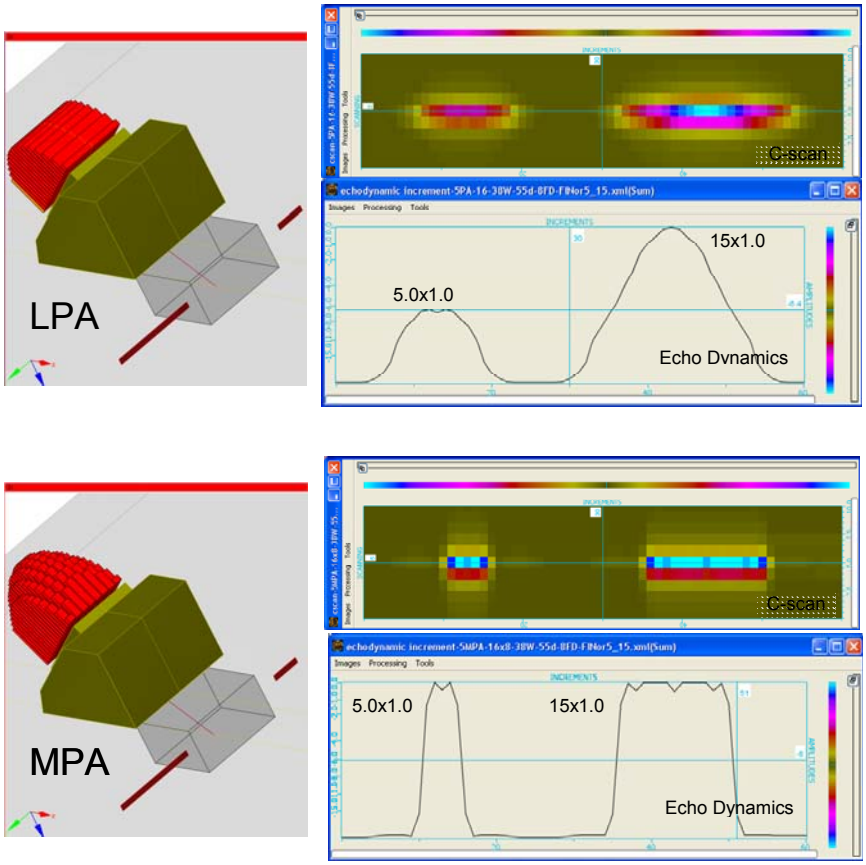

	Length Measurements (mm)	
	Notch 5×1	**Notch 15×1**
LPA	10.7	14.7
Error (%)	114	-2
MPA	5	15.1
Error (%)	0	0.7

Figure 8. Comparison of LPA and MPA Capabilities to Size the Length of Two Flaws: 5- and 15-mm Long

From the short notch seen on the C-Scan and echo dynamics plots, another noticeable difference between the signals produced with the LPA and MPA probes is the difference in amplitudes. This raises questions about the adequacy of the amplitude method for measurement of flaw height, when the flaw length is smaller than the beam size along the notch or flaw length.

Based on the modeling results, it is expected that the MPA probe will size smaller flaw lengths significantly better than the LPA probe under equal conditions.

3.1.1.3 Detection of Skewed Flaws

As discussed in the introduction, MPA probes have unique capabilities to steer the beam in two directions as compared to LPA probes that steer in one direction. This feature is particularly useful for detection and characterization of flaws that are not perfectly oriented to provide maximum reflection. This is particularly true for flaws that are skewed with respect to the probe position and orientation.

The capability of MPA to generate a beam that is skewed in the secondary direction is shown in Figure 9. This beam was generated to demonstrate the MPA capabilities in detecting and sizing of skewed and non-skewed flaws.

The modeling results comparing the performance of LPA and MPA in detecting and sizing of skewed and non-skewed flaws are shown in Figure 10. Two notches with identical length and height (15 by 1.0 mm, respectively) were modeled. The separation (20 mm) and length were selected to be larger than the beam size, so that their skew effect assessment was eliminated. One of the notches (non-skewed) was ideally oriented to produce maximum reflected signal, while the other was skewed at 5 degrees as shown in Figure 10. As the C-Scan and echo dynamics plots indicate, a skew angle of only 5 degrees is sufficient to render the notch undetectable at -6 dB with LPA. The model showed that both notches were well detectable and sized accurately with almost identical echo amplitude when the inspection was done using MPA with a beam skewed 5 degrees in the secondary direction. This again demonstrates the potential advantages of MPA over LPA probes investigated and developed during this project.

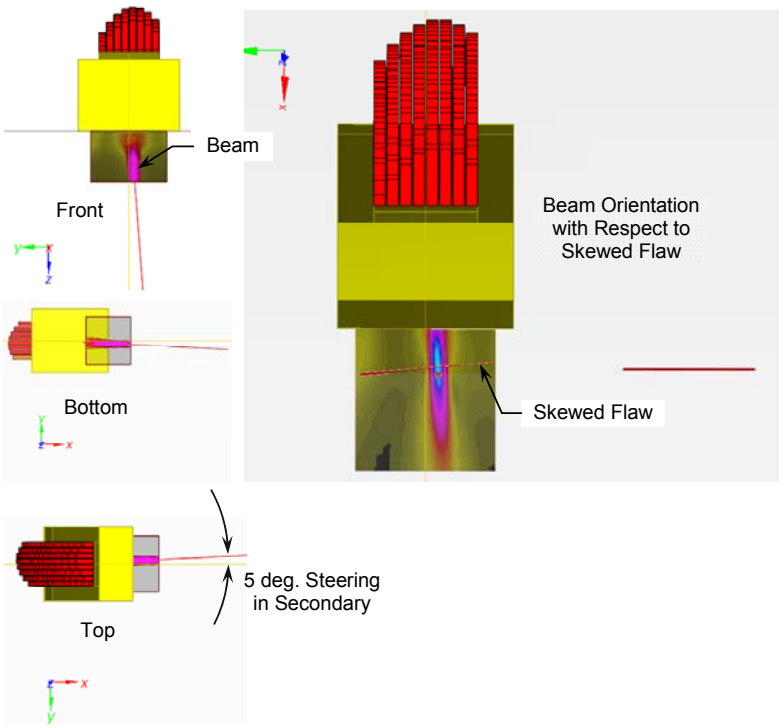

Figure 9. **Generation of Acoustical Beam with MPA Skewed in Secondary Direction for Improved Detection and Sizing of Skewed Flaws**

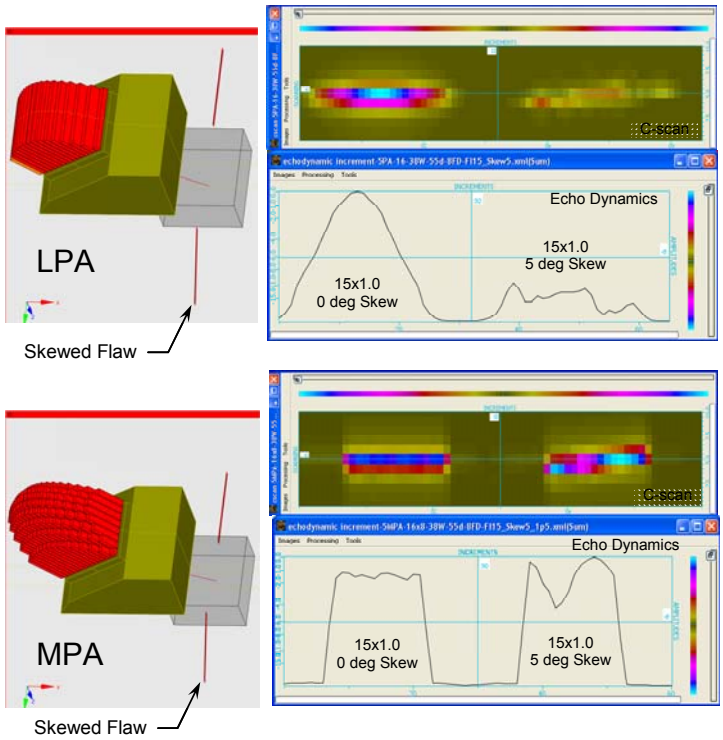

Figure 10. **Comparison of LPA and MPA Capabilities to Detect Skewed Flaws**

3.1.2 Flexible Array for Inspection from OD and in Dents (Concept 2)

Similar to a rigid MPA, a flexible matrix phased array (FMPA) is a 2D sensor array where the elements are arranged in a 2D pattern that allows beam steering in two directions: azimuthal and lateral. For the purposes of this project, the azimuthal direction was referred to as the "primary" direction and the lateral direction was referred to as the "secondary" direction (see Figure 11). Two flexible probe configurations were considered initially, based on recommendations from the probe manufacturer: Probe 1 with 4 × 12 elements, 3.1- × 2.1-mm pitch at 3.3 MHz; and Probe 2 with 5 × 12 elements, 3- × 1.5-mm pitch at 3 MHz. Probe 1 pitch (not shown) was not uniform along the primary due to the combining of elements into pairs. As shown in Figure 11, the design of Probe 2 (referred to as Layout 1) had uniform pitch along both directions and was accepted after initial modeling was used to investigate probe capabilities.

The element size (Sx and Sy) and gap (Gx and Gy) along the primary and secondary directions are also shown in Figure 11.

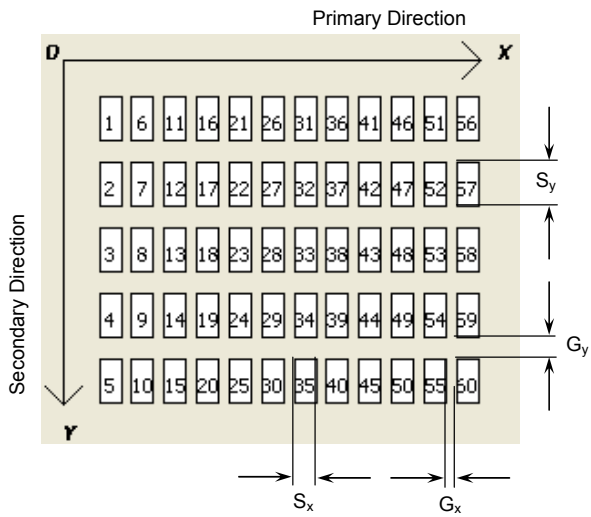

Figure 11. **Flexible Matrix Probe Design Layout** (Original Layout 1, Elements – 12 × 5) (Element size - S_x = 1 mm and S_y = 2 mm, Gaps - G_x = 0.5 mm and G_y = 1 mm)

3.1.2.1 Near Field Depth Verification

An important characteristic of FMPA which was investigated through modeling is the capability to steer and focus the acoustical beam along both directions at various depths in the inspected part. A major parameter determining the maximum focal depth is the size of the active group of elements or active aperture. The effective probe aperture changes due to the steering angle as well. The first step of the modeling efforts was to verify the depth of the near field at various refracted angles and apertures. The near field extent without any forced (mechanical and/or

electronic) focusing is a good indicator of the maximum focal depth possible at various conditions (e.g., refracted angles and aperture size).

The results of this initial stage of modeling are presented in Table 1. All modeling results for near field depth were obtained with a rigid probe model and a distance of 0.5 mm between the array elements and the inspected part representative of FMPA probe parameters. The 3-MHz longitudinal wave has an approximate wave length of 2 mm in typical carbon steel used for all modeling steps. The refracted angle was varied between 0 and 15 degrees and the aperture was varied through the number and configuration of the active elements from 12 × 5 to 4 × 3. In addition, the size and gap of elements in the secondary direction was also varied. Since the available modeling results clearly indicated the trends, there was no need to model all possible parameter combinations. The configuration was also limited to Layout 1 (Figure 11). Consequently, the models with different full array aperture layout (e.g., 10 × 6), reduced size and gap were built with the sole purpose of identifying promising design features for future applications.

The first group of simulation steps from 1 to 4 in Table 1 was conducted with the full array aperture of 12 × 5 and an element size and gap in accordance to Layout 1 (Figure 11). Side views of the beam at 0 and 15 degree refracted angles in the primary and secondary directions are shown in Figure 12. The near field depth was in the range from 43 to 48 mm (Table 1). A weak grating lobe is also visible in Figure 12(b) in the secondary direction.

A second set of simulation steps from 5 to 8 in Table 1 were carried out with the same aperture configuration (or full array 12 × 5) and reduced element size and gap (Sy = 1 mm and Gy = 0.5 mm) along the secondary direction (Figure 13). The grating lobe in the secondary direction disappeared; however, the beam divergence increased in the secondary direction (Figure 13), regardless of the refracted angle. The near field depth also decreased in the range from 40 to 43 mm (Table 1).

As expected, a reduction of near filed depth in the range from 26 to 32.5 mm was observed for a reduced aperture of 6 × 5 (Steps 9 through 13 in Table 1). Further reduction of aperture size to 4 × 3 caused the near field depth to decrease to 10.5 mm (Steps 14 and 15 in Table 1). A reduced size of the active group to a level of 4 × 3 will also cause problems in the secondary direction steering as shown in Figure 14(a) (Steps 16 and 17 in Table 1). While modeling showed that steering capability could be significantly improved if element size and gaps are reduced as shown in Figures 14(b) and 14(c) (Steps 18 to 21 Table 1), the near field depth would be decreased even further to a level of 6 mm. Based on these results, the element size and gap were kept constant in accordance with Layout 1 (Figure 11).

Table 1. Verification of Near Field Depth at Various Apertures and Refracted Angles

Step	Direction	Aperture (P el. X S el.)	Angle (Degree)	Near Field Depth H (mm)	Element Size and Gap
1	Primary	12×5	0	48	Layout 1
2	Secondary	12×5	0	48	Layout 1
3	Primary	12×5	+15	44	Layout 1
4	Secondary	12×5	+15	43	Layout 1
5	Primary	12×5	0	41	Reduced Sy = 1 mm and Gy = 0.5 mm
6	Secondary	12×5	0	41	Reduced Sy = 1 mm and Gy = 0.5 mm
7	Primary	12×5	+15	43	Reduced Sy = 1 mm and Gy = 0.5 mm
8	Secondary	12×5	+15	40.5	Reduced Sy = 1 mm and Gy = 0.5 mm
9	Primary	6×5	0	30	Layout 1
10	Secondary	6×5	0	30	Layout 1
11	Primary	6×5	+15	31	Layout 1
12	Secondary	6×5	+15	26	Layout 1
13	Secondary	6×5	+10	32.5	Layout 1
14	Primary	4×3	0	10.5	Layout 1
15	Secondary	4×3	0	10.5	Layout 1
16	Primary	4×3	+15	10	Layout 1
17	Secondary	4×3	+15	--	Layout 1
18	Secondary	4×3	+15	6	Reduced Sy = 1mm
19	Secondary	4×5	+15	12.6	Reduced Sy = 1mm
20	Secondary	4×5	+15	8	Reduced Sy = 1 mm and Gy = 0.5 mm
21	Secondary	4×4	+15	6	Reduced Sy = 1 mm and Gy = 0.5 mm

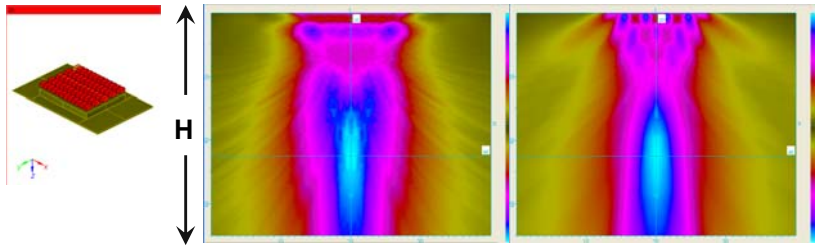

Primary Secondary

a) Normal Beam

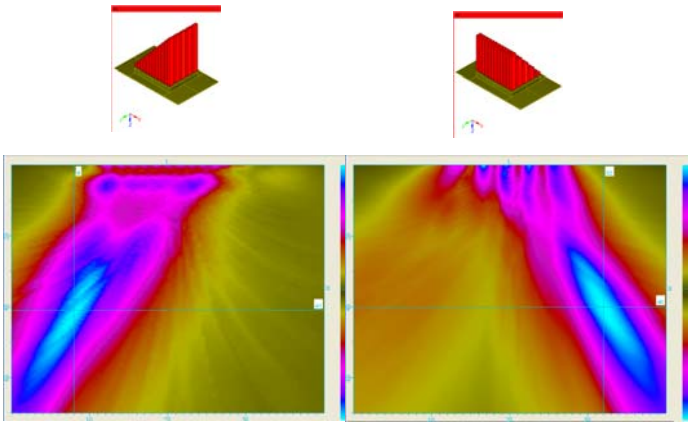

Primary Secondary

b) Refracted Beam at 15 degree

Figure 12. Near Field Depth (H) with Original Flexible Matrix Probe Layout 1 (Elements 12×5, Primary and Secondary Direction, 3 MHz, Longitudinal Wave)

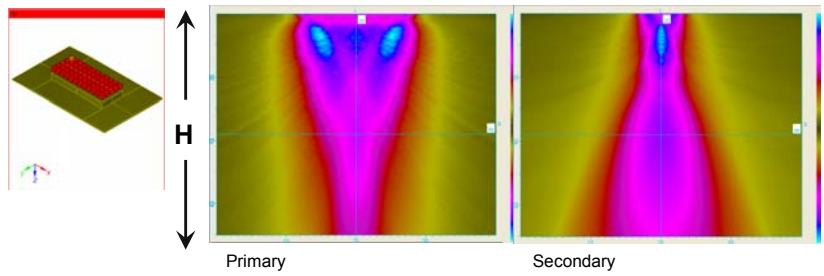

a) Normal Beam

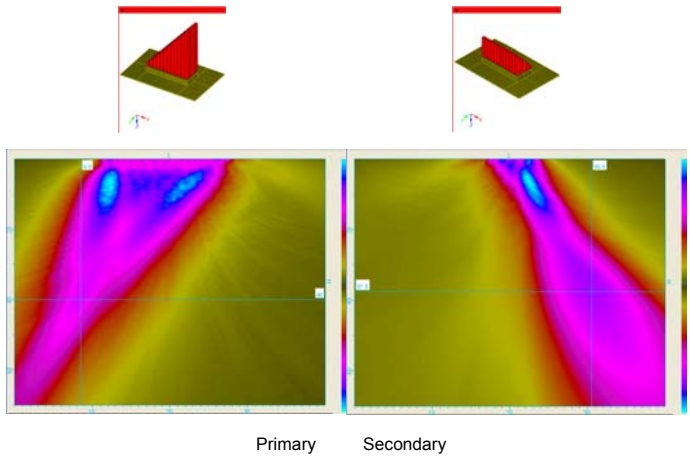

b) Refracted Beam at 15 degree

Figure 13. Near Field Depth (H) with Original Flexible Matrix Probe Layout 1 (Elements 12×5, Primary and Secondary Direction, 3 MHz, Longitudinal Wave, Reduced Size S_y = 1 mm and Reduced Gap G_y = 0.5 mm)

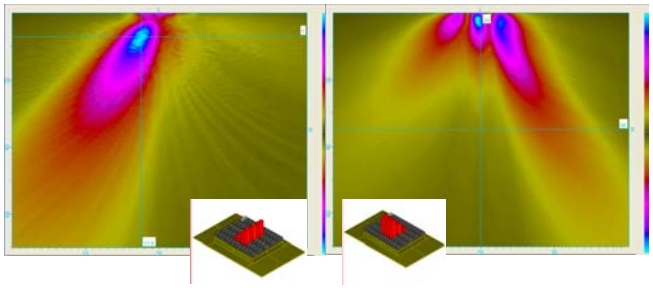

Primary Secondary

a) 4x3 Normal Size of Elements

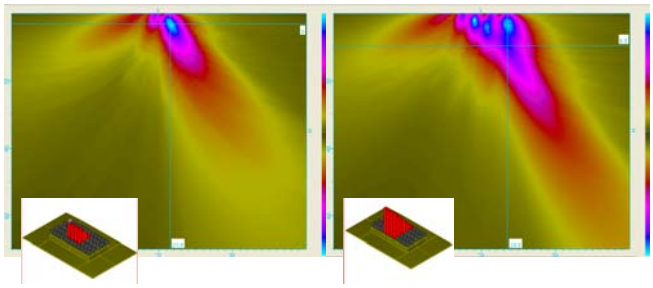

Secondary 4x3 Secondary 4x5

b) Reduced Element Size

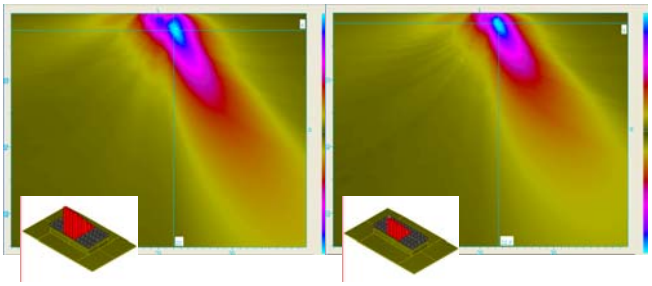

Secondary 4x5 Secondary 4x4

c) Reduced Element Size and Gap

Figure 14. Near Field Depth (H) with Modified Flexible Matrix Probe Design (Elements 12×5 and Variable Aperture, Primary and Secondary Directions, 3 MHz, Longitudinal Wave)

3.1.2.2 Optimization of Array Layout Element Size and Gap

The capability of FMPA to focus at various depths was verified initially by generating a longitudinal-wave normal beam in two simple geometries: pipe and plate. The full array aperture was used to produce the smallest possible focal spot size. A typical pipe specimen with an ID of 10 in. and three thicknesses (10, 20, and 30 mm) was modeled to simulate beam focusing at three focal depths (8, 16, and 25 mm). The focal spot size was measured at a -3 dB

level (6 dB width) in three planes; parallel to sound propagation along the primary and secondary directions and perpendicular to the sound propagation at the focal depth. The results for the pipe are summarized in Table 2.

The first three simulation steps (1 through 3) in Table 2 were for the Layout 1 probe shown in Figure 11. The beam shape and focal areas for the three focal depths (FD) of 25, 16, and 8 mm are illustrated in Figure 15. A common trend was the decrease of the size of the focal spot from 3 × 2.5 mm to 1.3 × 0.9 mm with the decrease of focal depth. The focal size (width and length) along the sound path was also decreased. The focal spot was at the highest acoustical pressure area (for FD of 8 mm) and moved further along the sound path as the FD increased. The intensity and closeness of the two grating lobes in the secondary direction increased to the level of -9.5 dB as the FD decreased.

In an attempt to verify the focusing capabilities using a smaller element size and gap in the secondary axis, two models were generated for FD 25 mm and 8 mm (Steps 4 and 5 in Table 2). The focal spot dimension in the secondary direction nearly doubled; however, the start of the focal area did not change. One significant improvement from this change was the removal of grating lobes for both FDs. Unfortunately, the focusing at a FD of 25 mm was not effective in the secondary direction.

The array layout was then changed from 12 × 5 to 10 × 6 to investigate the effect on focusing at the three FDs (Steps 6 through 7 in Table 2). The gap in the secondary direction (Gy) was made equal to the original gap of 1 mm, while the element size in the secondary direction (Sy) was reduced to 1 mm (Step 6) and 1.5 mm (Steps 7 and 8). At a FD of 25 mm (Step 6), the spot size increased and the focal spot moved even farther from the maximum pressure area compared to Layout 1 (Step 1). The spot size 2.9 × 2.9 mm at a FD of 25 mm (Step 7) with Sy of 1.5 mm was more uniform, but still larger compared to Layout 1 (Step 2). A small and uniform focal spot of 1.1 × 1.1 mm was generated at a FD of 8 mm (Step 8). There were no grating lobes in the secondary direction with the array parameters in Steps 6 through 8 in Table 2.

A final virtual comparison between Layout 1 (Figure 11) and the 10 × 6 array with reduced element size in the secondary direction was conducted on a plate specimen to avoid the surface curvature effect on focusing. Results are shown in Table 3 and Figures 16 and 17. The 10 x 6 array with Sy of 1.5 mm performed slightly better than the Layout 1 array producing more of a uniform focal spot with a size comparable to that of Layout 1 and a reduced level of grating lobes.

Table 2. Optimization of FMPA on Pipe (Normal Beam, Full Array)

Step	Specimen	Aperture	FD, mm	Focal Spot, mm	Focus Start, mm	Focus Height, mm	Elem. Size and Gap (Second.)	Notes
1	Pipe, 10-in. ID 30-mm WT	12×5	25	3×2.5	14	>16	2-mm Sy 1-mm Gy	--
2	Pipe, 10-in. ID 20-mm WT	12×5	16	2.1×1.7	10.5	>9.4	2-mm Sy 1-mm Gy	Small Y side lobes
3	Pipe, 10-in. ID 10-mm WT	12×5	8	1.3×0.9	5.5	>4.2	2-mm Sy 1-mm Gy	Visible Y side lobes start at 6.5-mm depth and <-9.5 dB
4	Pipe, 10-in. ID 30 mm WT	12×5	25	5×2.5	14	13.7 (at -2 dB)	1-mm Sy 0.5-mm Gy	Difficult to focus especially on Y
5	Pipe, 10-in. ID 10-mm WT	12×5	8	2.2×0.9	5	>4.7	1-mm Sy 0.5-mm Gy	No Y side lobes
6	Pipe, 10-in. ID 30-mm WT	10×6	25	3.6×2.9	11	18.1	1-mm Sy 1-mm Gy	FD outside of max pressure
7	Pipe, 10-in. ID 30-mm WT	10×6	25	2.9×2.9	12	>17.3	1.5-mm Sy 1-mm Gy	FD outside of max pressure
8	Pipe, 10-in. ID 10-mm WT	10×6	8	1.1×1.1	5.5	>4.4	1.5-mm Sy 1-mm Gy	Weak Y side lobes <-11.5 dB

FD – Focal depth
ID – Internal diameter
WT – Wall thickness

Table 3. Optimization of FMPA on Plate (Normal Beam, Full Array)

Step	Specimen	Aperture	FD, mm	Focal Spot, mm	Focus Start, mm	Focus Height, mm	Elem. Size and Gap (Second.)	Notes
1	Plate, 50-mm Thickness	10×6	25	3×3	12.5	18.3	1.5-mm Sy 1-mm Gy	FD very close to high pressure
2	Plate, 50-mm Thickness	10×6	16	2.1×2.1	10	11.3	1.5-mm Sy 1-mm Gy	FD very close to high pressure
3	Plate, 50-mm Thickness	10×6	8	1.1×1	5.5	5.4	1.5-mm Sy 1-mm Gy	FD at highest pressure. Some side lobes on Y from 6 to 12 mm at -11 dB
4	Plate, 50-mm Thickness	12×5	25	3×2.5	14	17.5	2-mm Sy 1-mm Gy	FD very close to high pressure
5	Plate, 50-mm Thickness	12×5	16	2.2×1.7	10.5	10.4	2-mm Sy 1-mm Gy	FD at highest pressure Some side lobes on Y from 9 to 19 mm at -13 dB
6	Plate, 50-mm Thickness	12×5	8	1.3×0.9	6	4.9	2-mm Sy 1-mm Gy	FD at highest pressure Some side lobes on Y from 6 to 14 mm at -9 dB

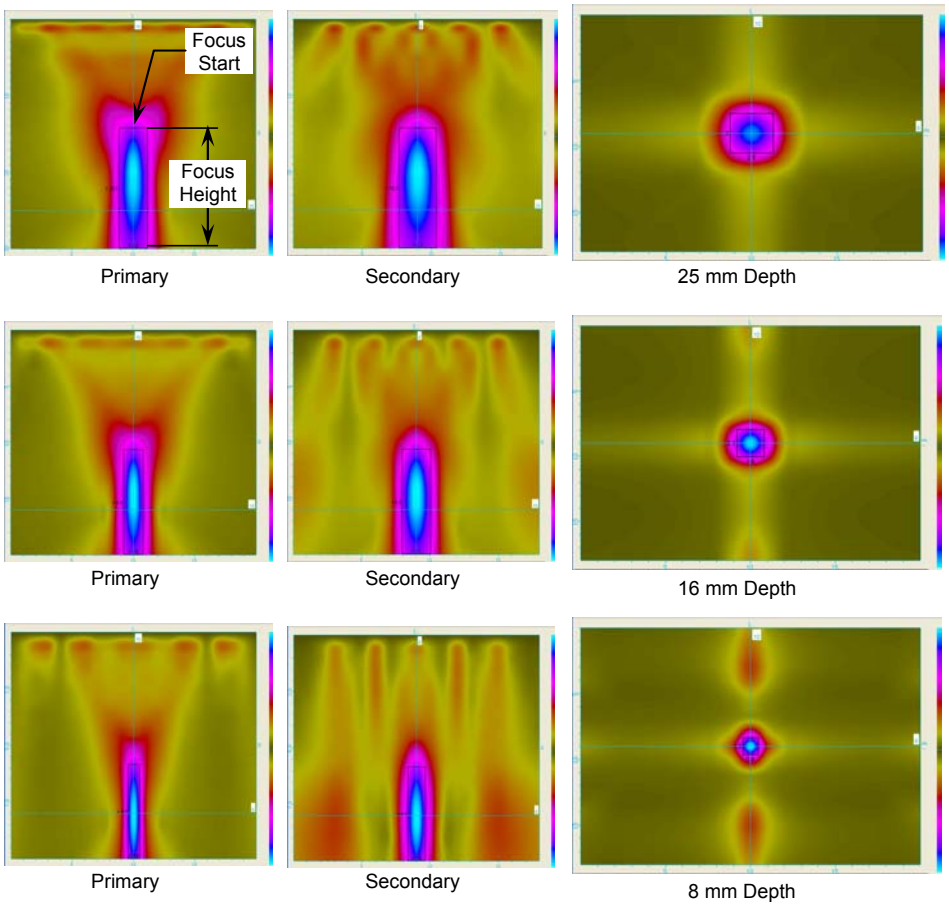

Figure 15. Layout Optimization – Longitudinal Wave Normal Beam Focusing at 25-, 16-, and 8-mm Depth with Layout 1 of FMPA (Elements - 12×5, Pipe Specimen, S_x = 1 mm, S_y = 2 mm, G_x = 0.5 mm and G_y = 1 mm)

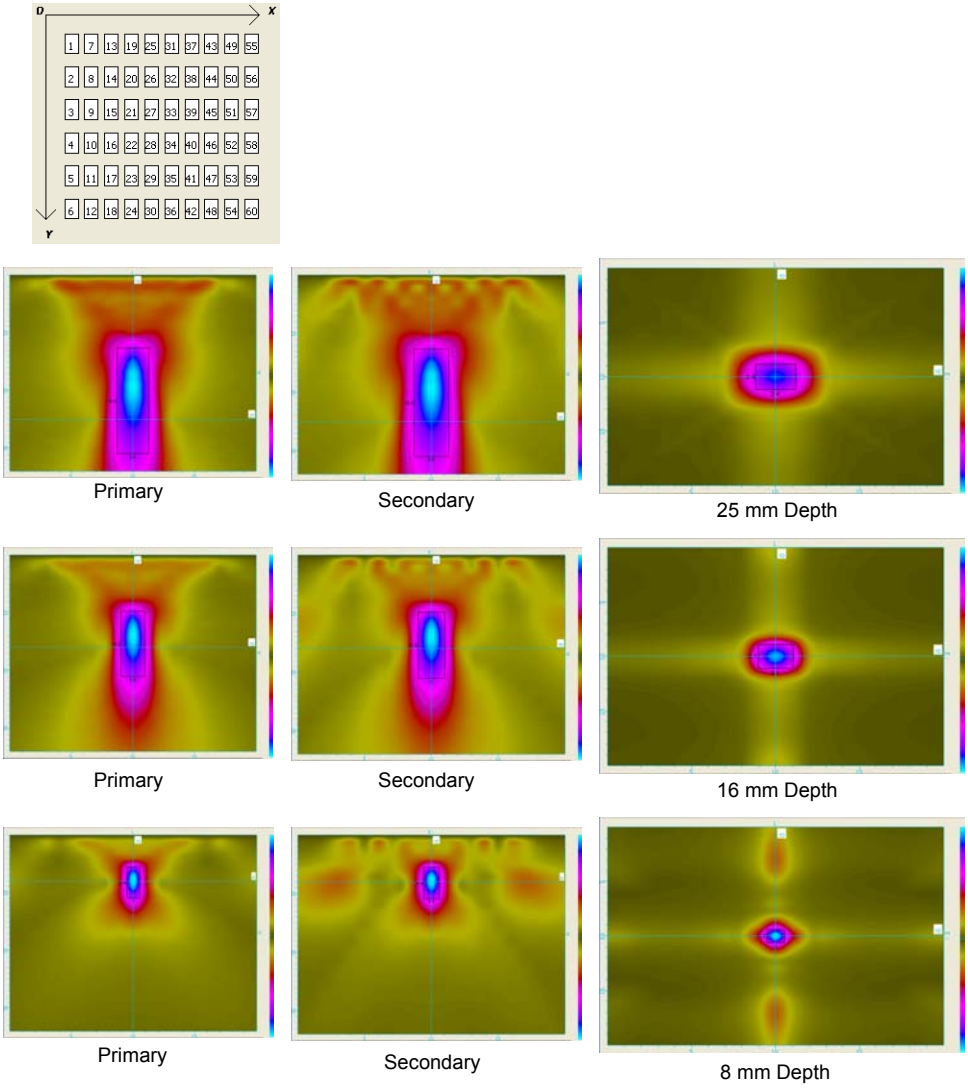

Figure 16. Layout Optimization – Longitudinal Wave Normal Beam Focusing at 25-, 16-, and 8-mm Depth with Design 4 of FMPA (Elements - 10×6, Plate Specimen, S_x = 1 mm, Reduced S_y = 1.5 mm, G_x = 0.5 mm and G_y = 1 mm)

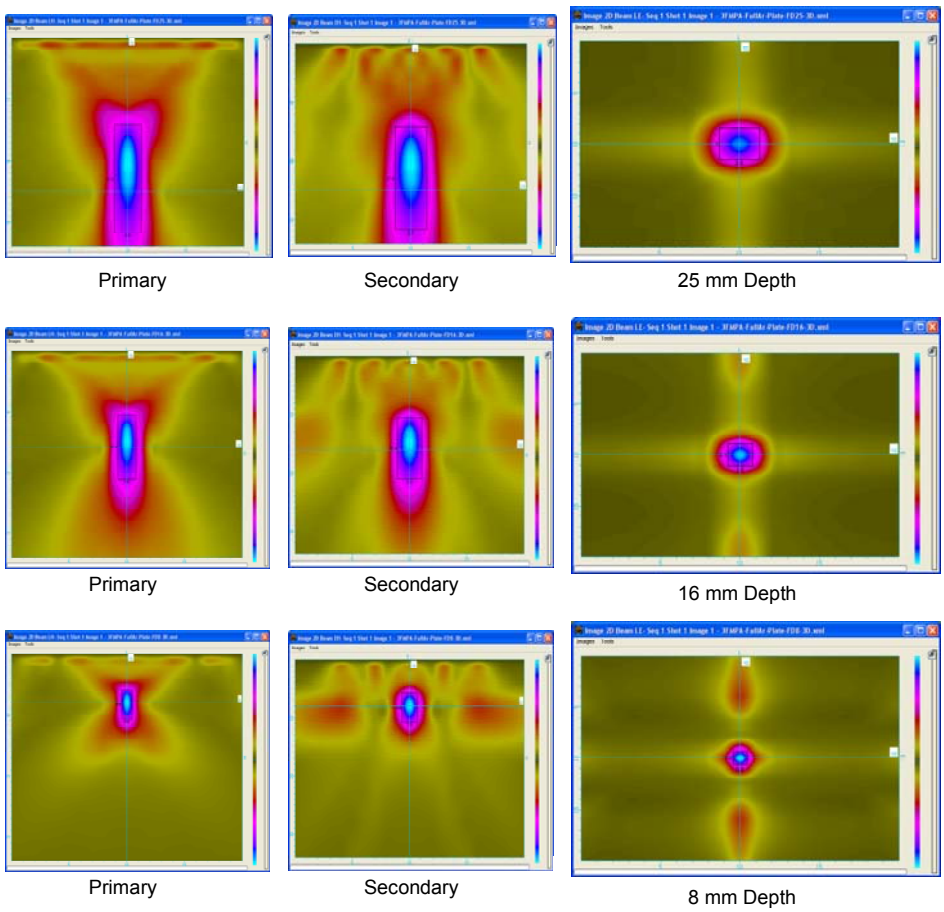

Figure 17. Layout Optimization – Longitudinal Wave Normal Beam Focusing at 25-, 16-, and 8-mm Depth with Layout 1 of FMPA (Elements - 12×5, Plate Specimen, Sx = 1 mm, Sy = 2 mm, Gx = 0.5 mm and Gy = 1 mm)

3.1.2.3 Verification of Beam Focusing for Dent Inspection from OD

One of the main drivers in the FMPA design is the requirement to inspect parts with complex-shaped scanning surfaces. Accidental damage (e.g., dents) to a critical structure, such as high pressure vessels and pipelines, will always require inspection to determine the presence of conditions and flaws that might affect the service life, maintenance and/or subsequent repair activities. Dents are difficult and sometimes impossible to inspect from the accessible surface with conventional probes due to sharp and unpredictable surface changes. In pipelines, dents or mechanical damage are caused by equipment and tools during excavation. In a recent PRCI study, typical dents were produced with various shapes, locations, and dimensions. The dents were either linear or round, depending on the impact or indentation tool (Figure 18). The pipe material was carbon steel with a 610-mm (24-in.) diameter and a 7.1- and 8.9-mm (0.28- and 0.35-in.) WT. The dent radius distribution from that study is plotted in Figure 18. The highest number of dents (35) was in the range from 203 to 254 mm (8 to 10 in.). A small number of

dents (less than 5) were located in the range from 0 to 51 mm (0 to 2 in.), which was the smallest dimension.

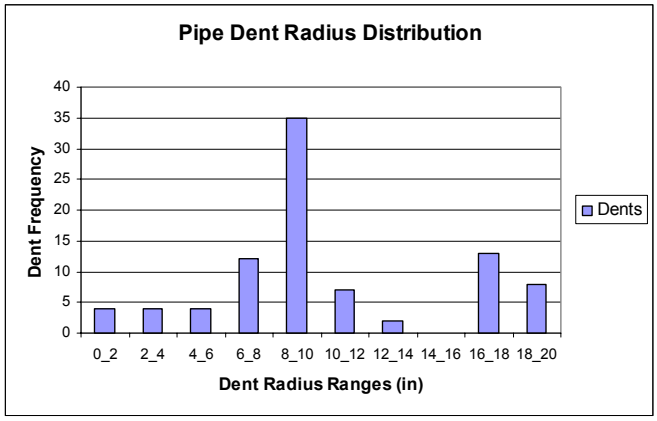

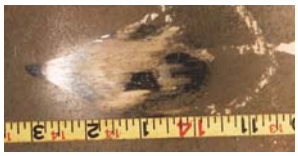

1.44” Deep, 3” Long, 2” Wide

0.72” Deep, 8” Long, 1” Wide

Figure 18. Pipe Dent Geometry

A portion of a standard specimen structure (“elbow”) available in the CIVA modeling software was selected to model the FMPA performance during dent inspection as shown in Figure 19. The dimensions of the modeled dent area were limited by the capability of FMPA to conform to surfaces with a curvature radius smaller than 30 mm (~1.25 in.). The radius of the dent (elbow) along the length and perpendicular to the length was specified to be 38.1 and 31.8 mm (1.5 and 1.25 in.) as shown in Figure 19.

Two probe orientations with respect to the dent length were initially investigated as shown in Figure 14:

- Longitudinal – Primary probe axis oriented along the dent length
- Transverse – Primary probe axis oriented perpendicular to the dent length.

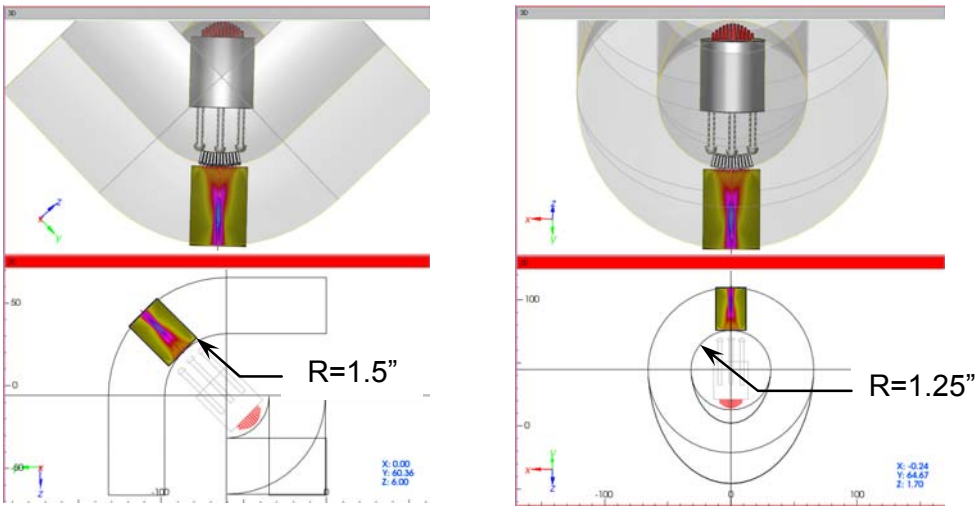

Longitudinal Orientation Transverse Orientation

Figure 19. Probe Longitudinal and Transverse Orientation in the Dent

The probe was positioned at the bottom of the dent, where the contact surface curvature was concave in both orientations. This was considered the worst condition for focusing. A normal and refracted (15 degree) longitudinal wave was generated to investigate both focusing and steering capabilities and their effects on focal spot size. All models were performed with the rectangular Layout 1 array layout. The WT was maintained at 34 mm. The focal spot size was measured at a -3 dB level (6 dB width) from the local maximum.

Simulation results are summarized in Table 4. The beam shape and focusing at three FDs of 25, 16, and 8 mm are shown in Figures 20 and 21 for a 15-degree refracted angle and probe transverse orientation. The data in Table 4 indicated that the focal spot size for a normal beam was practically unaffected by the probe orientation. Also regardless of probe orientation, the normal beam features were not different from the ones shown in Figures 15 and 17. The transverse orientation offers more flexibility in terms of beam steering for dent inspection and was selected to verify the focusing capabilities at a 15-degree refracted angle. The focal spot size slightly increased (less than 0.5 mm) for refracted angles different from normal (0 degrees). A single grating lobe was noticed at a FD of 25 and 16 mm, approximately mirroring the main lobe in the secondary direction (Figure 20). Two grating lobes at approximately a -8 dB level (Table 4) are visible close to the main lobe at a FD of 8 mm (Figure 21). The focal spot size decreased with the decrease of the FDs; however, the grating lobes in the secondary direction became stronger and closer to the FD. The focal spot size changed from 1.4 × 1.9 mm at a FD of 8 mm to approximately 3 × 3.7 mm at a FD of 25 mm.

The desired refracted angle was not always achievable due to the offset of the exit point. A comparison of desired and actual refracted angles is shown in Table 5. The actual refracted

angles decreased with the decrease of FD particularly in the secondary direction. The actual angles were equal to the desired at two FDs of 25 and 16 mm in the primary direction. It may be beneficial to increase the number of elements and reduce the element size in the secondary direction in order to improve steering for future applications.

It will be necessary to conduct electronic scanning with the FMPA for many practical applications. Electronic scanning would involve the use of an active group aperture smaller than the full-array aperture for generation, receiving and coverage of the inspection area. Based on the modeling results discussed previously (Table 1), an aperture of 8 × 5 is expected to provide sufficient near-field depth to cover the WT up to 25 mm and have a sufficient number of elements to focus effectively at the required depths. Beam steering and focusing capabilities are shown in Figure 22; the results are summarized in Table 6. The focal spot size parallel and transverse to the sound propagation increased slightly compared to the full-array aperture shown in Table 4. For example, the cross-section focal spot size at the FD of 8 mm increased slightly from 1.4 × 1.9 mm (Table 4) to 1.7 × 1.8 mm (Table 6) in the primary direction. Steering in the primary direction slightly improved from 10 degrees (Table 5) to 12 degrees (Table 6), while steering in the secondary slightly deteriorated by 1 degrees (Table 5) from 7 to 6 degrees (Table 6). The intensity of the grating lobes in the secondary direction (Figures 21 and 22) increased from approximately -8 dB (Table 4) to approximately -7 dB (Table 6). The steering and focusing capabilities of FMPA with this reduced aperture were acceptable and were used later to virtually investigate crack detection capabilities.

Table 4. Beam Focusing in Dent (FMPA at Various Angles and Probe Orientation)

FD (mm)	Refracted Angle (degree)	Probe Longitudinal Orientation – Focal Size			Probe Transverse Orientation – Focal Size			Notes
		Primary	Second	Cross	Primary	Second	Cross	
25	0	20×2.5	20×3.2	2.8×3.5	20.3×2.6	20.3×3.1	2.8×3.5	
	15 Primary	NM	--	NM	20.9×3	--	3×3.5	Grating lobe in secondary
	15 Second.	--	NM	NM	--	20.7×3.6	2.9×3.7	Grating lobe in secondary
16	0	12.6×1.9	12.6×2.5	2×2.6	12.7×2	12.7×2.4	2×2.5	--
	15 Primary	NM	--	NM	13.1×2.4	-	2.1×2.5	Grating lobe in secondary
	15 Second.	--	NM	NM	--	12.8×2.9	2.1×2.7	Grating lobe in secondary
8	0	6.2×1.3	6.2×1.9	1.3×1.9	6.2×1.4	6.2×1.8	1.4×1.9	Secondary side lobes at -7.8 dB
	15 Primary	NM	--	NM	6.4×1.8	-	1.4×1.9	Secondary side lobes at -7.7 dB
	15 Second.	--	NM	NM	-	6.3×2.2	1.4×1.9	Secondary side lobes at -7.7 dB

NM – Not modeled

FD – Focal depth

Table 5. Beam Steering in Dent (Comparison of FMPA Desired and Actual Refracted Angles)

FD (mm)	Desired Refracted Angle (degree)	Actual Refracted Angle		Notes
		Primary Degree	Secondary Degree	
25	15	15	12	Primary ok; secondary reduced
16	15	15	9	Primary ok; secondary reduced
8	15	10	7	Primary and secondary reduced

Table 6. Beam Focusing in Dent (Transversely Oriented FMPA at Various Angles. Reduced Active Group 8×5)

FD (mm)	Refracted Angle (degree)	Probe Transverse Orientation – Focal Size			Actual Refracted Angle (degree)	Notes
		Primary	Secondary	Cross		
8	0	7.5x1.6	7.5x1.8	1.7x1.8	0	Secondary side lobes at -6.9 dB
	15 Primary	7.5x1.9	--	1.7x1.8	12	Secondary side lobes at -7.1 dB
	15 Secondary	--	7.4x2.2	1.7x1.8	6	Secondary side lobes at -7.4 dB

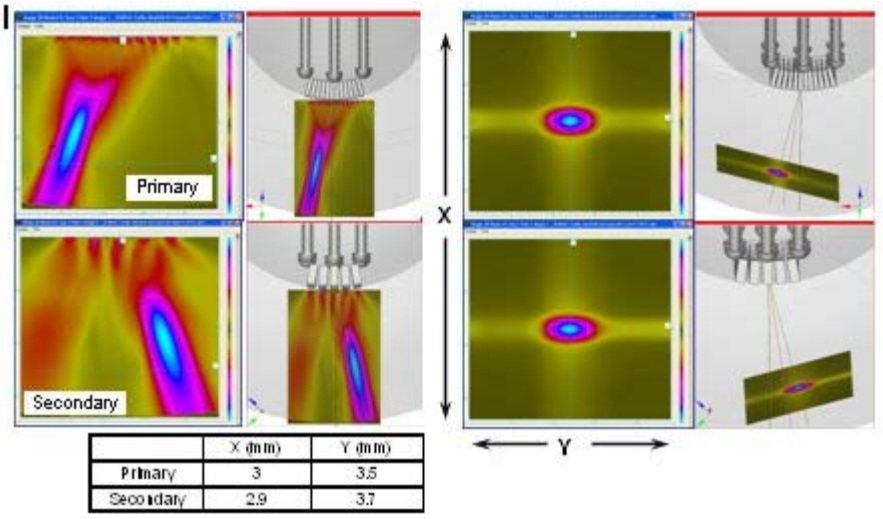

	X (mm)	Y (mm)
Primary	3	3.5
Secondary	2.9	3.7

Focal depth 25 mm

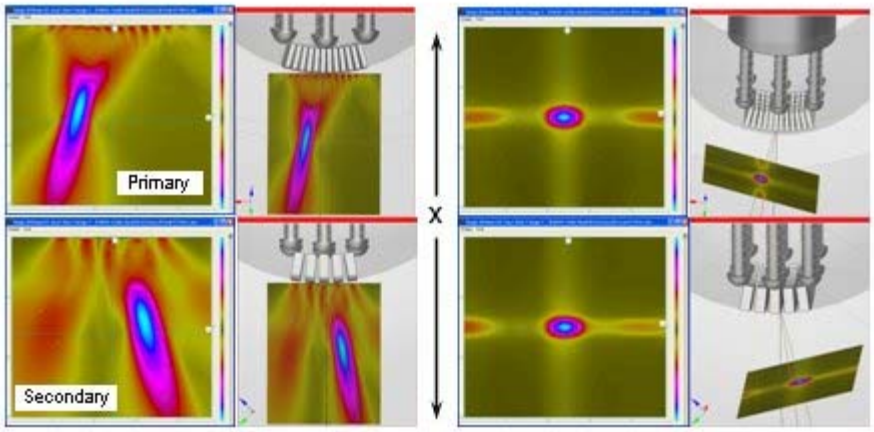

	X (mm)	Y (mm)
Primary	2.1	2.5
Secondary	2.1	2.7

Focal depth 16 mm

Figure 20. Focusing and Beam Steering at 25- and 16-mm Focal Depth with Full-Array Aperture

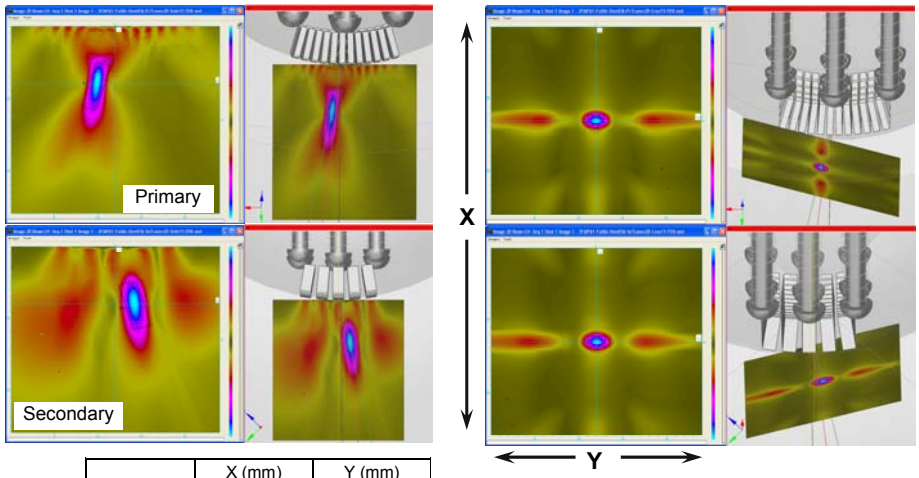

	X (mm)	Y (mm)
Primary	1.4	1.9
Secondary	1.4	1.9

Figure 21. Focusing and Beam Steering at 8-mm Focal Depth with Full-Array Aperture

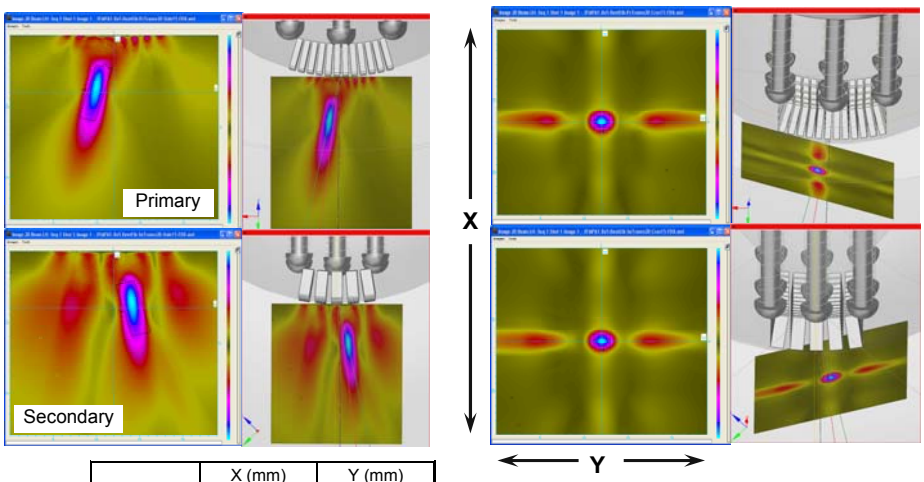

	X (mm)	Y (mm)
Primary	1.7	1.8
Secondary	1.7	1.8

Figure 22. Focusing and Beam Steering at 8-mm Focal Depth with Reduced FMPA Aperture 8×5

3.1.2.4 Simulation of Pipe Wall Thinning Detection

The detection of WT reduction or thickness monitoring is a common task in the oil and gas industry. High resolution and accuracy are desired. Virtual simulation was conducted to evaluate the FMPA probe resolution for wall thinning measurement. A 3-MHz, normal beam, longitudinal wave was generated with the full-array aperture (Layout 1 in Figure 11). A pipe

specimen made of typical carbon steel with an ID of 254 mm (12 in.) and WT of 25 mm (1 in.) was used in the model. The array was focused at a FD of 25 mm. To eliminate the effect that the curvature might have, the ID and the thinning were simulated with squares of 10 × 10 mm arranged along the pipe ID intermittently with wall thinning increments of 0.2 mm [Figure 23(a)] and 0.1 mm [Figure 23(b)]. The increased separation between the ID and the thinning is quite visible as the thinning increased on the B-Scan (Figure 23). The modeled difference in the arrival times between the ID and the 0.2 mm thinning was 68 ns [Figure 23(a)], while the 0.1 mm thinning produced a difference in the arrival times of 33 ns [Figure 23(b)]. The FMPA probe performance was also modeled at higher frequency of 7 MHz (Figure 24) with a thinning increment of 0.1 mm and an identical specimen as above. While the arrival time from the 0.1 mm thinning estimated at 35 ns did not practically change, the resolution improved as demonstrated on the B- and A-Scans due to the reduced wave length from 1.7 mm at 3 MHz to 0.84 mm at 7 MHz for carbon steel.

In summary, small thinning in the range of 0.1 to 0.2 mm is possibly resolvable provided the effect of temperature or other calibration variables that will strongly affect the thickness measurement accuracy are taken into account and compensated for.

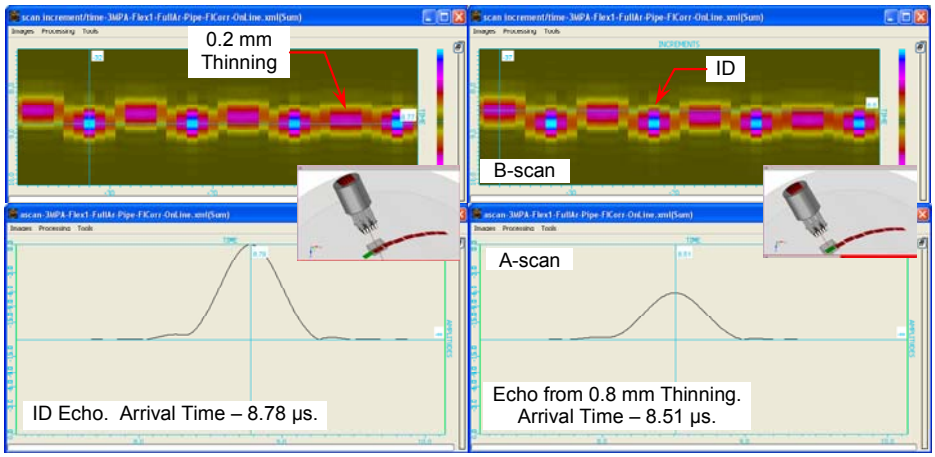

a) Wall Thinning Spots with 0.2 mm Increment

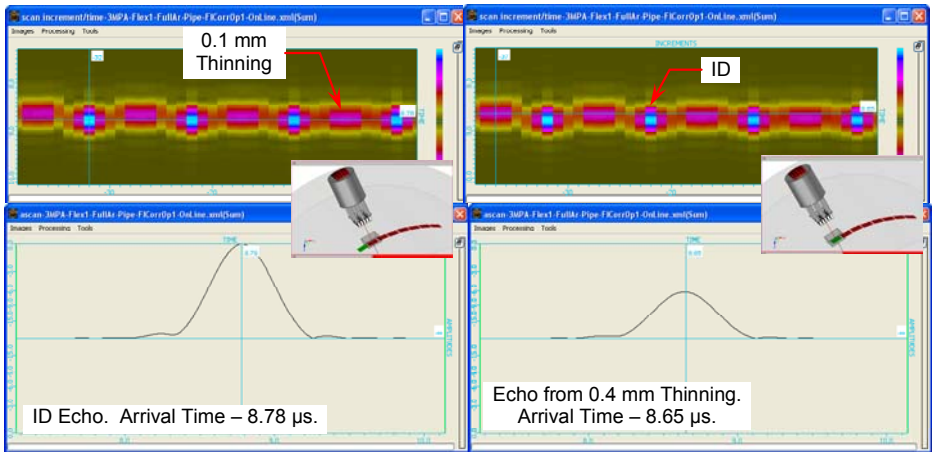

b) Wall Thinning Spots with 0.1 mm Increment

Figure 23. Pipe Wall Thinning (Four Spots at 0.1- and 0.2-mm Increment) Simulation with FMPA at 3 MHz

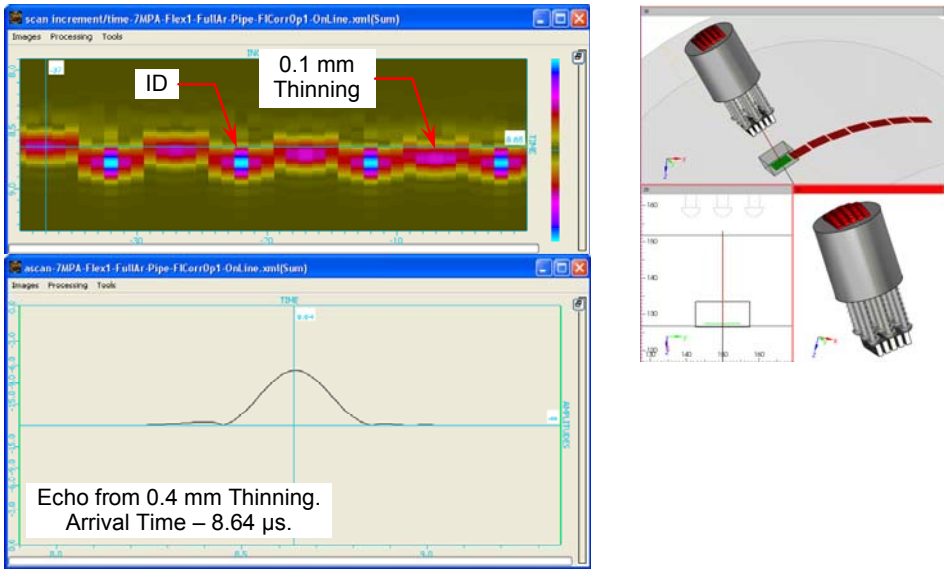

Figure 24. Pipe Wall Thinning (Four Spots) Simulation with FMPA at 7 MHz at 0.1-mm Increment

3.1.2.5 Crack Detection on Round and Elongated Dent ID with Longitudinal Waves

A model was generated with planar flaws (i.e., notches) to investigate the FMPA probe detection capabilities during round dent inspection. A severe dent with a radius along the length of 38.1 mm (1.5 in.) and radius perpendicular to the length 31.8 mm (1.25 in.) was modeled with the standard CIVA elbow specimen with a WT of 8 mm (see Figure 25). The flaw interaction was conducted using the CIVA “on-line beam computation” parameter that did not require preliminary calculation and import of the acoustical beam. The flaws were interacted with a longitudinal beam refracted at an angle of 15 degrees (12 degrees actual in Table 6) along the primary axis. The probe was oriented transversely with regard to the dent length (Figure 25) and the beam was generated with a reduced array aperture of 8 × 5. To cover the area of interest, a raster scan with a length of 45 mm parallel to the dent length and 10 degrees corresponding to a circumferential sector of approximately 7 mm perpendicular to dent length was simulated. A calibration notch of 5 × 0.8 mm was located outside the dent on the straight portion of the elbow to simulate a calibration specimen made of a pipe sector. An additional three notches were also modeled having the same length of 10 mm with heights from 0.5 to 1.5 mm in 0.5-mm increments. All of the notches were ID connected to simulate crack initiation and propagation from the pipe area with the highest level of strain due to mechanical damage. The notches were not tilted or skewed.

The C-Scan and echo dynamics plots (Figure 25) indicated that all flaws were detectable at -6 dB calibration signal level. Some increase of the base line signal was noticeable around the notches and could have possibly been caused by the grating lobes in the secondary direction (Figure 22). The echo dynamics plot indicated a possibility for height measurement. While the calibration notch length estimate of 5 mm from the echo dynamics was very accurate, the length of the notches located on the curved portion of the dent were undersized. This is due to the difference between the probe path measured along the axis of the elbow (dent) rather than the actual travel path of the probe focal spot in the material. This emphasized the need for careful consideration of the encoder mounting for correct positional data acquisition during actual dent scanning. The encoder should be attached to the FMPA in a way to measure the travel path of the focal spot in the material so that the MPA full potential for accurate length sizing is realized as demonstrated previously (Figure 8). The analysis from the B-Scan shown in Figures 26 and 27 indicated that the back wall and notch signals are well distinguished and separated. There was no tip diffraction signal visible. Some back wall reflection with subsequent reflection of the notches was also detectable on the B-Scans.

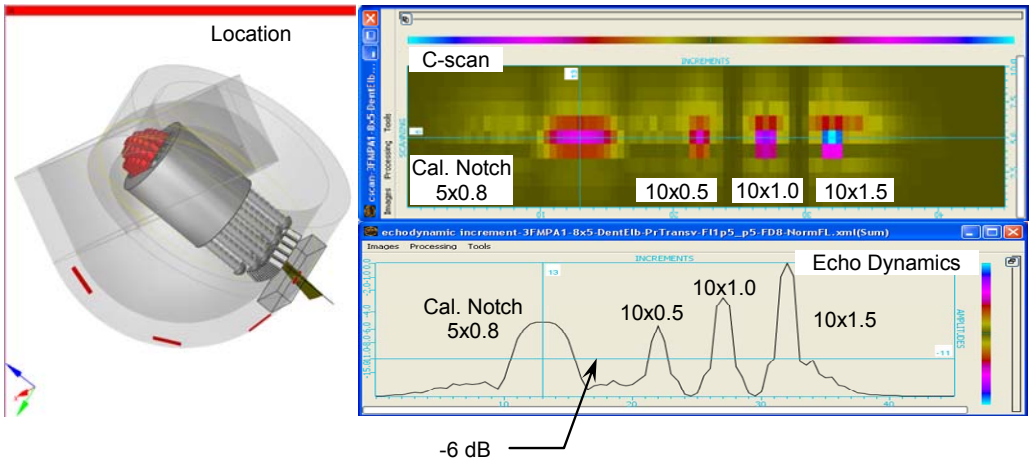

Figure 25. Flaws in Dent (Elbow) (FMPA 3 MHz, LW, C-Scan and Echo Dynamics)

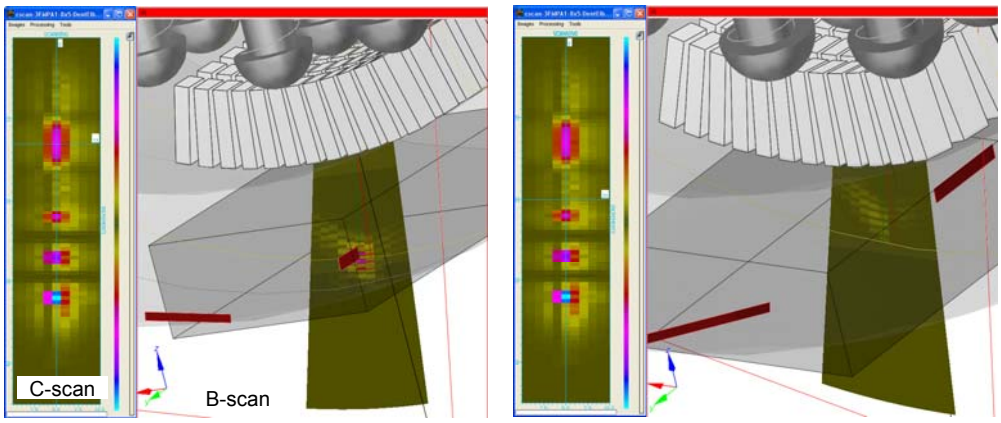

Figure 26. Flaws in Dent (Elbow) (FMPA 3 MHz, LW, Calibration Notch and ID Signals)

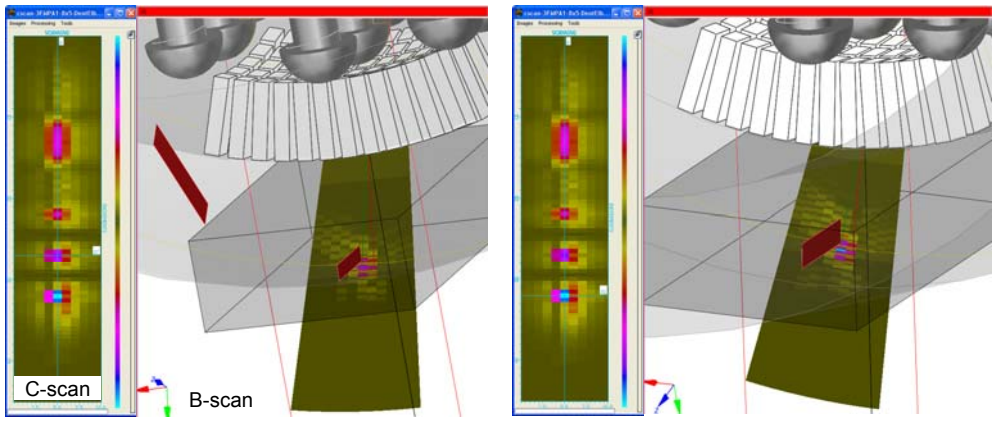

Figure 27. Flaws in Dent (Elbow) (FMPA 3 MHz, LW, 10- × 1.0- and 10- × 1.5-mm Notch Signals)

A second model was generated with planar flaws (notches) to investigate the FMPA probe detection capabilities during elongated dent inspection. A dent with radius of 31.8 mm perpendicular to the length was modeled with the standard CIVA pipe sector specimen. This shape of the specimen simulated an elongated dent or groove with a WT of 8 mm as shown in Figure 28. The flaw interaction was conducted using a CIVA “on-line beam computation” parameter that did not require preliminary calculation and import of the acoustical beam. The flaws were interacted with a longitudinal beam refracted at an angle of 15 degrees along the primary axis. No estimates of the actual refracted angle were conducted for this geometry. It was expected that the actual refracted angle might be between 12 and 15 degrees (Table 6) due to the better focusing capability in the secondary direction (straight line for elongated dent vs. convex line for round dent). The probe was oriented transversely with regard to the dent length (Figure 28) and the beam was generated with a reduced array aperture of 8 x 5. To cover the area of interest, a raster scan with length of 250 mm parallel to the dent length and 10

degrees corresponding to a circumferential sector of approximately 7 mm perpendicular to dent length was simulated. A calibration notch 5 × 0.8 mm was located in the dent to simulate calibration specimen made of pipe sector. Other four notches had the same length of 10 mm with heights from 0.5 to 2.0 mm in 0.5-mm increments. All of the notches were ID connected to simulate crack initiation and propagation from the pipe area with the highest level of strain due to mechanical damage. The notches were not tilted or skewed.

The C-Scan and echo dynamics plots (Figure 28) indicated that the flaws would be difficult to distinguish from the dent ID signal. The C-Scan plot indicated a possibility for length measurement (no curvature effect along the length) in a case of better detectability. The analysis from the B-Scans shown in 25 Figures 29 and 30 confirmed the strong back wall signal from the dent ID. There was no tip diffraction signal visible. The notches interfered with the back wall reflection as illustrated on the B-Scans, which in turn slightly improved their detectability on the C-Scan.

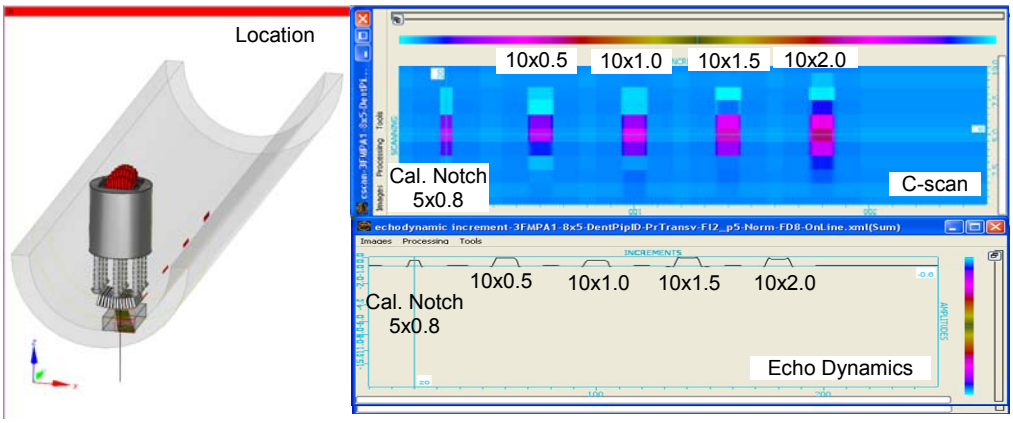

Figure 28. Flaws in Dent (Groove) (FMPA 3 MHz, LW, C-Scan and Echo Dynamics)

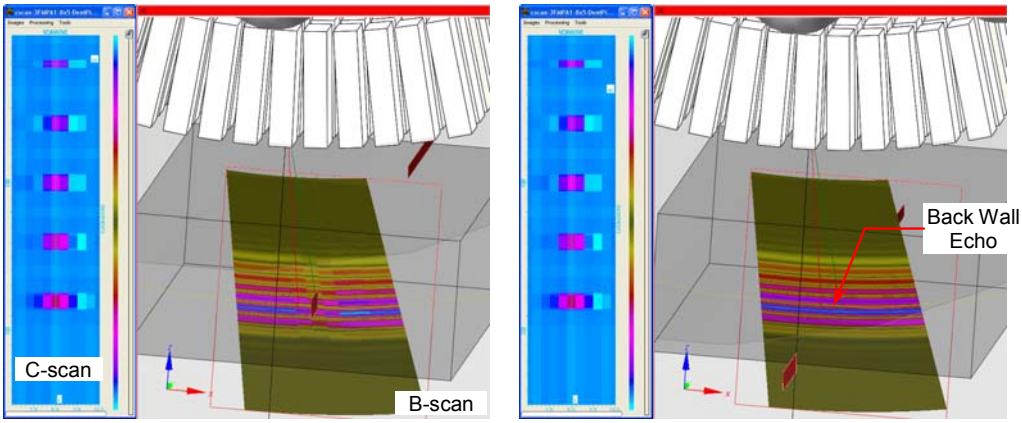

Figure 29. Flaws in Dent (Groove) (FMPA 3 MHz, LW, Calibration Notch and ID Signals)

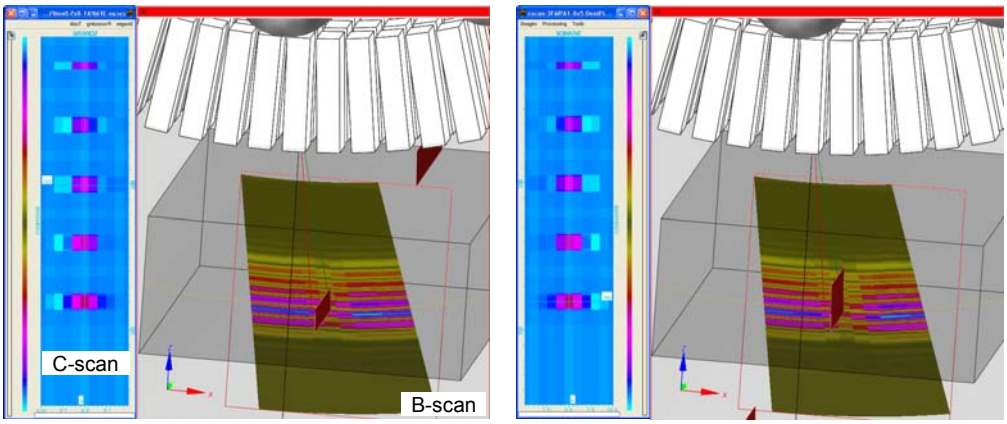

Figure 30. Flaws in Dent (Groove), FMPA 3 MHz, LW, 10- × 1.0- and 10- × 2.0-mm Notch Signals)

The following conclusions can be drawn from the planar flaw interaction simulations:

- The ID geometry of the dent has a very strong effect on the detectability of flaws perpendicular to ID surface. The larger the radius of the dent along the length, the worse the detectability. This may be explained by the focusing effect of the ID surface with the decreased radius along the length subject to field validation.

- Larger refracted angles and possibly shear waves will be required to improve the detectability of these types of ID connected flaws. It is not clear whether the FMPA will be capable of generating shear waves, since it was designed for longitudinal wave mode according to the probe vendor.

3.2 Rigid Array for Inspection from ID (Concept 3)

This concept uses a rigid 2D MPA probe module(s) to inspect localized damaged areas of pipes having diameters in the range of 4 to 8 in. (102 to 203 mm). The pipe damage could be corrosion pitting, SCC, or dents associated with mechanical damage. This inspection concept is performed by scanning from the ID surface and could be used in instances where access to the pipe OD is not possible due to insulation or other obstructions. The concept uses a robot (or crawler) to transport the probe module(s) to the area of interest. During inspection, the pipe is filled with water or other liquid, to provide a coupling medium for the ultrasound. The probe module(s) do not actually contact the ID surface of the pipe, but instead, stand off from the ID surface approximately 2 to 25 mm or larger. The ID MPA probe will act as immersion probe and the stand-off distance is referred to as water path (WP) distance. Electronic beam steering, focusing, and scanning can be used to ultrasonically measure the remaining pipe WT and to detect cracking associated with the surface damage. Advanced modeling tools were used to design, optimize, and evaluated a rigid 2D MPA probe for this application. A model of the probe inspecting the pipe wall from the ID is shown in Figure 31.

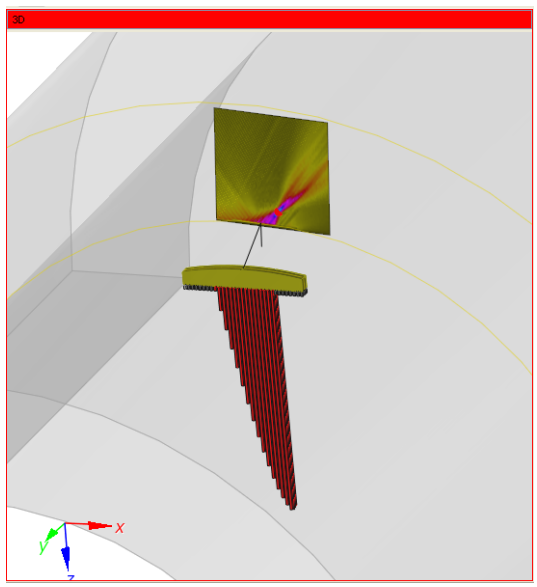

Figure 31. Position of MPA Probe for Pipe Inspection from the ID

The main objectives of the modeling efforts were to design a probe or probe segment that could generate an acoustical beam having a small focal spot size at the depth of interest. Further, the probe should have good beam steering capabilities in both the primary and secondary probe axis. In addition, the probe layout and active group selection must be such that maximum coverage of the ID/OD surface could be achieved given the focal size, steering angle, and WP conditions. These are conflicting requirements and required a significant amount of effort to achieve an acceptable optimized solution. In general, the optimization process involved

selection of element size, gap (see Figure 11) and active group configuration, as well as, subsequent verification of focal and steering capabilities at different depths and WPs.

The probe vendor indicated that, with the current technology, the minimum element size and gap was limited to 0.5 and 0.1 mm, respectively. For convenience, the following set of parameters is referred to in this report as the standard set of parameters for this optimization project and variations/deviations from the standard parameters are indicated relevant to any particular optimization modeling experiment:

- The maximum number of elements was limited to 128 elements arranged in a 32×4 2D matrix due to equipment availability for this project. This represents a probe segment that would provide inspection coverage of a portion of the ID circumference. Additional probe segments would be needed for complete coverage of the circumference.

- A typical carbon steel pipe with an ID of 152 mm (6 in.) was used in the models. The longitudinal and shear wave ultrasonic velocity of the material was VL – 5900 m/s and vs 3230 m/s.

- The probe surface was curved with the center of curvature on the pipe axis. The probe curvature radius was changed accordingly when the WP changed to comply with this condition.

- The probe skew with respect to the pipe cross-section plane was always kept at 0 degree.

- Most of the modeling was conducted at 5 MHz.

- An active element group or aperture of 16×4 elements was maintained. The 16-element aperture was in the primary probe axis (x), while the 4-element aperture was in the secondary probe axis (y). The primary probe axis was oriented parallel to the pipe circumference.

- Three FDs 3, 12, and 25 mm were used to cover a practical range of pipe WT and depth envisioned for this project.

- Three WPs 0.1 (probe in contact with ID) 20 and 40 mm were investigated to provide flexibility for probe mounting targeting different applications.

3.2.1 Initial Shear Wave (SW) Optimization (Parameter Variables: WP, FD, and Primary Inter-Element Gap (Gx)]

One initial numerical experiment was conducted to verify SW steering and focusing for a probe with the following element size and gap parameters: Sx - 0.5 mm, Sy - 0.5 mm, Gx - 0.1 mm and Gy - 0.1 mm. The results are presented in Figures 32 through 34 arranged for decreasing FD from left to right and two gaps 0.1 mm (top) and 0.3 mm (bottom). The focusing and steering was verified in primary direction only for three WPs 10, 5, and 0.1 mm. The steering to approximately 45 degrees was demonstrated. The focusing capabilities deteriorated when the FD was increased. Peak acoustical pressure occurred at a shallower depth than the FD (see coursers crossing at FD 12 mm in Figures 32 through 34). The focal size was getting larger with the increase of the FD. Some non-uniformity (streak pattern) in acoustical pressure distribution was observed at smaller WPs and FDs that was possibly caused by the increased gap between elements in the primary axis (Gx). The SW steering and focal capabilities with this set of parameters were acceptable; however, the surface coverage along the pipe circumference was limited to 11 degrees at maximum, which occurred when the WP was 10 mm and Gx was 0.3 mm.

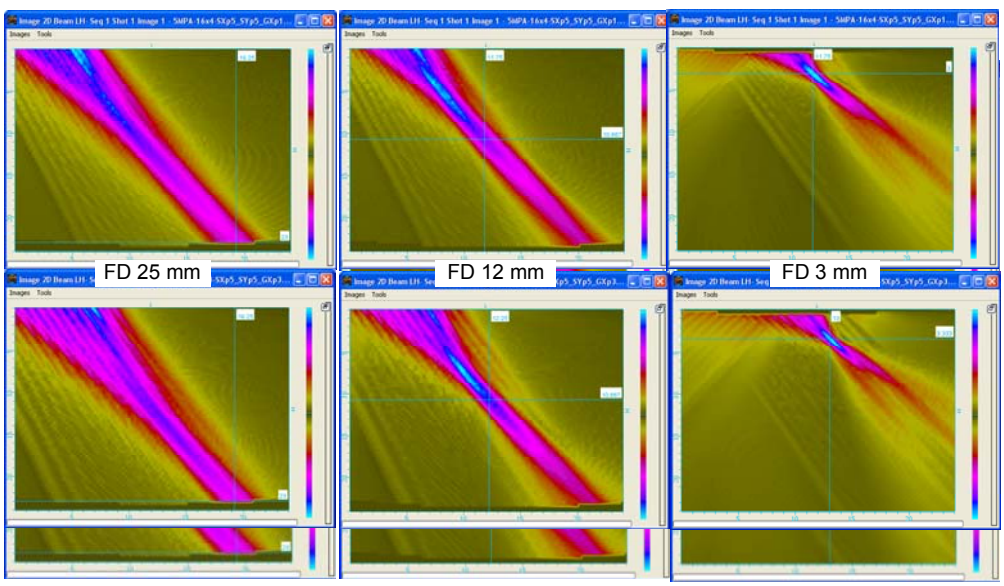

Figure 32. Variable FD and Gx - Gx 0.1 mm (Top) and Gx 0.3 mm (Bottom) (ID MPA 5 MHz, Active Aperture 16×4, WP 10 mm, SW 45 degrees)

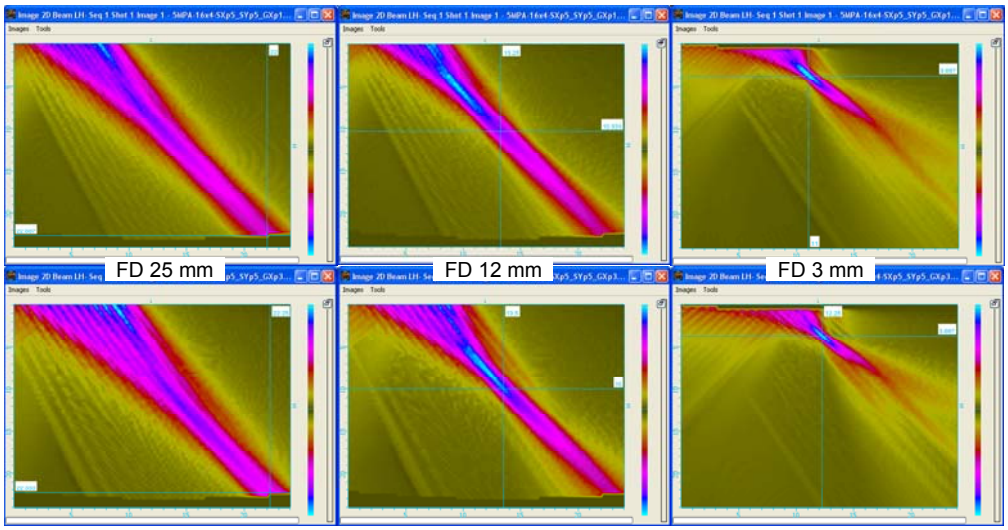

Figure 33. Variable FD and Gx – Gx 0.1 mm (Top) and Gx 0.3 mm (Bottom) (ID MPA 5 MHz, Active Aperture 16×4, WP 5 mm, SW 45 degrees)

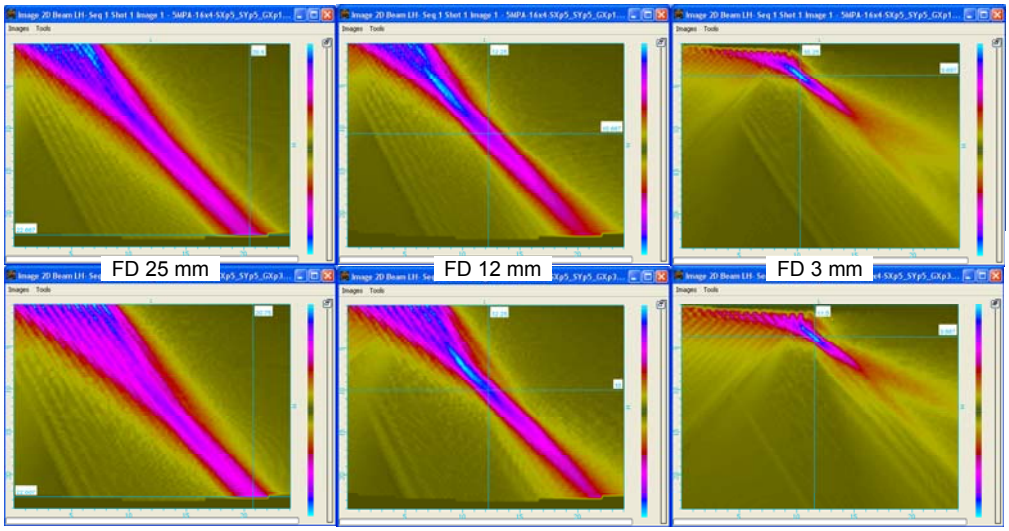

Figure 34. Variable FD and Gx – Gx 0.1 mm (Top) and Gx 0.3 mm (Bottom) (ID MPA 5 MHz, Active Aperture 16×4, WP 0.1 mm, SW 45 degrees)

To increase the surface coverage in the primary direction, larger Sx and Gx was required. A simulation with increased Sx of 0.75 and 1 mm is shown in Figure 35. Although some focusing and steering was possible, the beam streak-like pattern was unacceptable. Simulations with a larger Gx of 0.9 mm (not shown) produced similar unacceptable pressure distribution.

Reliable SW beam focusing and steering at higher frequency of 10 MHz was not possible to achieve as shown in Figure 36. Consequently, frequencies higher than 5 MHz were not

investigated during subsequent modeling stages because the larger Sx and Gx used to increase the circumference coverage would perform worse at higher frequencies compared to the beam shown in Figure 36.

Increased WP is another way to increase the inspection coverage at fixed other parameters. The acoustical beam shown in Figure 37 at a WP of 25.4 mm provided ID circumferential coverage of approximately 22 degrees but also indicated that it may not be possible to generate a SW when the WP was greater than 10 mm. A summary of the simulation experimental matrix and comments for SW generation are given in Tables 7 and 8.

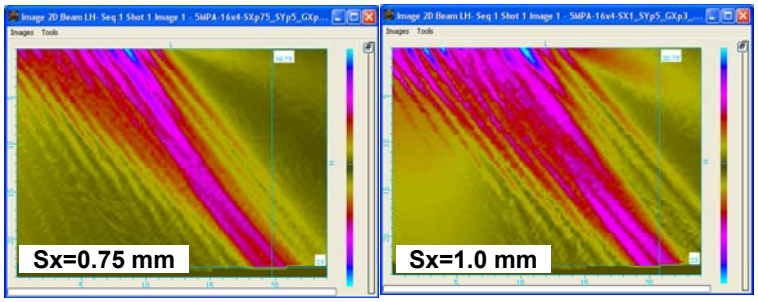

Figure 35. **Variable Large Sx** (ID MPA 5 MHz, Active Aperture 16×4, FD 25 mm, WP 10 mm, SW 45 Degrees, Sy – 0.5 mm, Gx – 0.3 mm, Gy – 0.1 mm)

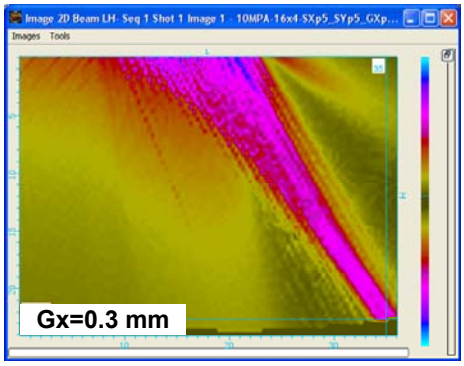

Figure 36. **Higher Frequency** (ID MPA 10 MHz, Active Aperture 16×4, FD 25 mm, WP 10 mm, SW 45 Degrees, Sy – 0.5 mm, Gx – 0.3 mm, Gy – 0.1 mm)

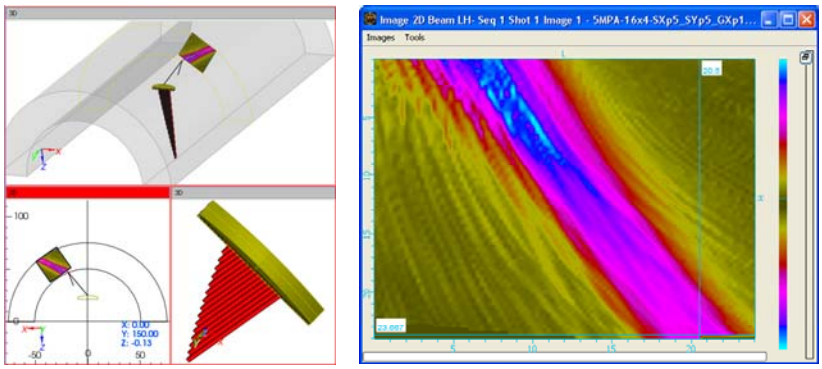

Figure 37. **Large WP 25.4 mm and Small ID Inch** (ID MPA 5 MHz, Active Aperture 16×4, FD 25 mm, SW 45 Degrees, Sx and Sy – 0.5 mm, Gx and Gy – 0.1 mm)

Table 7. **Variable WP, FD, and Gx** (ID MPA 5 MHz, 16×4 Active Aperture, 45-degrees SW)

Step No.	WP (mm)			FD (mm)			Gx (mm)		Notes
1			10			25	0.1		Steer but focus outside of max pressure
2			10			25		0.3	Same
3			10		12		0.1		Good focus and steer but focus slightly outside of max pressure
4			10		12			0.3	Same with some non-uniformity
5			10	3			0.1		Very good focus and steer
6			10	3				0.3	Same with some non-uniformity
7		5				25	0.1		Steer but focus outside of max pressure
8		5				25		0.3	Same
9		5			12		0.1		Good focus and steer but focus slightly outside of max pressure
10		5			12			0.3	Same with some non-uniformity
11		5		3			0.1		Very good focus and steer
12		5		3				0.3	Same with some non-uniformity
13	0.1					25	0.1		Steer but focus outside of max pressure
14	0.1					25		0.3	Same
15	0.1				12		0.1		Good focus and steer but focus slightly outside of max pressure
16	0.1				12			0.3	Same with some non-uniformity
17	0.1			3			0.1		Very good focus and steer
18	0.1			3				0.3	Good focus and steer but some non-uniformity

Table 8. Variable Frequency, WP, Sx, Gx, Gy, and Active Aperture (ID MPA 5 MHz, 45-degrees SW)

Step	Freq.		WP (mm)		Sx (mm)			Gx (mm)				Gy (mm)		Act. Group		Notes
1	5		10		0.5			0.1				0.1		32×4		Good focus and steer
2	5		10		0.5				0.3			0.1		32×4		Same
3	5		10		0.5					0.9		0.1			16×4	Good focus and steer but reduced strength and uniformity
4	5		10		0.5					0.9			0.3		16×4	Same
5	5		10			0.75			0.3			0.1			16×4	Steer but reduced focusing and uniformity
6	5		10				1.0		0.3			0.1			16×4	Same
7	5		10		0.5						0.2	0.1			16×4	Steer but focus outside of max pressure
8		10	10		0.5			0.1				0.1			16×4	Steer but reduced focusing and strength
9		10	10		0.5				0.3			0.1			16×4	Steer but reduced focusing, strength, and uniformity
10	5			25.4	0.5			0.1				0.1			16×4	Pipe ID reduced to 4 in.. Lack of focusing and uniformity. Large discrepancy between CIVA (65 degrees) and actual (45 degrees).

3.2.2 Initial Longitudinal Wave (LW) Optimization (Parameter Variables: WP, FD, and Primary Inter-Element Gap (Gx).]

Based on the initial SW models described above, it was decided that efforts would focus on probe optimization for generation of longitudinal waves. Modeling results indicated that shear waves would require smaller element gaps and WPs that would result in less coverage given the limited number of elements.

The first simulation of longitudinal waves was conducted for a single refracted angle of 15 degrees in the primary direction with standard WPs and FDs as shown in Table 9. The element size (Sx and Sy) was kept constant at 0.5 mm and the element gap in the secondary direction (Gy) was kept constant at 0.3 mm. Two gaps in the primary (Gx) of 0.3 and 0.6 mm were investigated.

Simulations showed that the ID circumferential coverage for this active group arrangement increased with larger WPs and larger primary element gap. ID coverage for the standard simulation water paths (0.1, 20, and 40 mm) with a Gx of 0.3 mm was 10, 13, and 20 degrees. When using a Gx of 0.6 mm, the coverage was 13, 18, and 28 degrees. It was also observed that the actual refracted angle became smaller than the requested angle of 15 degrees as the FD increased (Table 9). In general, the refracted angle was 15 or slightly smaller than 15 degrees for a FD of 12 and 25 mm and a Gx of 0.3 mm. The minimum actual refracted angle in the range of 5 to 6 degrees was observed at a FD 3 mm and Gx of 0.6 mm.

Table 9. **Variable WP, FD and Gx** (ID MPA 5 MHz, 16×4 Active Aperture, 1-degrees LW)

Step	WP (mm)			FD (mm)			Gx (mm)		Angle (degrees)	Notes
1			40			25	0.3		13	Good steer but focus slightly outside of max pressure
2			40			25		0.6	12	Good steer and focus at max pressure
3			40		12		0.3		12	Good steer and focus at max pressure
4			40		12			0.6	8	Focus at max pressure but slight reduction of actual refr. angle
5			40	3			0.3		6	Focus near max pressure but slight reduction of actual refr. angle
6			40	3				0.6	6	Same
7		20				25	0.3		14	Good steer but focus outside of max pressure
8		20				25		0.6	14	Very good steer and focus at max pressure
9		20			12		0.3		15	Very good steer and focus very near max pressure
10		20			12			0.6	15	Very good steer and focus at max pressure
11		20		3			0.3		8	Focus at max pressure but reduction of actual refr. angle
12		20		3				0.6	5	Focus at max pressure but reduction of actual refr. angle
13	0.1					25	0.3		15	Good steer but focus outside of max pressure
14	0.1					25		0.6	15	Very good steer and focus at max pressure
15	0.1				12		0.3		16	Good steer and focus very near max pressure
16	0.1				12			0.6	12	Good focus at max pressure but reduction of actual refr. angle
17	0.1			3			0.3		9	Focus at max pressure but strong reduction of actual refr. angle
18	0.1			3				0.6	5	Focus at max pressure but strong reduction of actual refr. angle

3.2.2.1 Investigation of LW Refracted Angle and Circumferential Coverage

This numerical experiment addressed the generation of refracted angles larger than 15 degrees in the primary axis and increased circumferential coverage. The larger refracted angles are helpful to improve detectability of planner flaws connected to the backwall (BW) or, in this case, the pipe OD. Half of the experimental matrix (Steps 1 through 6 in Table 10) was similar to the experiment discussed in the previous paragraph and was generated with Sx = Sy = 0.5 mm and a Gy of 0.3 mm. The other half of the test matrix (Steps 7 through 12 in Table 10) was generated with Sx = Sy = 1 mm and a Gy of 0.6 mm. Two different element gaps in the primary direction (Gx) of 0.6 and 1.2 mm were simulated as well. Refracted LW angles of 25, 35, and 45 degrees in primary direction only were specified in the software. The WP and FD were fixed at standard values of 40 and 25 mm, respectively.

The focusing and steering capabilities in primary direction for the first six simulation steps of Table 10 are shown in Figure 38. The actual refracted angles of 20, 27, and 35 degrees were smaller than the requested angles of 25, 35, and 45 degrees. The error in steering increased with the increase of the refracted angle. This is consistent with the results presented in Table 9 for the same WP and FD values and a 15-degree refracted angle. A side lobe started forming at larger refracted angles and Gx [Figure 38 (bottom, right)]. Focusing capabilities were demonstrated for both Gx values and all angles. However, the actual FD decreased with an increase in the refracted angle and decrease of Gx indicating the limits of electronic steering and focusing for these probe parameters. Some deterioration of beam uniformity is visible for large Gx of 1.2 mm. The circumference coverage was 20 and 28 deg for Gx 0.6 and 1.2 mm, respectively.

As discussed earlier, larger coverage in the primary direction can be achieved when Sx and Gx are increased. Simulation Steps 7 through 12 were conducted with Sx and Gx values shown in Table 10. Although the coverage was increased to 41 degrees (Gx 0.6 mm) and 56 degrees (Gx 1.2 mm), focusing and steering were unacceptable as shown in Figure 39. Strong grating lobes were also generated, particularly at the larger Gx of 1.2 mm. Based on the results of this simulation, the element size in the primary direction could be reduced below 1 mm.

While the element sizes and gaps were maintained at larger values (Sx 1 mm, Sy 1 mm, Gy 0.6 mm), the largest circumferential coverage would be achieved by electronically scanning using small active element groups as follows:

- 60.5 degrees with active aperture 8×4 and Gx – 0.6 mm
- 70.9 degrees with active aperture 4×4 and Gx – 0.6 mm
- 97.5 degrees with active aperture 4×4 and Gx – 1.2 mm.

Table 10. Variable Refracted Angle and Gx (ID MPA 5 MHz, 16×4 Active Aperture, 40-mm WP, 25-mm FD)

Step	Refr. Angle (mm)			Sx (mm)		Sy (mm)		Gx (mm)		Gy (mm)		Ray Trace (degrees)	Act. Angle (degrees)	Notes
1			25	0.5		0.5		0.3		0.3		20	20	G. steer but focus outside of max pressure
2			25	0.5		0.5			0.6	0.3		20	20	G. steer and focus at max pressure
3		35		0.5		0.5		0.3		0.3		26	26	G. steer and focus outside of max pressure
4		35		0.5		0.5			0.6	0.3		28	28	G. steer but focus slightly outside of max pressure
5	45			0.5		0.5		0.3		0.3		35	35	Steer but focus outside of max pressure
6	45			0.5		0.5			0.6	0.3		35	35	Same
7			25		1		1	0.6			0.6	21	~0	Focus slightly outside of max pressure grating lobe, poor steering, strongly reduced angle to 5 degrees
8			25		1		1		1.2		0.6	21	~0	Some focus at max pressure grating lobe, no steering, strongly reduced angle to almost 0 degrees
9		35			1		1	0.6			0.6	30	~0	Some focus at max pressure grating lobe, no steering, strongly reduced angle to almost 0 degrees, beam bending
10		35			1		1		1.2		0.6	31	~0	Some focus near max pressure grating lobe, no steering, strongly reduced angle to almost 0 degrees, non-uniformity
11	45				1		1	0.6			0.6	37	~0	Grating lobe, no focus and steering, strongly reduced angle to almost 0 degrees, beam bending
12	45				1		1		1.2		0.6	38	~0	Grating lobe, some poor focus at max pressure, no steering, strongly reduced angle to almost 0 degrees, beam bending

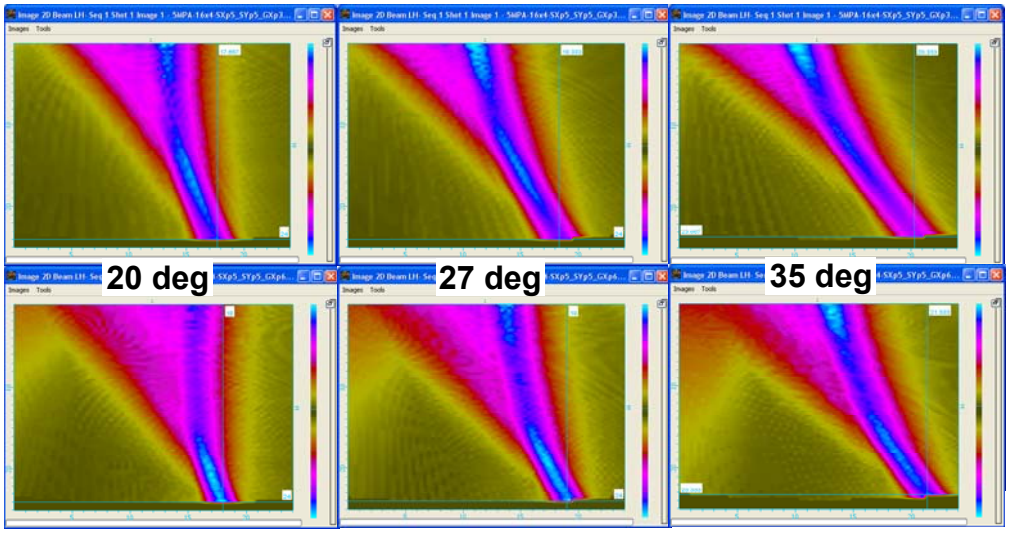

Figure 38. Variable Refracted Angle and Gx – Gx 0.6 mm (Top) and Gx 1.2 mm (Bottom) (ID MPA 5 MHz, Active Aperture 16×4, FD 25 mm, WP 40 mm, Sx and Sy 0.5 mm, Gy 0.3 mm)

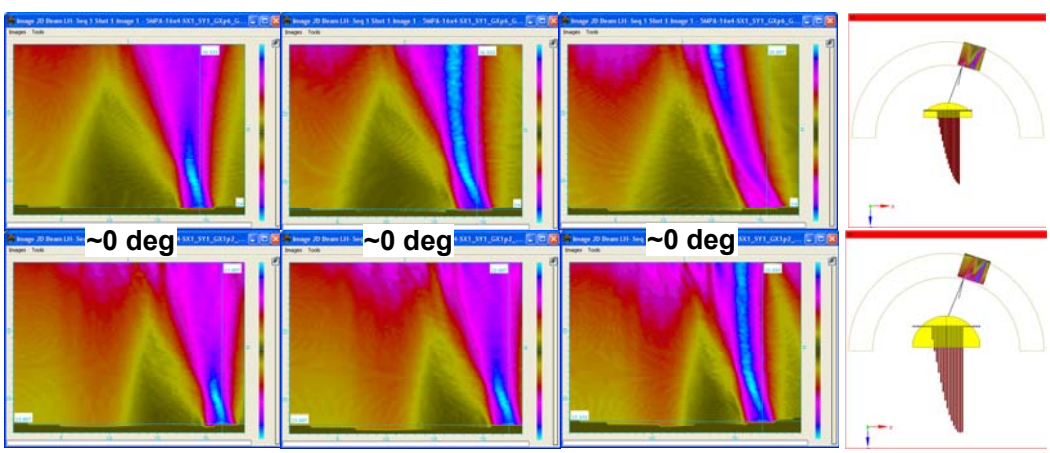

Figure 39. Variable Refracted Angle, Large Sx and Gx – Gx 0.6 mm (Top) and Gx 1.2 mm (Bottom) (ID MPA 5 MHz, Active Aperture 16×4, FD 25 mm, WP 40 mm, Sx and Sy 1 mm, Gy 0.6 mm)

Consequently, beam models were calculated to determine how these reduced aperture sizes would perform. Focusing and steering were verified in the primary direction only using a fixed WP of 40 mm and two FDs of 12 and 25 mm for the reduced active aperture. The requested refracted angle was kept constant at 25 degrees. A summary of the experimental matrix and beam shape are shown in Table 11 and Figure 40. Results showed that beam steering was affected by the smaller apertures as evidenced by reduction in actual refracted angles to a

range of 14 to 16 degrees (Table 11). Overall, neither focusing nor steering, nor the high intensity grating lobes were acceptable as shown in Figure 40.

For the next set of numerical experiments shown in Table 12, the WP and refracted angles were fixed at 40 mm and 25 degrees, respectively (same as Table 11). The first four steps (Steps 1 through 4) in Table 12, with a FD 25 mm, were obtained using an active aperture of 16×4 to in an effort to improve focusing and steering compared to those shown in Figure 40. The circumferential coverage for the different element size and gap combinations were as follows:

- 27.9 degrees with Sx 1 mm and Gx 0.1 mm
- 32.9 degrees with Sx 1 mm and Gx 0.3 mm
- 26.6 degrees with Sx 0.75 mm and Gx 0.3 mm
- 34.2 degrees with Sx 0.75 mm and Gx 0.6 mm.

As expected, the focusing and steering improved as shown in Figure 41. A promising direction for optimization was found to be in the reduction of Sx to 0.75 mm and the increase of Gx to 0.6 mm [Figure 41 (bottom, right)]. This appeared to be a good compromise for obtaining a large circumferential coverage while maintaining focusing and steering capabilities.

While fixing Sx at 0.75 mm and Gx at 0.6 mm, the focusing and steering was verified for a two apertures (8×4 and 12×4) and the 3 standard FDs as shown in Table 12, Steps 5 through 8. A side view of the beam in the primary direction is shown in Figure 42. The focusing capabilities were acceptable with the exception of the 8×4 aperture (Step 5 in Table 12) shown in the bottom left of Figure 42. For the 12×4 aperture, the steering was still limited to a maximum of 14 degrees when using a FD of 25 mm (Step 6 in Table 12) as shown in the top right image of Figure 42. The reduced apertures of 12×4 and 8×4 allowed increased circumferential coverage of 42.7 and 51.3 degrees, respectively.

Table 11. Reduced Active Aperture (ID MPA 5 MHz, 1-mm Sx, 1-mm Sy, 0.6-mm Gy, 40-mm WP, 25-degrees LW)

Step	Active Group		FD (mm)		Gx (mm)		Ray Trace (degrees)	Act. Angle (degrees)	Notes
1	8×4			25	0.6		20	14	Some steer and poor focus outside of max pressure - actual refracted angle reduced significantly to 14 degrees
2		4×4		25	0.6		20	16	Steer but no focus - actual refracted reduced significantly to 16 degrees
3		4×4		25		1.2	20	15	Same
4		4×4	12		0.6		20	14	Same
5		4×4	12			1.2	20	15	Same

Table 12. Variable Aperture, FD, Sx, and Gx (ID MPA 5 MHz, 40-mm WP, 25-degrees LW)

Step	Pr. Act. Group			FD (mm)			Sx (mm)		Gx (mm)			Angle (degrees)	Notes
1	16					25		1	0.1			10	Some focus, poor steering, strongly reduced refracted angle, beam bending
2	16					25		1		0.3		10	Same
3	16					25	0.75			0.3		12	Focus at max pressure, steering to reduced refracted angle
4	16					25	0.75				0.6	12	Same
5		8				25	0.75				0.6	16	Focus close to max pressure, steering to reduced refracted angle
6			12			25	0.75				0.6	14	Same
7			12		12		0.75				0.6	10	Focus at end of max pressure, steering to reduced refracted angle
8			12	3			0.75				0.6	11	Same

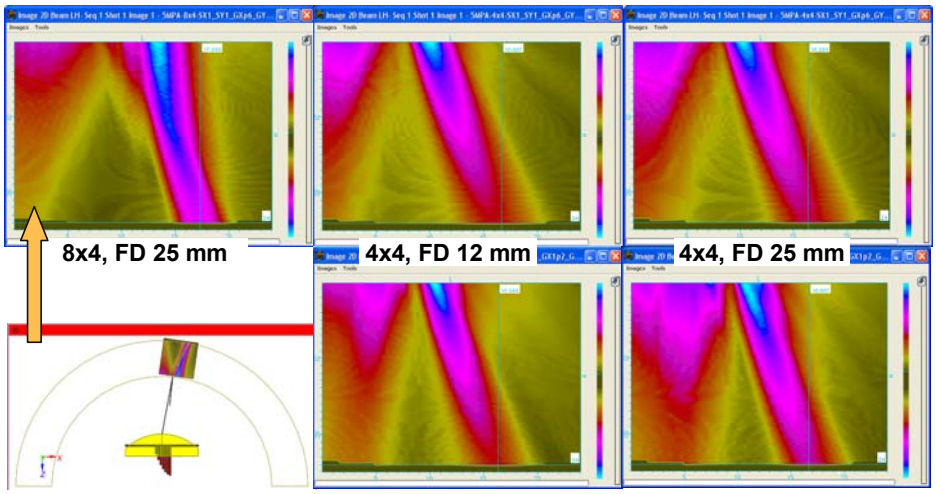

Figure 40. Reduced Active Aperture, Variable FD and Gx – Gx 0.6 mm (Top) and Gx 1.2 mm (Bottom) (ID MPA 5 MHz, WP 40 mm, LW 25 degrees, Sx 1 mm, Sy 1 mm, Gy 0.6 mm)

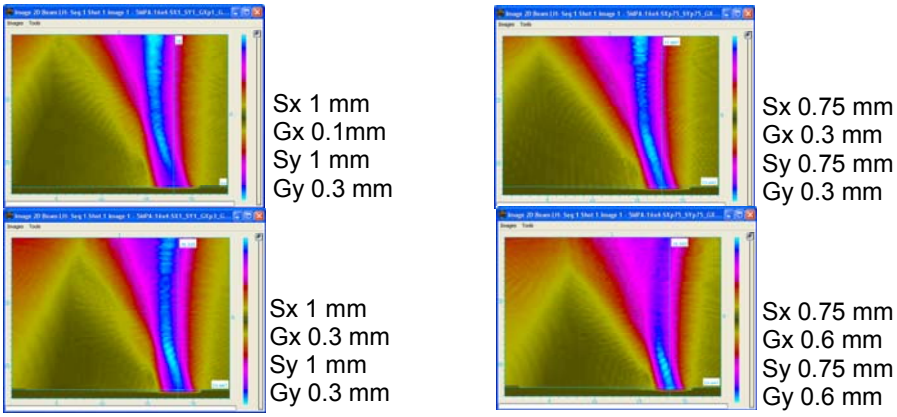

Figure 41. Variable Element Size and Gap – Increased Sx and Gx (ID MPA 5 MHz, Active Aperture 16×4, FD 25 mm, WP 40 mm, LW 25 degrees)

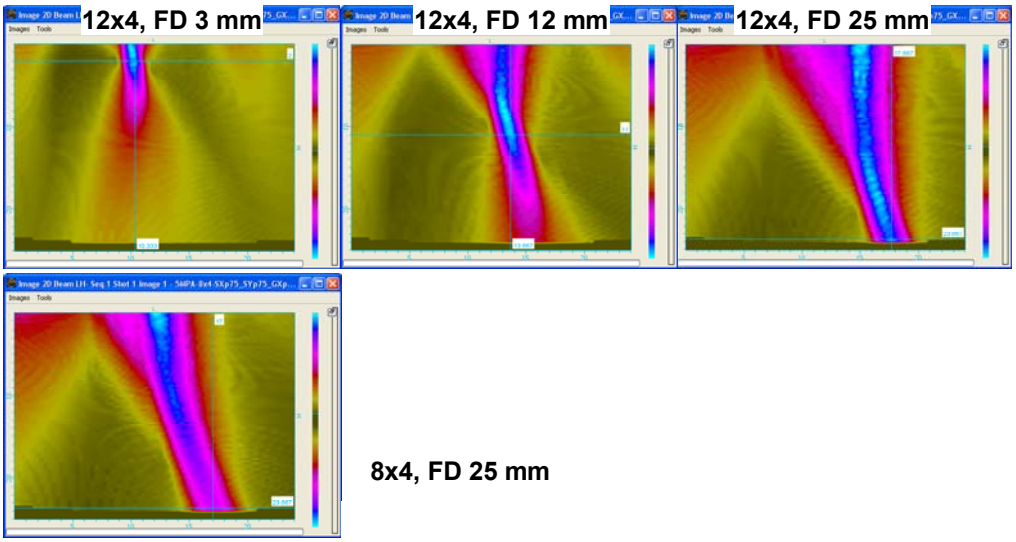

Figure 42. Variable Aperture and FD – Increased Sx – 0.75 mm and Gx – 0.6 mm (ID MPA 5 MHz, WP 40 mm, LW 25 degrees)

3.2.2.2 Investigation of Reduced Aperture Size (12×4)

Based on the previous LW modeling results, adequate steering and focusing could not be achieved when using large element sizes and gaps (Sx and Gx), or when the active aperture was smaller than 12×4. The next numerical experiment was designed to further investigate the capabilities of a 12×4 active aperture with Sx = Sy = 0.5 mm and Gx = Gy = 0.6 mm. Beam modeling was done for LW refracted angles of 15, 25, 35, and 45 degrees at the three standard FDs. Focusing and steering were verified in the primary direction only for a WP 40 mm.

Modeling results are summarized in Table 13 and beam side views are shown in Figures 43 and 44. The pipe circumference coverage in the primary direction was 34.8 degrees for this active aperture, element size, and gap. As previously noted, the absolute steering error increased with the increase of the requested refracted angle. The absolute steering error also increased when the FD was decreased. On the other hand, the focusing improved as the FD decreased. These errors indicated the limits for steering for these particular parameters. There were no significant side or grating lobes visible.

Table 13. Variable FD and Refracted Angle (ID MPA 5 MHz, 12×4 Active Aperture , 40-mm WP, Sx = Sy = 0.5 mm, Gx = Gy = 0.6 mm)

Step	FD (mm)			Requested Angle (degrees)				Focus (mm)	Angle (degrees)	Notes
1			25				45	3.4	36	Steer but focus outside max pressure, reduced angle
2			25			35		3.27	28	Same
3			25		25			3.01	20	Steer and focus close to max pressure, reduced angle
4			25	15				2.83	13	Good steer and focus very close to max pressure, slightly reduced angle
5		12					45	2.4	31	Steer and focus at end of max pressure, reduced angle
6		12				35		2.38	24	Same
7		12			25			2.21	16	Same
8		12		15				1.98	9	Same
9	3						45	1.74	24	Steer and good focus at end of max pressure, reduced angle
10	3					35		1.6	19	Steer and good focus at max pressure, reduced angle
11	3				25			1.52	11	Same
12	3			15				1.59	7	Same

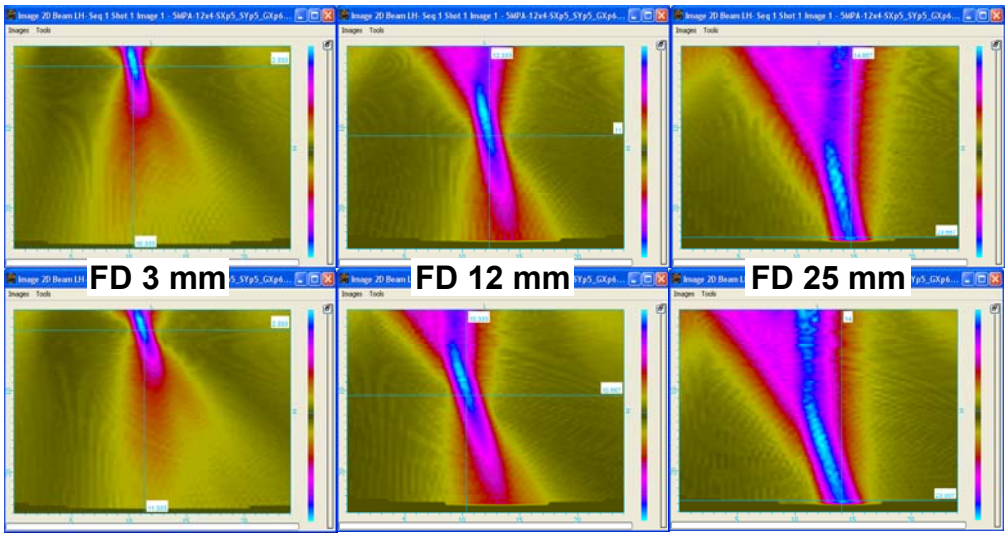

Figure 43. **Variable Angle and FD – Top - Requested Refracted Angle 15 Degrees, Actual 7-13 degrees, Bottom – Requested Refracted Angle 25 Degrees, Actual 11-20 Degrees** (ID MPA 5 MHz, Active Aperture 12×4, WP 40 mm, Sx and Sy 0.5 mm, Gx and Gy 0.6 mm)

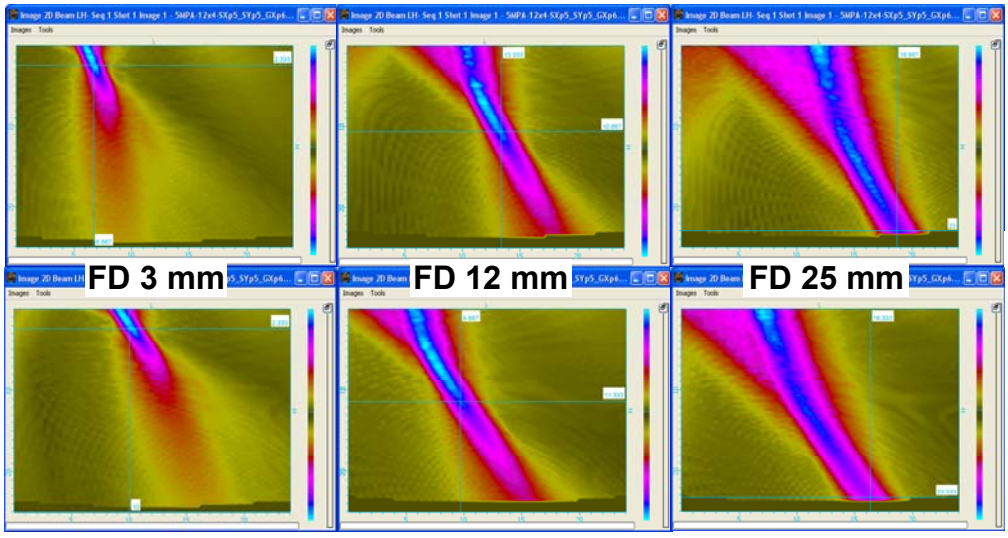

Figure 44. **Variable Angle and FD – Top - Requested Refracted Angle 35 Degrees, Actual 16-28 Degrees, Bottom – Requested Refracted Angle 45 Degrees, Actual 24-36 Degrees** (ID MPA 5 MHz, Active Aperture 12×4, WP 40 mm, Sx and Sy 0.5 mm, Gx and Gy 0.6 mm)

3.2.2.3 Summary Optimization Plots for Sx, Gx, and Number of Active Elements

A summary of optimization results for beam shape, steering, and focusing in the primary direction is presented on 3D and 2D plots shown in Figures 45 through 51.

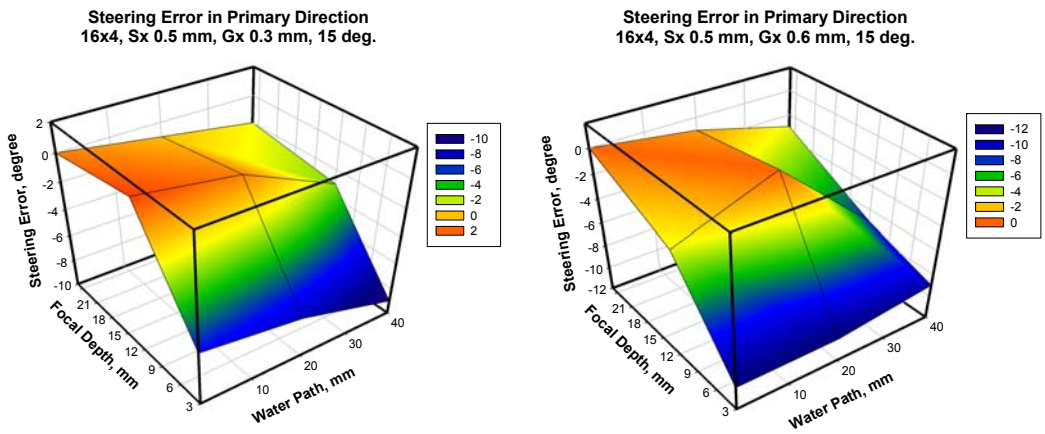

Figure 46. Primary Steering Error vs. WP, FD, and Gx (ID MPA 5 MHz, Active Aperture 16×4, LW 15 Degrees)

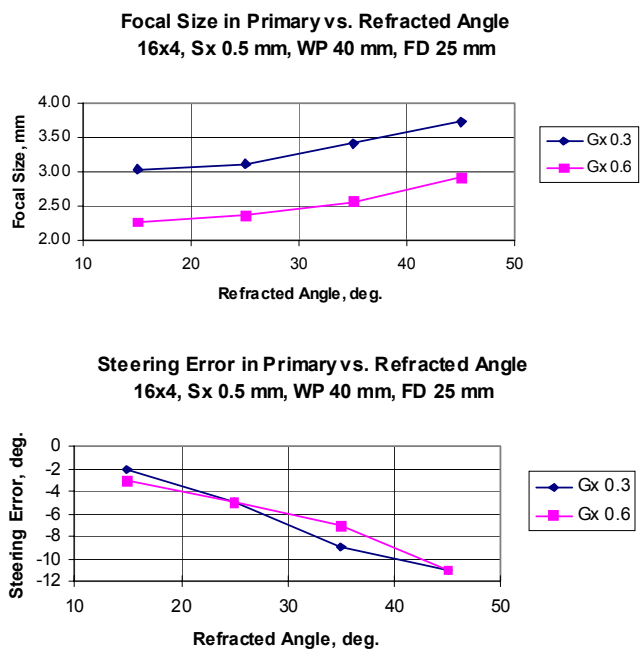

Figure 47. Primary Focal Size and Steering Error vs. Refracted Angle and Gx (ID MPA 5 MHz, Active Aperture 16×4, FD 25 mm, WP 40 mm)

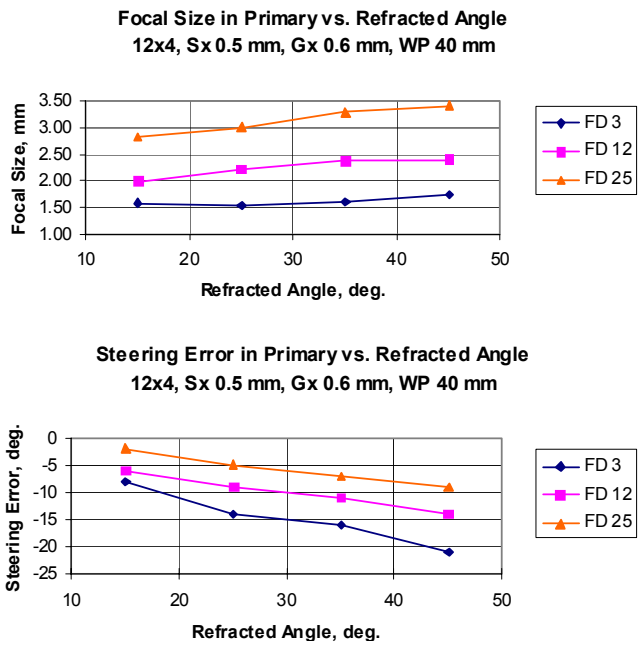

Figure 48. **Primary Focal Size and Steering Error vs. Refracted Angle and FD** (ID MPA 5 MHz, Active Aperture 12×4, WP 40 mm)

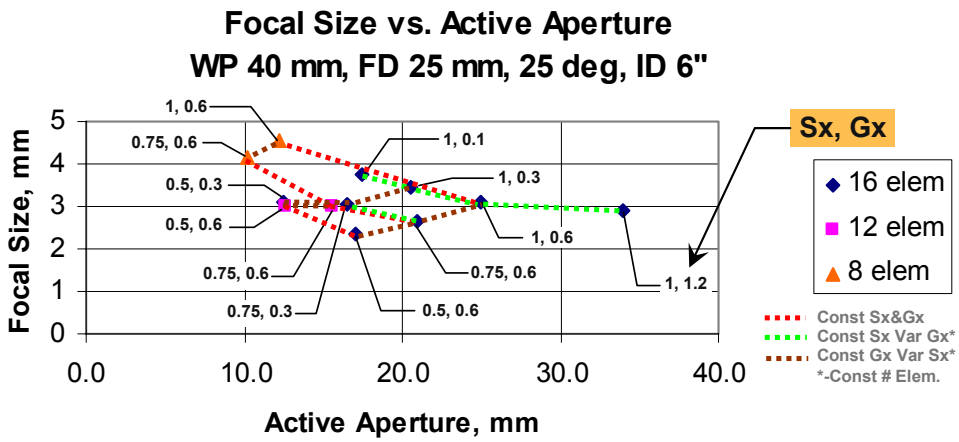

Figure 49. **Primary Focal Size vs. Active Aperture, Sx, and Gx** (ID MPA 5 MHz, FD 25 mm, WP 40 mm, LW 25 Degrees)

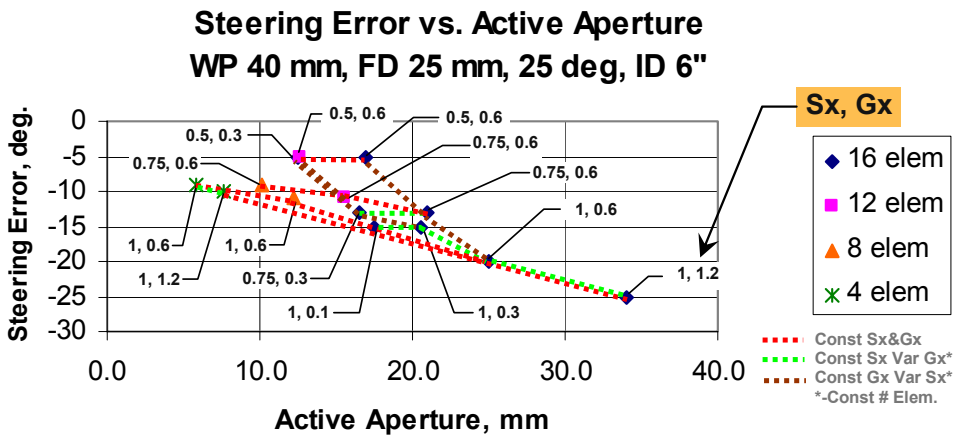

Figure 50. **Primary Steering Error vs. Active Aperture, Sx, and Gx** (ID MPA 5 MHz, FD 25 mm, WP 40 mm, LW 25 Degrees)

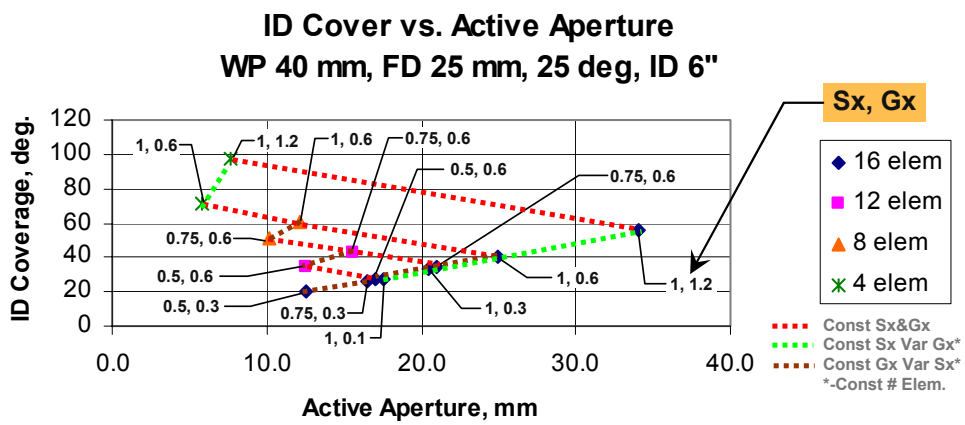

Figure 51. **Primary Coverage vs. Active Aperture, Sx, and Gx** (ID MPA 5 MHz, FD 25 mm, WP 40 mm, LW 25 Degree)

The first pair of 3D plots shown in Figure 45 illustrates how the focal capabilities change depending on WP and FD for two gap (Gx) variations. The active group was 16×4 with an Sx of 0.5 mm and a refracted angle of 15 degrees. The focal spot size did not depend on the WP when the FD was in the range of 15 to 25 mm; however, the focal size appears to increase with the increase of the WP for smaller FDs. The focal size decreased almost linearly as the FD was decreased. The focal size decreased at a faster rate at smaller WPs. The focal size for a Gx of 0.6 mm was smaller compared to a Gx of 0.3 mm for all simulated WPs and FDs combinations.

The second pair of optimization 3D plots shown in Figure 46 for the same range of parameters (see Figure 45) illustrates the change in steering capabilities. For the plot with a Gx of 0.3 [Figure 46 (left)], better steering (smaller error) was produced at WP<30 mm and FD>9 mm. The steering capabilities improved slightly with the decrease of the WP. For the plot with a Gx

of 0.6 [Figure 46 (right)], better steering was demonstrated at WP<25 mm and FD>12 mm. The steering error was slightly smaller when using a Gx of 0.3 mm.

As discussed previously, the focus and steering capabilities will depend on the refracted angle as well. Figure 47 shows the focal size and steering error vs. refracted angle for a 16×4 active aperture with a 40 mm WP and FD of 25 mm. The element size in the primary axis (Sx) was 0.5 mm. Steering errors are shown for two values of Gx (0.3 and 0.6 mm). The focal size increased with the increase of the refracted angle. The focal size was smaller for Gx 0.6 mm (see Figure 45). The steering error increased with the increase of the refracted angle. An important conclusion from the analysis of this plot is that the steering error depends very little (if at all) on Gx.

Figure 48 shows effects on beam size and steering error at different FDs for a 12×4 active aperture with a Sx of 0.5 mm, a Gx of 0.6 mm, and a WP of 40 mm. The focal size increased with the increase of the FD. The focal size increased with the increase of the refracted angle similar to the previous 16×4 aperture models. However, the focal size increase was less pronounced or not present at small FD indicating that the combined water path and metal path was within the focusing range (near field). The steering error increased with the increase of the refracted angle and decrease of the FD. The steering error increase was more pronounced at smaller FDs which was opposite to the effect that the FD had on the focal size shown in Figure48 (top).

A different arrangement of the simulation data for the primary direction optimization is presented in Figures 49 through 51 where the focal size, steering error, and coverage vs. active aperture are shown. The WP, FD, and refracted angle were fixed as follows: WP 40 mm, FD 25 mm, and refracted angle 25 degrees.

The focal size plot vs. the active aperture is shown in Figure 49. The increase of Sx and reduction the number of elements in the primary direction, in order to increase the coverage, caused the focal size to increase. The very small apertures such as 4×4 (not shown) and 8×4 with large Sx 1 mm and Gx 0.6 and 1.2 mm were not capable of focusing (see Figure 40). As expected, the focal size was the smallest with a Sx of 0.5 mm and a Gx of 0.6 mm for a 16×4 element aperture. It was determined that other possible combinations that would provide increased circumferential coverage were Sx 0.5 mm, Gx 0.6 mm and Sx 0.75 mm, Gx 0.6 for an active aperture of 12×4, and an Sx 0.75 mm, Gx 0.3 for an active aperture of 16×4. The increased coverage, however, would be realized at the expense of an increased focal size.

The effect that the active aperture has on the steering error is shown in Figure 50. Only three combinations Sx 0.5 mm, Gx 0.6 mm and Sx 0.5 mm, Gx 0.3 for an active aperture of 16×4; and Sx 0.5 mm, Gx 0.6 for an active aperture of 12×4 provided a relatively small steering error of 5 degrees. All other combinations caused the steering error to become equal or larger than 10

degrees. Some trends are clearly identified on the plot. For example, the steering error increased with the increase of Sx and the number of elements. A major factor for the steering error increase was the increase of Sx. The steering error was not significantly affected by Gx for smaller Sx and Gx.

The last summary plot of pipe circumference or ID coverage vs. active aperture is shown in Figure 51. As expected, the smallest active apertures with the largest element size and gap produced the largest coverage. The focal and steering capabilities of these configurations were not adequate as discussed and demonstrated previously. The focal and steering capabilities were considered to be of higher priority compared to coverage. The combination of Sx 0.5 mm and Gx 0.6 mm with an active aperture of 12×4 would provide better electronic scan coverage compared to an active aperture of 16×4. This of course came at the expense of an increased focal spot size (see Figure 49).

3.2.2.4 Optimization of Secondary Probe Axis Element Size (Sy) and Inter-Element Gap (Gy)

After finalizing the optimization in primary direction discussed above, the following simulation efforts focused on element size and gap optimization in secondary direction. It was realized that steering and focusing in secondary direction would be limited due to the limitation of the number of elements in secondary direction to only four. The main optimization objective in the secondary direction was to limit the beam divergence and grating lobes while providing some minimal steering and focusing capabilities. The element size and gap in the primary direction Sx and Gx were kept constant at 0.5 and 0.6 mm, respectively. The steering and focusing capabilities in secondary direction were investigated at a WP of 40 mm, using the three standard FDs, two refracted angles (15 and 30 degrees), three secondary element sizes (0.5, 1, and 2 mm), and two secondary gaps (0.6 and 1 mm).

A summary of simulation results is given in Tables 14 and 15. Beam side views for an Sy of 1 mm are shown in Figures 52 and 53. The focal size was the smallest when using the largest Sy of 2 mm, but this produced very strong grating lobes especially at larger refracted angle of 30 degrees and larger Gy 1 mm (see Tables 14 and 15). The smallest Sy of 0.5 mm produced the smallest grating lobes; however, the beam divergence or lack of focusing was the largest. The grating lobes produced with an element size Sy of 1 mm had less intensity (< -6 dB) compared to the main lobe and provided reasonable steering and focusing. The secondary gap Gy was selected to be 0.6 mm based again on the smaller intensity of the grating lobes (see Figures 52 and 53). The actual steering angles were smaller than requested. The absolute steering error increased with an increase of refracted angle and decrease of FD (Tables 14 and 15). The focal size decreased with a decrease of FD and an increase of Sy and Gy.
Another way to represent the simulation results for the secondary direction element size and gap optimization is through 3D optimization plots shown in Figures 54 through 57. The pairs of

plots shown in Figures 54 and 56 represent the change of focal size for refracted angles of 15 and 30 degrees, respectively, with two gaps (Gy) of 0.6 and 1 mm. The focal size decreased almost linearly as the FD decreased. The decrease of focal size was steeper at the smaller Sy value. The larger Gy improved the focusing, especially at larger FD. The smallest focal size was produced at the largest Sy and the smallest FD as discussed earlier. As would be expected, the focal size at a 30-degree refracted angle was larger compared to a 15-degree refracted angle. The resulting effect the FD and Sy will have on the steering error for the two refracted angles is shown in Figures 55 and 57. The Sy and Gy did not have a significant effect on the steering error especially at a FD < 12 mm (see Figure 57). The steering capabilities improved with increased FD. Using the same Sy and FD, the steering error at a 30-degree refracted angle was approximately two times larger compared to a 15-degree refracted angle.

Table 14. Secondary Direction - Variables FD, Sy, and Gy (ID MPA 5 MHz, 16×4 Active Aperture, 40-mm WP, 15-degrees LW, 0.5-mm Sx, 0.6-mm Gx)

Step	FD (mm)			Sy (mm)			Gy (mm)		Focus (mm)	Angle (degrees)	Notes
1			25			2		1	4.91	11	Steer reduced angle, focus, side lobe -7 degrees at -7.5 dB at FD
2			25			2	0.6		5.4	11	Same with side lobe -7 degrees at -8.7 dB at FD
3			25		1			1	6.85	12	Same with side lobe -20 degrees at -10.1 dB at FD
4			25		1		0.6		8.41	12	Same with side lobe -26 degrees at -12.8 dB at FD
5			25	0.5				1	8.93	11	Same with side lobe -35 degrees at -11.8 dB at FD
6			25	0.5			0.6		12.15	9	Same with low-intensity side lobe at large angle
7		12				2		1	3.18	7	Same with two side lobes 0 and -15 degrees at -7.8 and -14.1 dB at FD
8		12				2	0.6		3.48	6	Same with side lobe -6 degrees at -9 dB at FD
9		12			1			1	4.26	8	Same with side lobe -20 degrees at -10.2 dB at FD
10		12			1		0.6		5.35	8	Same with side lobe -30 degrees at -13.1 dB at FD
11		12		0.5				1	5.63	9	Same with two side lobes -32 degrees at -11.7 dB at FD and other low intensity
12		12		0.5			0.6		7.51	9	Same with low-intensity side lobe
13	3					2		1	2.19	4	Same with two side lobes -6.9 and -8.5 dB at FD
14	3					2	0.6		2.39	4	Same with two side lobes -8.4 and -10.5 dB at FD
15	3				1			1	2.59	4	Same with two side lobes -10.3 and -12 dB at FD
16	3				1		0.6		3.19	5	Same with two side lobes -12.8 and -15.4 dB at FD
17	3			0.5				1	3.39	5	Same with two side lobes -11.4 and -13.2 dB at FD
18	3			0.5			0.6		4.49	4	Same with two low intensity side lobes

Table 15. Secondary Direction - Variables FD, Sy, and Gy (ID MPA 5 MHz, 16×4 Active Aperture, 30-degrees LW, 0.5-mm Sx, 0.6-mm Gx)

Step	FD (mm)			Sy (mm)			Gy (mm)		Focus (mm)	Angle (degrees)	Notes
1			25			2		1	5.56	22	Steer reduced angle, focus, strong side lobe -0 degrees at -1.6 dB at FD
2			25			2	0.6		6.18	18	Same with strong side lobe -4 degrees at -2 dB at FD
3			25		1			1	7.46	23	Same with side lobe -9 degrees at -6.6 dB at FD
4			25		1		0.6		9.02	23	Same with side lobe -15 degrees at -7.8 dB at FD
5			25	0.5				1	9.64	22	Same with side lobe -22 degrees at -8.4 dB at FD
6			25	0.5			0.6		12.8	23	Same with side lobe -30 degrees at -10.6 dB at FD
7		12				2		1	3.85	16	Same with strong side lobe -7 degrees at -4.4 dB at FD
8		12				2	0.6		4.3	17	Same with strong side lobe -0 degrees at -4.6 dB at FD
9		12			1			1	4.37	18	Same with side lobe -10 degrees at -7.8 dB at FD
10		12			1		0.6		5.45	17	Same with side lobe -18 degrees at -9.3 dB at FD
11		12		0.5				1	5.83	17	Same with side lobe -25 degrees at -9.1 dB at FD.
12		12		0.5			0.6		7.84	17	Same with side lobe -33 degrees at -12.6 dB at FD
13	3					2		1	2.28	8	Same with two side lobes -6.3 and -9.2 dB at FD
14	3					2	0.6		2.48	8	Same with two side lobes -7.4 and -12 dB at FD
15	3				1			1	2.67	9	Same with two side lobes -9.5 and -13.3 dB at FD
16	3				1		0.6		3.17	8	Same with two side lobes one at -11.7 dB at FD and other low intensity
17	3			0.5				1	3.37	8	Same with two side lobes -10.5 and -14.5 dB at FD
18	3			0.5			0.6		4.56	8	Same with two side lobes -14.5 dB at FD

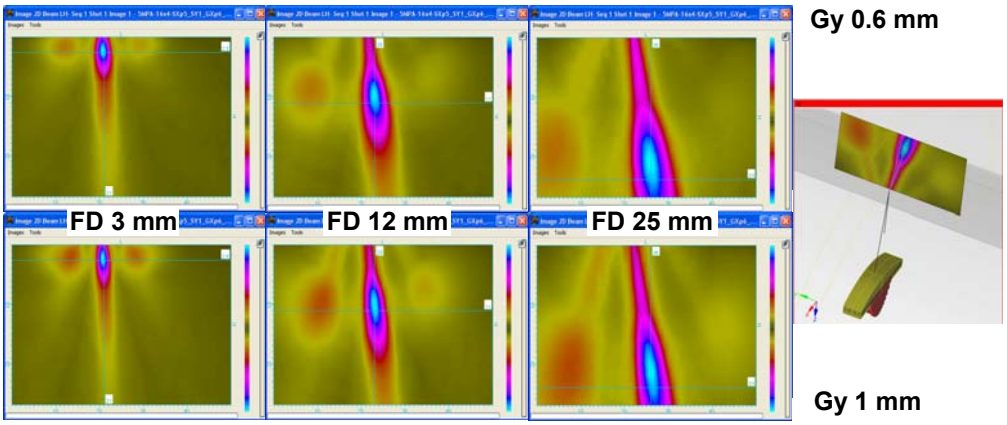

Figure 52. **Variable Gy and FD** (ID MPA 5 MHz, Active Aperture 16×4, WP 40 mm, LW 15 Degrees, Sx 0.5 mm, Gx 0.6 mm, Sy 1 mm)

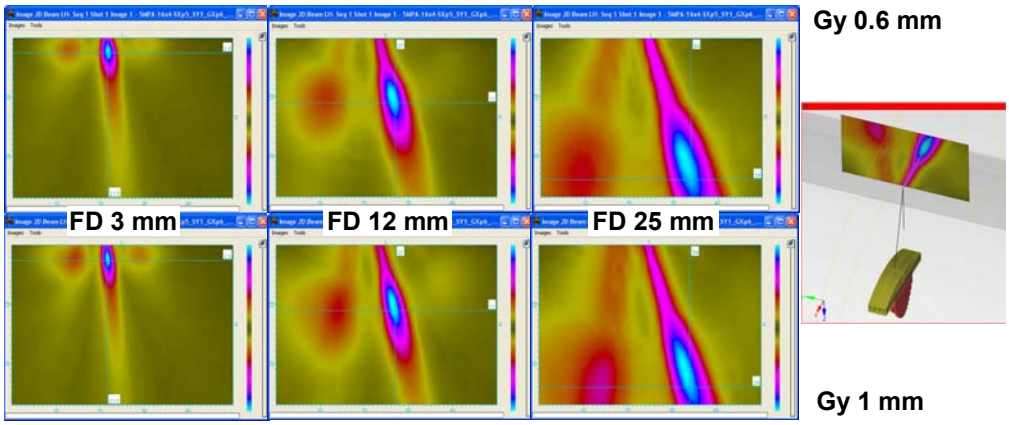

Figure 53. **Variable Gy and FD** (ID MPA 5 MHz, Active Aperture 16×4, WP 40 mm, LW 30 Degrees, Sx 0.5 mm, Gx 0.6 mm, Sy 1 mm)

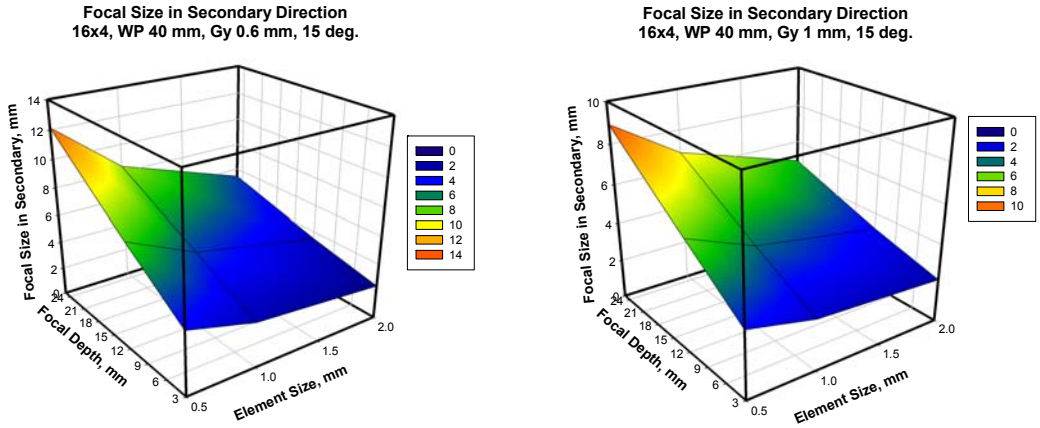

Figure 54. **Secondary Focal Size vs. FD, Sy, and Gy** (ID MPA 5 MHz, Active Aperture 16×4, WP 40 mm, LW 15 Degrees, Sx 0.5 mm, Gx 0.6 mm)

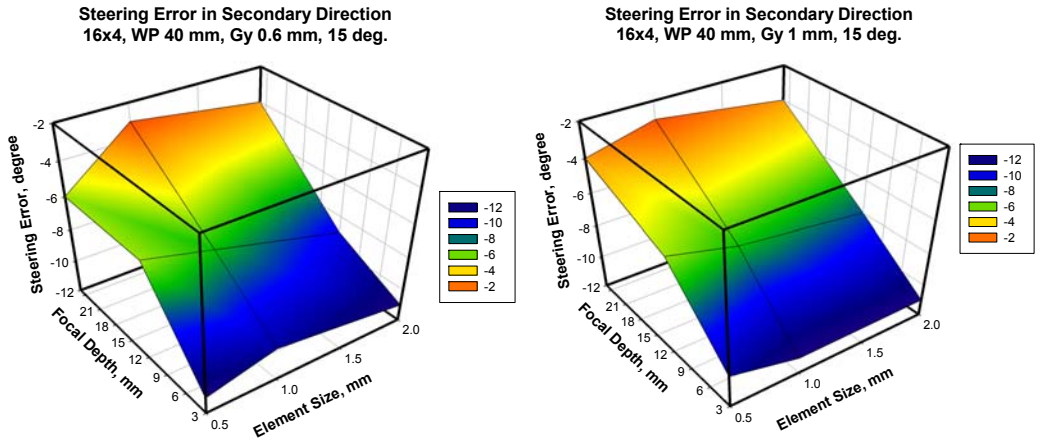

Figure 55. **Secondary Steering Error vs. FD, Sy, and Gy** (ID MPA 5 MHz, Active Aperture 16×4, LW 15 Degrees, Sx 0.5 mm, Gx 0.6 mm)

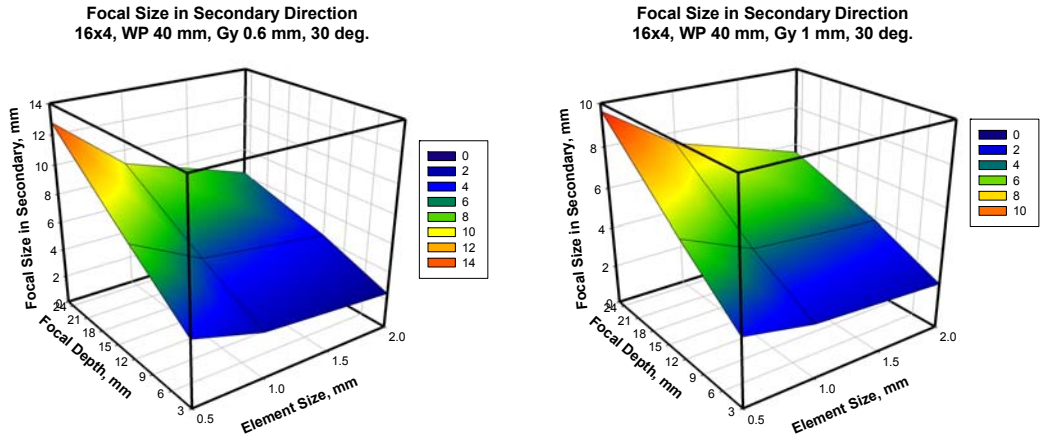

Figure 56. Secondary Focal Size vs. FD, Sy, and Gy (ID MPA 5 MHz, Active Aperture 16×4, WP 40 mm, LW 30 Degrees, Sx 0.5 mm, Gx 0.6 mm)

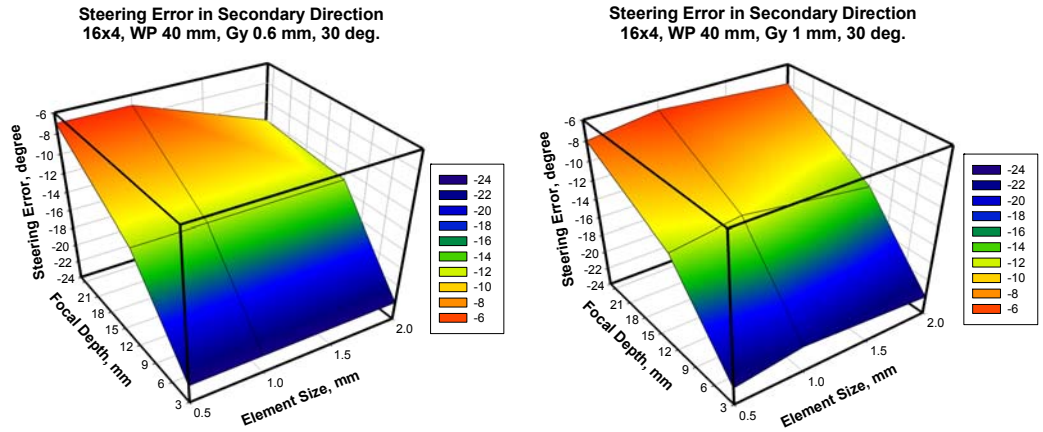

Figure 57. Secondary Steering Error vs. FD, Sy, and Gy (ID MPA 5 MHz, Active Aperture 16×4, LW 30 Degrees, Sx 0.5 mm, Gx 0.6 mm)

3.2.2.5 Optimized Probe Steering and Focal Capabilities

Following the selection of element sizes and gaps in primary and secondary directions, the final simulation steps addressed the verification of beam steering and focusing for all standard WP, FD, normal beam, and two refracted angles – 45 degrees in primary and 30 degrees in secondary. The simulation results for the focal spot sizes (-6 and -3 dB levels) and the actual refracted angles achieved are summarized in Table 16 for all 36 parameter combinations.

As expected the smallest focal size was produced with the normal beam. Side views and cross-sections of the beam in primary and secondary directions for the three standard FDs are shown in Figures 58 through 60 at a WP of 40 mm. The focal spot shifted slightly from being outside of the maximum pressure to the maximum pressure as the FD decreased. The focal size

decreased as the FD decreased. The focal size in the secondary direction became almost equal to the probe aperture in the secondary direction (5.8 mm) at a FD of 12 mm and was reduced further at a FD of 3 mm. Some weak grating lobes started appearing in the secondary direction at a FD of 3 mm and intensified, as expected, with a decrease in the WP (not shown). Beam steering and focal capabilities at a WP of 40 mm are illustrated in Figures 61 through 63 and for a WP of 0.1 mm in Figures 64 through 66. The trend of improved focal capabilities with the decrease of FD is similar to the one observed for the normal beam. Intensity of the grating lobes in the secondary direction increased with the decrease of WP and FD.

The focal size trends vs. WP, FD, and steering direction are better illustrated with 3D plots for the optimized probe shown in Figures 67 through 69. The focal size in the primary direction decreased almost linearly with the decrease of the FD. The effect of the FD was more pronounced at smaller WPs. In the secondary direction (right plots of Figures 67 through 69), the decrease of focal size was almost linear with the decrease of FD and WP. The effect of FD on focal size was stronger than the WP effect. The smallest focal size was produced at the smallest FD and WP.

The steering error vs. WP, FD, and steering direction are illustrated in Figure 70 with 3D plots for the optimized probe. Better steering (smaller error) was demonstrated in primary direction at a WP<20 mm and a FD>12 mm as shown in Figure 70 (left). Steering in the secondary direction was better for a FD>6 and a WP<20 [see Figure 70 (right)].

Table 16. Summary Table (Optimized ID MPA 5 MHz, 16×4 Active Aperture, LW)

Step	WP (mm)			FD (mm)			Primary (degrees)		Secondary (degrees)		Act. Angles - Primary and Secondary (degrees)		Focus -6 dB (mm)	Focus -3 dB (mm)
1			40			25		45		30	-	-		
2			40			25		45	0		32	0	3.1×9.1	2.2×6.6
3			40			25	0			30	0	22	2.4×9.2	1.8×6.7
4			40			25	0		0		0	0	2.3×8.1	1.6×5.8
5			40		12			45		30	-	-		
6			40		12			45	0		30	0	2.2×5.7	1.6×4.2
7			40		12		0			30	0	16	1.7×5.5	1.2×3.9
8			40		12		0		0		0	0	1.6×5.2	1.2×3.7
9			40	3				45		30	-	-		
10			40	3				45	0		22	0	1.6×3.3	1.1×2.3
11			40	3			0			30	0	9	1.2×3.2	0.9×2.3
12			40	3			0		0		0	0	1.2×3.1	0.9×2.4
13		20				25		45		30	-	-		
14		20				25		45	0		38	0	3.3×8.1	2.4×5.9
15		20				25	0			30	0	24	2.4×8.5	1.7×6.1
16		20				25	0		0		0	0	2.2×7	1.6×5.2
17		20			12			45		30	-	-		
18		20			12			45	0		38	0	2×4.6	1.4×3.3
19		20			12		0			30	0	21	1.5×4.6	1×3.3
20		20			12		0		0		0	0	1.4×4.2	1×3
21		20		3				45		30	-	-		
22		20		3				45	0		30	0	1.3×2.2	0.9×1.5
23		20		3			0			30	0	13	0.9×2.2	0.6×1.5
24		20		3			0		0		0	0	0.9×2.1	0.6×1.5
25	0.1					25		45		30	-	-		
26	0.1					25		45	0		44	0	3.8×7.1	2.8×5.1
27	0.1					25	0			30	0	27	2.6×7.7	1.8×5.6
28	0.1					25	0		0		0	0	2.2×5.7	1.4×4
29	0.1				12			45		30	-	-		
30	0.1				12			45	0		40	0	2.2×3.7	1.6×2.6
31	0.1				12		0			30	0	26	1.4×3.9	1×2.8
32	0.1				12		0		0		0	0	1.2×3	0.9×2.1
33	0.1			3				45		30	-	-		

Step	WP (mm)			FD (mm)			Primary (degrees)		Secondary (degrees)		Act. Angles - Primary and Secondary (degrees)			
34	0.1			3				45	0		35	0	1.2×1.4	0.9×1
35	0.1			3			0			30	0	25	0.8×1.4	0.5×1
36	0.1			3			0		0		0	0	0.8×1.4	0.5×0.9

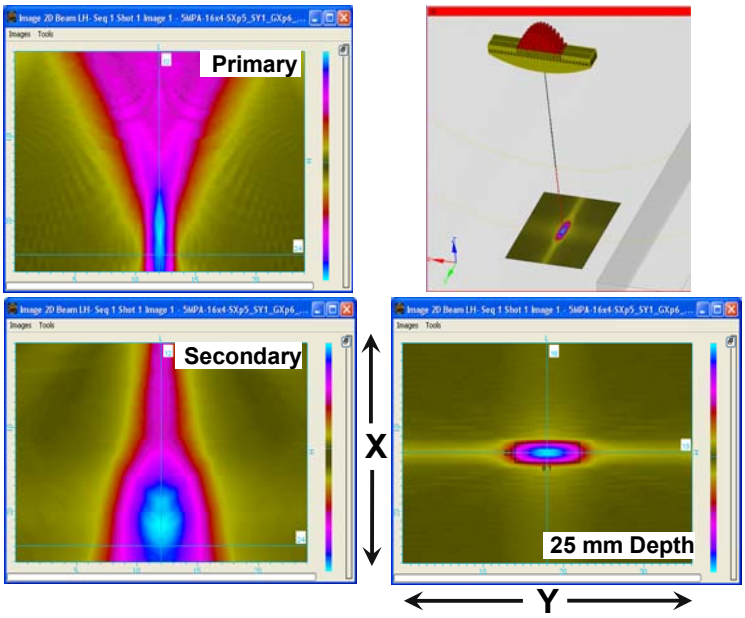

FD (mm)	X (mm)	Y (mm)
25	2.3	8.1

Figure 58. **Normal Beam** (Optimized ID MPA 5 MHz, Active Aperture 16×4, FD 25 mm, WP 40 mm)

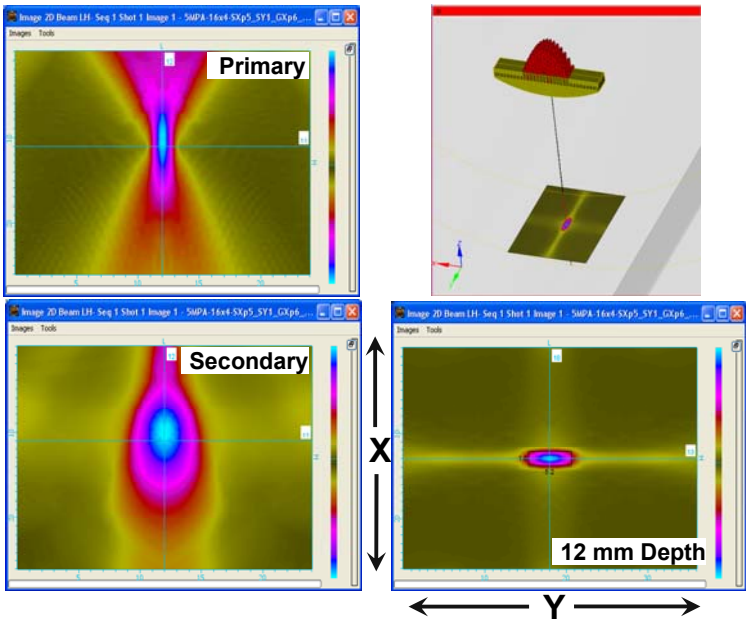

FD (mm)	X (mm)	Y (mm)
12	1.6	5.2

Figure 59. **Normal Beam** (Optimized ID MPA 5 MHz, Active Aperture 16×4, FD 12 mm, WP 40 mm)

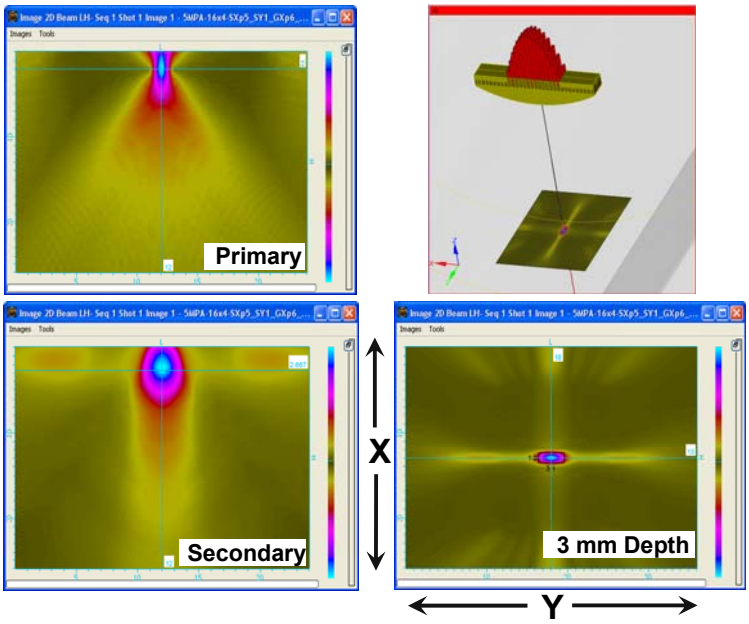

FD (mm)	X (mm)	Y (mm)
3	1.2	3.1

Figure 60. **Normal Beam** (Optimized ID MPA 5 MHz, Active Aperture 16×4, FD 3 mm, WP 40 mm)

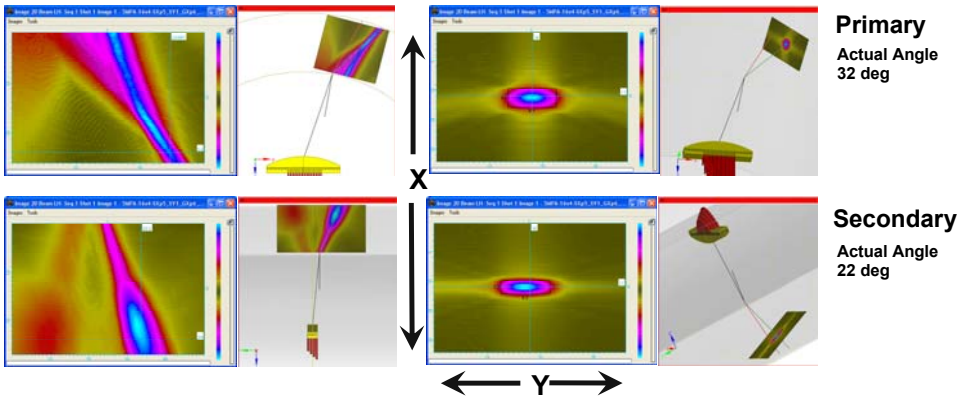

Steering	FD (mm)	X (mm)	Y (mm)
Primary	25	3.1	9.1
Secondary	25	2.4	9.2

Figure 61. Optimized ID MPA 5 MHz, Active Aperture 16×4, FD 25 mm, WP 40 mm, Top – Primary 45 Degrees, Secondary 0 Degrees, Bottom – Primary 0 Degrees, Secondary 30 Degrees

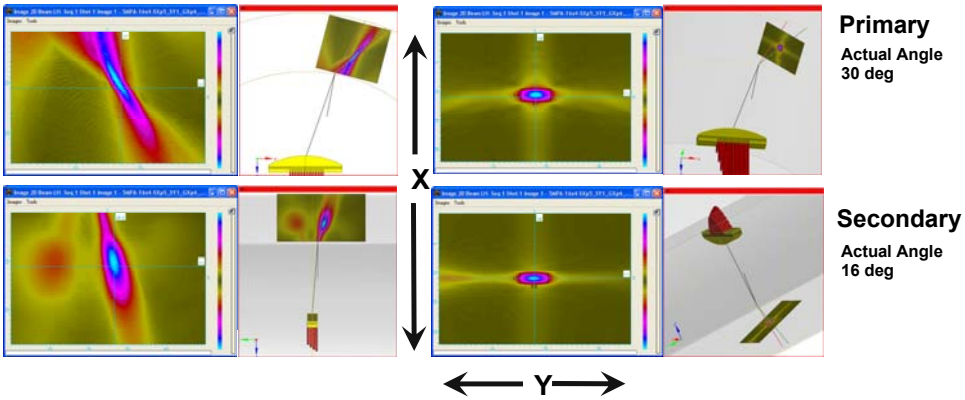

Steering	FD (mm)	X (mm)	Y (mm)
Primary	12	2.2	5.7
Secondary	12	1.7	5.5

Figure 62. Optimized ID MPA 5 MHz, Active Aperture 16×4, FD 12 mm, WP 40 mm, Top – Primary 45 Degrees, Secondary 0 Degrees, Bottom – Primary 0 Degrees, Secondary 30 Degrees

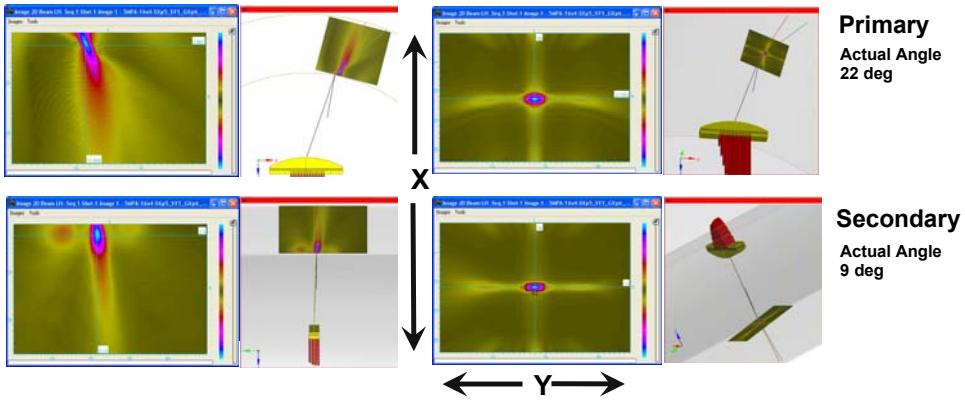

Steering	FD (mm)	X (mm)	Y (mm)
Primary	3	1.6	3.3
Secondary	3	1.2	3.2

Figure 63. **Optimized ID MPA 5 MHz, Active Aperture 16×4, FD 3 mm, WP 40 mm, Top – Primary 45 Degrees, Secondary 0 Degrees, Bottom – Primary 0 Degrees, Secondary 30 Degrees**

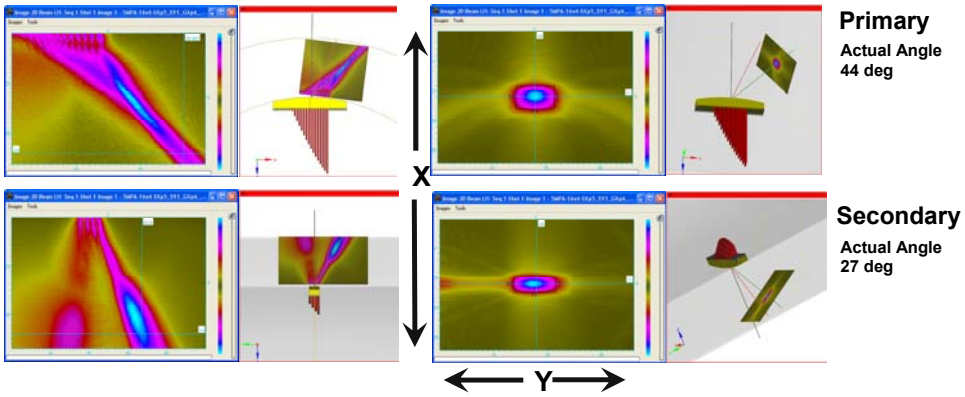

Steering	FD (mm)	X (mm)	Y (mm)
Primary	25	3.8	7.1
Secondary	25	2.6	7.7

Figure 64. **Optimized ID MPA 5 MHz, Active Aperture 16×4, FD 25 mm, WP 0.1 mm, Top – Primary 45 Degrees, Secondary 0 Degrees, Bottom – Primary 0 Degrees, Secondary 30 Degrees**

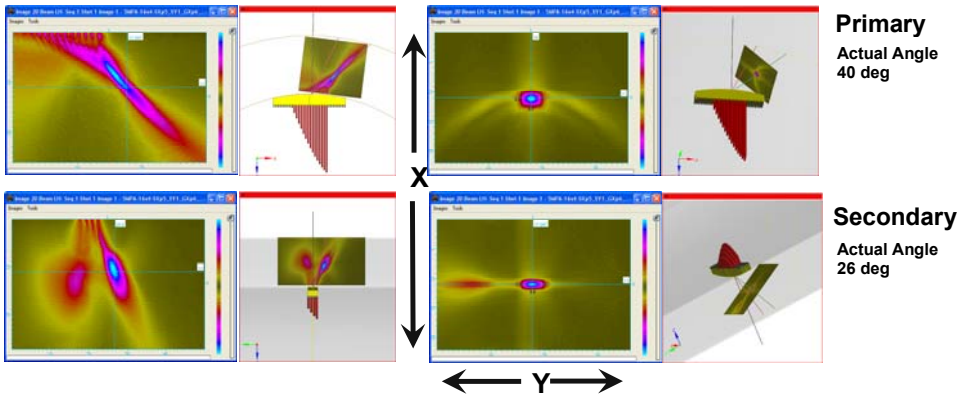

Steering	FD (mm)	X (mm)	Y (mm)
Primary	12	2.2	3.7
Secondary	12	1.4	3.9

Figure 65. **Optimized ID MPA 5 MHz, Active Aperture 16×4, FD 12 mm, WP 0.1 mm, Top – Primary 45 Degrees, Secondary 0 Degrees, Bottom – Primimary 0 Degrees, Secondary 30 Degrees**

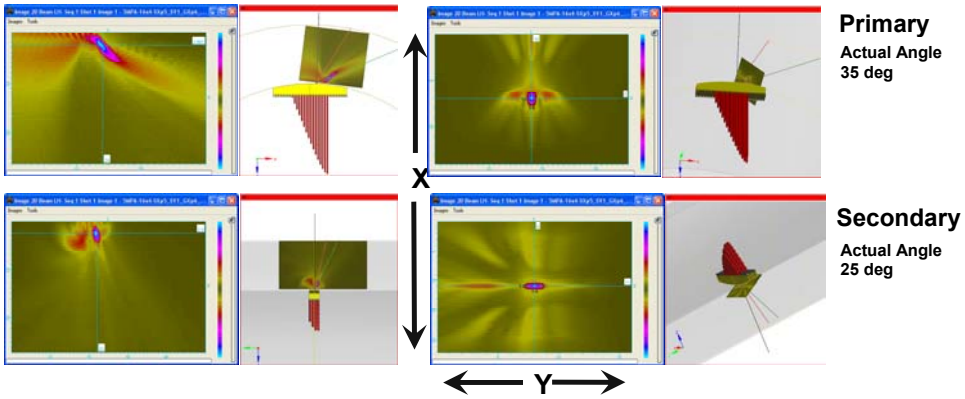

Steerung	FD (mm)	X (mm)	Y (mm)
Primary	3	1.2	1.4
Secondary	3	0.8	1.4

Figure 66. **Optimized ID MPA 5 MHz, Active Aperture 16×4, FD 3 mm, WP 0.1 mm, Top – Primary 45 Degrees, Secondary 0 Degrees, Bottom – Primary 0 Degrees, Secondary 30 Degrees**

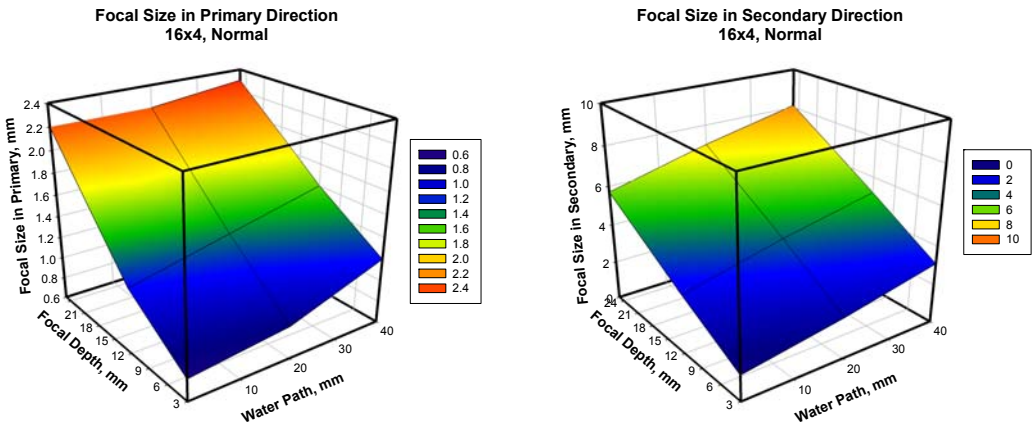

Figure 67. Primary and Secondary Focal Size vs. FD and WP – Optimized ID MPA 5 MHz, Active Aperture 16×4, Normal Beam

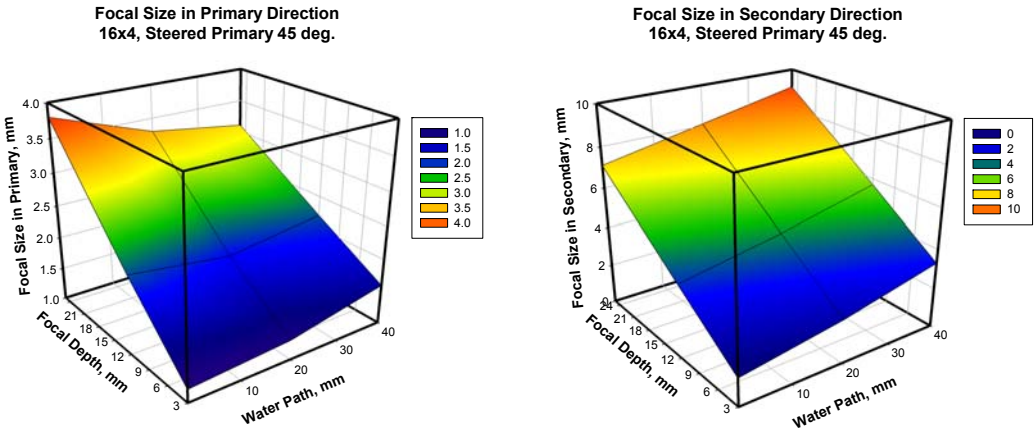

Figure 68. Primary and Secondary Focal Size vs. FD and WP – Optimized ID MPA 5 MHz, Active Aperture 16×4, Primary 45 Degrees, Secondary 0 Degrees

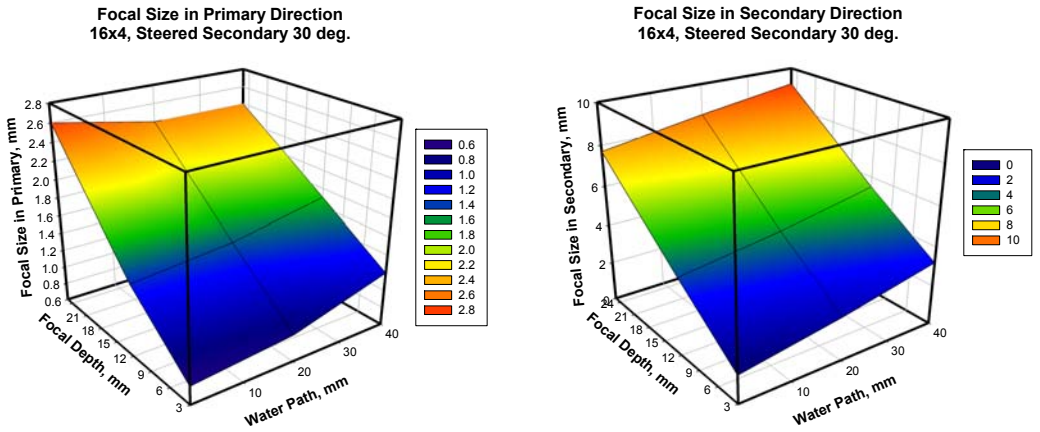

Figure 69. Primary and Secondary Focal Size vs. FD and WP (Optimized ID MPA 5 MHz, Active Aperture 16×4, Primary 0 Degrees, Secondary 30 Degrees)

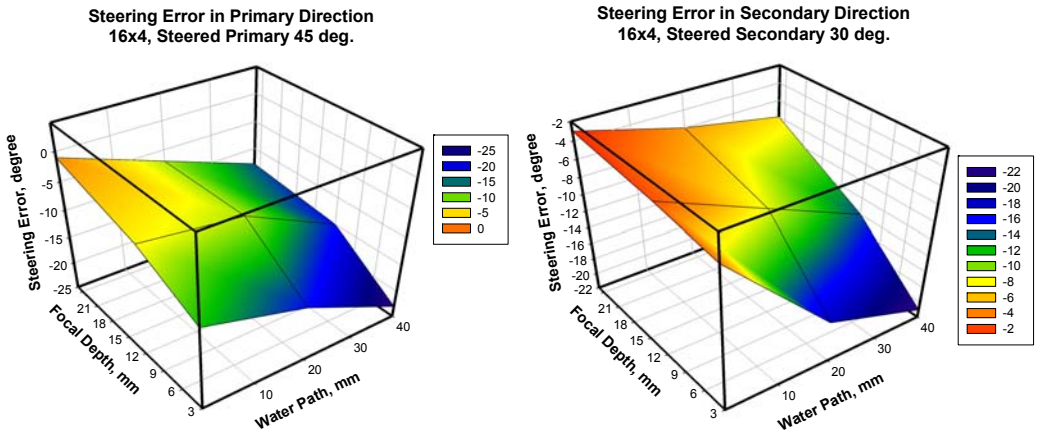

Figure 70. Primary and Secondary Steering Error vs. FD and WP (Optimized ID MPA 5 MHz, Active Aperture 16×4, Left – Primary 45-Degrees, Secondary 0 Degrees, Right – Primary 0 Degrees, Secondary 30 Degrees)

3.2.2.6 Specifications of Optimized Probe

Some hardware and inspection limitations had to be considered in the probe optimization. Consequently, the probe could only be optimized within these limitations. Due to inspection hardware used for the project, the probe was limited to a maximum of 128 elements. In addition, importance was placed on optimizing electronic scan coverage of the pipe circumference which further limited probe performance as described previously. Based on the modeling efforts, specifications for the prototype ID MPA probe were formulated. The resulting probe parameters were applicable for longitudinal wave (straight beam and refracted beam) inspection of 152-mm (6-in.) diameter water-filled, carbon steel pipe from the ID pipe surface.

The probe was designed to be carried along the pipe length by a portable platform that could be inserted into the pipe. Following are the parameters for the prototype ID MPA probe:

- 5-MHz, 128-element probe capable of immersion in water.
- Number of elements in the primary axis = 32. Number of elements in the secondary axis
- = 4.
- The probe-face-surface shall have a 36.2-mm radius in the primary axis for inspection of pipe with an ID diameter of 152 mm (76.2-mm radius) at a constant WP of 40 mm.
- Element size in the primary axis (Sx) shall be 0.5 mm. Element size in the secondary axis (Sy) shall be 1.0 mm. Inter-element gap in the primary axis (Gx) shall be 0.6 mm. Inter-element gap in the secondary axis (Gy) shall 0.6 mm.

As designed, the recommended operating parameters for the probe are as follows:

- A typical active aperture of 16×4 is recommended; however, a smaller aperture of 12×4 could also be used to increase circumferential coverage.
- The probe design is applicable for a 152-mm ID, using a fixed WP of 40 mm. If a different pipe diameter or WP is used the probe design would need to be modified. To cover a larger range of pipe diameters, future work should focus on the use of a flexible array for this application.
- Electronic focusing selected for this probe should be in the range of 3 to 25 mm.
- The actual refracted angle is expected to change from 22 to 32 degrees in the primary and from 9 to 22 degrees in the secondary for different FDs as shown in Table 16 and Figure 70 for a WP of 40 mm and an aperture of 16×4.
- Depending on the electronic FD selected, the -6 dB focal size is expected to change from 1.2 to 3.1 mm in the primary and from 3.1 to 9.1 mm in the secondary for a WP of
- 40 mm and an aperture of 16×4.

3.2.2.7 Flaw Interaction of Optimized Probe with Flat-Bottom Holes (FBH) and Hemi-Spherical Bottom Holes (HSBH)

The first set of flaw interaction simulations was conducted to investigate detection of localized wall thinning and surface pitting using the optimized ID probe parameters at a WP of 40 mm. For these simulations FBH and HSBH of different sizes and at different depths from the ID surface were used as targets. Four FBH and HSBH with diameters from 0.5 to 3 mm as shown in Figures 71 and 72 were simulated at a 3-mm depth from the ID. Using an electronic FD of 3 mm, the probe was scanned in 1-degree increments along a circumference line centered on the FBH. All four holes, regardless of the reflective surface shape, were detected and separated from the ID. Signals from the 2- and 3-mm FBH (Figure 71) were stronger than those from the HSBH (Figure 72).

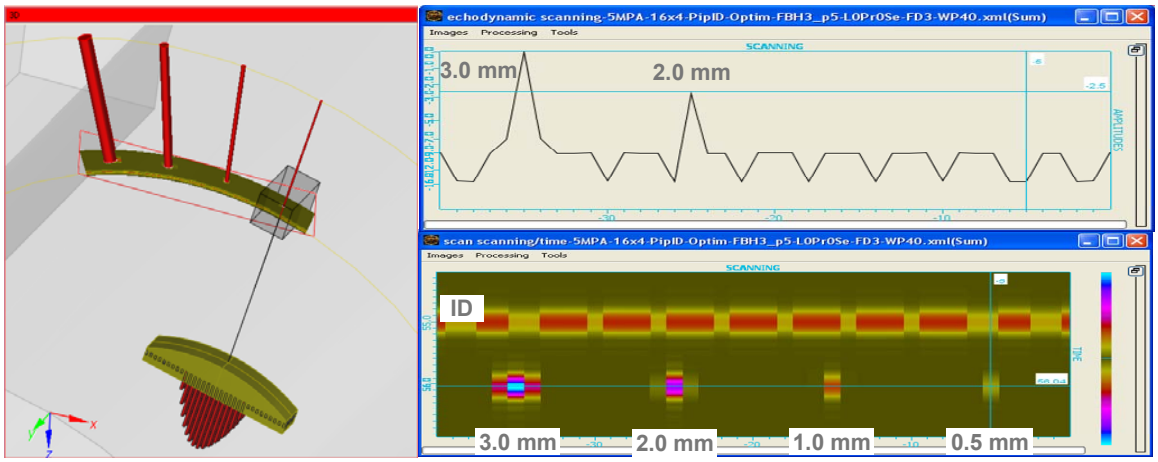

Figure 71. FBH (Variable Diameter) Interaction at 3 mm from ID, B-Scan, and Echo Dynamics (ID MPA 5 MHz, Active Aperture16×4, FD 3 mm, WP 40 mm, Normal Beam)

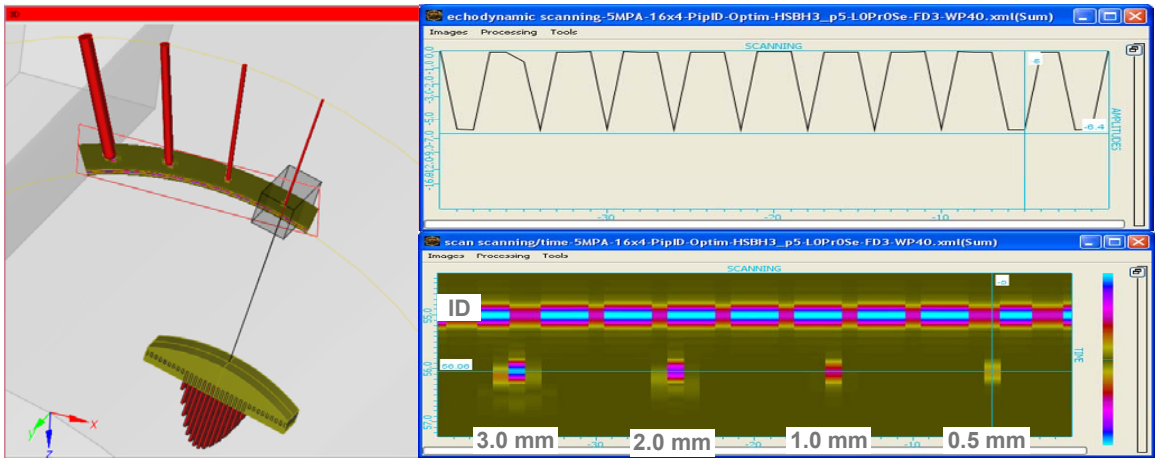

Figure 72. HSBH (Variable Diameter) Interaction at 3 mm from ID, B-Scan, and Echo Dynamics (ID MPA 5 MHz, Active Aperture16×4, FD 3 mm, WP 40 mm, Normal Beam)

Another simulation was run to assess probe resolution capabilities for flaws close to the OD surface (e.g., shallow corrosion pitting from the external OD surface). Results from this simulation are illustrated in Figure 73. Four FBH with 2-mm diameter were simulated connected to the OD and with height (depths) in the range from 0.1 to 0.8 mm. The simulation was performed at three different WT: 25, 12, and 6 mm. The probe was generating normal beam focused on the OD surface. The probe was rotated in 1-degree increments along a circumference line centered on the FBH at a WP of 40 mm. The detectability improved as the WT and FD decreased because the focal size decreased (see Table 16 and Figure 67).

Although the model indicated that all four FBH would be detectable, surface roughness and irregularities might mask pitting and corrosion less than 0.2-mm deep. A possible feature for improvement of detectability of shallow FBH (pitting) might be the sharp drop of BW reflection. The OD or BW reflection reduction was stronger for smaller WT < 12 mm and FD as shown in Figure 74 (top). The standard distance/arrival time technique was used for FBH (corrosion pitting) height (depth) measurement [see Figure 74 (bottom)] where it was possible to separate the FBH or flaw indication from the OD or BW signal.

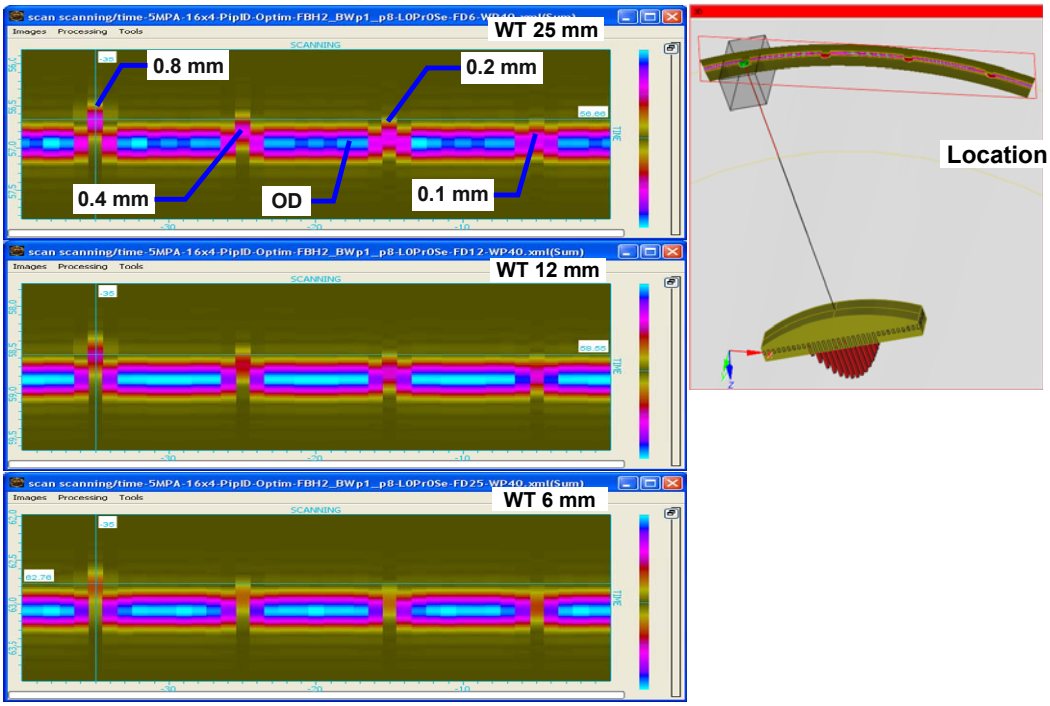

Figure 73. FBH (2-mm Diameter) Interaction at Variable Distance from OD, B-Scans, FD 6, 12, and 25 mm (ID MPA 5 MHz, Active Aperture16×4, WP 40 mm, Normal Beam)

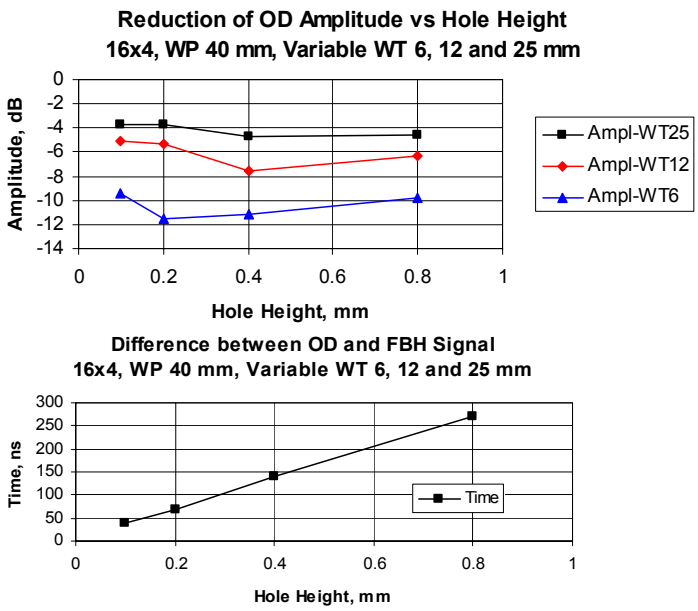

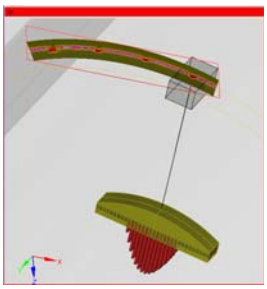

Figure 74. Signal Strength, FBH (2-mm Diameter) Interaction at Variable Distance from OD, FD 6, 12, and 25 mm (ID MPA 5 MHz, Active Aperture16×4, WP 40 mm, Normal Beam)

An assessment of the effect of the reflective surface FBH vs. HSBH (0.5- to 3-mm diameter) was conducted for mid-wall flaws presented in Figures 75 and 76. The FBH and HSBH surfaces were positioned at metal path distances of 3, 12, and 25 mm from the ID to study the effect of focal size changes. The beam was again normal with a WP of 40 mm and the probe electronically focused at the three standard FDs. Similar to the previous simulations, the probe was rotated in 1-degree increments along a circumference line centered on the holes. The WT was increased as applicable to eliminate any interference between BW signals and signals from the hole bottom surfaces.

A typical signal echo-dynamic is shown in Figure 75 for FD 12. The FBH signals decreased faster compared to the HSBH signals with the reduction of the hole diameter. Signals from the FBH were stronger than those from the HSBH and the difference increased with increased hole diameter.

A summary plot shown in Figures 76 presents in more details the reflective surface vs. FD and diameter interaction. The largest signal (used for reference “0 dB” on the plot) was obtained from 3-mm FBH at a 3-mm depth. The effect of diameter was stronger for FBH compared to HSBH. As the diameter decreased, the difference between the FBH and the HSBH became smaller. This is likely caused by the fact that the HSBH provides only a small surface area that is actually perpendicular to the sound beam. Consequently, much of the sound energy striking the HSBH surfaces is not reflected back to the probe, even when the hole diameter is large.

The signal difference between holes with identical shape and size due to the difference in depth from the ID was almost constant at ~8 dB for the HSBH and in the range of approximately 3 to 9 dB for the FBH.

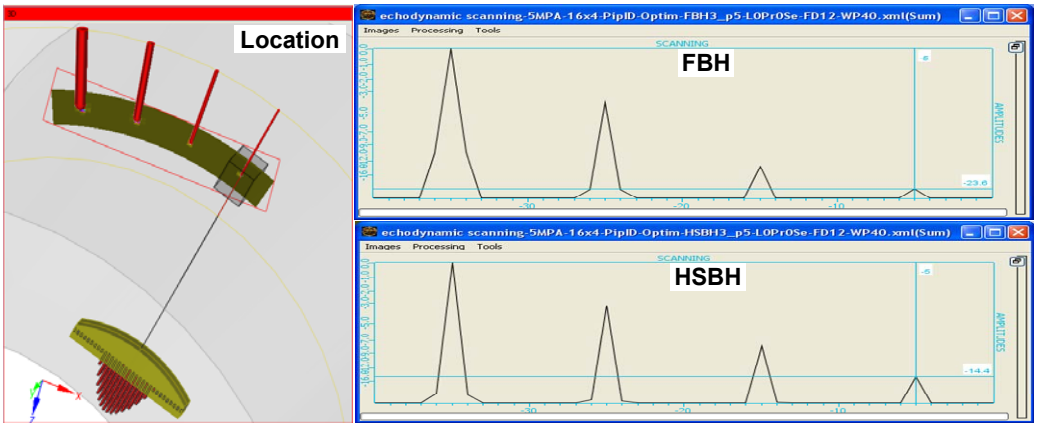

Figure 75. Mid-Wall FBH and HSBH (Variable Diameter) Interaction, Typical Echo Dynamics at 12 mm from ID (ID MPA 5 MHz, Active Aperture16×4, FD 12 mm, WP 40 mm, Normal Beam)

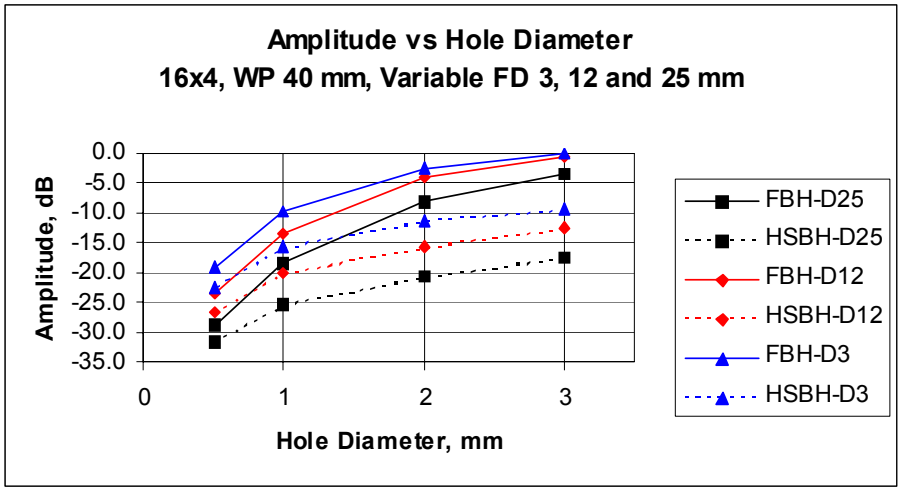

Figure 76. Signal Strength, FBH and HSBH Interaction, Variable Diameter and Distance from ID, FD 3, 12, and 25 mm (ID MPA 5 MHz, Active Aperture16×4, WP 40 mm, Normal Beam)

In summary it would be expected that:

- Flaw reflective surface irregularities effects would be more pronounced for pits with diameters > 0.5 mm.
- If calibration was performed using 3-mm FBH, pits >2-mm diameter should be detectable if the reflective surface is oriented parallel to the OD (ID).

3.2.2.8 Interaction of Optimized Probe with Planar Flaws Connected to the OD

The simulation of probe interaction with notches allows assessment of probe capabilities to detect and size planar flaws such as cracks and lack of fusion propagating from the external or OD surface. The beam was steered in the primary direction to 45 degrees. The actual refracted angle varied from 22 to 32 degrees for a WP of 40 mm, from 30 to 38 degrees for a WP of 20 mm, and from 35 to 44 degrees for a WP of 0.1 mm for various FDs (see Table 16). Three WT were simulated - 6, 12, and 25 mm with the beam focused on the OD (back surface) for each WT. The probe was rotated along the circumference with a small step of 0.5 degree symmetrical with respect to notch length. The notches simulating planar flaws were positioned along the pipe OD circumference without any skew or tilt. One of the notches was considered to be a calibration notch having dimensions of 5 × 0.8 mm. The other six notches had a length 10 mm and a height ranging from 0.5 to 3 mm in increments of 0.5 mm.

The B-Scans for a WP of 40 mm are shown in Figure 77 with corresponding signal echo-dynamic in Figure 78. With the exception of the 10- × 0.5-mm notch, all other notches were detected with an amplitude greater than that from the calibration notch. The corner trap signal was more pronounced at larger refracted angles (larger FD) as illustrated in Figure 77. The tip diffraction signals might be sufficient for detection and height sizing (Figure 77) in the entire range of simulated heights. The height sizing based on amplitude might be possible for a WT of 6 and 12 mm in a limited range from 1 to 2.5 mm (see Figure 78). The BW reflected signal strength increased with the decrease of the WT (see Figures 77 and 78) due to the decrease of the actual refracted angle as discussed above (Table 16). The detectability of flaws with height 1.0 mm and smaller might be affected at WT <12 mm.

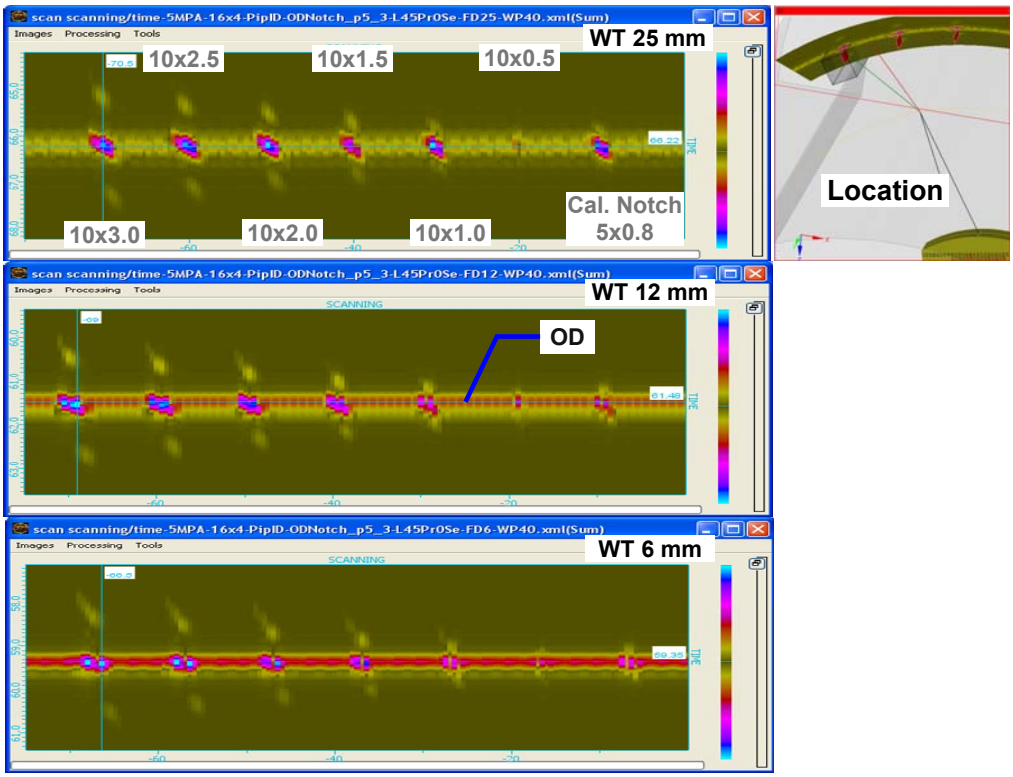

Figure 77. OD Connected Notch Interaction, Variable Height, and WT, B-Scans (ID MPA 5 MHz, Active Aperture 16×4, FD 6, 12, and 25 mm, WP 40 mm, Primary 45 Degrees, Secondary 0 Degrees)

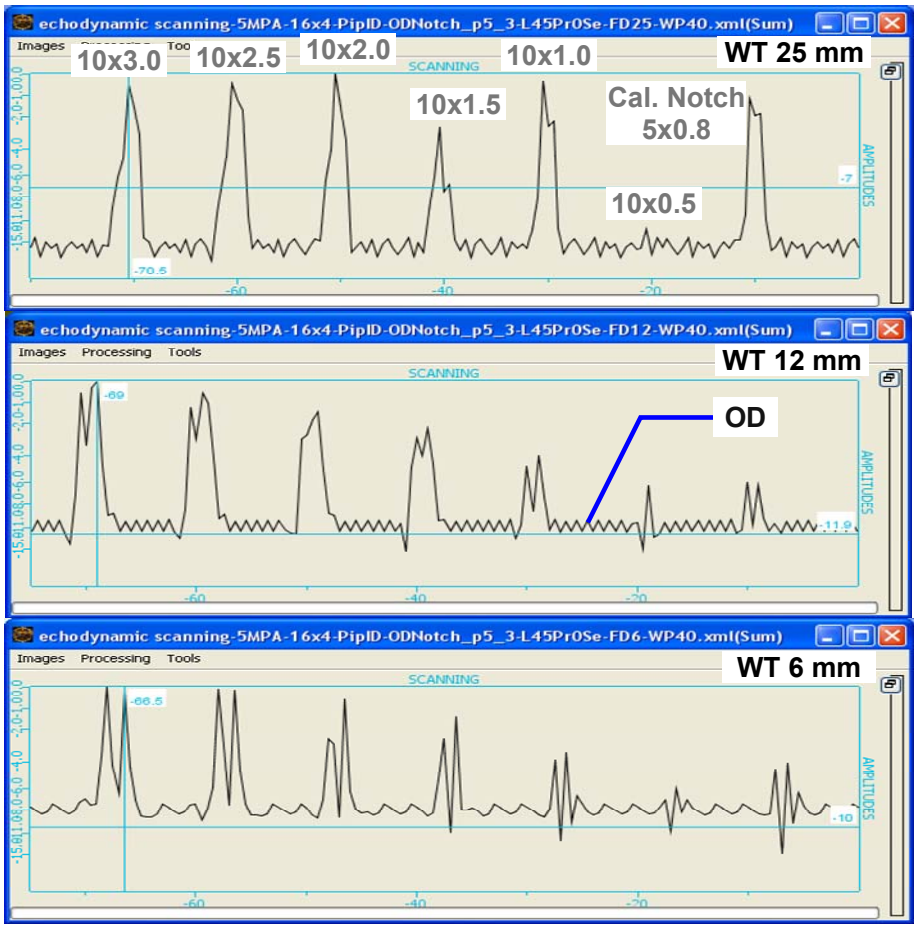

Figure 78. OD Connected Notch Interaction, Variable Height, and WT, Echodynamics (ID MPA 5 MHz, Active Aperture 16×4, FD 6, 12 and 25 mm, WP 40 mm, Primary 45 Degrees, Secondary 0 Degrees)

Similar trends and conclusions are valid for the simulated notch signals at a WP of 20 mm shown in Figures 79 and 80. One major exception is that the detectability of the10- × 0.5-mm notch improved at WT <12 mm due to the improved focusing (smaller focus) and beam steering (larger actual refracted angle). The BW or OD signal intensity dropped slightly with respect to the calibration signal and WP 40 mm (see Figures 78 and 80) due to the larger refracted angles produced at the smaller WP. Further, the amplitude did not correlate to flaw height at a WP of 20 mm (see Figure 80).

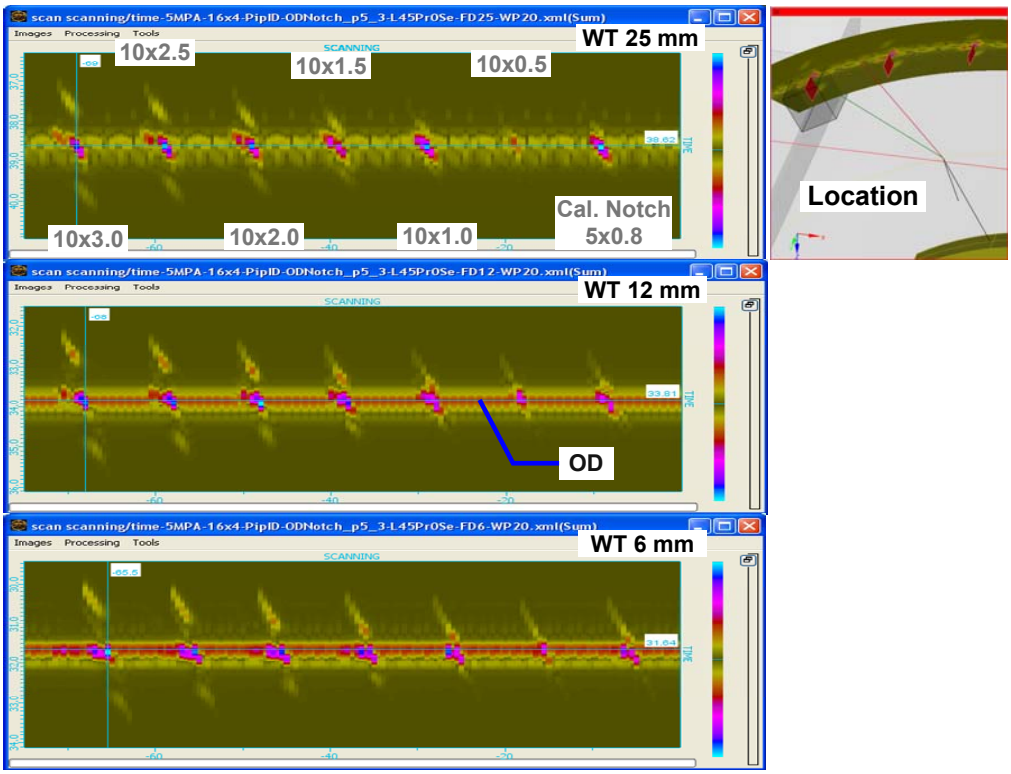

Figure 79. OD Connected Notch Interaction, Variable Height, and WT, B-Scans (ID MPA 5 MHz, Active Aperture 16×4, FD 6, 12, and 25 mm, WP 20 mm, Primary 45 Degrees, Secondary 0 Degrees)

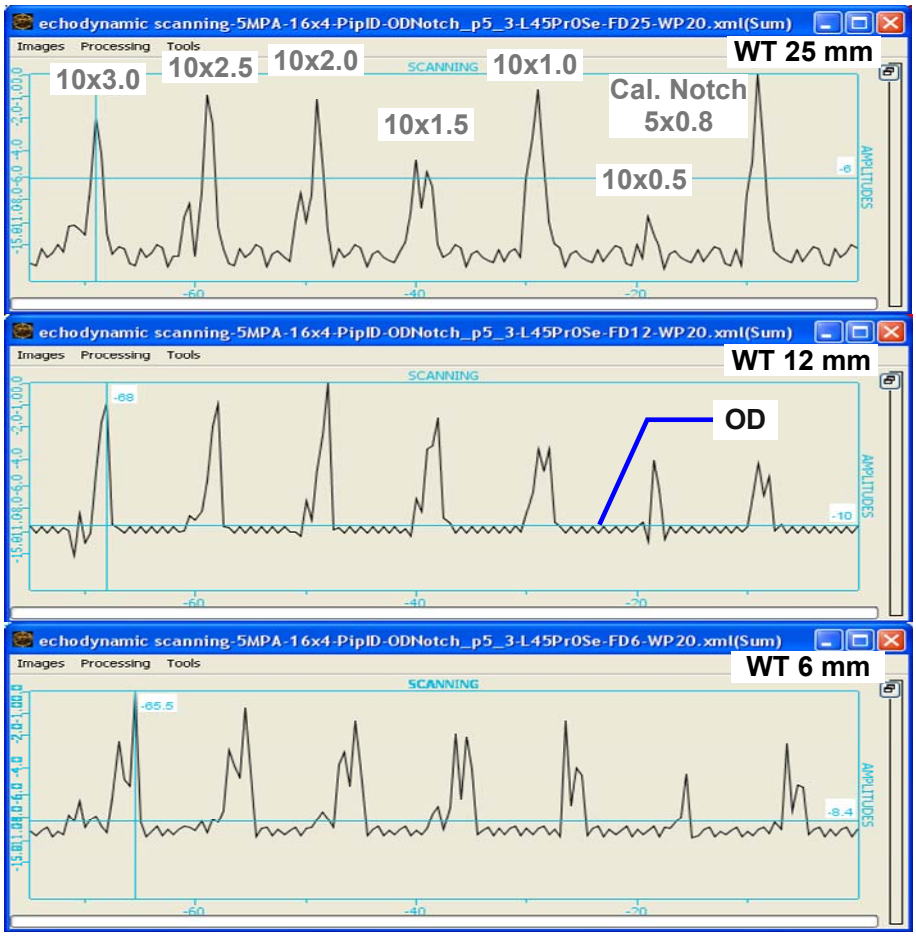

Figure 80. OD Connected Notch Interaction, Variable Height, and WT, Echodynamics (ID MPA 5 MHz, Active Aperture 16×4, FD 6, 12 and 25 mm, WP 20 mm, Primary 45 Degrees, Secondary 0 Degrees)

Detectability of smaller flaws further improved for probes that would be in contact with the ID at a WP of 0.1 mm shown in Figures 81 and 82. Although the signal from the 10- × 0.5-mm notch increased at WT 25 mm, it was still below the amplitude of the calibration signal (see Figure 82 top). Better focusing would be required along with the largest steering angle (44 degrees) obtained at this FD to improve the detectability of OD connected flaws having a small height. The BW signal intensity dropped to the lowest level with respect to the calibration signal when compared to that of larger WPs of 20 and 40 mm (see Figures 78, 80, and 82). This was due to the larger refracted angles produced at the smallest WP 0.1 mm. The improved detectability and height sizing along with reduced BW signal intensity is clearly visible on the B-Scan plots shown in Figure 81. Similar to results obtained at WP 20 mm, the amplitude may not be usable for flaw height sizing at WP 0.1 mm (see Figure 82).

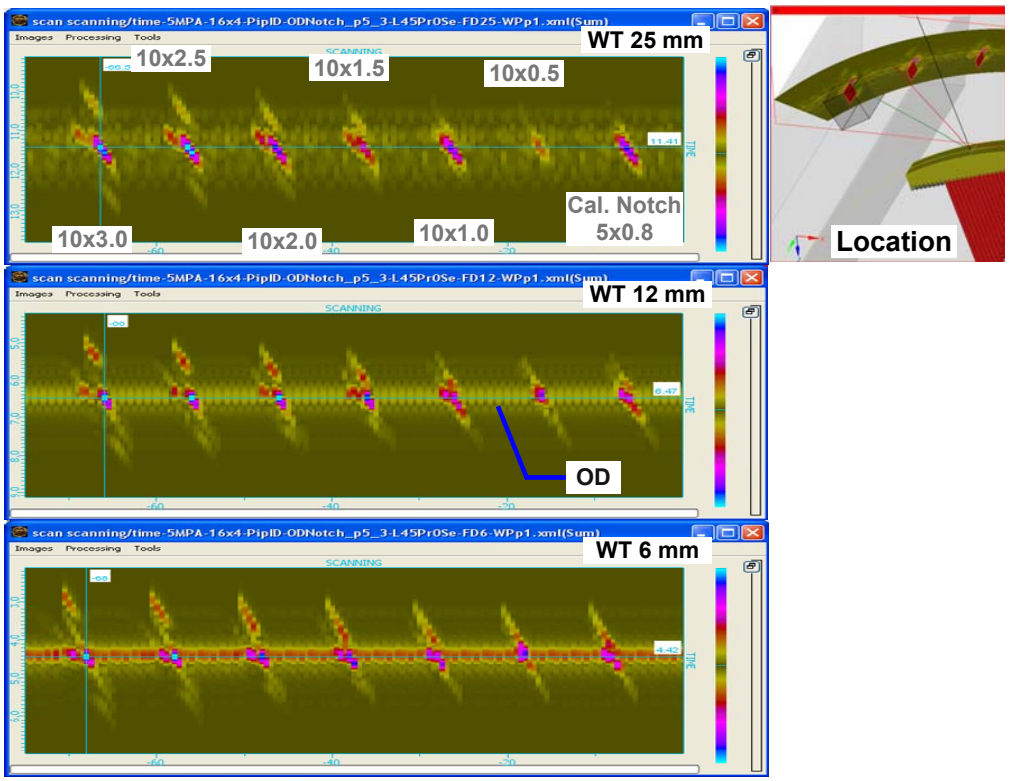

Figure 81. OD Connected Notch Interaction, Variable Height, and WT, B-Scans (ID MPA 5 MHz, Active Aperture 16×4, FD 6, 12, and 25 mm, WP 0.1 mm, Primary 45 Degrees, Secondary 0 Degrees)

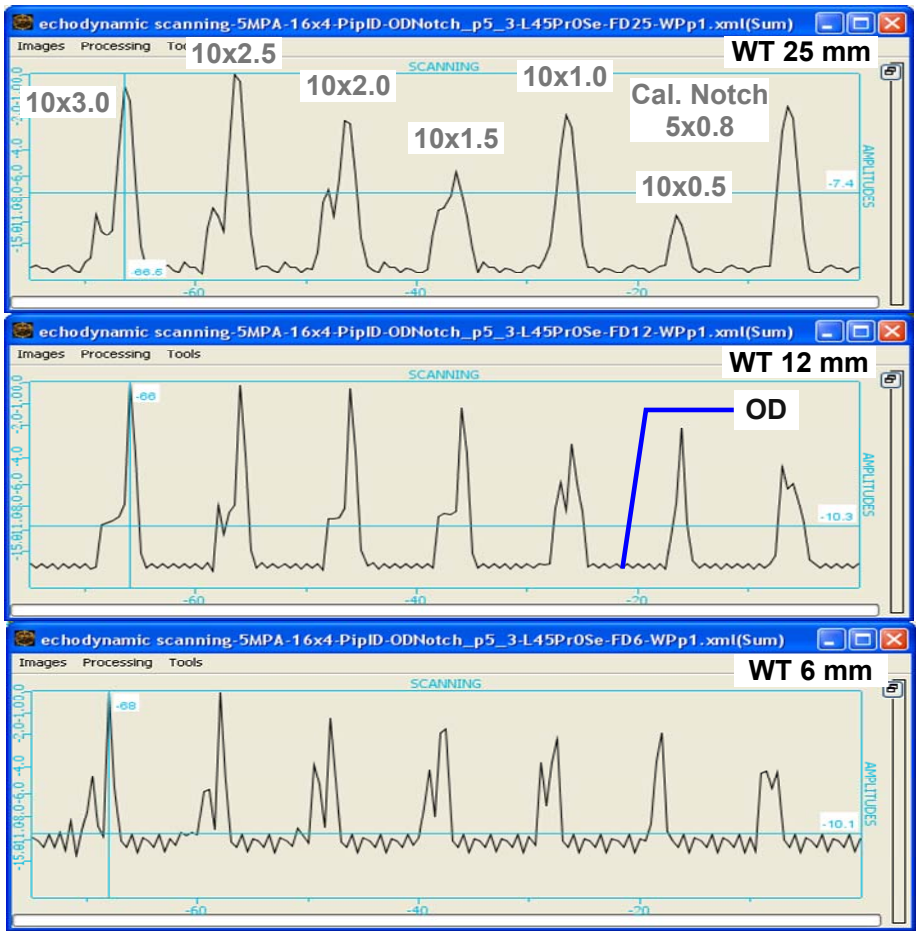

Figure 82. OD Connected Notch Interaction, Variable Height, and WT, Echodynamics (ID MPA 5 MHz, Active Aperture 16×4, FD 6, 12, and 25 mm, WP 0.1 mm, Primary 45 Degrees, Secondary 0 Degrees)

In summary, the simulation indicated that planar flaws perpendicular to the OD with a height of 1.0 mm and larger would be detectable if calibration was performed on a 5- × 0.8-mm notch. The detectability (particularly flaws with a height <1 mm) improved with the reduction of WP and FD. This corresponded with the improved steering (larger refracted angles) and smaller focal size determined for the optimized probe design (Table 16). The interference of OD surface echoes increased with the reduced WT and increased WP due to reduced actual refracted angles.

3.2.2.9 Interaction of Optimized Probe with SCC Flaws Connected to OD

CEA developed and delivered to EWI a beta version of CIVA computational software for this project. The newly developed tool included the capability for delay law calculation for tilted, skewed, and series scanning. In addition, the software also provided the ability to model flaw interaction for multi-branching defects. These options were developed by CEA for this project

and will be incorporated in future versions of the CIVA version that will be commercially available.

Within the software, the skew angle induces a rotation of the plane containing various shots around the Z axis while the bigle angle corresponds to a deflection of the plane containing shots in the XZ plane (Figure 83). When dealing with simultaneous skew and bigle deflections, the skew angle is applied first then the bigle angle. It is important to note that the software is capable of calculating and accounting for up to three reflections or rebounds off the OD, ID, between flaw branches and other combinations as applicable.

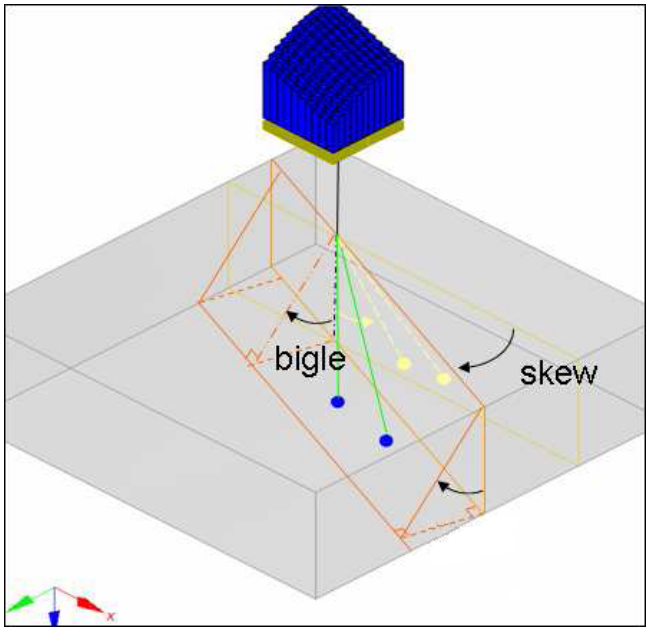

Figure 83. MPA Beam Spatial Steering and Definitions

To investigate the interaction of the optimized ID MPA probe with SCC flaws in the pipe wall, a model was built as shown in Figure 84. A pipe made of typical carbon steel with a diameter of 152 mm (6 in.) and WT of 12 mm was simulated. To demonstrate the greatly enhanced capabilities of the MPA to steer and focus the acoustical beam in 3D space, 21 focal spots were defined. These were grouped at two focal depths: 12 mm (on OD) and 10 mm (at 2 mm below OD) with constant primary steer angle of 45 degrees (actual 30 degrees see Table 16), a bigle angle of 0 degrees, and a range of skew angles from +20 to -20 with a step of 2 degrees. The probe was scanned for 40 degrees around the pipe circumference with 0.25-degree increment using a 40-mm WP.

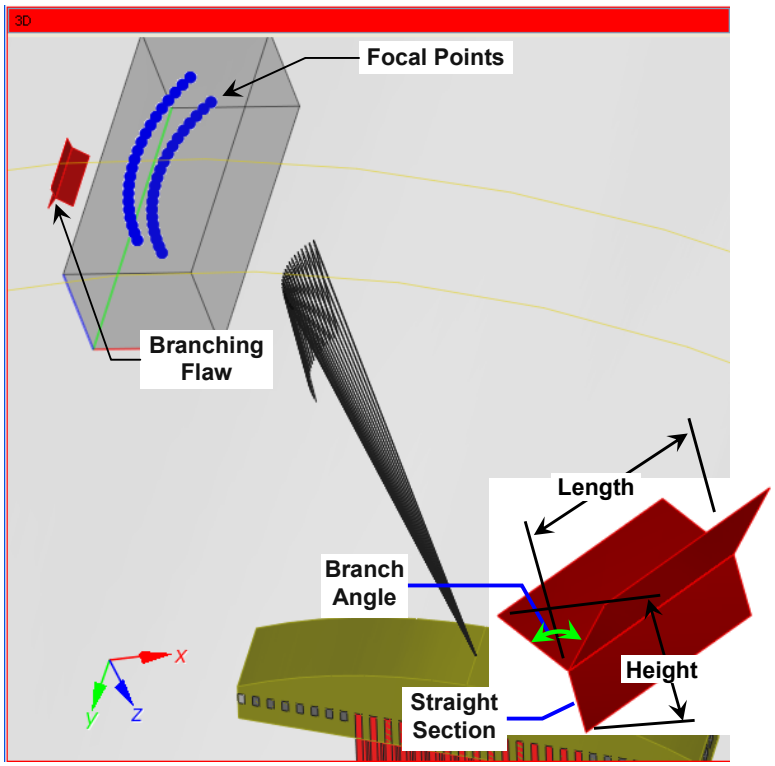

Figure 84. Setup for SCC Detection, 3D Steering

A SCC flaw was modeled connected to the OD (Figure 84) with a length of 5 mm and a total height of 2 mm. The straight portion of the flaw and the branched section each had heights of 1 mm, or half of the total height. Three branch angles were simulated: 30, 45, and 60 degrees. As the branch angle increased, the branch dimension along the circumference was increased to maintain a constant through-wall height of 1 mm for the branch section. The active group was 16×4 elements.

Merged C-Scans from the 2 FDs for each branch angle are shown in Figure 85. The signal intensity, distribution, and pattern changed as the branch angle increased. The SNR was the largest with a 60-degree branch angle. This was probably caused by the normal incidence of the acoustical beam (30 degree actual refracted angle) on the 60-degree branch. Due to the multiple rebounds between the OD and branches (Figure 86), the extent of the signal on the C-Scans, along the direction of scanning, might be misleading if used for flaw size estimates.

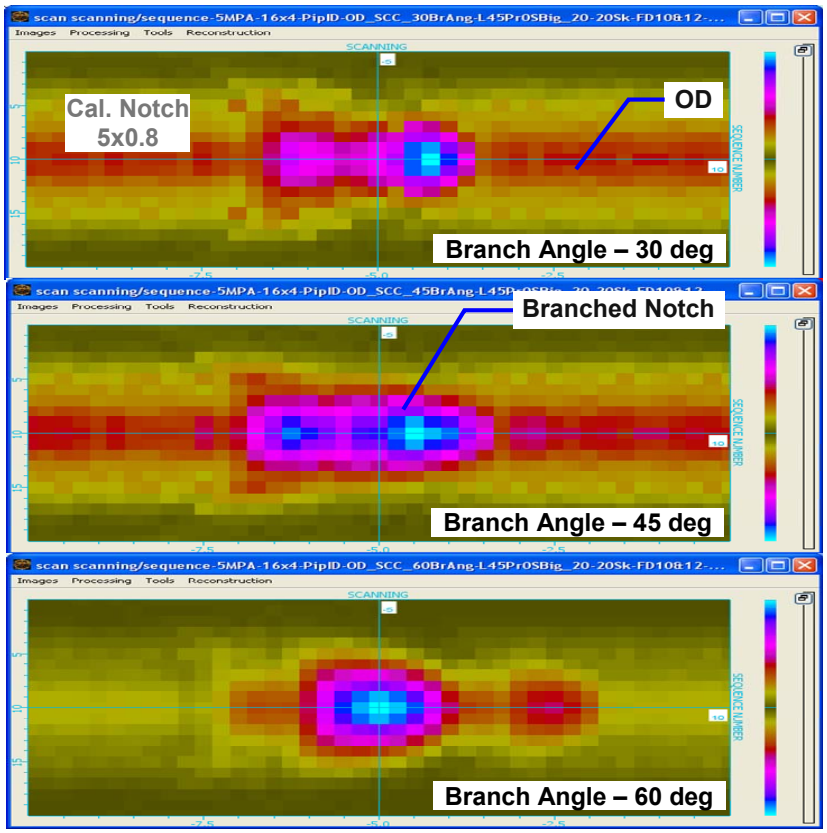

Figure 85. ID MPA 5 MHz, 16×4, 3D Steering, Variable Branch Angle, C-Scans

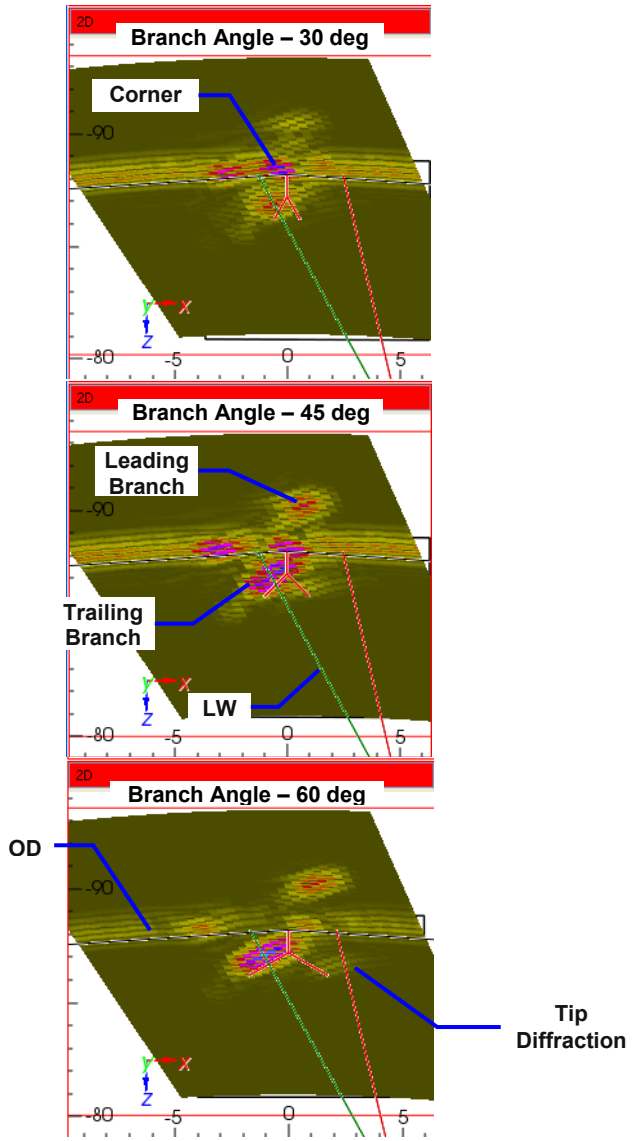

Figure 86. ID MPA 5 MHz, 16×4, 3D Steering, Variable Branch Angle, B-Scans

The B-Scans in Figure 86 are superimposed on the flaw geometry to identify the sources of signals specific to the SCC. The B-Scans shown in Figure 86 were acquired at a FD of 12 mm on the symmetry plane at the middle of the flaw length. There are 21 B-Scans at each FD 10 and 12 mm, respectively. The signal from the corner trap formed between the straight section of the SCC and the OD is strong and easily identified. SCC damage with a branch angle of 30 degrees and smaller might be difficult to classify as such because the different branches are undistinguishable. One signal feature that could be used for SCC detection and characterization is the trailing branch shadowing of the BW (OD) at larger angles of 45 and 60 degrees. Another feature for SCC detection and characterization is the strong signal projected outside of the OD caused by the acoustic beam rebound off the OD and leading branch at larger

branch angles. The tip diffraction from the leading edge, where available, might also indicate the SCC branch presence and height.

The same set of B-Scans from Figure 86 is shown in Figure 87 in a format that the PA equipment operator would see. It is used for flaw height sizing. The modeling results indicate that accurate height (2 mm) sizing (from corner signal on OD to branch tip) might be possible with the advanced and optimized MPA probe.

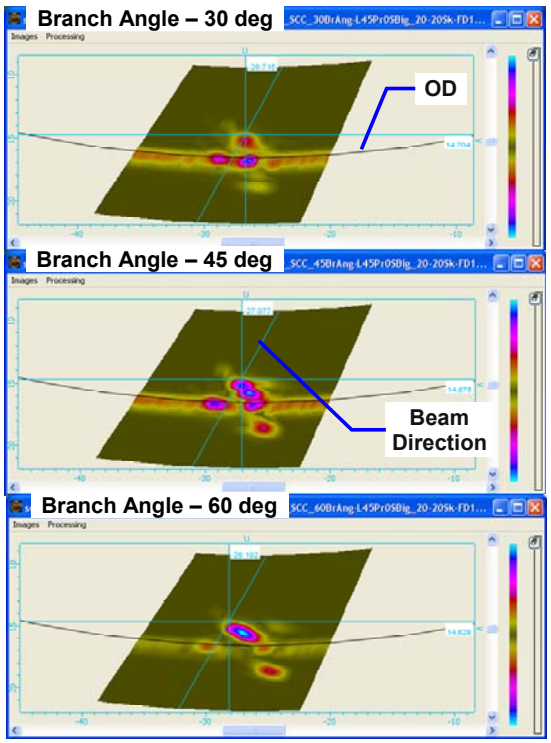

Figure 87. ID MPA 5 MHz, 16×4, 3D Steering, SCC Height Sizing on Simulated B-Scans

As discussed previously, MPA allows beam steering and focusing not only in primary but is secondary direction as well. To take full advantage of advanced MPA capabilities, however, imaging and interpretation of large volumes of data might become challenging if the software processing capabilities are inadequate. The new CIVA tool provides additional capabilities to assess MPA performance in the secondary direction while accounting for beam skew. A set of secondary sectorial scans accounting for the skew angle (S2s-scans) as well is shown in Figure 88 in a form that the phased array equipment operator would see. The S2s-scans are taken at a position that provided maximum signal from the flaw. The signals are slightly shifted along the circumference depending on the branch angle and the interference with the BW (OD) signal. The S2s-scans indicate that accurate length (5 mm) sizing might also be possible.

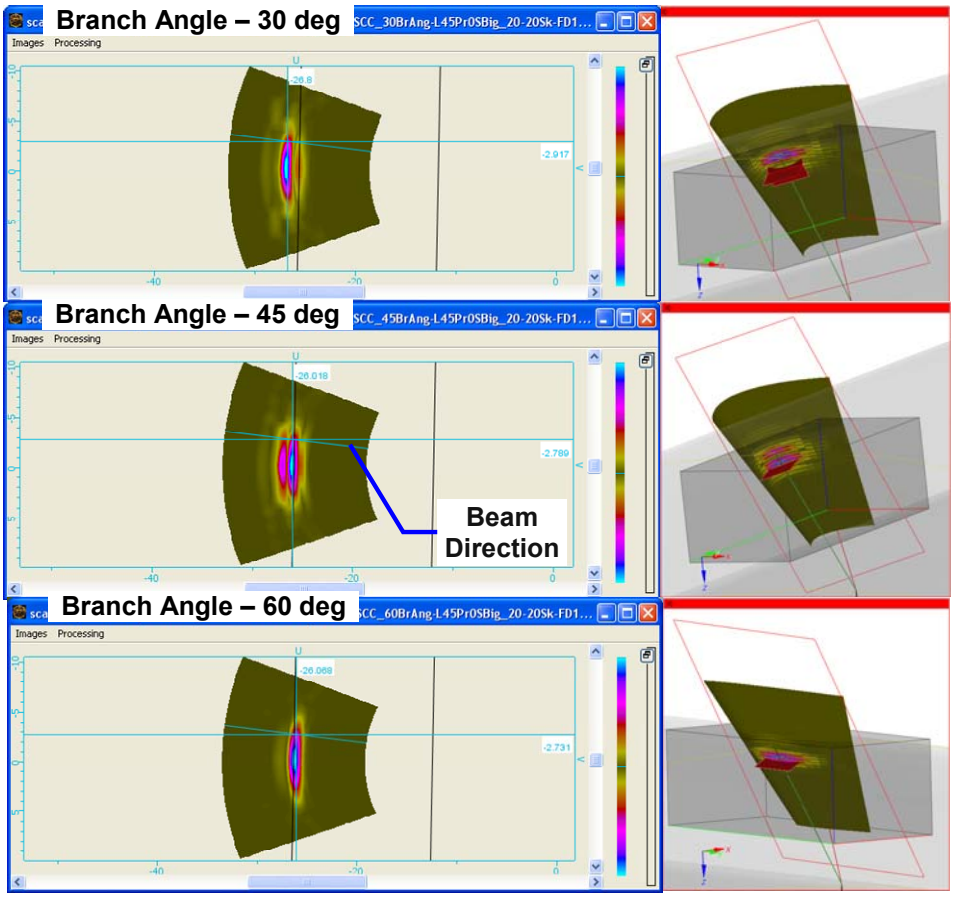

Figure 88. ID MPA 5 MHz, 16×4, 3D Steering, SCC Length Sizing on Simulated Skew-Enhanced Sectorial Scan in Secondary Direction S2s-Scans

The new computational tool allows fast and easy comparison of interaction with different types of SCC flaws and typical simple planar flaws usually used for equipment calibration and standardization. One SCC and one planar flaw were simulated connected to the OD as shown in Figure 89 (top). The same array setup was used as shown in Figure 84. The flaws had identical height. The simulated SCC flaw consisted of three sections: 2, 3, and 5 mm along the total length of 10 mm. Half of the total SCC height was a straight section while the other half was a branched section with symmetrical branches and 30-degree branch angle. Further, each branch along the length was with 30 degrees to each other. The length of the planar flaw/notch was identical to the SCC length: 10 mm. Two numerical experiments were conducted: 1 and 2 mm total flaw height. The merged C-Scans and echodynamic results are shown in Figure 89 (bottom): 2-mm height (left) and 1 mm height (right). The SCC with a height identical to the planar flaw height always produced a stronger signal than the planar flaw: 1.4 and 5.1 dB for heights of 2 and 1 mm, respectively. The SCC signal amplitude decreased very little (-1.4 dB) with the height reduction while the planar flaw amplitude decreased almost twice (-4.9 dB). The branching and irregular reflective surface of the SCC flaw might increase the flaw detectability

and sizing accuracy when advanced techniques with MPA are employed. A practical conclusion from these two numerical experiments is that a calibration with simple notches is expected to be adequate for detection of SCC flaws having a height equal to or larger than the calibration notch in the height range from 1 to 2 mm.

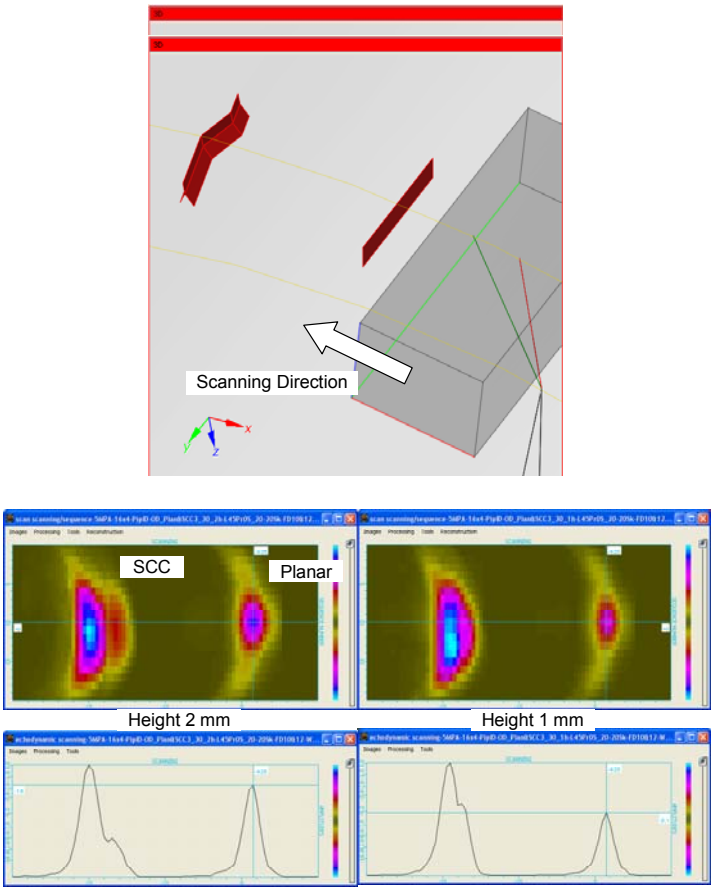

Figure 89. ID MPA 5 MHz, 16×4 (Comparison of SCC and planar flaws)

3.3 Rigid and Flexible Arrays for Continuous Localized Monitoring from OD (Concept 4)

This concept can be accomplished using either a directly mounted flexible MPA probe without LVDTs or a rigid MPA probe attached to a replaceable wedge. If used with a flexible array, the probe (without LVDTs) can be attached directly to the pipe OD surface in a permanent or semi-permanent manner. If used with a rigid array, a wedge is attached to the pipe surface allowing the probe to be re-used. The wedge must be machined to match the pipe OD surface.

The purpose of this concept is to monitor characteristics such as wall thinning, corrosion mapping, or flaw propagation over an extended time period. This concept can be used for in-service monitoring or for corrosion and crack growth studies. Electronic beam steering, focusing, and scanning are used to ultrasonically measure the remaining pipe WT and to monitor flaw propagation at the probe location.

3.3.1 Illustration of Scanning Patterns and Techniques for Corrosion Detection

For example, a rigid probe can be permanently mounted on the OD to monitor for flaw initiation and propagation on the pipe ID as shown in Figure 90. The simulated pipe specimen was made of typical carbon steel with a WT of 6 mm. The simulated probe had the same element size and gap as the immersion ID probe discussed above. The probe size, though, was modified to allow for better coverage in both directions – primary and secondary because a mechanical scanning in either direction would not be an option for permanently mounted probes. The 24×12 matrix layout with total of 288 elements is shown in Figure 90 (top). The smallest active group/aperture of 12×6 elements was used that would still provide acceptable focusing and steering as demonstrated earlier (see Table 13, Figures 43 and 44). The active group was scanned electronically in a raster scan across the entire matrix along X and Y axes with steps of 1.1 and 1.6 mm, respectively [Figure 90 (top)]. At each raster scan position, a sectorial scan along the primary direction (X) was performed with a step of 1 mm and focusing near the ID surface as shown in Figure 90 (bottom). A corrosion pitting 2 × 2 mm with depth of 1 mm from the ID was simulated as well. Several sequences and shots are shown in Figure 91. The Sequence 0, Shot 0 shown in Figure 91 (top) corresponds to the first position from the raster scan with maximum refracted angle in the primary direction (Shot 0 out 11 shots per single sectorial scan). The other three images (Sequence 33, Shot 3, Sequence 47, Shot 5 and Sequence 61, Shot 7) illustrate detection of the corrosion pit at different positions (sequences) of the active group and different refracted angles (shots). Another inspection pattern (not shown) with sectorial scanning in the secondary and a raster scan at 90 degrees with respect to the one shown in Figure 90 top was also simulated. Thus, each spot under the MPA probe will be tested with different refracted angles from two different directions – primary and secondary to allow reliable detection and sizing regardless of flaw skew and tilt. The pit height measurement from the sectorial scans was very accurate which indicated that good sizing capabilities could be expected.

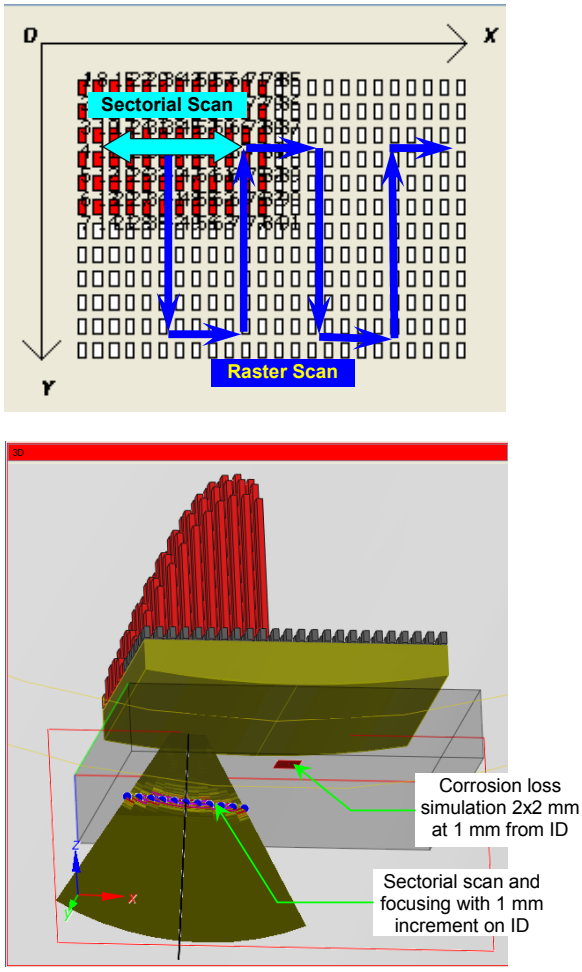

Figure 90. Permanently Mounted FMPA 24×12 for Health Monitoring

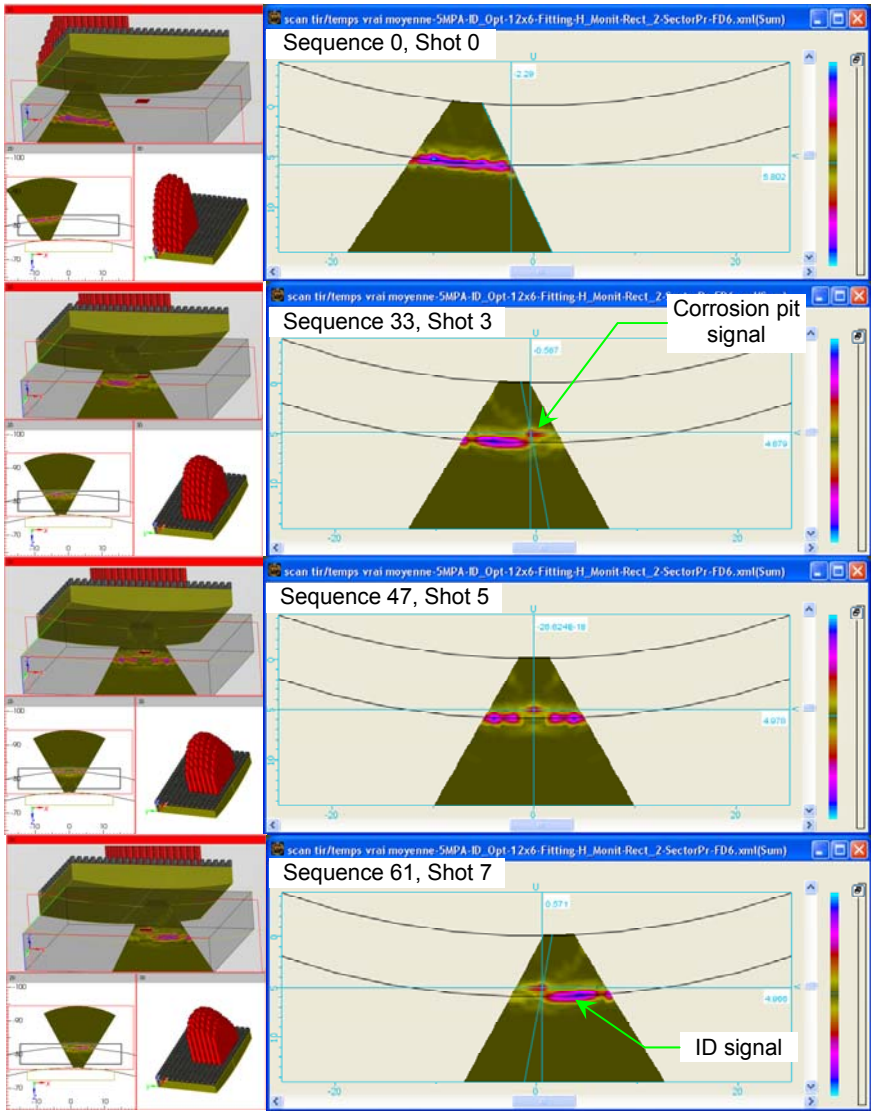

Figure 91. Health Monitoring Scanning and Signals

3.3.2 Optimization of Beam Forming and Steering for Permanently Mounted (Dry Couplant) Probe

Simulations were conducted to evaluate the use of an existing 5-MHz 128-element MPA probe for health monitoring of steel pipe from the OD surface. A commercially available dry couplant was used in the models to couple the probe to the steel. Following are simulations parameters used for this task:

- Rigid MPA probe inspecting from pipe OD. Modeling performed on plate.
- Longitudinal wave at 5-MHz frequency
- MPA total number of elements 128 (16×8)
- Element size – primary Sx-0.9 mm, secondary Sy-1.3 mm

- Gaps – primary Gx-0.1, secondary Gy-0.2 mm
- Active apertures used to generate beams - 4×4, 8×4, 12×6
- Probe permanently mounted with dry couplant Sonemat - thickness – 5 mm, velocity - 1021 m/s, attenuation - 0.041 dB/mm
- Material – typical carbon steel VLW - 5900 m/s
- Plate thickness – 32 mm
- Four FD at 3, 6, 12, and 25 mm
- Focusing and steering modeled for normal beam (0 degrees) and refracted angles of 10 degrees in both the primary and secondary directions.

Beam models were generated using different combinations of beam apertures and electronic focal depths to determine beam focusing capabilities. Figures 92 through 94 show examples of some of these beam models for apertures of 4×4, 8×4, and 12×6 at focal depths of 6 and 12 mm and a 0-degree beam angle. Additional simulations were performed to evaluate beam steering capabilities in both the primary and secondary directions. Beam steering models showed that the actual beam was typically less than the requested beam angle due to beam phasing limitations for different aperture and focal depth combinations. For example, with a large aperture and short focal distance, it was not possible to obtain the requested beam angle of 10 degrees. It was also noted that beam steering in the secondary axis was further limited by the larger element pitch of the probe (1.5 mm). This can be seen by comparing the secondary axis beam profile in Figure 95 to that in Figure 96. Figure 95 shows the beam steering prediction for an 8×4 aperture focused at 3 mm while Figure 96 shows is the beam steering prediction for a 12×6 aperture focused at 25 mm. Secondary apertures of 4 and 6 elements appeared to provide the best combination of beam focusing and steering at focal depths of 12 to 25 mm. Based on parameters evaluated, an aperture of 4×4 would work well for a WT of approximately 3 to 6 mm, while an aperture of 8×4 or 12×6 would work well for WT of approximately 6 to 12 mm. The 12×6 aperture models indicated that good focusing and steering could be achieved up to approximately 25 mm. Beam focusing results for other apertures, focal depths, and apertures are provided in Tables 17 through 19 and Appendix A.

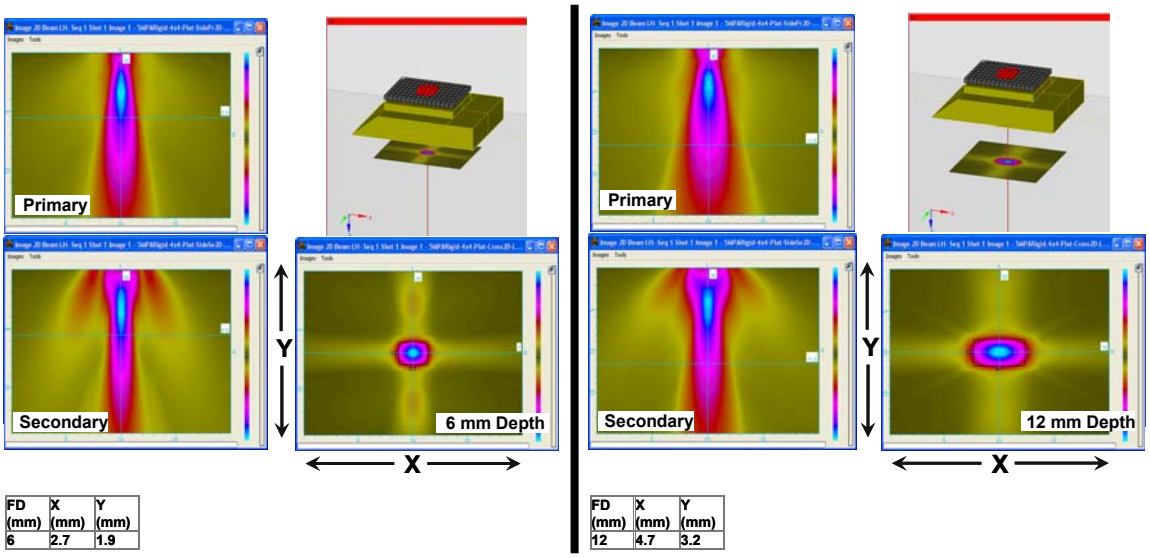

FD (mm)	X (mm)	Y (mm)
6	2.7	1.9

FD (mm)	X (mm)	Y (mm)
12	4.7	3.2

Figure 92 **Normal Beam, Rigid MPA 5 MHz, Active Aperture 4×4, FD 6 mm (L), FD 12 mm (R), Dry Couplant**

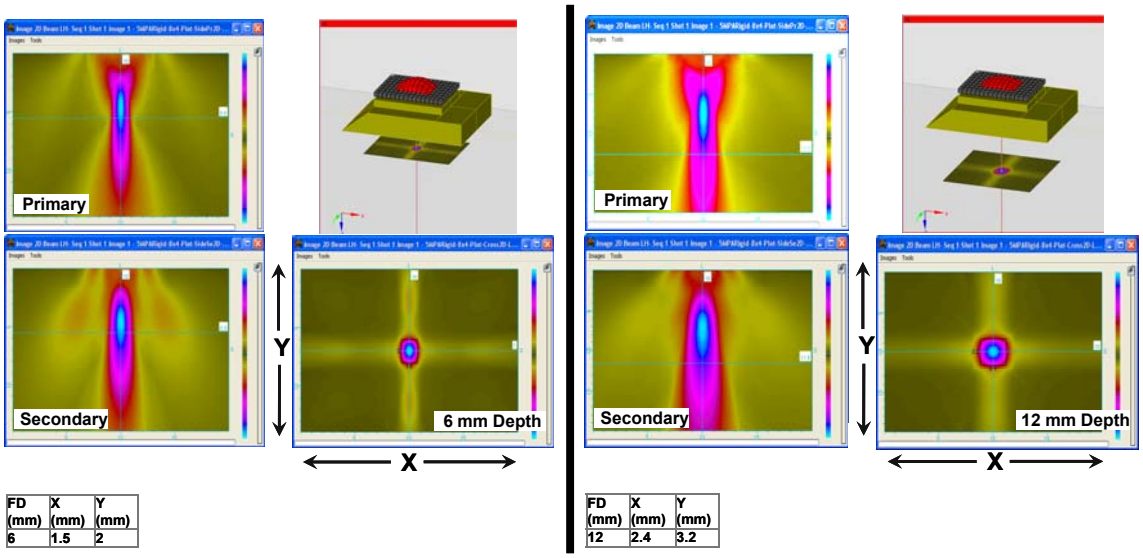

FD (mm)	X (mm)	Y (mm)
6	1.5	2

FD (mm)	X (mm)	Y (mm)
12	2.4	3.2

Figure 93. **Normal Beam, Rigid MPA 5 MHz, Active Aperture 8×4, FD 6 mm (L), FD 12 mm (R), Dry Couplant**

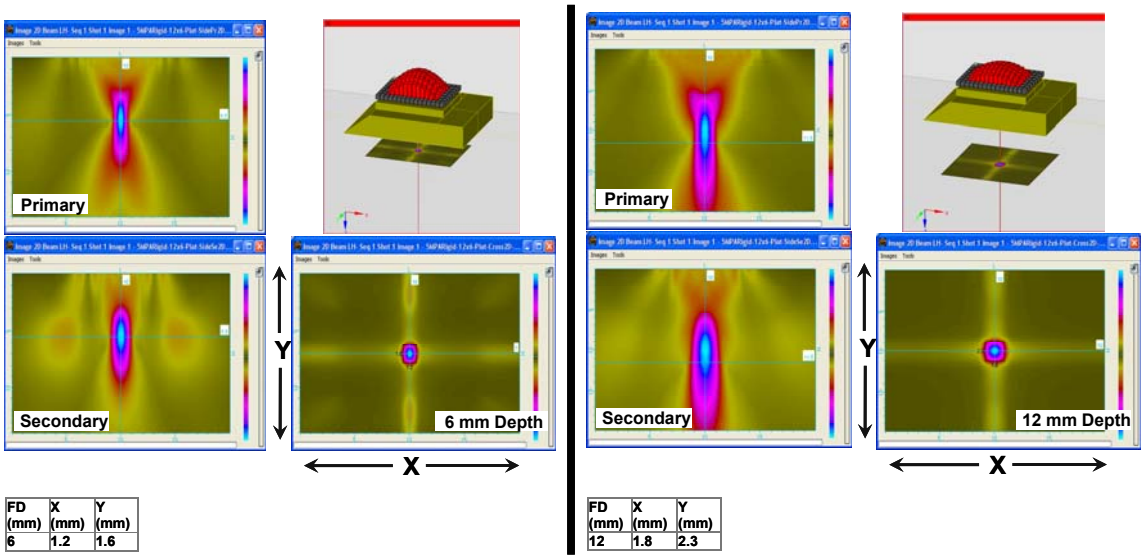

FD (mm)	X (mm)	Y (mm)
6	1.2	1.6

FD (mm)	X (mm)	Y (mm)
12	1.8	2.3

Figure 94. **Normal Beam, Rigid MPA 5 MHz, Active Aperture 12×6, FD 6 mm (L), FD 12 mm (R), Dry Couplant**

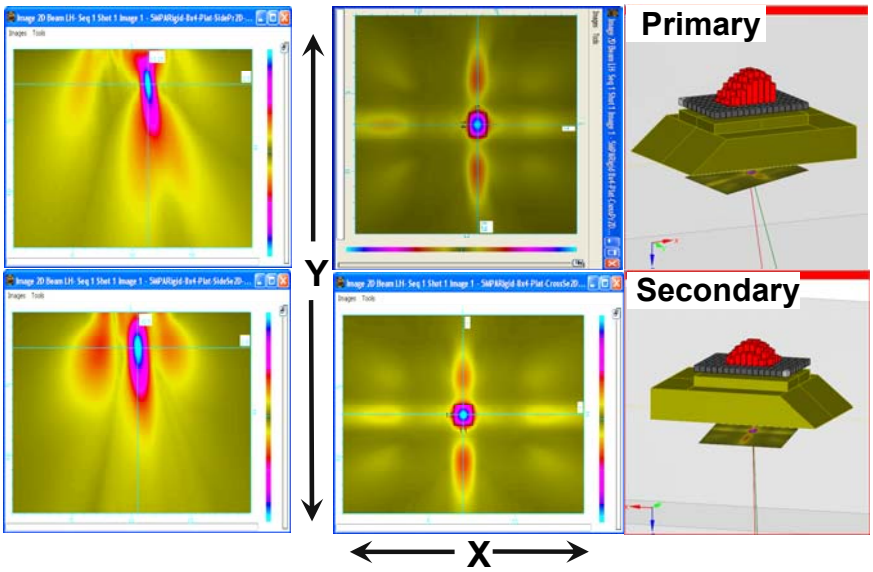

Steering	FD (mm)	X (mm)	Y (mm)
Primary	3	1.1	1.4
Secondary	3	1.1	1.5

Figure 95. **Beam Steering 10 Degrees, Rigid MPA 5 MHz, Active Aperture 8×4, FD 3 mm, Dry Couplant**

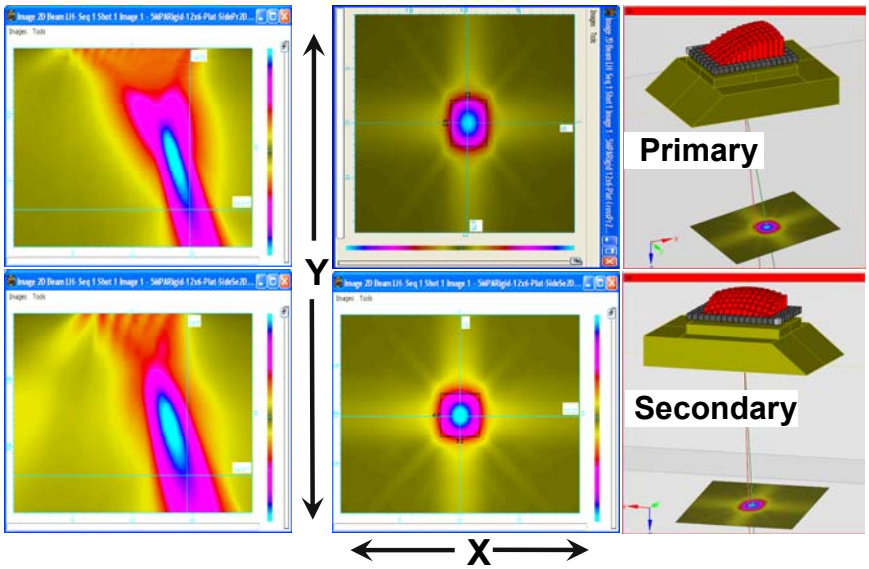

Steering	FD (mm)	X (mm)	Y (mm)
Primary	25	3.3	4.3
Secondary	25	3.2	4.4

Figure 96. Beam Steering 10 Degrees, Rigid MPA 5 MHz, Active Aperture 12×6, FD 25 mm, Dry Couplant

Table 17. Summary Table (Condition Monitoring, Rigid MPA 5 MHz, 4×4 Active Aperture, LW)

Step	FD (mm)				Primary (degrees)		Secondary (degrees)		Actual Angles - Primary and Secondary (degrees)		Focus -6 dB (mm)	Focus -3 dB (mm)	Notes
1				3		0		0	0	0	1.7×1.4	1.2×1	G. focus at max pres. Se grating lobes
2				3	10			0	10	0	1.7×1.4	1.2×1	Good focus max pres. and steer. Se grating lobes - weak Pr grating lobe mirror to main
3				3		0	10		0	4	1.7×1.4	1.2×1	Focus at max pres - steer to small angle - Se grating lobes
4				3	10		10		NA	NA	NA	NA	
5			6			0		0	0	0	2.7×1.9	1.9×1.4	G. focus end of max pres. - weak Se gr. Lobes
6			6		10			0	10	0	2.7×1.9	1.9×1.4	Focus at end of max pres. and steer - weak Se grating lobes
7			6			0	10		0	5	2.7×2	1.9×1.4	Focus at end of max pres - steer to small angle. Se grating lobe mirror to main
8			6		10		10		NA	NA	NA	NA	
9		12				0		0	0	0	4.7×3.2	3.4×2.3	No focus in Pr. - some focus in Se
10		12			10			0	NA	NA	NA	NA	
11		12				0	10		NA	NA	NA	NA	
12		12			10		10		NA	NA	NA	NA	
13	25					0		0	0	0	9.1×6.2	6.4×4.6	No focus
14	25				10			0	NA	NA	NA	NA	
15	25					0	10		NA	NA	NA	NA	
16	25				10		10		NA	NA	NA	NA	

Table 18. Summary Table (Condition Monitoring, Rigid MPA 5 MHz, 8×4 Active Aperture, LW)

Step	FD (mm)				Primary (degrees)		Secondary (degrees)		Actual Angles - Primary and Secondary (degrees)		Focus -6 dB (mm)	Focus -3 dB (mm)	Notes
1				3		0		0	0	0	1.1×1.5	0.8×1.1	G. focus at max pres. Se grating lobes - weak Pr grating lobes
2				3	10			0	5	0	1.1×1.4	0.8×1	G. focus at max pres. - steer to small angle - Se grat. lobes - W. Pr grat. lobe mirror to main
3				3		0	10		0	2	1.1×1.5	0.8×1.1	G. focus at max pres. - steer to small angle - Se grating lobes - weak Pr grating lobes
4				3	10		10		NA	NA	NA	NA	
5			6			0		0	0	0	1.5×2	1.1×1.5	G. focus at max pres. - weak Se grating lobes
6			6		10			0	8	0	1.5×2	1.1×1.4	G. focus at max pres. - steer to small angle - weak Se grating lobes
7			6			0	10		0	4	1.5×2	1.1×1.5	G. focus at max pres. - steer to small angle - Se grating lobe mirror to main
8			6		10		10		NA	NA	NA	NA	
9		12				0		0	0	0	2.4×3.2	1.8×2.3	Focus at end of max pres.
10		12			10			0	8	0	2.5×3.3	1.8×2.4	Focus end of max pres. - steer to small angle
11		12				0	10		0	7	2.5×3.3	1.8×2.4	Focus at end of max pres. - steer to small angle
12		12			10		10		NA	NA	NA	NA	
13	25					0		0	0	0	4.7×6.3	3.4×4.6	No focus
14	25				10			0	NA	NA	NA	NA	
15	25					0	10		NA	NA	NA	NA	
16	25				10		10		NA	NA	NA	NA	

Table 19. Summary Table (Condition Monitoring, Rigid MPA 5 MHz, 12×6 Active Aperture, LW)

Step	FD (mm)				Primary (degrees)		Secondary (degrees)		Actual Angles - Primary and Secondary (degrees)		Focus -6 dB (degrees)	Focus -3dB (degrees	Notes
1				3		0		0	0	0	0.9×1.3	0.7×0.9	G. focus at max pres. - Se grating lobes
2				3	10			0	7	0	1×1.3	0.7×0.9	G. focus at max pres. -steer to small angle. Se grating lobes
3				3		0	10		0	2	0.9×1.3	0.7×0.9	G. focus at max pres. - steer to small angle - Se grating lobes
4				3	10		10		NA	NA	NA	NA	
5			6			0		0	0	0	1.2×1.6	0.8×1.1	G. focus at max pres. - weak Se grating lobes
6			6		10			0	8	0	1.2×1.6	0.9×1.1	G. focus at max pres. - steer to small angle - weak Se grating lobes
7			6			0	10		0	3	1.2×1.6	0.8×1.1	G. focus at max pres. - steer to small angle - weak Se grating lobes
8			6		10		10		NA	NA	NA	NA	
9		12				0		0	0	0	1.8×2.3	1.3×1.7	G. focus at max pres.
10		12			10			0	8	0	1.8×2.3	1.3×1.8	G. focus at max pres. - steer to small angle
11		12				0	10		0	7	1.8×2.4	1.3×1.7	G. focus at max pres. - steer to small angle - weak Se grating lobe mirror to main
12		12			10		10		NA	NA	NA	NA	
13	25					0		0	0	0	3.2×4.3	2.3×3.1	Focus at end of max pres.
14	25				10			0	10	0	3.3×4.3	2.4×3.1	Focus at end of max pres.
15	25					0	10		0	9	3.2×4.4	2.3×3.2	Focus at end of max pres.
16	25				10		10		NA	NA	NA	NA	

3.3.3 Health Monitoring Flaw Interaction Simulations

Inspection simulations were performed to look at the capability of the 5-MHz, 16×8 element probe to detect wall thinning. The simulated component was carbon steel having WT of 12 and 25 mm. Inspection simulations were conducted using two different active apertures: 4×4 and 8×4. For the 4×4 aperture only a 12-mm WT was modeled using FDs of 3, 6, and 12 mm. With the 8×4 aperture both 12 and 25 mm WT were modeled using FDs of 6, 12, and 25 mm. Due to software limitations, square planar flaws had to be used instead of FBH. Consequently, hole diameters discussed in the following paragraphs are equivalent areas based on the planar flaw dimensions used for modeling. The models were constructed to simulate FBH of various diameters at depths (heights) of 0.5 and 1.0 mm from the back wall surface.

Figure 97 shows an example of a modeling simulation for a 4×4 aperture with a 12 mm WT and three FDs. The results are shown in C-Scan format with the hole dimensions given in height from the back wall surface along with diameter. For example, “1 x 2.55” in the figure is interpreted as a FBH drilled to a depth of 1 mm from the back wall surface with a diameter of 2.55 mm. Similarly, Figures 98 and 99 show A-Scan and B-Scan results for a 4×4 aperture at FDs of 12 and 3 mm, respectively. Viewing these examples show that the BW resolution is similar for both FDs and that the reflection from the largest hole (2.55-mm diameter) is stronger than the BW signal when using a FD of 3 mm. Additional observations from these simulation results indicate that the 0.64-mm-diameter hole would not be detectable due to the low signal amplitude, and that the 1.27-mm-diameter hole may be detectable with the 3-mm FD but probably not with the 12-mm FD. These simulations also reveal that a 1-mm-deep hole could be resolved at the BW.

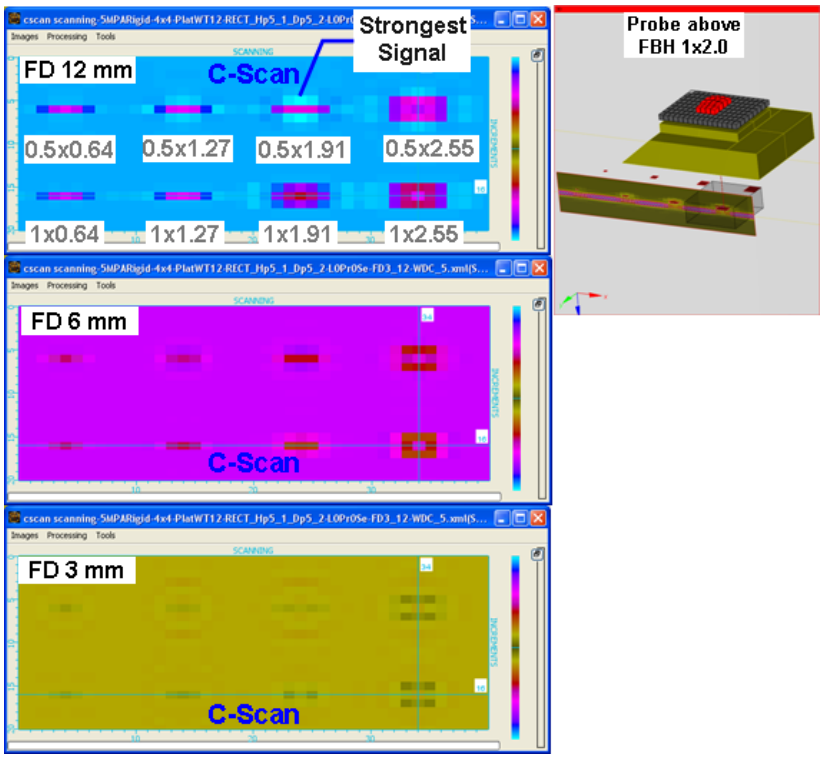

Figure 97. Detection of FBH Reflectors in a 12-mm WT Using a MPA 5-MHz Probe with a 4×4 Active Aperture and a 0-Degree Beam Angle (C-Scan Views)

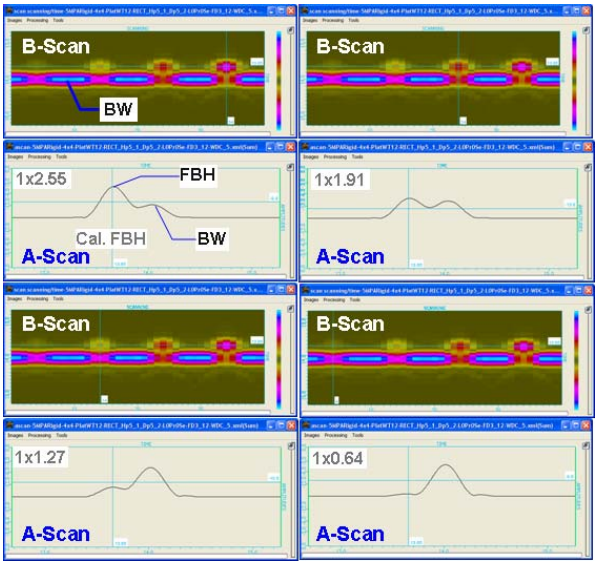

Figure 98. Detection of FBH Reflectors in a 12-mm WT Using a MPA 5-MHz Probe with a 4×4 Active Aperture, 12-mm FD, and a 0-Degree Beam Angle

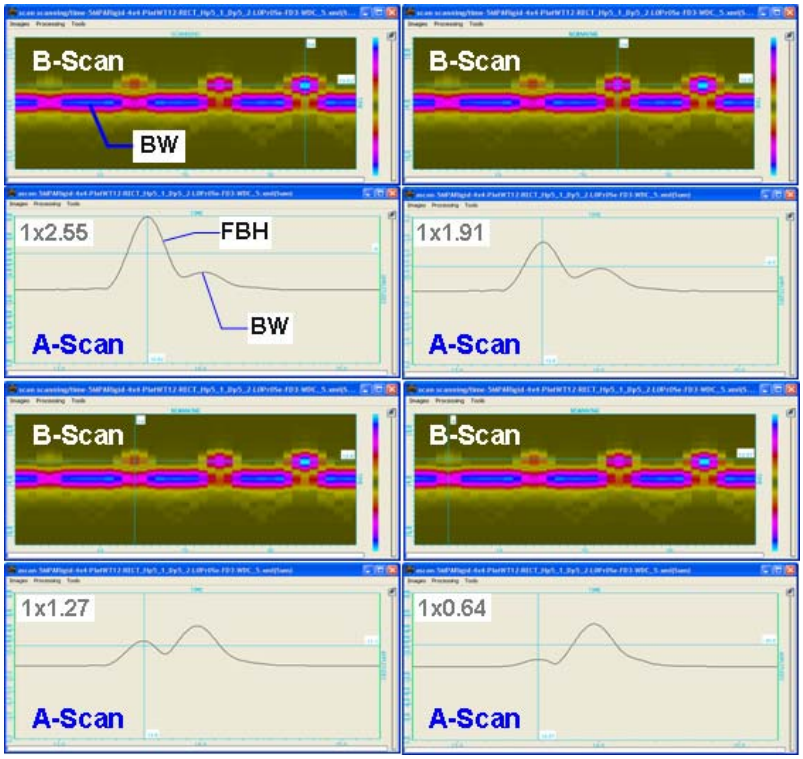

Figure 99. Detection of FBH Reflectors in a 12-mm WT Using a MPA 5-MHz Probe with a 4×4 Active Aperture, 3-mm FD, and a 0-Degree Beam Angle

Flaw interaction simulations were also conducted to look at detectability of FBH reflectors using a 10-degree refracted beam angle. Figure 100 shows results from this scenario for a 4×4 aperture with a FD of 12 mm. While the simulations show a possible improvement in detection and resolution with a beam angle of 10 degrees, the results could be inaccurate due to the planar flaws used as a substitute for FBH because of software limitations. Other flaw interaction models using different beam parameters are provided in Appendix B.

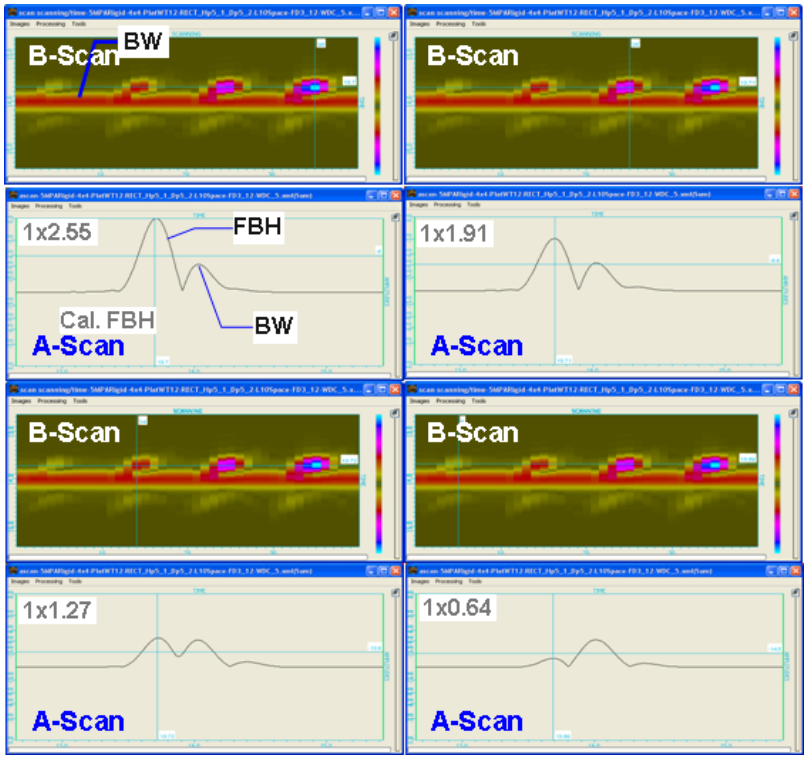

Figure 100. Detection of FBH Reflectors in a 12-mm WT Using a MPA 5-MHz Probe with a 4×4 Active Aperture, 12-mm FD, and a 10-Degree Beam Angle

In general, the flaw interaction simulations, shown in Appendix B, revealed the following:

- FBH of 0.5 mm in height were marginally detectable but would be difficult to measure because they were not fully separated from the BW signal.
- An active aperture size of 8×4 improved detectability for some holes in the 12-mm WT simulations.
- In all simulation scenarios, the 2.55-mm-diameter hole was always detected, but the 0.64-mm-diameter hole was not detectable. Other hole diameters were detected in some scenarios but not others. Tables 20 through 22 summarize detectability based on the flaw interaction results.

Table 20. Detectability Summary Rigid MPA 5 MHz, 4×4 Active Aperture, WT 12 mm

FBH Height (mm)	FBH Diameter (mm)	Normal Beam FD (mm)			10-Deg Spatial FD (mm)		
		3 (cal)	6	12	3	6	12
1.0	0.64	N	N	N	N	N	N
0.5	0.64	N	N	N	N	N	N
1.0	1.27	Y	N	N	N	Y	Y
0.5	1.27	N	N	N	N	Q	N
1.0	1.91	Y	Y	Y	Y	Y	Y
0.5	1.91	Y	Q	Q	N	Y	Y
1.0	2.55	Y	Y	Y	Y	Y	Y
0.5	2.55	Y	Q	Q	Y	Y	Y

*Q = Questionable

Table 21. Detectability Summary Rigid MPA 5 MHz, 8×4 Active Aperture, WT 12 mm

FBH Height (mm)	FBH Diameter (mm)	Normal Beam FD (mm)		10-Deg Spatial FD (mm)	
		6	12	6	12
1.0	0.64	N	N	N	Q
0.5	0.64	N	N	N	N
1.0	1.27	Y	Y	Y	Y
0.5	1.27	Q	N	N	Q
1.0	1.91	Y	Y	Y	Y
0.5	1.91	Y	Y	Y	Y
1.0	2.55	Y	Y	Y	Y
0.5	2.55	Y	Y	Y	Y

*Q = Questionable

Table 22. Detectability Summary Rigid MPA 5 MHz, 8×4 Active Aperture, WT 25 mm

FBH Height (mm)	FBH Diameter (mm)	Normal Beam FD (mm)			10-Deg Spatial FD (mm)		
		6 (cal)	12	25	6	12	25
1.0	0.64	N	N	N	N	N	N
0.5	0.64	N	N	N	N	N	N
1.0	1.27	N	N	N	N	Y	Y
0.5	1.27	N	N	N	N	Q	Q
1.0	1.91	Y	Y	Q	Q	Y	Y
0.5	1.91	Q	N	Q	N	Y	Y
1.0	2.55	Y	Y	Y	Y	Y	Y
0.5	2.55	Q	Q	Q	Q	Y	Y

*Q = Questionable

3.3.4 Task Observations and Conclusions

Overall, the virtual optimization task revealed the usefulness of UT modeling and simulations for probe design and for inspection procedure development. In addition, it provides a means of assessing detection and sizing capabilities for various inspection scenarios to help determine what is feasible with a given range of parameters. The complexity of MPA in particular, makes virtual optimization a valuable tool for sorting through a larger number of parameters to determine the best ones for a given application.

A CIVA software feature developed during this project provides a means to simulate beam to flaw interaction with branching flaws. This feature appears to provide a good prediction of the expected ultrasonic response from complex flaws and has been incorporated into the current revision of the software.

3.4 Task 4 – Fabrication of MPA Probes

Two MPA probes were fabricated during this project. One was a flexible MPA probe (Concept 2) and the second was a rigid ID probe (Concept 3). Other probes used during this project were existing probes owned by EWI or other project participants.

Concept 2 was a flexible MPA probe for inspection of the parent pipe material from the OD pipe surface. The ultrasonic characteristics of the probe were modeled and optimized during Task 2 of this project and the probe was built for evaluation.

During this project the flexible MPA probe shown in Figure 101 was built by Imasonic and used by EWI to acquire data on pipes having dents. Following are the flexible MPA probe parameters:

- Nominal frequency: 2.7 MHz
- Elements: 12 × 5 grid (60 elements total)
- Total active area: 17.4 × 14.4 mm
- Element size:
    - Primary = 0.9 mm
    - Secondary = 2.4 mm
- Pitch:
    - Primary = 1.5 mm
    - Secondary = 3.0 mm
- Inter element spacing:
    - Primary = 0.6 mm
    - Secondary = 0.6 mm
- Profilometer contains 9 points in a 3 × 3 grid of LVDTs with spacing between points of 6.5 mm

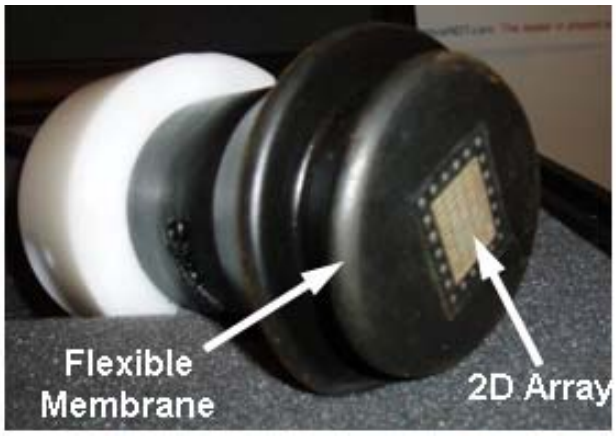

Figure 101. Concept 2; 2D Flexible Array Probe Fabricated During the Project

Concept 3 was a rigid MPA probe, designed for inspection of the parent pipe material from the ID pipe surface of fluid-filled pipes. The Concept 3 MPA probe and technique was primarily designed for detection of in-service damage on the OD surface. The ultrasonic characteristics of the probe were also modeled and optimized during Task 2 of this project and the probe was built for evaluation. The ID MPA probe, shown in Figure 102 was fabricated by Imasonic and used by EWI to acquire data on a demonstration pipe. Following are the ID MPA probe specifications:

- Nominal frequency: 5.0 MHz
- Radius in primary: 36.2 mm
- Elements: 32 × 4 grid (128 elements total)
- Total active area: 34.6 × 5.8 mm
- Element size:
    - Primary = 0.5 mm
    - Secondary = 1.0 mm
- Pitch:
    - Primary = 1.1 mm
    - Secondary = 1.6 mm
- Inter element spacing:
    - Primary = 0.6 mm
    - Secondary = 0.6 mm

Figure 102. Concept 3; ID MPA Probe Fabricated During the Project

Other probes used during the project were existing probes already owned by EWI or project participants. Figure 103 shows a 5-MHz, 16×8 element probe that was part of EWI's probe inventory. This probe was used for some data acquisition for Concept 1 and for Concept 4. Probe wedges were fabricated to adapt the probe for use on both concepts.

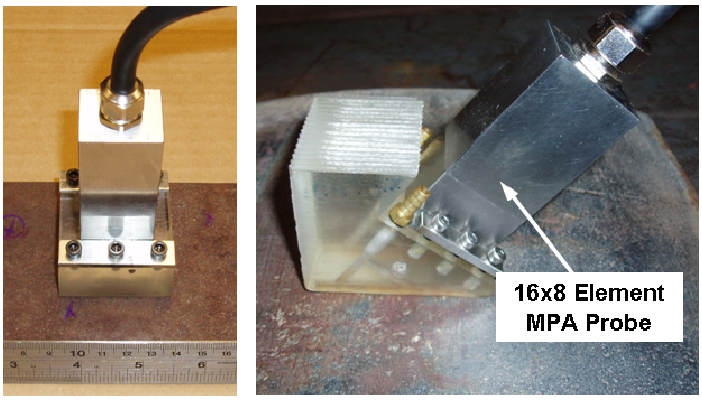

Figure 103. Existing 5-MHz, 16×8 Element MPA Probe

Figure 104 shows one of two 5-MHz, 6×8 element probes used by a project participant to gather data for Concept 1 evaluations. This probe and a sister probe were used for blind trial data collection on the girth weld samples discussed elsewhere in this report.

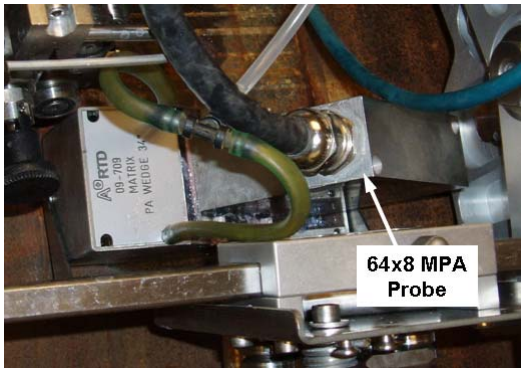

Figure 104. Existing 5-MHz, 64×8 Element MPA Probe

Figure 105 shows another EWI probe that was used for health monitoring evaluations for Concept 4. This probe was a 15-MHz, 11×11 element probe.

Figure 105. Existing 15-MHz, 11×11 Element MPA Probe

3.5 Girth Weld Inspection from OD (Concept 1)

Concept 1 pertained to MPA inspection of pipeline girth welds. The idea was to determine the feasibility of using MPA probes in a manner currently used with LPA and multi-element probes. Typically, girth weld inspection is performed using a zonal technique described in ASTM E1961.[6] This technique assumes that flaws are oriented perpendicular to the sound beam. In the past 5 to 10 years, LPA has gained in popularity for girth weld inspection because the electronic steering and focusing capability of LPA provides good zonal coverage with only two probes instead of 12 or more conventional probes. However, one disadvantage of LPA is that the beam can only be focused and steered in one direction; the primary probe axis. This generally results in an elliptical-shaped beam. Prior to using LPA for girth weld inspection, conventional probes having a spherical focus were used. This produced a tight spherical beam but the focal point was fixed. When a different weld geometry was to be inspected and the metal

path changed, it was often necessary to purchase new probes with the appropriate focal distance.

Because MPA probes have elements in a 2D pattern, the ultrasonic beam can be steered and focused in two directions. This can help produce a spherical beam and add other advantages such as beam steering and beam focusing in both the primary and secondary probe axis. With better control of the beam, it should be possible to improve flaw detection and sizing capabilities. In order to quantify MPA detection and sizing, test welds containing flaws were scanned with two MPA systems and the results were compared to LPA results obtained from a previous USDOT-sponsored project.

3.5.1 Design and Fabrication of Test Welds

Two groups of test welds were designed and fabricated for use on EWI Project 50454GTH (U.S. DOT PHMSA Transaction Agreement No. DTPH56-07-T-000002) and were also used to evaluate Concept 1 of this project. Each group consisted of girth welds in 30-in.-diameter X80 pipe having a 15.6-mm nominal WT. The first group consisted of four welds containing natural flaws that were created primarily by varying welding parameters to create flaws in a manner consistent with how actual flaws would be produced. The second group consisted of six welds containing implanted flaws that were more controlled as to flaw type, location, orientation, and size. The implanted flaw samples were identified as W1 through W6. The circumference of all 10 welds was divided into 60 sectors, each having a length of approximately 40 mm. This was done to assist in reporting and subsequent statistical analysis. Each sample was designed so that the weld contained approximately 20 to 25 intentional flaws that were at different depths within the pipe wall. Some sectors contained flaws while others did not. Specifications for through wall flaw heights ranged from 0.5 mm to approximately 12.0 mm, and lengths ranged from approximately 5 to 60 mm. Test welds identified as W5 and W6 were designed with several flaws in close proximity to each other in order to evaluate the effects of flaw interaction.

Early fingerprinting and verification testing of the four natural flaw samples revealed that the intended flaws were generally more severe than anticipated and that several unintentional and undesirable flaws had been created during the fabrication process. The number and size of flaws made interpretation very difficult and time consuming for determining POD and sizing accuracy. Consequently, it was decided to only use the implanted flaw samples for blind trial scans related to POD and sizing accuracy. Limited scans were conducted on the natural flaw samples for demonstration purposes only. Implanted flaw sample W1 was designated as an open trial sample to allow AUT operators to test out their equipment and procedures prior to performing the blind trials.

3.5.1.1 Fingerprinting

Following fabrication of the 10 samples, EWI performed visual testing (VT), fluorescent magnetic particle testing (MT), radiography testing (RT), and LPA ultrasonic scans on the welds to document both intentional and unintentional flaws. This process was referred to as fingerprinting the samples, and was later used in conjunction with destructive tests to determine actual flaw locations and dimensions. Visual and fluorescent MT was performed on the weld and heat-affected zone (HAZ) on both the OD and ID surfaces. RT was done using film and computed radiography (CR) with phosphorus plates. LPA UT scans were conducted using a raster scan technique to cover the entire weld circumference from both the upstream (US) and downstream (DS) sides of the weld. In addition to PA, the welds were also scanned with TOFD and transverse probes. The LPA setup for fingerprinting was a sector scan technique where the ultrasonic beam was electronically steered through refracted shear wave angles of 40 to 70 degrees in 1-degree steps. The LPA probe was a 60-element probe having a 7.5-MHz frequency. Instrument gain and distance settings were established using 2-mm-diameter FBH.

During fingerprinting it was noted that weld Samples W2, W3, and W4 contained locations where the WT had been reduced by grinding. This was done by the sample fabricator to facilitate fit up prior to welding. Estimates from the fingerprinting results showed the wall thinning to be as much as 2 mm. This equated to approximately 12.8% of the nominal WT which was greater than what is allowable for WT deviations per API 5L, “Specification for Line Pipe”. For pipe having an OD of 20 in. or greater, API specification 5L stipulates a WT tolerance of +19.5, -8% for X80 welded pipe used for this project. It was decided to use flaws located in the thin areas to evaluate the effect of wall thinning on AUT results. If AUT results showed a significant effect, flaws in these locations would be excluded from the POD and sizing data.

3.5.1.2 TomoCAR Fingerprinting

As part of this project, BAM Federal Institute for Materials Research and Testing in Berlin, Germany, provided an in-kind contribution of their Tomographic Computer Aided Radiology (TomoCAR) system for evaluation of two test welds.[7] TomoCAR uses planar tomography to visualize component features and flaws in three dimensions (3D). TomoCAR has been demonstrated to accurately measure flaw dimensions within 1 mm. TomoCAR uses a mechanized manipulator to scan an X-ray tube across the weld and acquire an image on a digital detector array (DDA) positioned behind the pipe or pipe wall (Figure 106). Several hundred images are required for Tomographic 3D reconstruction.

This project provided a good opportunity to evaluate TomoCAR as an alternative to DT. It is well known that it is time consuming and costly to fabricate samples with known flaw types, sizes, and orientations, and then cut them up in order to measure the flaws. Therefore, TomoCAR was evaluated as a potential fingerprinting technique for measuring flaws without the need for

metallographic cross-sectioning. TomoCAR results from selected locations were compared to those from metallographic cross-sections.

One weld used for the TomoCAR evaluation was an open trial implanted flaw sample (Implanted Weld 1). The other weld was a natural flaw sample (Natural Flaw Weld 2). The TomoCAR images re vealed good detection of flaws in the samples and had a measurement resolution of 0.1 mm. The flaw extremities were easy to identify and measure as shown in Figure 107. Flaw depth was the most difficult measurement to obtain because it was difficult to accurately locate the OD surface of the pipe in the TomoCAR images. The weld toes were the best indicator of the OD surface, but radiation scattering at the weld toes made precise location difficult.

In order to compare TomoCAR results with metallography results, three metallographic cross-sections were removed from Natural Flaw Weld 2. Comparisons of the destructive cross-sections and the TomoCAR results are shown in Figures 108 through 110. In general the comparisons showed that TomoCAR measurements agreed quite well with the destructive cross-section measurements and may offer a good option when destructive analysis is not desirable.

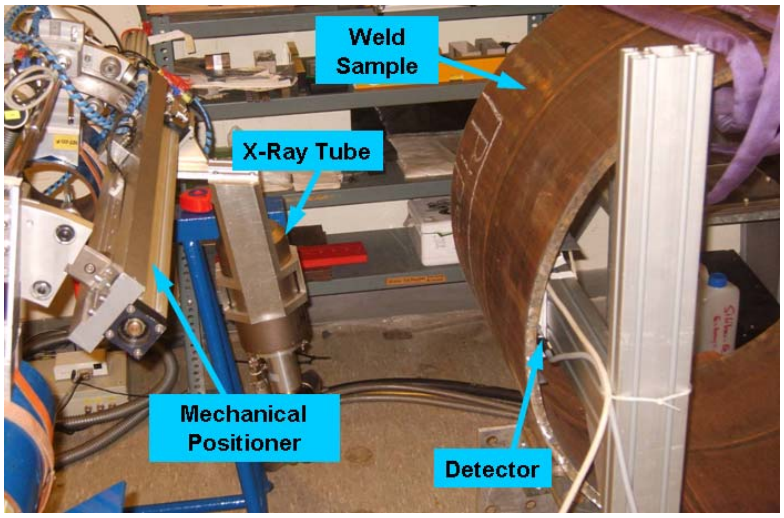

Figure 106. TomoCAR Setup

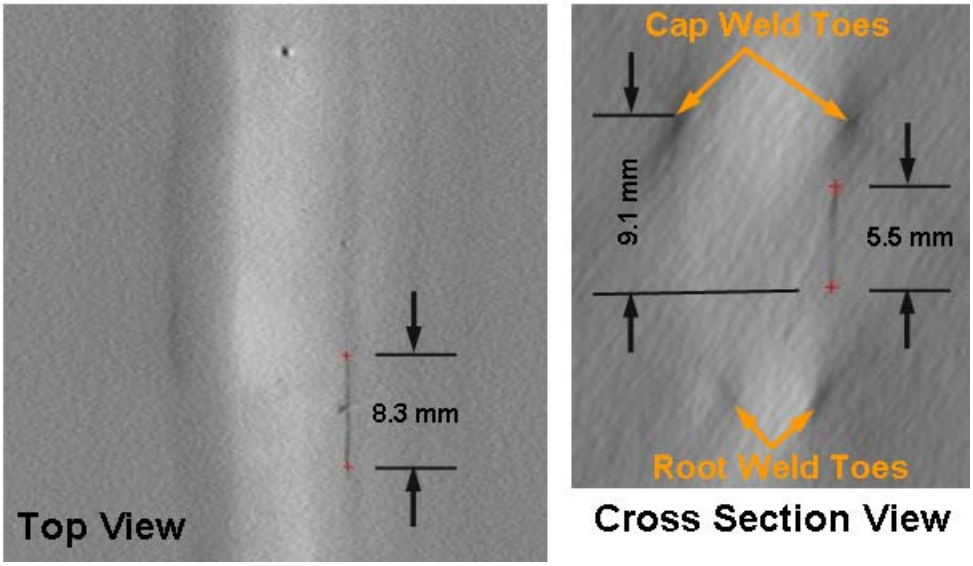

Figure 107. TomoCAR Images from Implanted Flaw Sample 1, Location 1610-1618

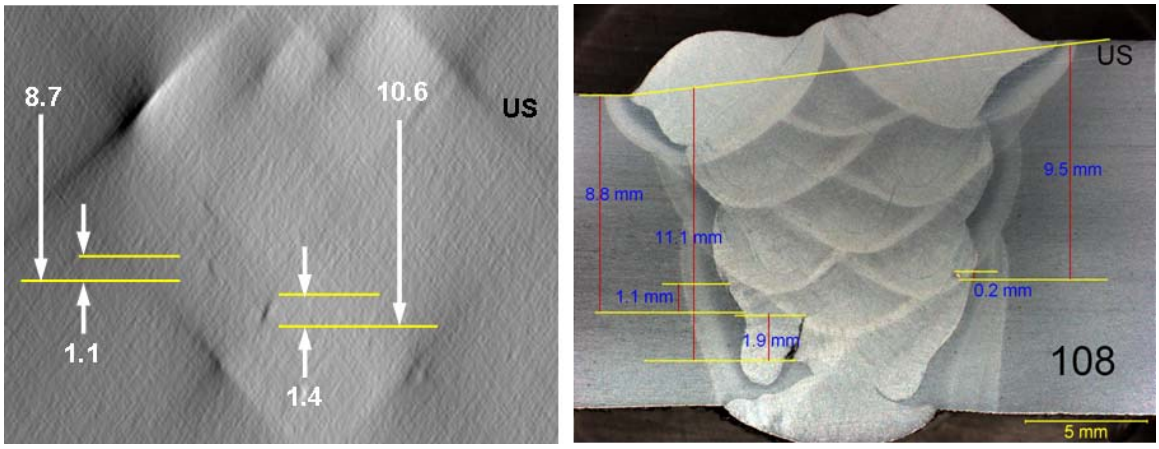

Figure 108. Location 108: Comparison of TomoCAR (L) and Metallographic Cross-Section (R)

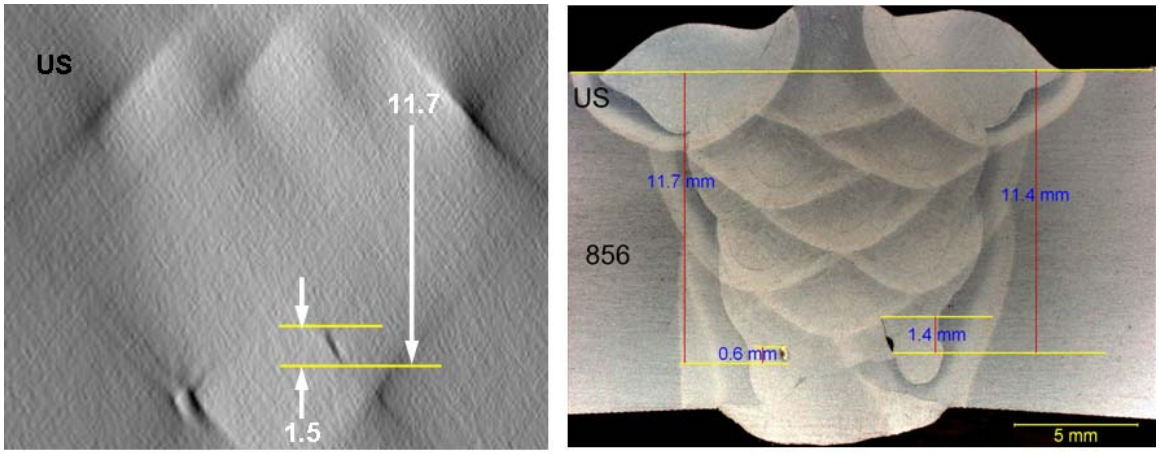

Figure 109. Location 856: Comparison of TomoCAR (L) and Metallographic Cross-Section (R)

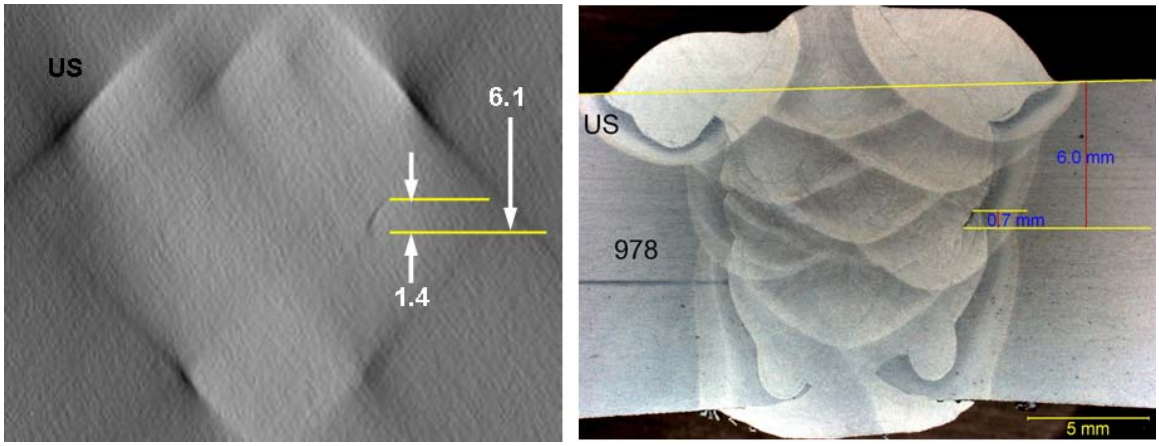

Figure 110. Location 978: Comparison of TomoCAR (L) and Metallographic Cross-Section (R)

3.5.2 MPA AUT Scanning

One open and one blind MPA trial was conducted using the six implanted flaw samples (W1 through W6). The MPA open trial was a non zonal technique that was used as a supplemental fingerprinting technique. The MPA blind trial was a zonal inspection technique similar to what is commonly used for pipeline girth weld inspection. The MPA instrumentation and software were part of a new product development and consequently was still being tested and evaluated. While it was not a finished product, this project provided a good opportunity for the developers to test out the system and also provided some valuable information for benchmarking MPA technology for this application.

3.5.3 MPA Open Trial Setup

The open trial setup used a 5-MHz, 16×8 element probe (Figure 111) with a mechanical raster scan and was performed as a non zonal approach with electronic sector scanning (S-Scan) and beam skewing. Refer to Tables 23 and 24 for more details. For the sector scans the beam was electronically steered in the primary probe axis from 48 to 73 degrees in one degree steps. Three S-Scans were used; each having a different skew angle. One S-Scan had a skew angle of 0 degrees and the remaining two had electronic skew angles of +5 and -5 degrees. Instrument gain and distance settings were established using 2-mm-diameter FBH and 1-mm-deep × 10-mm-long ID and OD notches. Figure 112 shows a typical display of the open trial output screen. S-Scans were used as the primary method for determining flaw height and depth during open trial data interpretation. Indications that appeared to be flaws and not geometry were evaluated regardless of amplitude.

The probe angle beam wedge design used for the MPA open trial setup was not optimal for inspection of the test welds used for this project. The size and shape of the wedge was primarily driven by the MPA probe design. Consequently, the wedge had to be designed to accommodate the existing probe. The wedge is shown in the right most image of Figure 111. The front portion of the wedge was too long resulting in limited forward scanning because of the wedge contacting the weld cap. Consequently, lower beam angles, less than approximately 67 degrees could not be used for inspection of the root and hot pass areas of the welds on the first leg of the sound beam. This limited data analysis to mostly second leg data, after the beam reflected from the ID pipe surface.

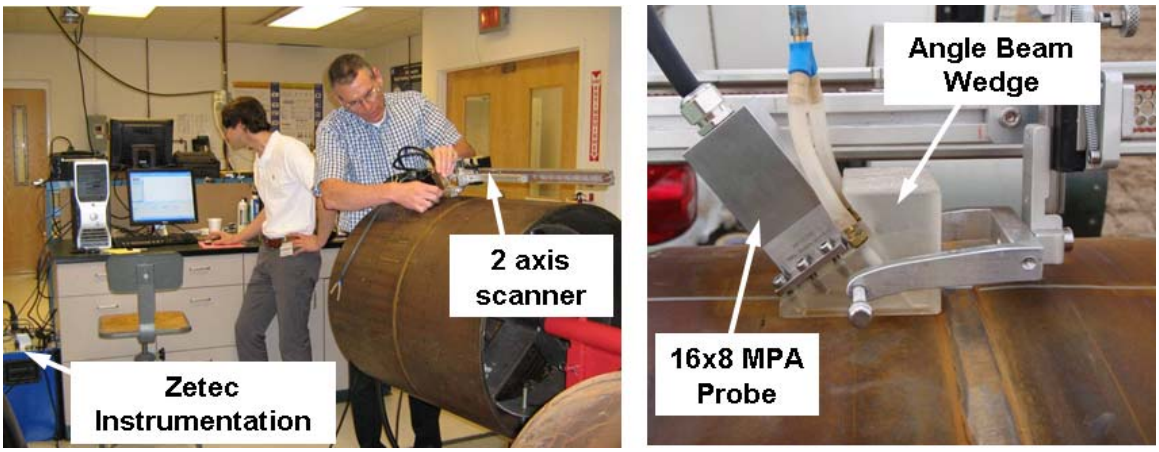

Figure 111. MPA Open Trial Scan

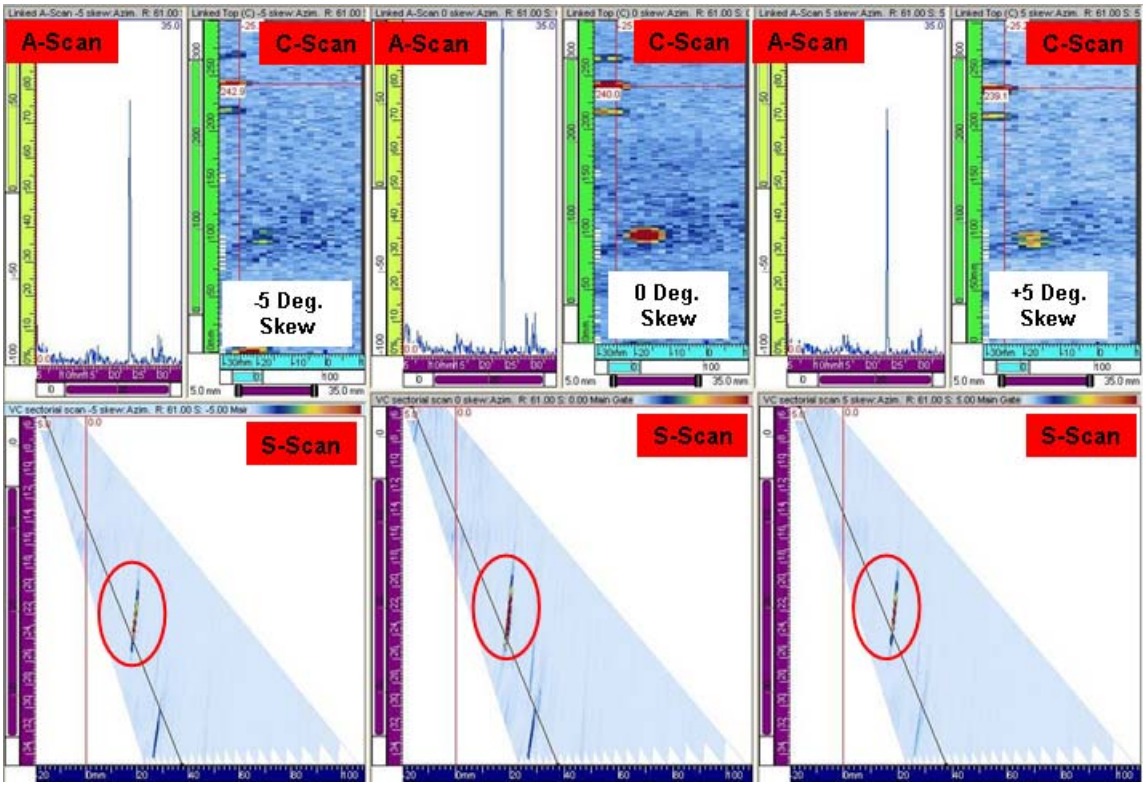

Figure 112. Screen Output Display for Open Trial Scans

3.5.4 MPA Blind Trial Setup

The blind trial setup used two 5-MHz, 64×8 element probes (Figure 113) with a mechanical line scan and was much more complex than the open trial setup. Refer to Tables 23 and 24 for more details. One of the probes was positioned on the US side of the weld and one on the DS side of the weld to allow zonal inspection similar to approaches currently used for multi-probe, and LPA girth weld inspection per ASTM E1961. The biggest difference was the ability of the MPA to electronically focus the beam in two directions and to electronically skew the beam in each weld zone. The blind trial probes, electronics (Figure 114), and software were specifically adapted for MPA inspection of pipeline girth welds. This required development of inspection procedures and data analysis methods for this unique setup.

Three blind trial scans were performed on each of the six test welds using the same test equipment and operator. Different setups were used for each scan and are designated as Setups ‘A’, ‘B’, and ‘C’ in this report. Element apertures varied according to sound path distance but the secondary axis always used the full eight elements while the primary axis varied from 12 to 32, depending on the zone. The calibration sample for all setups contained 2-mm-diameter FBH for the hot pass and fill zones, 1.5-mm-diameter holes for the volumetric channels, and 1-mm-deep × 5-mm-long OD and ID notches for the root and cap zones. The

three setups primarily differed in the number of tilt and skew sequences (channels) used and the tilt and skew angles selected. The same calibration block was used for each setup. Table 25 provides information regarding the tilt and skew sequences used for each setup.

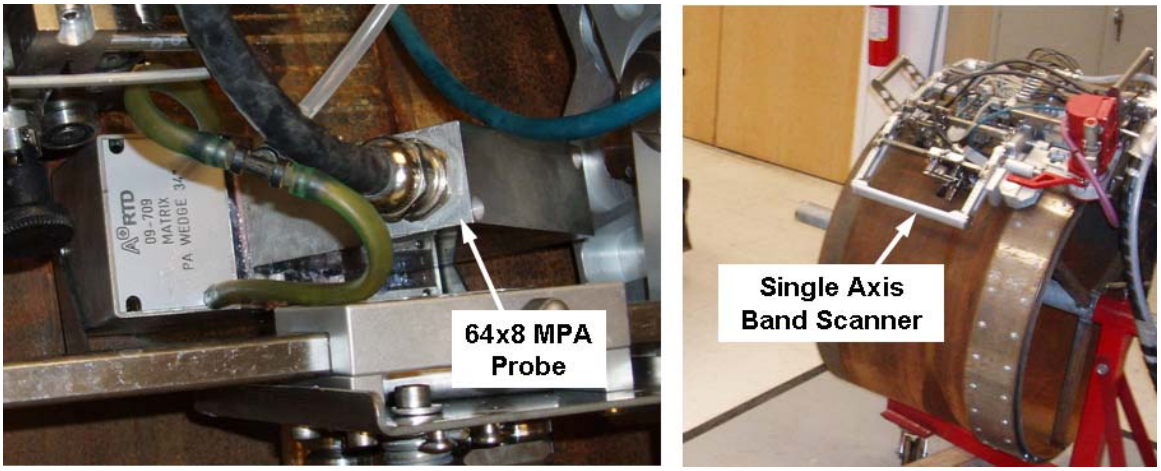

Figure 113. MPA Blind Trial Scan

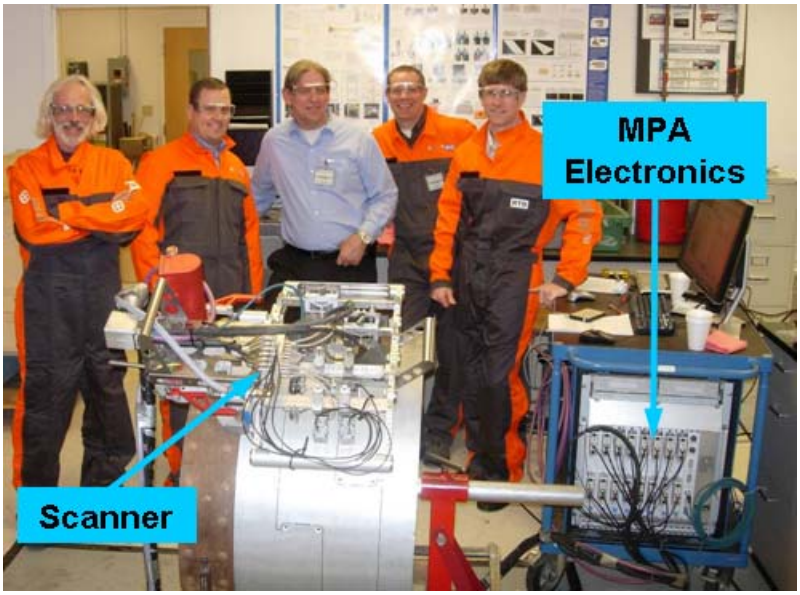

Figure 114. MPA Electronics and Scanner

The first scan, using Setup ‘A’, had the greatest number of sequences and the largest data files. In addition to the nominal UT sequences (0-degree tilt, 0-degree skew), Setup ‘A’ had full sectorial scans plus two additional tilt sequences and two additional skew sequences for each weld zone. The additional skew angles were +5 and -5 degrees from nominal while the additional tilt angles were +4 and -4 degrees from the nominal inspection angle. These additional tilt and skew sequences were referred to as “children” sequences because they were

derived from the nominal ("parent") sequences for a specific zone. This resulted in a total of five channels for each inspection zone. For example, Fill Zone 2 (F2) for Setup 'A' consisted of the following channels:

- F2 (z-4) – child sequence; minus 4-degree tilt
- F2 (y-5) – child sequence; minus 5-degree skew
- F2 – parent sequence; nominal zone angle with no tilt or skew
- F2 (y+5) – child sequence; plus 5-degree skew
- F2 (z+4) – child sequence; plus 4-degree tilt.

This setup resulted in a total of 81 UT sequences for the US side of the weld and another 81 sequences for the DS side of the weld. A TOFD scan was also incorporated into the setup for a total of 163 sequences. Because of the large amount of data generated by Setup 'A', only 1 meter of weld length was scanned for each file. Three scan files were required to cover the entire weld circumference.

The second scan was conducted using Setup 'B'. For this setup no additional tilt sequences (children sequences) were used and no sectorial sequences were used. Additional skew angles were still used as in Setup 'A'; however, the skew angles were increased to +10 and -10 degrees. With the changes made in Setup 'B' the data files were small enough to allow full circumferential coverage of the samples with a single scan. The changes also allowed larger aperture sizes to be used for each zone. By increasing the aperture size, the beam spot size became smaller.

The third scan, using Setup 'C', also did not use sectorial scans or additional tilt sequences. The electronic skew angles were +5 and -5 degrees and beam spot sizes were the same as those used for Setup 'A'.

3.5.4.1 MPA Blind Trial Data Evaluation

A sample reporting template was supplied by EWI and it was requested that an equivalent methodology be used for reporting. This included reporting by sector location and the desired flaw terminology to be used. There was no request to determine acceptability or reject ability of indications, but to simply report all indications that were judged to be valid weld flaws and not geometric indications.

Since the data set from Setup 'A' contained information available from the additional tilt sequences, it was decided to use this data set for evaluation and reporting. Cross referencing to data obtained with the other two setups was made, but this was for information purposes only. Due to the huge amount of data and the lack of experience with those undertaking the evaluation, sectorial scan data was not used.

During data analysis a reporting amplitude threshold of 10% was used; length reporting was generally from 10% to 10%, minus beam spread values from the calibration standard. Determination of flaw depth and flaw height was based on a combination of zonal sizing concepts and TOFD data. Flaw signal amplitude values were reported as the highest amplitude values obtained from any sequence within the zone containing a flaw. This was true whether the sequence was a nominal beam or one of the tilt or skew children sequences. Comments were provided in the report as to the estimated flaw orientation. This was determined based on which sequence had the greatest response.

General observations of the MPA blind trial data showed that additional tilt sequences produced a greater signal response from tilted flaws in approximately 38% of the cases. A total of 32 flaws were reviewed having tilt angles that varied 2 to 10 degrees from the actual weld bevel angle. Likewise, data showed that additional skew sequences produced a greater signal response from skewed flaws in approximately 38% of the cases. A total of 8 skewed flaws were reviewed having skew angles that varied 2 to 6 degrees from the weld centerline plane. One caveat was that all skewed flaws also had some tilt to them as well. The MPA blind trial setups all had additional sequences with either tilt or skew but not both. It is not known if flaws that were skewed only, would have been detected better by the additional skew sequences, but it is quite probable based on review of flaws having tilt only. There were a total of 24 flaws having tilt with no skew. Of the 24 flaws, 12 (50%) were detected better with the additional tilt sequences.

Additional observations revealed that approximately 45% of root flaws having no tilt or skew were detected better with root tilt sequences having less beam angle than the nominal angle of 60 degrees. These tilt sequences, showing higher signal amplitude from root flaws, had a refracted beam angle of 56 degrees.

3.5.4.2 Limitations to MPA Data Interpretation for Blind Trial Welds

Following are limitations identified by the AUT operator regarding interpretation of the MPA data.

- Four of the six implanted flaw samples had areas of internal taper that was approximately 400 to 500 mm in length. Two of the four samples had locations where the wall thinning was over 10%. The AUT operator reported that these taper locations were not always apparent in TOFD and as such, the assumption was made that the taper did not exist, and that flaw orientation was based on the greatest amplitude from a specific sequence, whether nominal or a child sequence of tilt/skew. Knowledge of locations containing internal taper were made available by EWI but were not used by the operator during interpretation.

- The large file sizes did not allow for multiple files to be open at the same time. This prevented checks between the calibration standard and weld typically accomplished by opening multiple windows.

- The software did not allow for visually observing upper tip profiles over 100% amplitude. Amplitudes could be obtained by running the mouse cursor over the echo only. Visually observing the echo dynamics in multiple channels by viewing the upper tips would have been a valuable aid.

- The software did not allow a printing option or the ability to record indications and print reports. Extracting amplitude values for any sequence was possible only by handwriting the results and using a print screen/screen capture approach.

- When wishing to check both nominal and children sequences for a few select pulse-echo (PE) zones, the screen became overcrowded with too many channels. It was extremely time consuming to switch off undesired PE channels in the gate list to view only channels of interest.

Table 23. MPA Probe Parameters

Probe	Total No. of Elements	No. of Elements in Primary Axis	No. of Elements in Secondary Axis	Probe Freq.
Open Trial	128	16	8	5.0
Blind Trial	512	64	8	5.0

Table 24. MPA Scan Setups

MPA Setup	Zonal	Non Zonal	PA Freq.	Cal. Sample(s)	Comments
Open Trial		X	5.0	2-mm FBH (not Zed block)	Raster sector scan (48-73 deg.) with 3 skew angles (-5, 0, & +5 deg.)
Blind Trial	X		5.0	2-mm FBH (Zed block)	One line linear scan

Table 25. Breakdown of MPA Blind Trial Setups

Setup	Tilt Sequences per Zone	Skew Sequences per Zone	Sectorial Sequences	Tilt Angles (Deg.)	Skew Angles (Deg.)
A	2	2	1	-4 & +4	-5 & +5
B	0	2	0	---	-10 & +10
C	0	2	0	---	-5 & +5

MPA data was formatted in preparation for statistical analysis and comparison to LPA results obtained during a previous project. A summary of LPA setups used for comparison are provided in Table 26. The three zonal LPA setups (2, 4, and 5) were based on ASTM E1961 and were similar in application to the blind trial MPA setups except for the LPA steering and focusing limitations previously described. All LPA setups had at least one TOFD channel.

Table 26. Summary of Linear PA AUT Setups

Setup No.	Zonal	Non Zonal	No. of Fill Zones	PA Freq.	Cal. Sample(s)	Comments
1		X	--	7.5	2-mm FBH (not Zed block)	3 staggered sector scans (45-65 degrees)
2	X		4	5.0	2-mm FBH (Zed block)	--
3		X		5.0	NAVSHIPS block	1.2-mm side-drilled holes (SDH). Zed block used for setup verification. Single-sector scan (35-70 degrees).
4	X		6	5.0	2-mm FBH (Zed block)	--
5	X		4	5.0	2-mm FBH (Zed block)	--

3.5.5 Destructive Evaluation

Following completion of all LPA and MPA AUT scanning activities, destructive testing (DT) of the implanted flaw samples began. Five implanted flaw samples (W2 through W6), that were part of the blind trial study, were cut down to a manageable size using a combination of flame cutting and saw cutting. Flame cutting allowed a ring, containing the weld, to be removed from the pipe section. Flame cuts were made approximately 100 mm (4 in.) on each side of the weld. For each weld, the resulting ring was then saw cut into four smaller segments and excess material on each side of the weld was removed. As part of this process, saw cuts were made parallel to the weld on both the US and downstream DS sides of the weld. Cuts on the US side were approximately 25 mm (1 in.) from weld centerline while cuts on the DS side were approximately 13 mm (0.5 in.) from weld centerline as shown in Figure 115. This was done so that the US and DS sides were easily identifiable throughout the DT process.

Figure 115. Example of Saw Cut Segment

After saw cutting, the sample segments were then prepared for water jet cutting to remove weld cross-sections for subsequent metallographic preparation and measurement. In preparation for removing metallographic sections from the welds, tests were conducted with the water jet cutting system to determine the width (kerf) of the water jet cuts. In addition, previous data was reviewed to determine the amount of material that would be removed from each sample during grinding and polishing. Results of these evaluations showed that the water jet kerf was consistently 0.8 mm (0.03 in.) and that approximately 0.5 mm (0.02 in.) would be removed during metallographic processes related to grinding and polishing. Based on these results, it was decided to make water jet cuts at 3-mm (0.12-in.) intervals along the length of each flaw to be measured during the DT. After cutting, grinding, and polishing this resulted in weld cross-section samples having a thickness of approximately 2 mm (0.08 in.).

Cutting locations were selected based on a compilation of intended flaw location from the fabrication drawings and actual locations reported by multiple AUT scans conducted during the project. The number of cross-sections for each flaw was determined by the flaw length and any skewing of the flaw. For flaws with no skewing, the typical minimum number of cross-sections is shown in Table 27. When cross-sectioning skewed flaws, metallographic samples were generally removed every 3 mm along the length of the flaw.

Table 27. Number of Metallographic Cross-Sections for Non-Skewed Flaws

Flaw Length (mm)	Typical Number of Cross-Sections
<8	1
8-12	2
>12	3

For flaws less than 8 mm (0.31 in.), one sample was removed at the flaw center. Generally, for flaw lengths of 8 to 12 mm (0.31 to 0.47 in.), a minimum of two samples were removed with one being near flaw center and the second near the beginning of the flaw. For flaw lengths greater than 12 mm, at least three samples were typically removed with one being at flaw center and the other two taken 3 mm on each side of flaw center. Cross-sections were also removed from selected locations where UT indications were noted by multiple AUT systems, or where

radiography indications were present. In addition, samples were also removed in locations where no flaws were planned or detected.

Circumferential weld positions on the samples were relative to the center of the water jet cut. As each sample was water jet cut, both faces of the thin samples were identified by weld number and circumferential weld position relative to the zero scan start position. Since water jet cuts were made at 3-mm (0.12-in.) intervals, the identification on opposing faces of the same sample differed by 3 mm. For example, Sample 2-100 would represent Weld No. 2, Location 100. This sample would be identified on one face as 2-100 and as 2-103 on the opposite face.

After removal of the metallographic samples by water jet, photographs were taken of the samples in the as-cut condition. It was thought that these photographs may help with flaw identification and measurements by allowing access to both sides of the thin samples. Review of these photographs revealed that most flaws were typically not visible in the photographs (Figure 116); consequently, the process of photographing the as cut surfaces was discontinued.

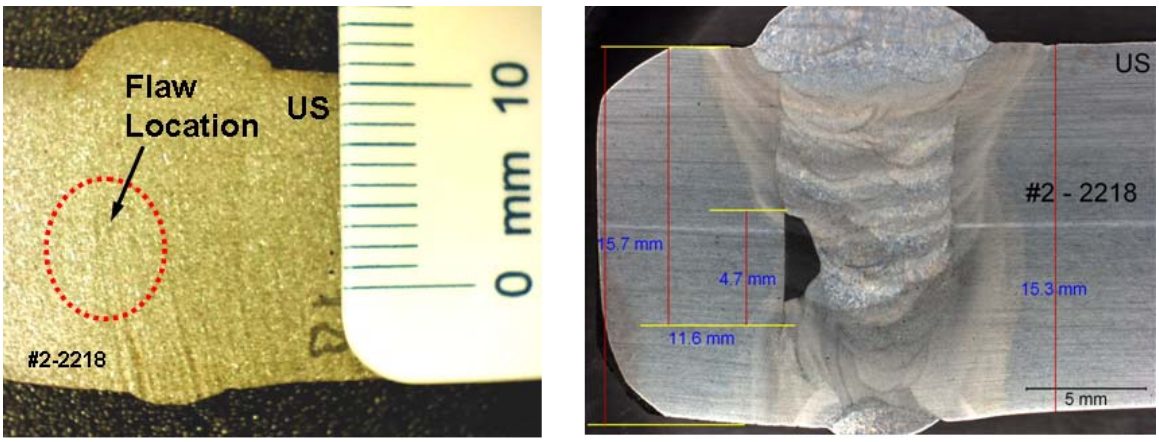

Water Jet As-Cut Surface

After Grind, Polish, and Etch

Figure 116. Photos Before (Left) and After (Right) Grind, Polish, and Etch

Prior to grinding and polishing, each sample was radiographed so that the flaw height could be seen through the 3-mm sample thickness. Radiography was conducted using computed radiography to obtain a digital image (Figure 117). This technique helped provide good verification of flaw height measurements obtained by metallography, as well as detection and location of other unintended flaws.

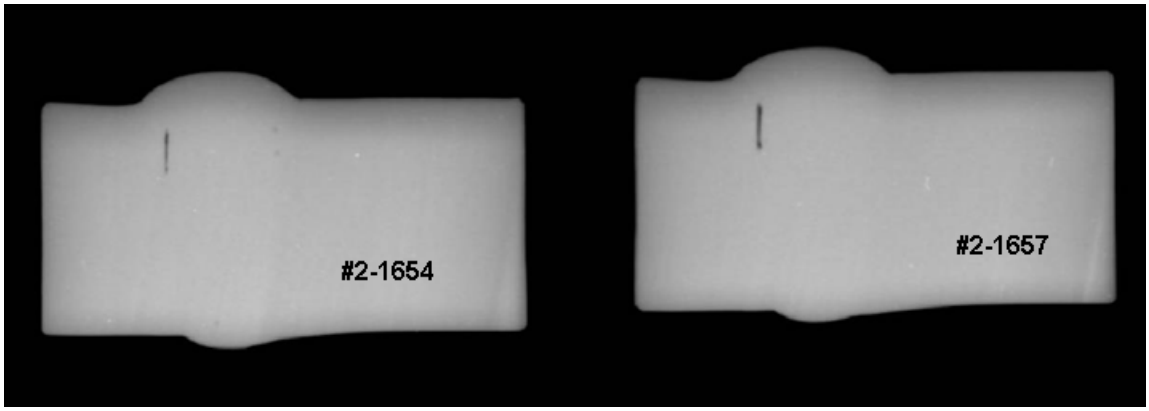

Figure 117. Example of CR on Un-Polished Water Jet Cut Samples

Metallography of the samples was accomplished by trimming the samples to fit within 38-mm (1.5-in.)-diameter mounts and oriented so that the sample face corresponding to the lowest circumferential weld position was polished for evaluation. Samples were polished to a final surface finish using 0.05-µm polishing compound and then lightly etched using a 2% nital etch solution. Photographs were then taken of each weld cross-section sample at a magnification of 5×. Linear measurements were made to determine the depth and height of flaws observed on the samples. Additional measurements of WT and misalignment were also obtained in locations where these parameters could have a possible effect on the AUT results. Figure 118 shows typical measurements performed on metallographic weld cross-sections.

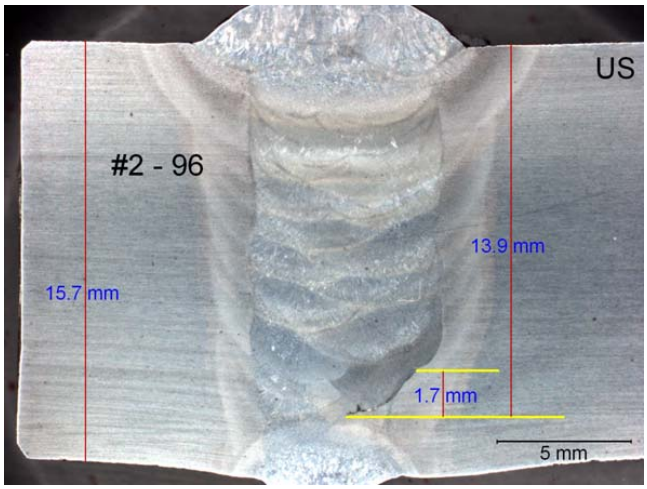

Figure 118. Polished and Etched Weld Cross-Section Showing Typical Measurements

As the metallographic weld cross-sections were evaluated, it became apparent that higher magnification was needed to determine the extent of some flaws. Lack of sidewall fusion flaws in particular were often difficult to view at 5× (Figure 119). This led to changing the

measurement technique so that higher magnifications of up to 100× were used to find the extent of flaws prior to photographing at 5×.

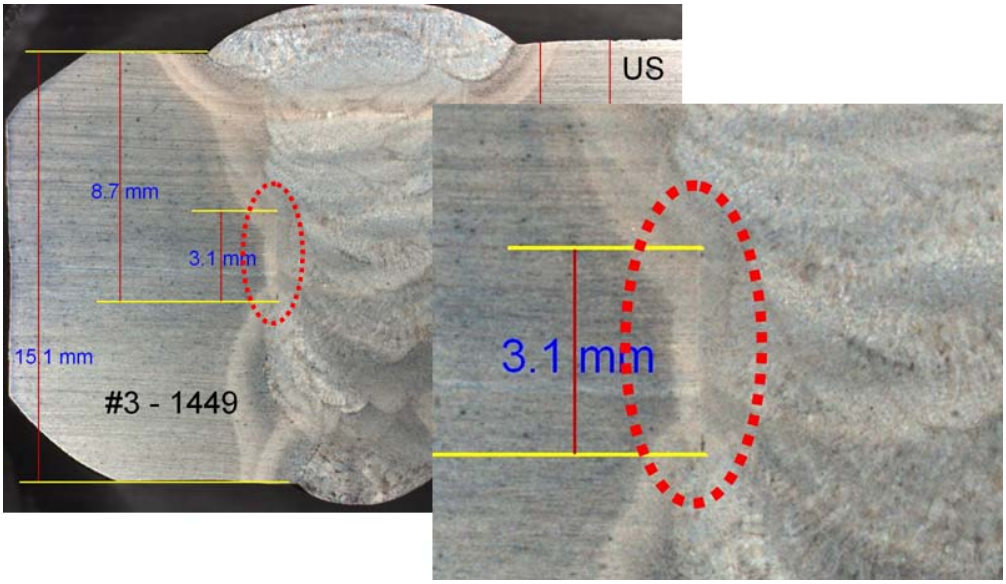

Figure 119. Example of Difficulty in Viewing Tight Flaws at 5×

Flaw dimensions were obtained from the macro photographs and were input into spreadsheet format for statistical analysis.

POD and Sizing Comparisons

Ultrasonic test data obtained during the MPA open and blind trial was used to statistically determine POD and accuracy of flaw sizing. Statistical methods used for the calculations were from MIL-HDBK-1823A. Measurements obtained from the destructive tests were used as the reference or "actual" values for flaw height and depth; while LPA fingerprinting was used as the reference for flaw length. The MPA statistical results were then compared to those obtained from LPA open and blind trials from a previous project that used the same weld samples. During the previous project, five LPA AUT systems were evaluated. As explained earlier and shown in Table 26, two of the LPA systems used a non zonal approach and three used a zonal approach (ASTM E1961 approach) similar to that used for the MPA blind trial.

POD curves, with respect to flaw height, for MPA blind trials, MPA open trials, and combined LPA blind trials are shown in Figures 120 through 122, respectively. The a90/95 value is circled in each POD chart and has units of millimeters. This value is the flaw height with having a 90% POD and 95% confidence. This is the most quoted parameter in the literature. It means that 90% of the flaws with this size and larger will be detected and this is true in 95% of the inspections under similar conditions (equipment, operators, environment, etc.). The charts also

show the a50 and a90 values. These values are expressed as flaw heights having 50% and 90% POD. For example, in Figure 120 the a50 value is 1.849 mm. This means that flaws having a through-wall height of 1.849 mm or larger will be detected 50% of the time under similar testing conditions. The same scenario applies to the 90% POD value as well.

The a90/95 POD result for the MPA blind trial was approximately 3.6 mm (Figure 120) while the MPA blind trial result was approximately 3.1 mm (Figure 121). By way of comparison, the combined LPA POD result from five blind trials was 4.2 mm (Figure 122) with the best LPA result being 3.2 mm (Figure 123). POD results for LPA and MPA trials are provided in Table 28. These results show that POD values for MPA were similar to those obtained for LPA. Given that MPA is an emerging technology for girth weld inspection, the overall results were encouraging.

While data files from the MPA blind trials were not available for review by EWI, it appeared that some flaws were likely detected by the AUT instrumentation but were not reported by the operator. When considering the amount of AUT data obtained by the MPA blind trial scans and the newness of the technology; it is quite conceivable that these factors caused some flaws to be missed by the operator. Observations noted by the AUT operator and discussed previously in the *"MPA Blind Trial Data Evaluation"* section of this report, mention some limitations that likely impacted the POD results.

As mentioned earlier, the open trial MPA setup used a probe wedge that was not fully optimized for the weld samples used during this project. This resulted is less than ideal conditions for flaw detection and sizing since most analysis had to be performed with second leg data that is not as desirable since the sound beam must first reflect from the ID pipe surface.

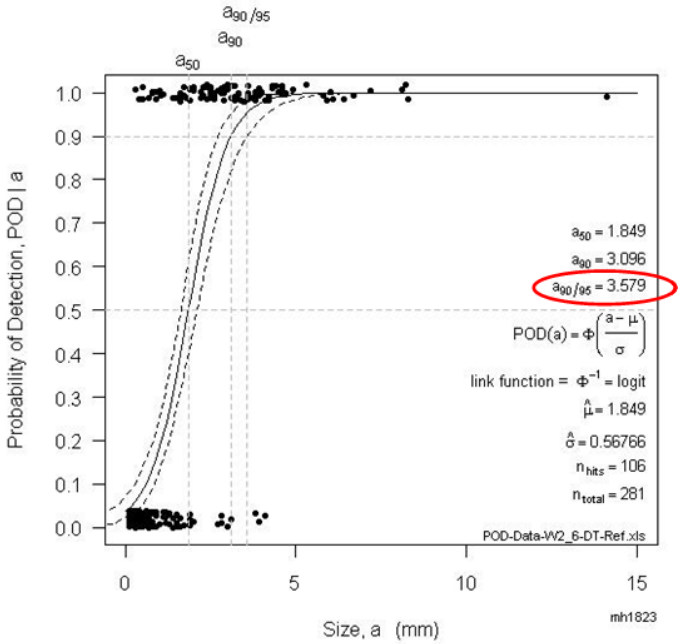

Figure 120. POD Curve for MPA Blind Trial

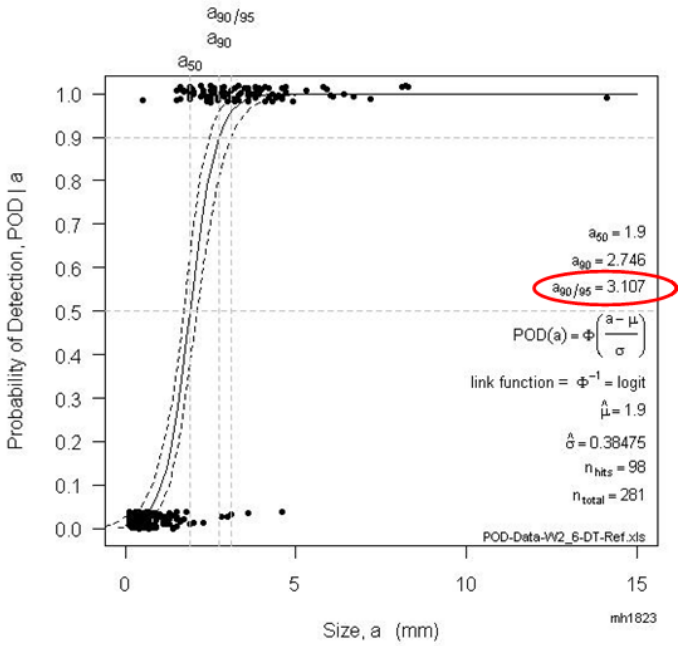

Figure 121. POD Curve for MPA Open Trial

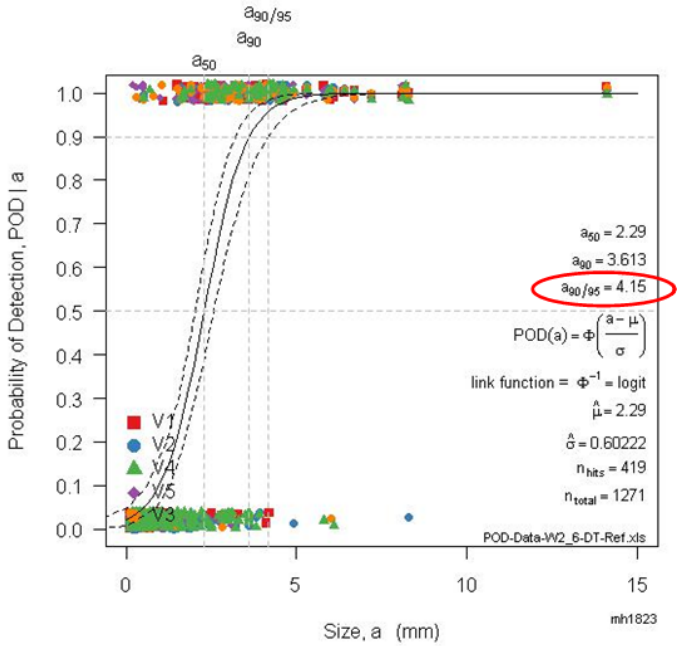

Figure 122. Combined Blind Trial POD Curve for all Five LPA AUT Systems

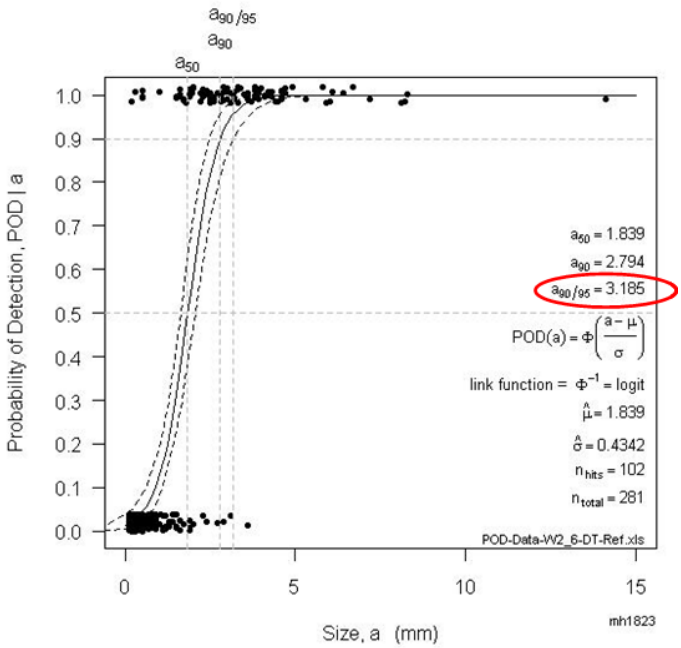

Figure 123. POD Curve for Best LPA Blind Trial

Table 28. POD Summary for LPA and MPA Trials

Trial	a50 (mm)	a90 (mm)	a90/95 (mm)
Blind LPA V1	2.0	3.0	3.4
Blind LPA V2	2.6	4.1	4.7
Blind LPA V3	3.0	4.6	5.3
Blind LPA V4	1.8	2.8	3.2
Blind LPA V5	1.7	3.0	3.6
Combined LPA Blind Trials	2.3	3.6	4.2
Blind MPA	1.8	3.1	3.6
Open MPA	1.9	2.7	3.1

AUT sizing accuracy was also calculated for both LPA and MPA and are provided in Tables 29 and 30. Table 29 contains data for all flaws used in the study, while Table 30 shows results for flaws that were tilted and skewed only. It should be noted that the standard deviation is often referred to as standard uncertainty in literature. A comparison of flaw sizing results showed that the MPA accuracy was similar to LPA, with the average error being in the range of the best performing LPA results. The MPA blind trial length sizing, however, was much worse than those obtained with LPA. The reason for this could not be determined from the AUT data but it is believed to be largely from the algorithm used for length sizing.

Table 29. Summary of LPA and MPA Sizing Accuracy for All Flaws

Trial	Height		Length		Depth	
	Avg. Error	Std. Dev.	Avg. Error	Std. Dev.	Avg. Error	Std. Dev.
Blind LPA V1	-0.90	2.14	-1.52	6.01	-0.82	2.20
Blind LPA V2	-0.60	1.97	2.21	4.70	-0.41	1.85
Blind LPA V3	-0.92	1.61	-2.79	5.82	-2.56	2.48
Blind LPA V4	-1.12	1.37	0.36	5.48	-0.21	1.66
Blind LPA V5	-0.82	1.27	0.78	4.60	-0.15	1.59
Open LPA	0.28	1.27	---	---	-0.01	1.36
Blind MPA	-0.34	1.76	3.90	5.53	-0.33	1.93
Open MPA	0.29	1.15	-0.13	3.77	0.33	1.42

Table 30. Summary of LPA and MPA Sizing Accuracy for Tilted and Skewed Flaws Only

Trial	Height		Length		Depth	
	Avg. Error	Std. Dev.	Avg. Error	Std. Dev.	Avg. Error	Std. Dev.
Blind LPA V1	-1.67	2.58	-3.73	2.42	-2.08	1.55
Blind LPA V2	-1.54	1.06	-0.13	4.49	-2.41	1.60
Blind LPA V3	-1.82	1.97	-5.60	3.97	-6.10	2.95
Blind LPA V4	-2.04	1.15	-2.43	6.45	-1.83	1.42
Blind LPA V5	-1.58	1.26	-2.25	6.85	-1.28	1.53
Open LPA	0.15	0.86	---	---	-0.88	1.16
Blind MPA	-0.84	1.72	2.86	3.44	-0.86	1.52
Open MPA	0.24	1.52	-1.75	3.01	-0.46	2.10

3.5.6 Task Conclusions and Significance

During the course of this task, some conclusions came to light and are summarized below:

- The probe angle beam wedge design used for the MPA open trial setup was not optimal for inspection of the test welds used for this project due to the physical size of the existing probe. The wedge design was driven by the probe dimensions. Angle beam wedges should be designed to allow the root area to be inspected with refracted beam angles of approximately 55 degrees on the first leg of the sound beam.

- It was a challenge to manage the large amount of data available through the different MPA tilt and skew channels. It appears that flaw evaluation and sizing algorithms currently used for conventional and LPA may not be sufficient for MPA. For example, algorithms need to address which channel(s) should be used for determining flaw size.

- Despite the challenge of large amounts of data, POD values and flaw sizing accuracy obtained for MPA were similar to those obtained for LPA. Given that MPA is an emerging technology for girth weld inspection, the overall results were encouraging.

- The process of making controlled flaws in the samples was difficult using changes in welding parameters alone. Samples made by this method resulted in relatively large flaws that were not useful for POD and sizing accuracy studies. It was found that implanted flaws could be controlled more accurately as to length, height, depth, and flaw type. The major disadvantage is that implanted flaws may not be produced by the welding process used during actual pipeline welding.

- There were a few attempts to make short flaws that would generally be shorter in length than those considered rejectable by most ECA acceptance criteria. When flaws became shorter than the ultrasonic beam width, ultrasonic sizing became dependant on both flaw length and flaw height. In order to adequately evaluate flaw height-sizing accuracy as an independent quantity, flaw lengths should be longer than the ultrasonic beam width.

- Fingerprinting proved useful as a means of comparing test results. In particular, the PA raster scans and TOFD scans helped to locate both intentional and unintentional flaws, as well as, providing additional flaw position information for the DT.

- As a result of additional beam angles, it was noted that approximately 45% of root flaws having no tilt or skew were detected best with a refracted beam angle of approximately 56 degrees while the remaining were detected best at a beam angle of approximately 60 degrees.

- TomoCAR measurements of flaw dimensions were in good agreement with measurements obtained from metallographic cross-sections. Of the three samples used for comparison, the largest variation was 0.7 mm. The TomoCAR technology shows good promise as an option for destructive measurements currently used as reference values during AUT qualification/quantification trials.

- During DT it was found that it was easier to keep track of US and DS sides of the weld by leaving the base metal longer on one side of the weld. For this project the US side was longer than the DS side.

- Typically, the ultrasonic beam size ("acoustical footprint") was at least 2 to 3 mm in through-wall height and 5 to 10 mm in width for each AUT technique used. MPA beam widths were in the range of approximately 3 to 5 mm. This resulted in each AUT data point being an average of this acoustical footprint at each data collection step.

- During the salami sectioning, water jet cutting was used to make cuts approximately 3-mm apart. Other options such as EDM, milling, and grinding were considered but water jet cutting was preferred. EDM was not used because of higher cost and the higher possibility of destroying samples due to wire breaks. Since most cross-section locations contained flaws, it was recommended by EWI's EDM source that EDM not be used. Grinding and milling was a good option; however, the cross-sections could not have been preserved, which was an important consideration for this project.

- Some flaws were tilted and/or skewed which influenced uncertainties in AUT results. Based on observations from the data, smaller steps in the DT would not have significantly influenced these results.

- Radiographs of the water jet slices proved to be beneficial as a verification of flaw location, depth, and height.

- In several cases it was necessary to view the weld cross-sections at magnifications up to 100× to determine the full extent of the flaws. Since metallography is used as the reference measurement for "actual" flaw dimensions; the POD and sizing accuracy will only be as accurate as the metallography.

3.6 Inspection of Pipe Wall Damage from OD Pipe Surface (Concept 2)

Concept 2 was a flexible MPA probe for inspection of the parent pipe material from the OD pipe surface. The ultrasonic characteristics of the probe were modeled and optimized during Task 2 of this project and the probe was built for evaluation. The concept was evaluated to determine its performance for detecting conditions such as cracking, corrosion damage, and wall thinning. The flexible probe allows scanning to be conducted in areas of the pipe where dents or other surface irregularities could have an influence on beam propagation (Figure 124). In addition to the MPA steering and focusing capabilities, the probe was also equipped with LVDT to provide surface contour feedback. The data acquisition software would then take the LVDT information and adjust the focal laws to maintain the steering angle and focal point as the OD surface changed. For example, when a conventional probe encounters a dent in the surface of a pipe, the beam angle propagating within the pipe wall will change as the probe orientation changes. With LVDT feedback the software senses that the contour has changed and compensates to maintain the desired inspection angle within the material (Figures 125 and 126).

Figure 124. Example of Flexible 2D MPA Probe in Dent

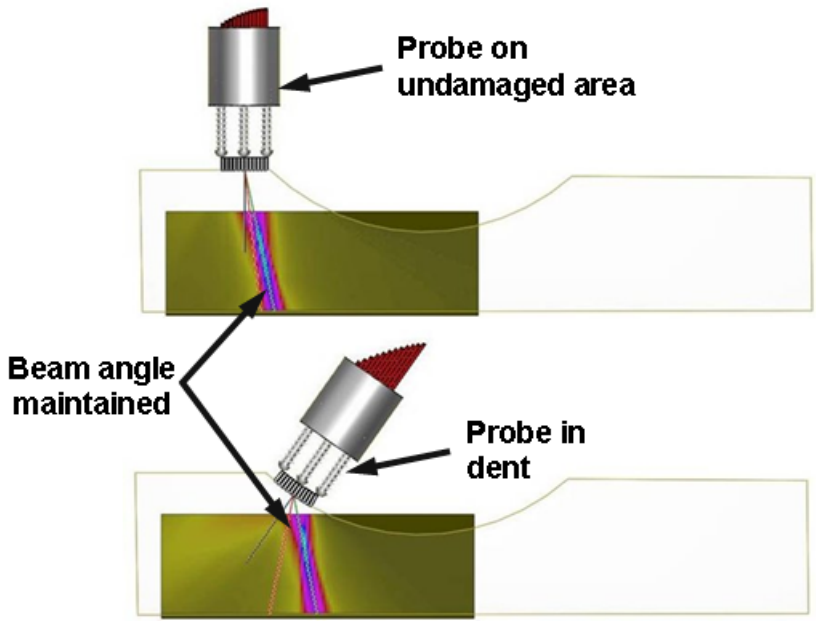

Figure 125. Simulation Example of Beam Compensation for Surface Contour

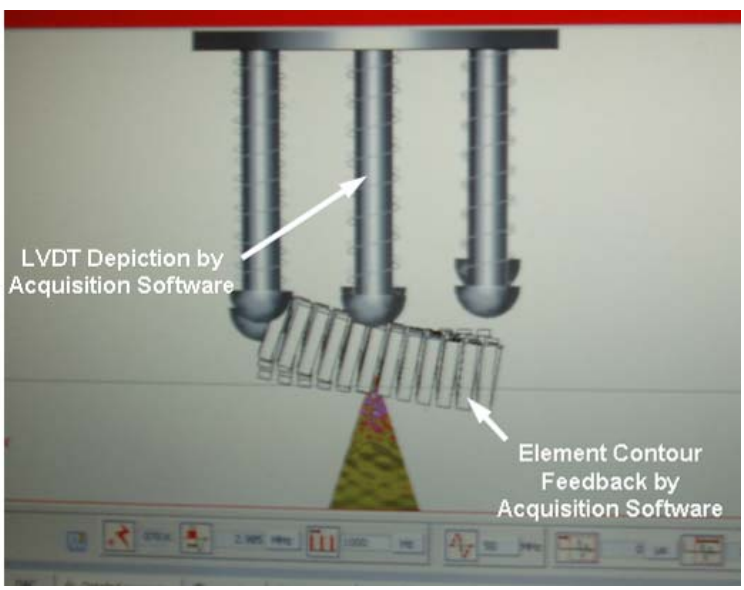

Figure 126. Screen Display of LVDT Surface Contour

During this project the flexible MPA probe shown in Figure 127 was built by Imasonic and used by EWI to acquire data on pipes having dents. Following are the probe parameters:

- Nominal frequency: 2.7 MHz
- Elements: 12 × 5 grid (60 elements total)
- Total active area: 17.4 × 14.4 mm
- Element size:

    - Primary = 0.9 mm
    - Secondary = 2.4 mm
- Pitch:
    - Primary = 1.5 mm
    - Secondary = 3.0 mm
- Inter element spacing:
    - Primary = 0.6 mm
    - Secondary = 0.6 mm
- Profilometer contains 9 points in a 3 × 3 grid of LVDT with spacing between points of 6.5 mm

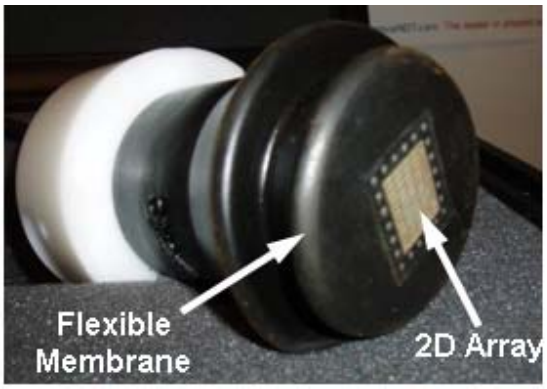

Figure 127. 2D Flexible Array Probe Used for Experimental Trials

The pipe used for the experimental work was 24 in. in diameter with a WT approximately 6.8 mm. A probe carriage was designed and built by EWI to hold the probe perpendicular to the pipe surface. Perpendicularity of the probe was necessary in order to obtain accurate feedback from the LVDT. Figure 128 shows the probe carriage and probe mounted on one of the test pipes. The pipes were made available by Battelle at their West Jefferson, Ohio, pipeline test facility. The pipes contained dented areas having machined notches and also dented areas containing pitting and cracking. The notches were oriented parallel to the longitudinal axis of the pipe and all flaws were on the OD surface of the pipe. It was desirable to test the probe on ID flaws as well; however, none were available at the facility.

A total of six areas were scanned using the flexible MPA probe. Three contained through-wall cracks, two contained notches, and one had no known flaws. Because the pipe wall was relatively thin most of the useful data was obtained on the second full skip using low angle refracted longitudinal beams. This scenario of thin wall, OD flaws, and low-frequency refracted longitudinal waves was a less than desirable inspection technique. The combination of array size (number of elements and size of elements) and probe frequency did not work well with the pipe WT that was available for the evaluations. Figure 129 shows some of the best data

obtained from notches that were over 50% of the WT. Likewise, Figure 130 shows test results obtained from a location having a through-wall crack.

In order to test the probe on thicker material, scans were conducted on 25-mm-thick plate having notches on the back surface. Figure 131 shows results obtained from these scans. As the scans show, the probe appears to work well for inspection of thicker material with flaws located on the back surface.

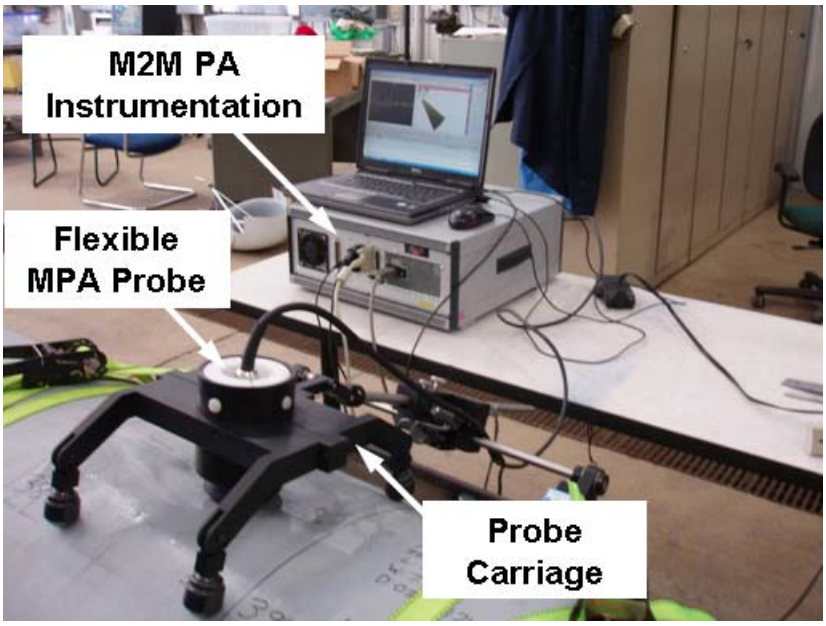

Figure 128. Flexible MPA Probe Scanning Carriage and Instrumentation

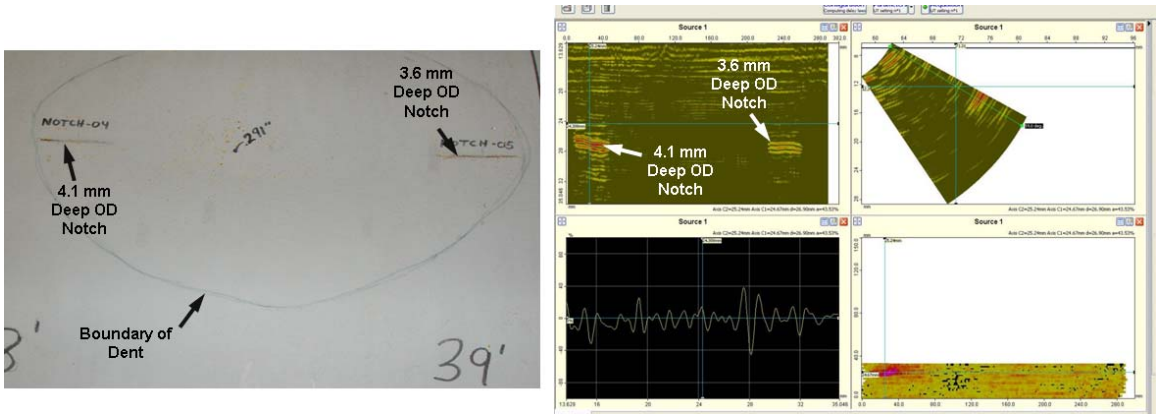

Figure 129. Flexible MPA Scan of OD Notches in Dent Location

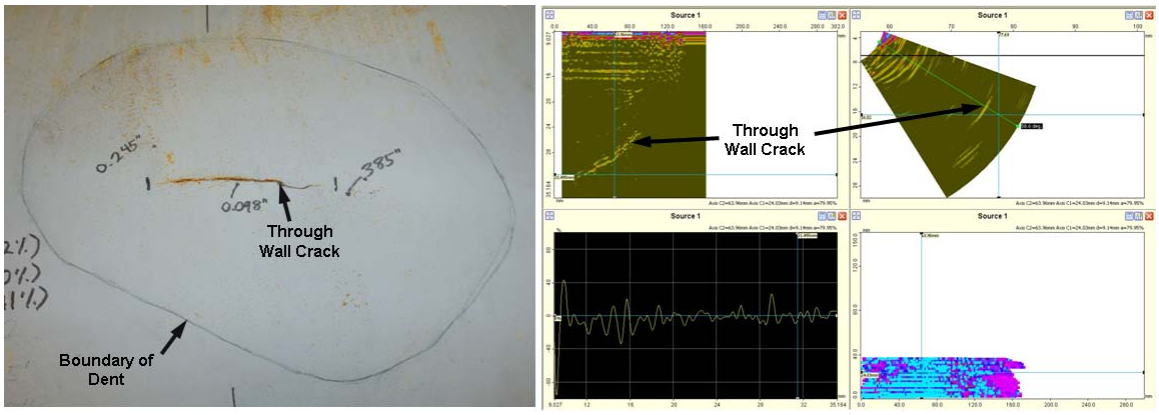

Figure 130. Flexible MPA Scan of Through-Wall Crack in Dent Location

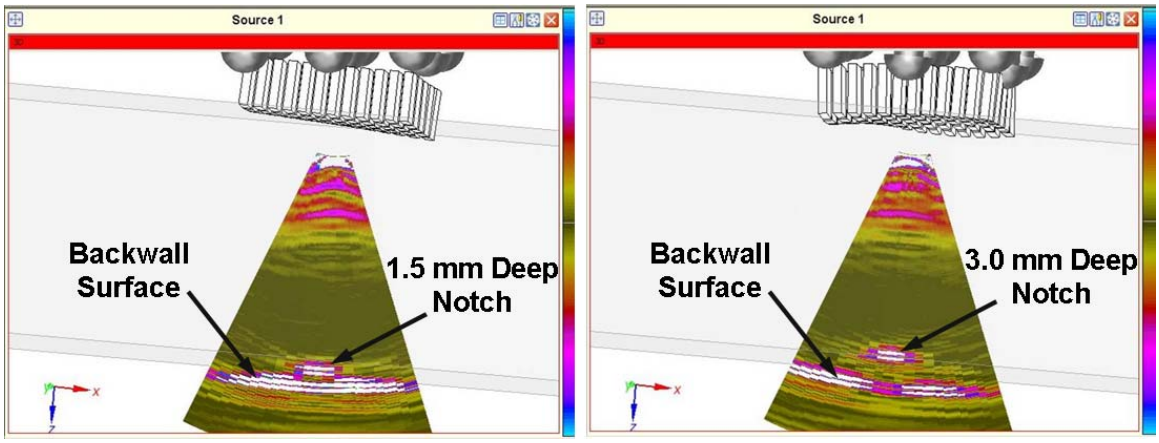

Figure 131. Scan of Notches in 25-mm-Thick Sample

3.6.1 Task Observations and Conclusions

The flexible MPA probe used on this project provided good results on material approximately 25 mm in thickness where longitudinal and refracted longitudinal beams could be used to detect reflectors on the opposite (back) surface. A possible application for the probe would be to detect ID corrosion damage when inspecting from the OD pipe surface.

While the ultrasonic part of the probe functioned well, problems were experienced with the LVDT pistons used for surface contour measurements. In three different instances an LVDT piston stopped functioning resulting in the inability to use the real-time focal law feedback. For field applications, a more robust probe would be required.

3.7 Inspection of Pipe Wall Damage from ID Pipe Surface (Concept 3)

Concept 3 was a rigid MPA probe, designed for inspection of the parent pipe material from the ID pipe surface of fluid-filled pipes. The Concept 3 MPA probe and technique was primarily designed for detection of in-service damage on the OD surface. The ultrasonic characteristics of the probe were modeled and optimized during Task 2 of this project and the probe was built for evaluation. The concept was evaluated to determine its performance for detecting conditions such as cracking, corrosion damage, and wall thinning. Figure 132 shows the ID MPA probe designed and built for use on this project. The probe was a 5-MHz, 128-element probe having 32 elements in the primary probe axis and 4 elements in the secondary axis. Additional information regarding the probe design can be found in the virtual optimization section of this report.

Figure 132. ID MPA Probe

For evaluation of the probe, two reference samples were designed and fabricated from 6-in. (152-mm)-diameter Schedule 40 pipe having a WT of approximately 6.3 mm. The first sample contained FBH and round bottom holes, of different diameters and depths, machined on the OD surface of the pipe (Figure 133). This sample was used to simulate volumetric flaws propagating from the OD surface of the pipe. Round bottom holes were used to emulate rounded corrosion pits, while FBH were used to emulate conditions such as laminations or hydrogen-induced cracking (HIC); also known as step-wise cracking. The second sample contained EDM notches of different depths, lengths, and orientations also machined on the OD surface of the pipe (Figure 134). The width of all notches was 0.25 mm. This sample was used to emulate surface-breaking planar flaws on the OD surface such as radial cracking. The notch sample also contained a branching flaw that was fabricated using EDM (Figure 134). Figure 135 shows images of the two reference samples after machining.

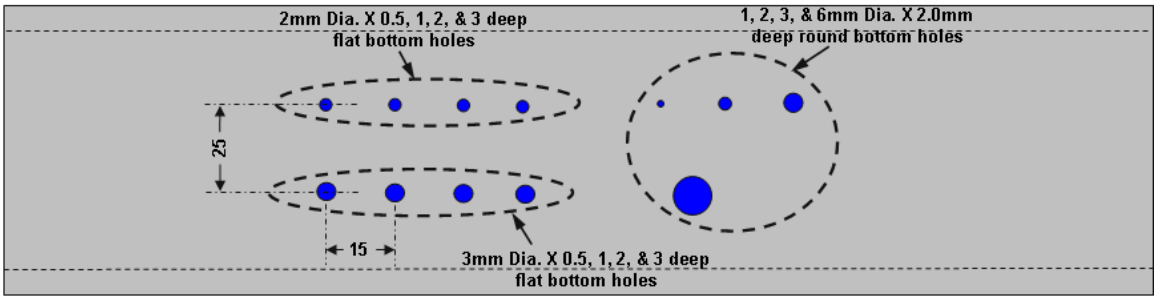

Figure 133. Sketch of Hole Sample

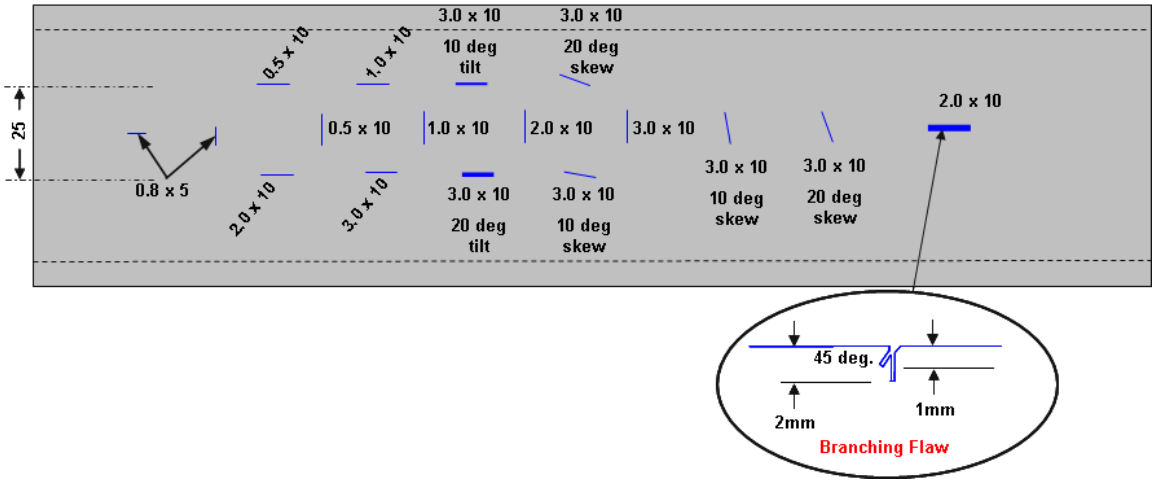

Figure 134. Sketch of Notch Sample

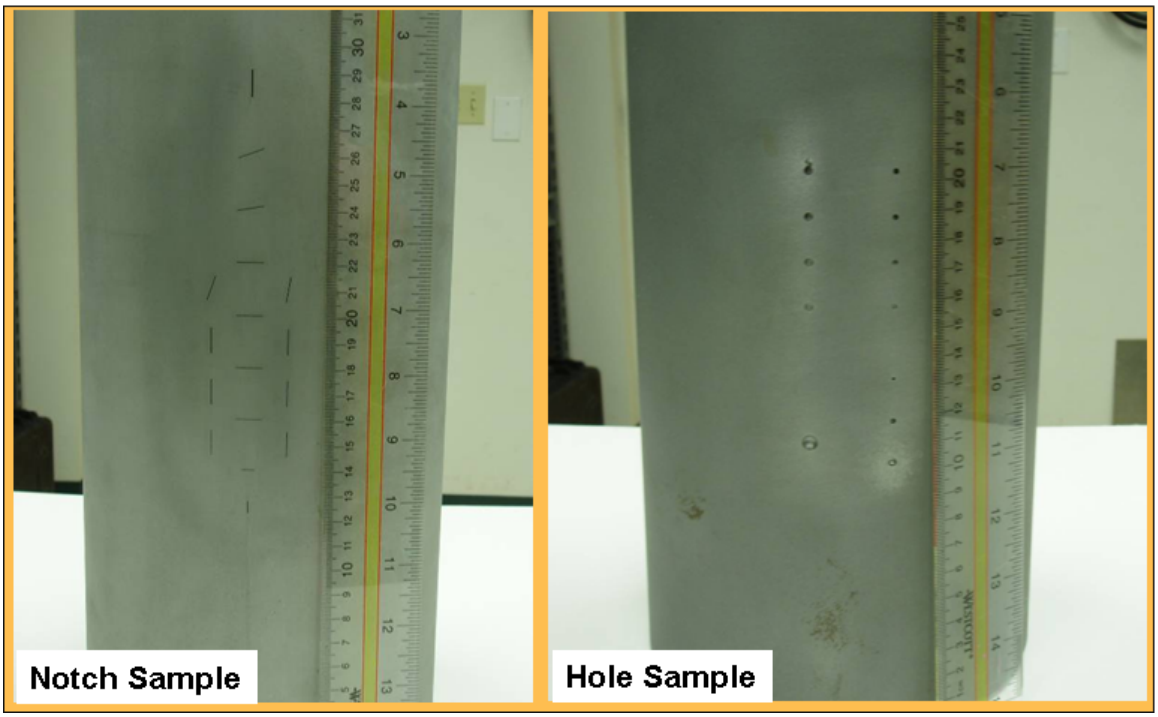

Figure 135. Machined Reference Samples

Initial scans were conducted on the two samples by immersing them in water and scanning the probe along the inside as shown in Figure 136. These scans, in combination with the virtual probe optimization process discussed previously, were used to establish setup files and scanning parameters for evaluating the detection and sizing of the machined reflectors. The immersion scans also provided good experimental scan data for comparison to the modeling and simulation results.

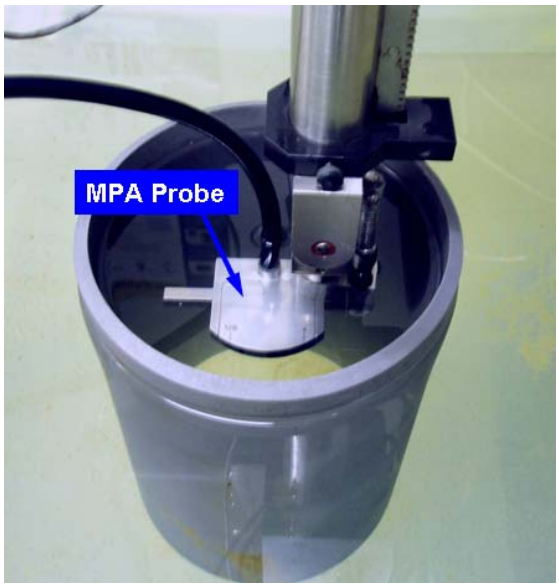

Figure 136. Initial Evaluation Setup for ID MPA Probe

During the experimental evaluations it was found that a 6×4 element aperture with a 5-mm electronic focal depth offered a good compromise between signal noise, inspection coverage, and beam focusing and steering capabilities. Scans were conducted using electronic focal depths of 5 and 10 mm and aperture sizes from 4×4 to 12×4 elements. The machined hole sample was beneficial in comparing various setups because a simple 0-degree longitudinal wave could be used rather than a more complex angle beam needed for detection of the notches. Figures 137 through 140 show comparisons of results from a 2-mm-diameter FBH that was 2-mm deep from the OD surface using different aperture sizes and focal depths. By comparing the images, it can be seen that the reflections from the holes elongate in the secondary probe axis as the number of primary elements is increased. This was caused by the decrease in beam size in the primary probe axis as the number of elements was increased. These experimental results were in agreement with beam spot sizes predicted by modeling during the virtual optimization task.

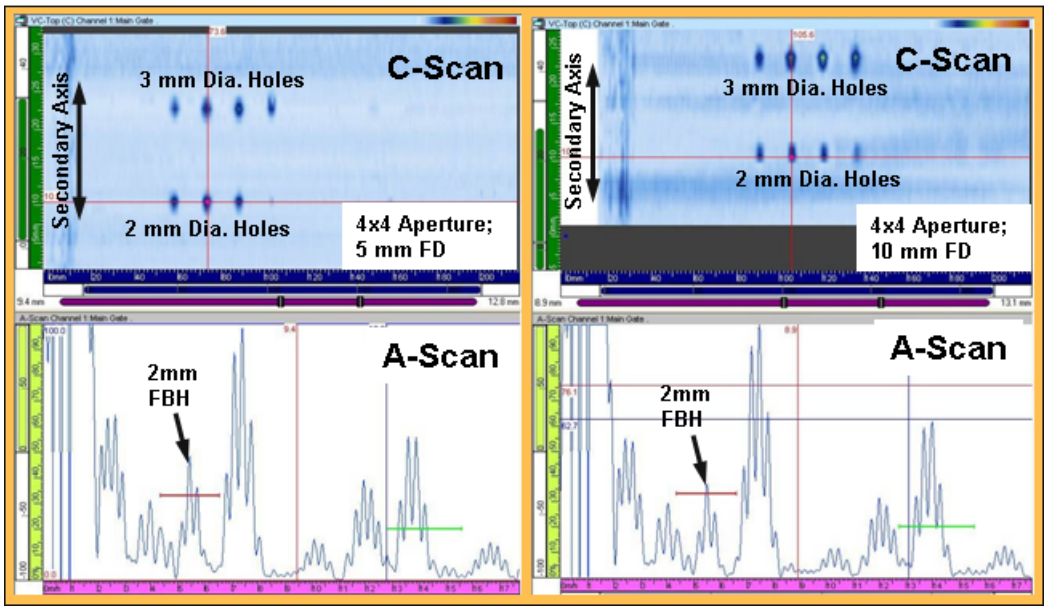

Figure 137. Hole Sample Using 4×4 Element Aperture at Focal Depths of 5 and 10 mm

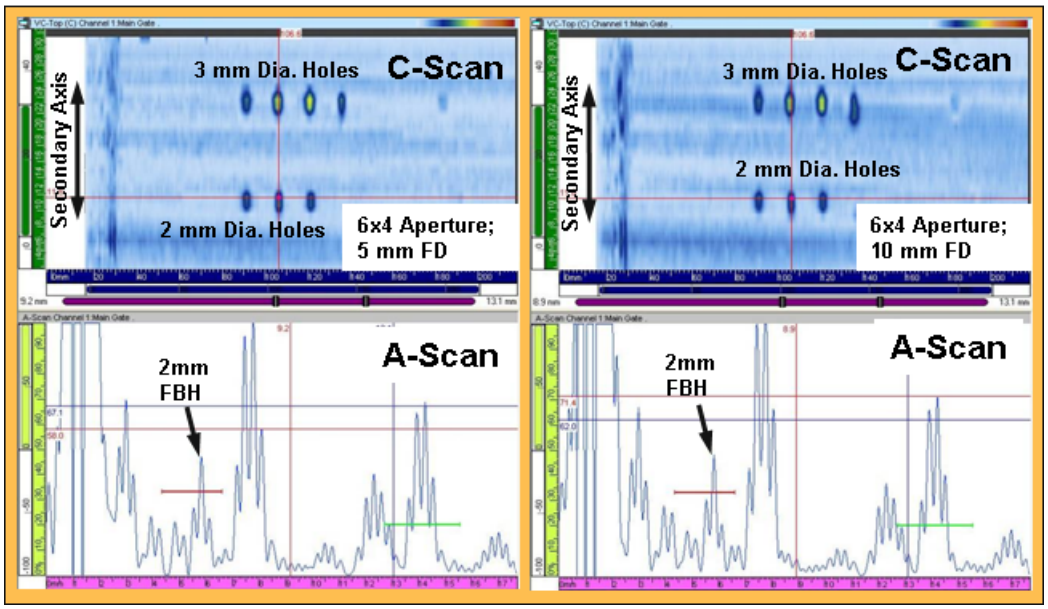

Figure 138. Hole Sample Using 6×4 Element Aperture at Focal Depths of 5 and 10 mm

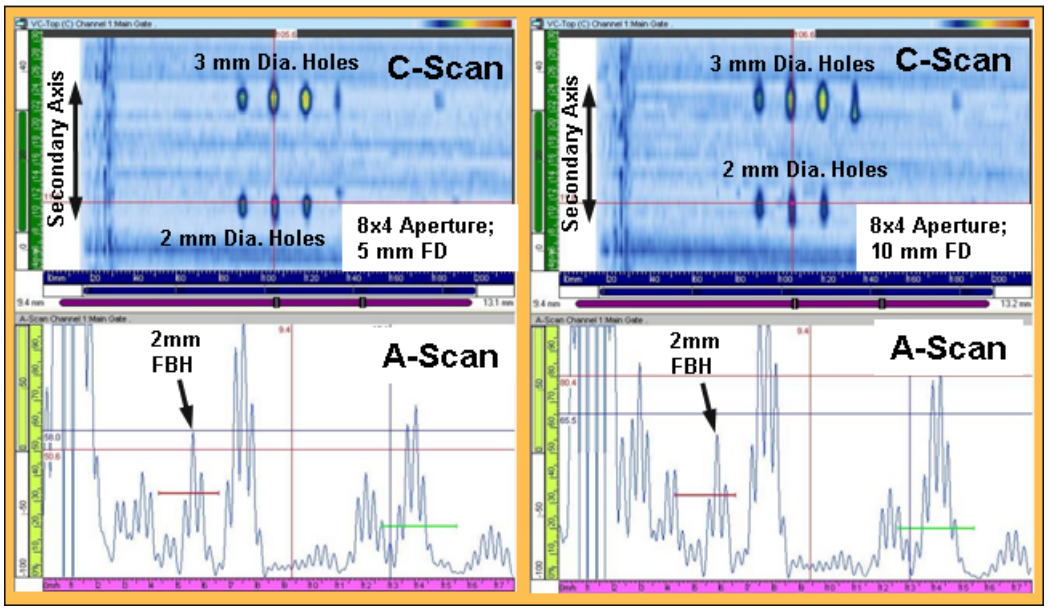

Figure 139. Hole Sample Using 8×4 Element Aperture at Focal Depths of 5 and 10 mm

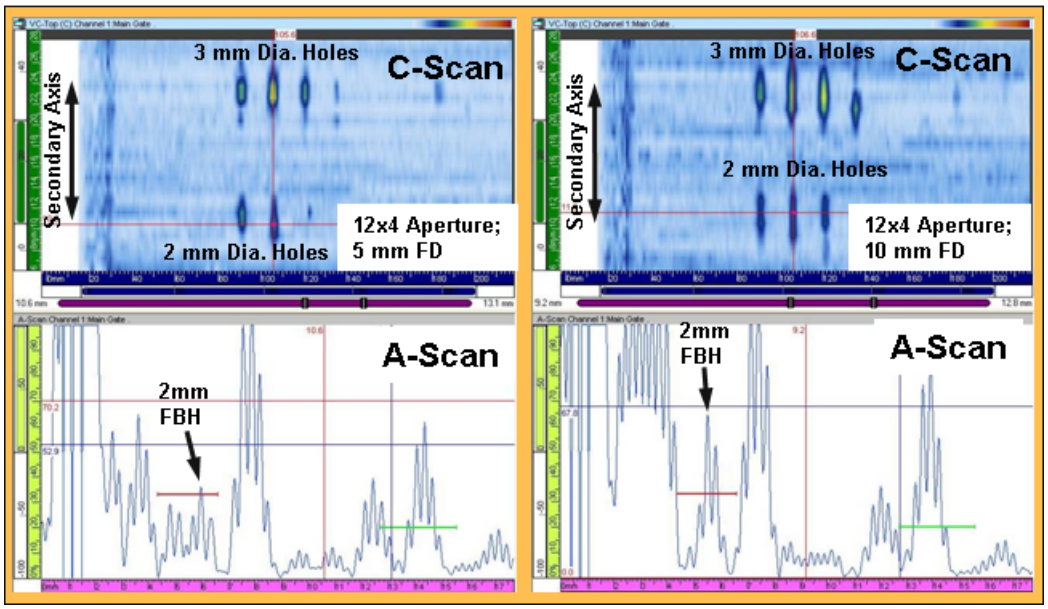

Figure 140. Hole Sample Using 12×4 Element Aperture at FD of 5 and 10 mm

Scans performed on the machined hole sample showed a fairly high noise level between the front surface signal and the first back reflection as shown in Figure 141. But, it was noted that the FBH produced a good reflection that could be detected between the multiple back reflections. The reflections were good enough to provide accurate depth measurements of the

smallest FBH which was 2 mm in diameter at a depth of 0.5 mm from the OD surface. This level of detection and resolution agreed well with the modeling results as shown in Figure 142.

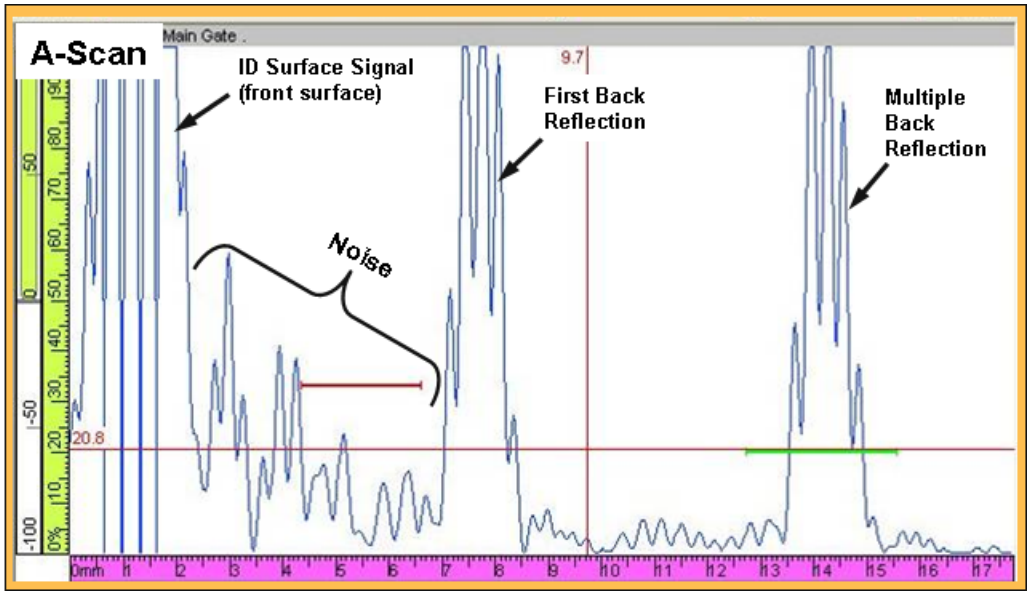

Figure 141. Noise Level Between Front Surface and First Back Wall Reflection

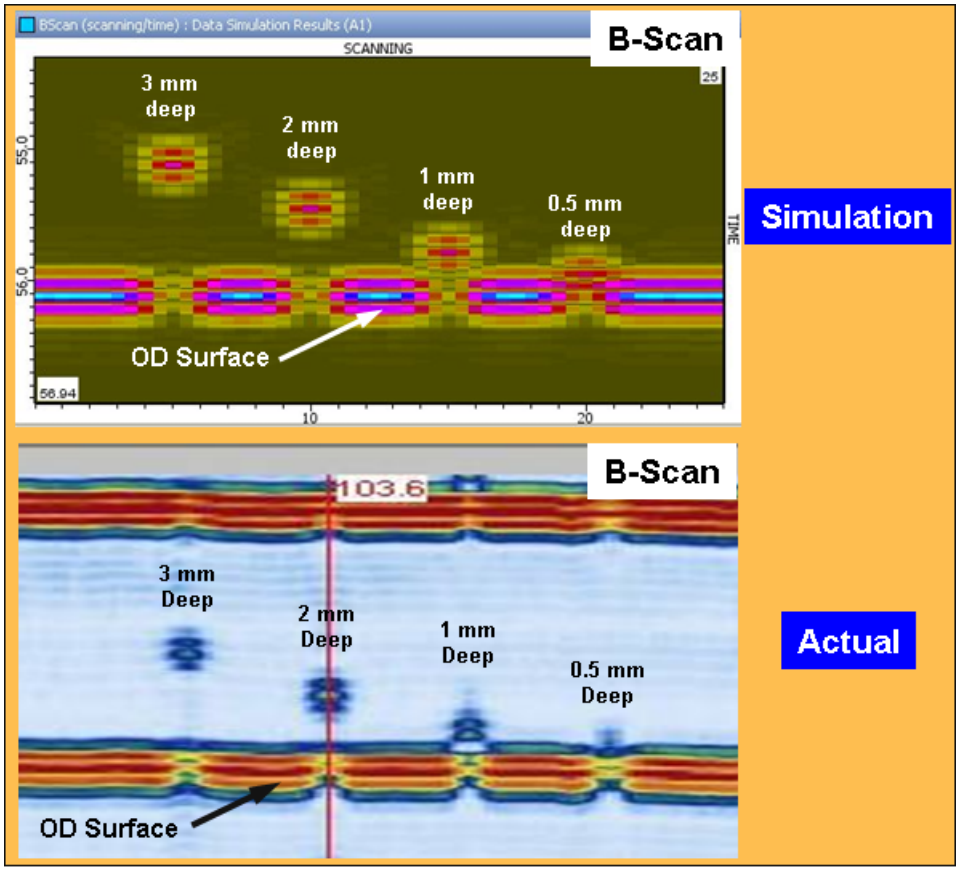

Figure 142. Comparison of Modeling Simulation and Actual Results of 2-mm FBH Using 6×4 Element Aperture and 5-mm FD

Reflections from the round bottom holes were very weak in comparison to the FBH. This was primarily caused by the relatively small reflecting surface of the round bottom. Because of this condition, it was noted that there was only slight changes in reflected signal amplitude between round bottom holes of different diameters. For example, only a 0.5 dB difference in signal amplitude was seen between a 3- and 2-mm-diameter round bottom hole. By comparison, the 3-mm-diameter FBH consistently had higher reflected amplitudes than the 2-mm-diameter FBH by approximately 3 to 4 dB. This comparison confirms the well known fact that flaw geometry has a significant affect on signal amplitude, and therefore signal amplitude is not necessarily a good measure of flaw size.

When reviewing scan data for the round bottom holes it was noted that the holes could be detected by simply monitoring the amplitude of the back surface multiples. The 2-mm-diameter round bottom hole produced approximately an 8 dB loss in the back reflection amplitude, while the 3-mm-diameter hole produce a 12 dB loss. Multiple back reflections were used because of the high noise level between the front surface and first back surface reflections as seen in Figure 143.

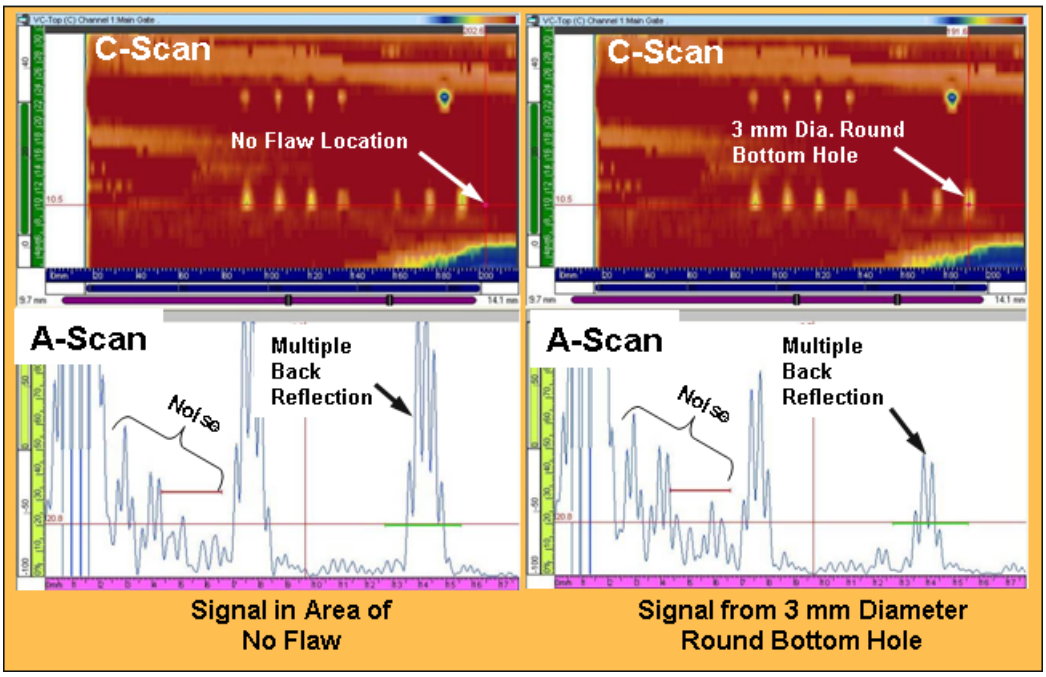

Figure 143. Detection of Round Bottom Holes Using Loss of Back Surface Signal

Scans were also performed on the notched sample. It was found that a 6×4 aperture with a 5-mm focal depth also worked well for detection of the notches . Based on previous inspection simulations, it was determined that the maximum refracted longitudinal beam angle in the primary probe axis was approximately 22 degrees and about 12 degrees in the secondary axis.

These beam angles were used for scanning the notch sample. Results showed that all EDM notches in the sample were detectable. These included the smallest notches which were 0.5 mm in through-wall height and those that were tilted and skewed up to 20 degrees from the circumferential and axial pipe axis. Additionally, the branching flaw was also detected very well. Angle beam scan images from the notch sample are shown in Figure 144.

A 0-degree longitudinal scan was also performed on the EDM notch sample and is shown in Figure 145. Because of the small focal spot size of approximately 1.0 mm, the EDM notches were detected fairly well with this technique even though they were only 0.25 mm in width. While 0 degrees is not likely to detect tight planar flaws, detection of the narrow EDM notches shows the capability of the technique to detect small flaws.

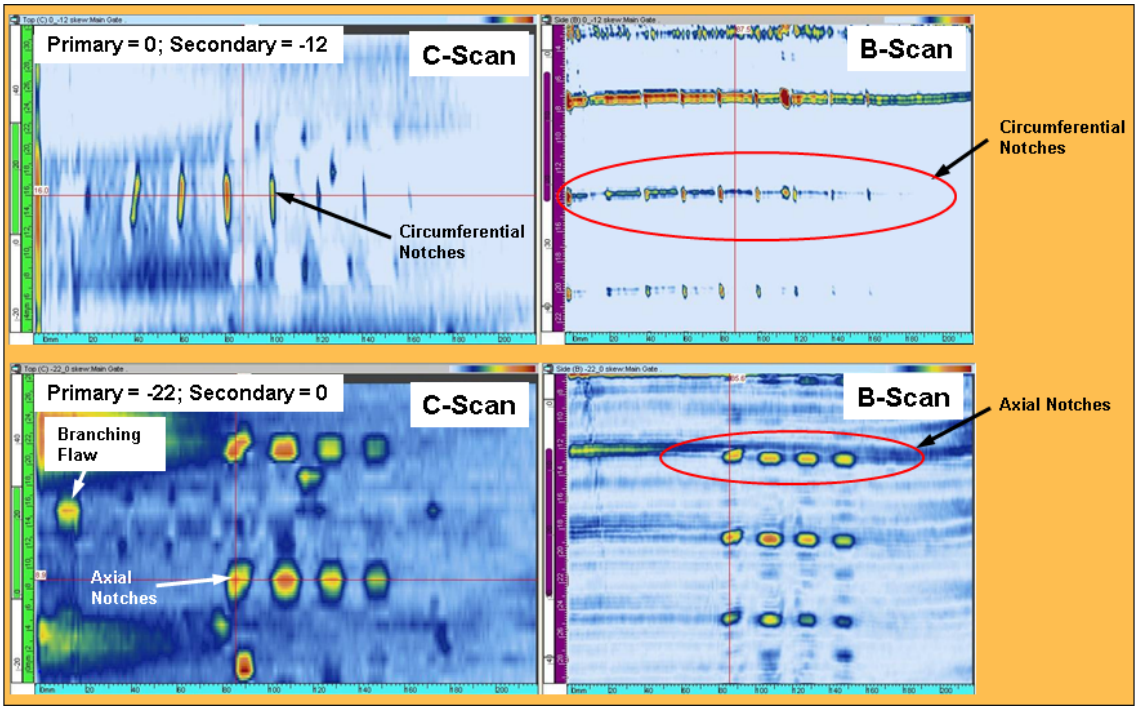

Figure 144. Detection of Axial and Circumferential Notches in Reference Sample

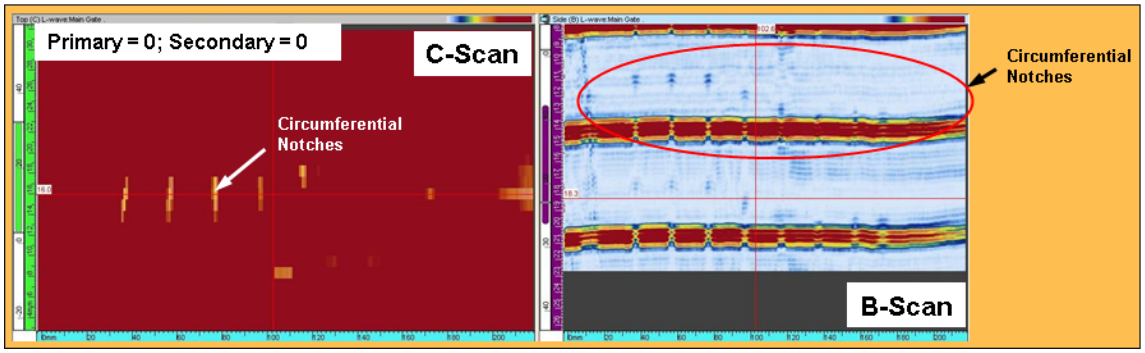

Figure 145. Detection of Circumferential Notches Using 0-Degree L-Wave with a 6×4 Element Aperture

Following initial evaluations, the two reference samples were then welded into a small demonstration pipe loop (Figure 146) that could be filled with water to more closely simulate actual inspection conditions. The probe was designed so that it could be mounted to a probe carrier (Figure 147) that would provide a fixed distance from the ID surface of the pipe while the carrier was pulled through the pipe by a motorized cart. Results from the initial evaluation scans showed that probe alignment was critical for obtaining good scan results. This became more difficult when performing scans in the demonstration loop due to elbows and weld root buildup. For this project the probe and probe carrier was tethered, as shown in Figure 148, to

evaluate feasibility and performance without the need for sealed electronics packages. During actual deployment, it is envisioned that the probe and electronics could be self contained.

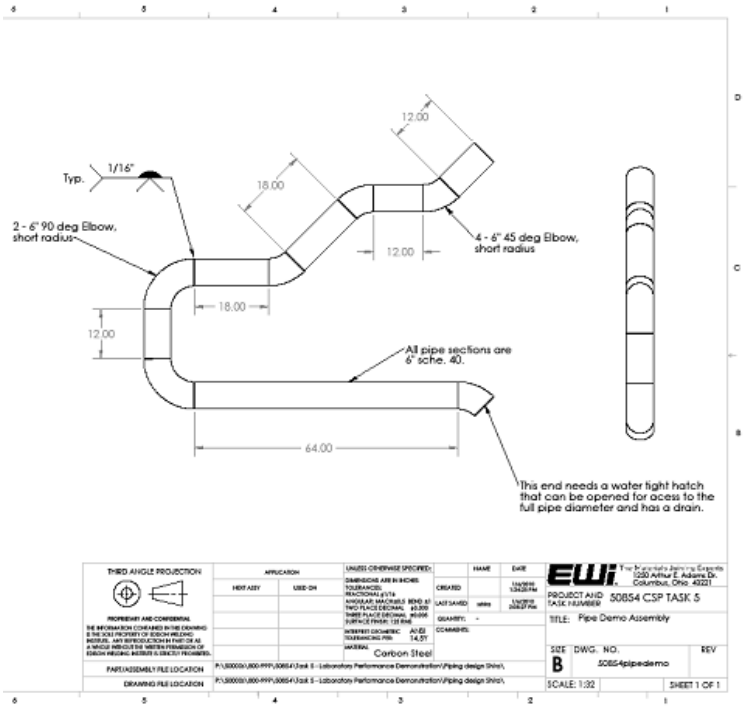

Figure 146. Original Pipe Demonstration Loop

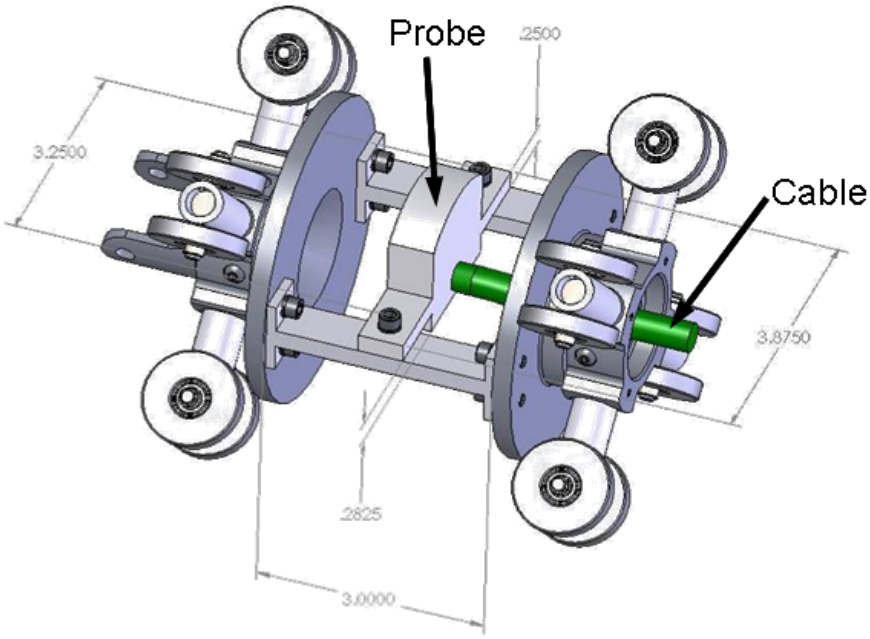

Figure 147. Original Probe Carrier

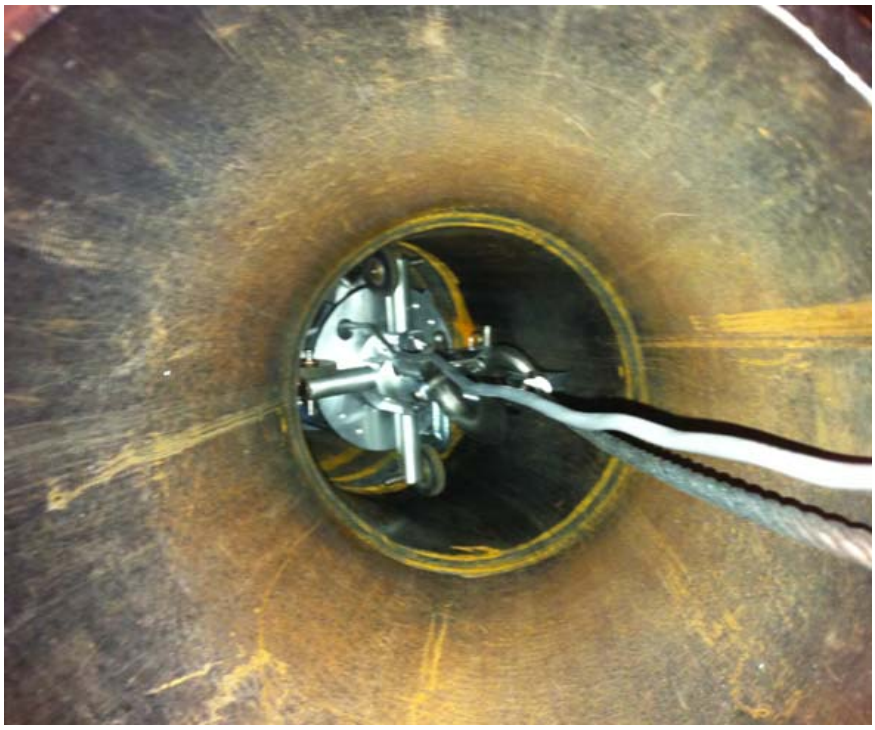

Figure 148. Tethered Probe Carrier in 6-in.-Diameter Pipe

During the project, the supplier of the probe carrier and motorized cart, who was a project contributor, was unable to fully participate in the project. The supplier was able to provide the probe carrier, but the motorized cart was unavailable for use on the project. As a result, two workaround strategies were used. The first involved a manual scan, where the probe carrier was attached to a semi-rigid tube to push and pull the carrier through the pipe. The second strategy was to motorize the probe carrier itself (Figure 149) in an attempt to provide a more consistent scan rate with less misalignment of the probe. Each of these strategies had drawbacks. When using the semi-rigid tube approach, it was found that the push/pull force could not be maintained through the centerline of the carrier. This resulted in side loads that caused misalignment of the probe as it traveled through the demonstration loop. Although the push/pull approach caused some probe misalignment it was possible to gather some limited scan data. When the probe carrier was modified to be driven by a motor, the magnetic drive wheel would often slip as the carrier passed through elbows or traversed across root weld beads causing the carrier to become immobile. Data acquisition was not attempted with the motorized carrier approach because of the potential for damage to the probe.

In order to improve the chances for acquiring scan data using the demonstration pipe, the original pipe loop shown in Figure 146 was modified to produce just a straight run containing five girth welds with no elbows. Additionally, a bore scanner was adapted to the pipe which allowed a uniform mechanized scan to be performed. The modified demonstration pipe with bore scanner attached is shown in Figure 150.

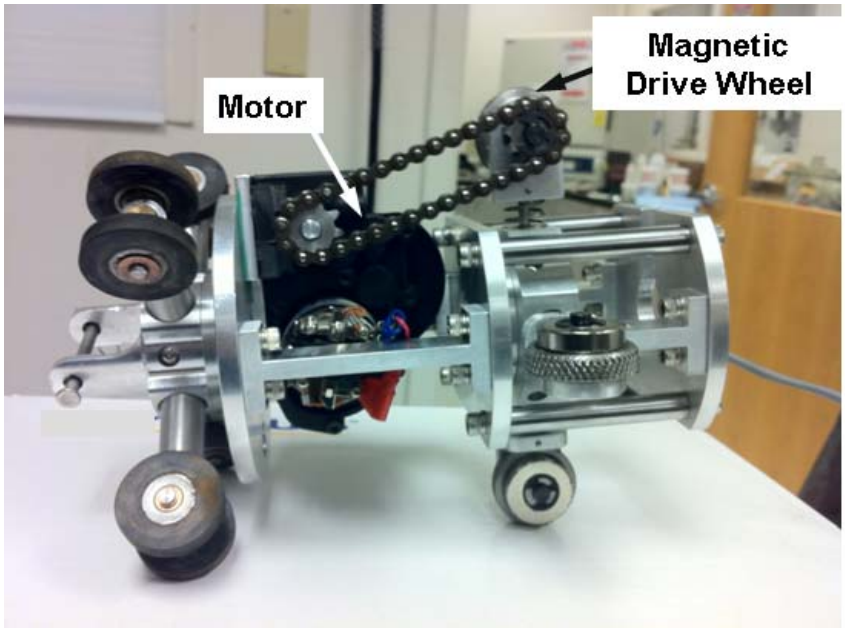

Figure 149. Modified Probe Carrier with Motor

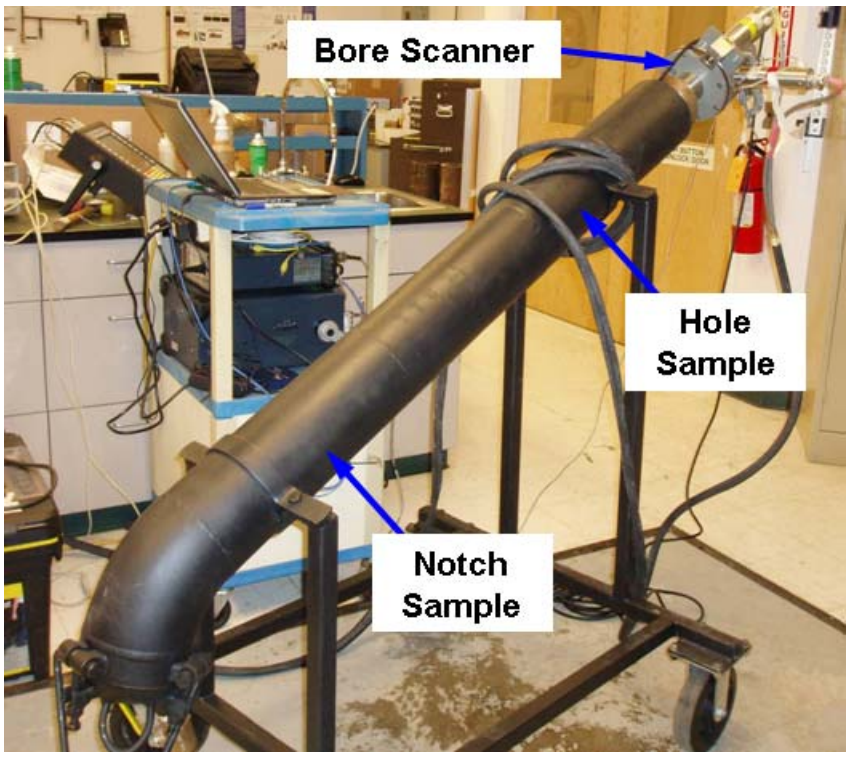

Figure 150. Modified Demonstration Pipe with Bore Scanner

Scan data collected on the straight demonstration pipe showed that the holes and notches could be detected but probe misalignment combined with minor deviations in pipe ovality resulted in some signal fluctuations. Figures 151 through 153 show scan results obtained after modifications to the demonstration pipe. As can be seen most notches and holes were detected quite well. Figure 153 shows that 0-degree L-wave may also be a possible technique for detection of some planar flaws. Data from two opposing circumferential scans, two opposing axial scans, and a 0-degree longitudinal scan was all collected in a single line scan down the pipe. This was made possible by the electronic scanning and steering capabilities of the 2D MPA probe.

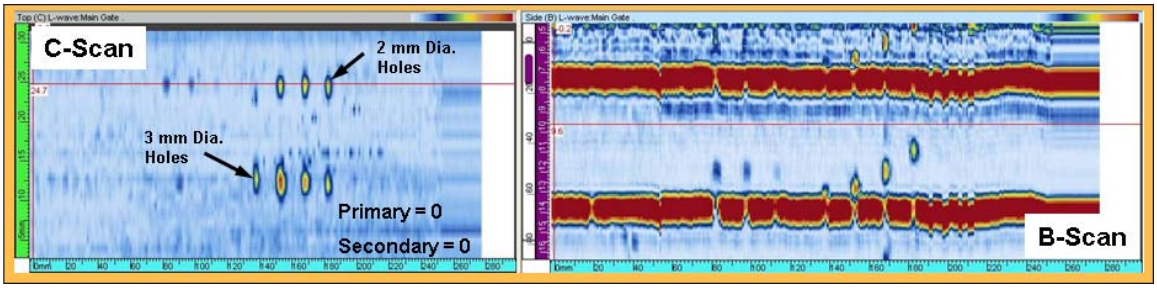

Figure 151. 0-Degree Longitudinal Scan of Hole Sample in Demonstration Pipe

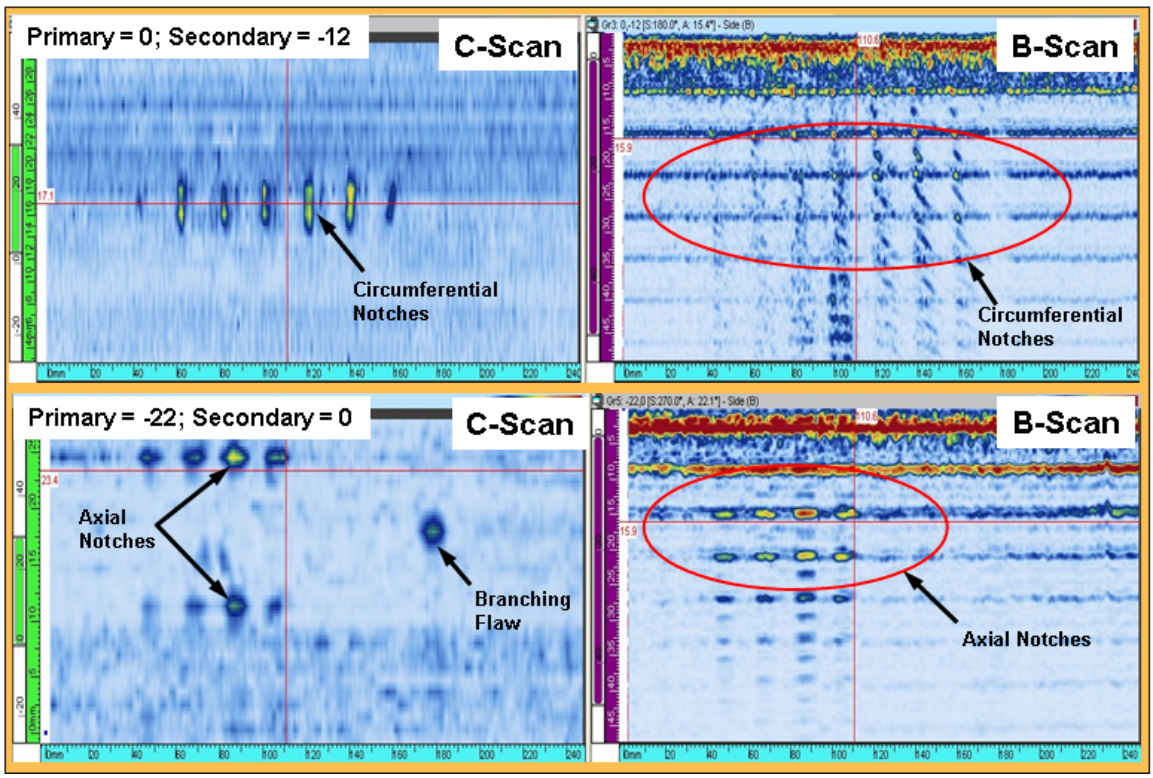

Figure 152. Scan of Notch Sample in Demonstration Pipe Showing Circumferential and Axial Notches

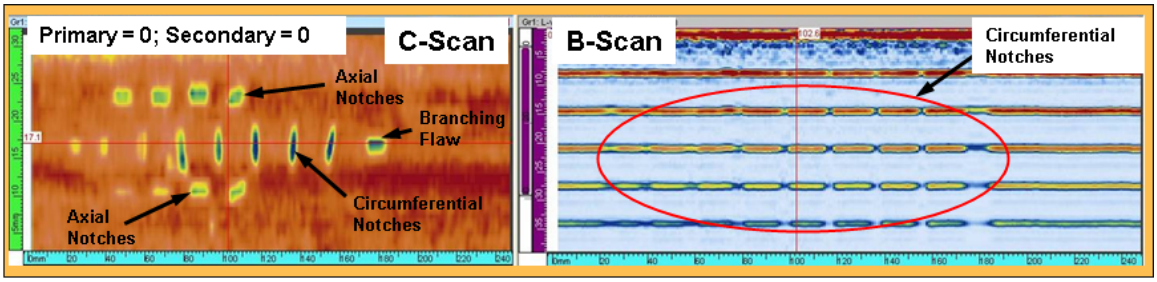

Figure 153. 0-Degree Longitudinal Scan of Notch Sample in Demonstration Pipe Showing Circumferential and Axial Notches

3.7.1 Task Observations and Conclusions

The experimental results obtained with the ID MPA probe agreed well with predicted results from the modeling and simulation task used for probe design.

The ultrasonic performance of the probe was good; however, a method for transporting the multiple probe segments through a fluid-filled pipe is needed. For optimal performance, the transporting mechanism would need to maintain probe alignment and constant radial distance from the pipe ID surface.

Probe alignment would be less critical at shorter water paths. But, in order to obtain the maximum electronic scan coverage for this project a longer water path of 40 mm was selected. Modeling and simulation conducted during this project showed that shorter water paths would provide good detection. Consequently, for future field deployment of this technology, it is recommended that a shorter water path distance be considered.

A consistently high noise level was observed near the front surface signal. While not ideal, good detection was still obtainable for both the 0-degree and angle beam scans by monitoring flaw reflections occurring after the first back reflection. The source of the noise was not precisely determined, but it appeared to be caused in part by the curvature of the ID surface.

Wall thinning as small as 0.5 mm was detectable and measurable. This was verified through the use of FBH on the OD surface having 2- and 3-mm diameters.

OD flaws that had rounded bottoms were difficult to detect with PE due to scattering of the sound energy. However, rounded flaws did cause a significant reduction in the back wall (OD) signal. The reduction in back reflection should be used as a detection technique for volumetric flaws such as corrosion that is open to the OD surface.

EDM notches were used to simulate surface breaking cracks on the OD surface. Detection of notches oriented in both the axial and circumferential direction was achieved for notches having

through-wall heights of approximately 0.5 mm in height. Beam steering in the circumferential and axial directions provided refracted longitudinal wave beams angles of approximately 22 degrees in the primary and 12 degrees in the secondary probe axis. Detection was also demonstrated when notches were tilted and skewed by as much as 20 degrees from the axial and circumferential planes.

The 0-degree longitudinal wave scan was able to detect holes and notches quite well. Because of the small focal spot size of approximately 1.0 mm, the EDM notches were detected fairly well with this technique even though they were only 0.25 mm in width. While 0 degree is not likely to detect tight planar flaws, detection of the narrow EDM notches shows the capability of the technique to detect small flaws.

The refracted longitudinal wave scans were able to detect the tips of the circumferentially oriented notches, but not from the axially oriented notches. Consequently, it may not be possible to accurately measure through wall height of axially oriented planar flaws with the refracted longitudinal wave technique described.

An EDM branching flaw was easily detectable with angle beam steering. The multiple branches provided good reflection of the sound energy that aided in detection. The UT technique could not distinguish between individual flaw branches.

3.8 Stationary 2D Array Monitoring of Pipe Wall from OD Pipe Surface Concept 4

Concept 4 was for stationary health monitoring purposes (see Figure 154). The advantage of using MPA technology is the ability to electronically scan over the entire probe footprint and obtain a stationary C-Scan image in real time. The probe initially used for this performance evaluation was the 5-MHz, 16×8 element probe modeled during the virtual optimization task discussed earlier in this report. While this probe provides a good evaluation of the health monitoring concept, a probe having two to three times the number of elements would be preferred because of the larger footprint. For comparison purposes, data was also collected using an 11×11 element, 15-MHz MPA probe. Table 31 contains information about the two probes. It should be noted that these probes were existing probes used to evaluate the MPA health monitoring concept, and were not optimal for this application.

Table 31. Probe Parameters

Probe	Frequency (MHz)	Number of Elements		Element Pitch	
		Primary	Secondary	Primary	Secondary
A	5.0	16	8	1.0	1.5
B	15.0	11	11	1.2	1.2

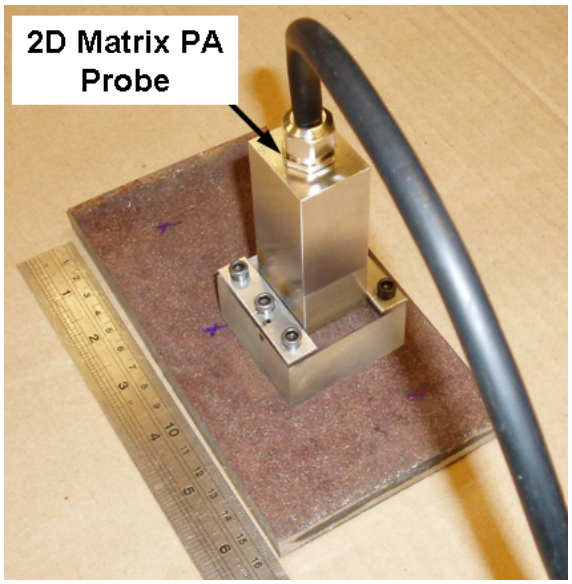

Figure 154. 2D MPA Probe; 5 MHz (16×8 Elements)

During evaluation of the 5-MHz probe, stationary C-Scan data was collected using an electronic scan over the entire probe footprint. Element grouping was 6 in the primary probe axis and 4 in the secondary axis. A 13.2-mm-thick steel demonstration sample was fabricated having a 1.2-mm-deep notch and several grouping combinations of 3.7-mm-diameter holes. The holes were taper bottom holes drilled to different depths and grouped together in groups of 3 or 4 to emulate corrosion pitting. Holes depths were in the approximate range of 7.5 to 8.7 mm with hole spacing in the range of 1.0 to 1.5 mm edge to edge. Figure 155 shows an image of the demonstration sample used.

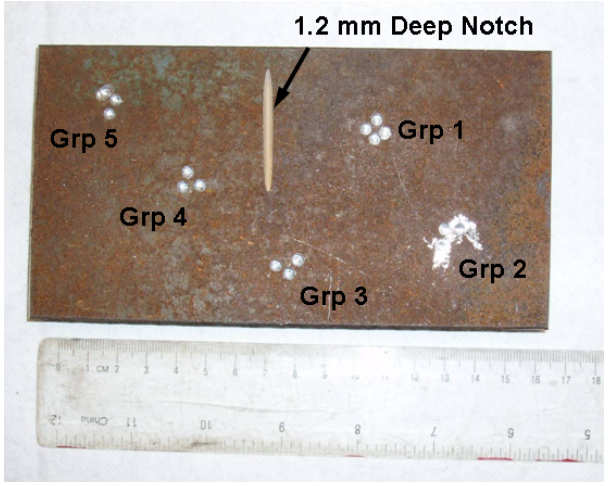

Figure 155. Health Monitoring Demo Sample

Stationary electronic scans were conducted at various positions on the demo sample. Figure 156 is a screen capture with the probe positioned over the 1.2-mm notch shown in Figure 155. The A-Scan shows the BW reflection as well as the signal from the notch. The displayed A-Scan is from the electronic scan position indicated by the intersection of the vertical and horizontal cursors (magenta circle) shown in the C-Scan windows of Figure 156. In the B-Scan window, the notch reflection can be seen along with a reduction in the BW echo. Two amplitude C-Scan windows are shown in Figure 156. The first one, labeled “Amplitude C-Scan of BW”, is the amplitude of the second (multiple) BW reflection. The second, labeled “Amplitude C-Scan” is the amplitude of the reflection from the notch. The two amplitude C-Scans compliment each other because a reflector between the front and back surface should result in a loss of BW signal. The window labeled “Position C-Scan” shows the relative depth of flaws using the color palette as an indicator. Figure 157 is provided for comparison purposes and shows an A-Scan in an unflawed location adjacent to the notch. Again, the displayed A-Scan is from the intersection of the cursors (magenta circle) shown in the C-Scan windows.

It is important to note that the screen captures shown in Figures 156 and 157 were from the same data file. The only difference between the two images is that a different A-Scan is presented by selecting a different location on the stationary C-Scan image. This feature allows measurements to be obtained from all points of the C-Scan.

Stationary electronic scans were also performed on the various hole groups in the demo sample shown in Figure 155. Figure 158 shows a screen capture obtained from Group 1 holes using the 5-MHz probe with a 4×4 element aperture. The four individual holes making up Group 1 were detected but the lateral resolution was not sufficient to resolve each hole separately. The “Amplitude C-Scan of BW” window shows nearly a complete loss of BW, indicated by white in the image. By way of comparison, Figure 159 shows a screen capture of Group 1 holes using the 15-MHz probe with a 3×3 element aperture. The 15-MHz probe was able to provide good

resolution of the holes as is evident by looking at the B-Scan and C-Scan windows of Figure 159. Using the 15-MHz probe, the individual holes in the demo sample were resolved.

Additional stationary electronic scans were performed on hole Group 3 using both MPA probes. Figure 160 shows results for the 5-MHz probe and Figure 161 shows results for the 15-MHz probe. As in the previous case, the 15-MHz probe was able to resolve the three holes while the 5 MHz did not.

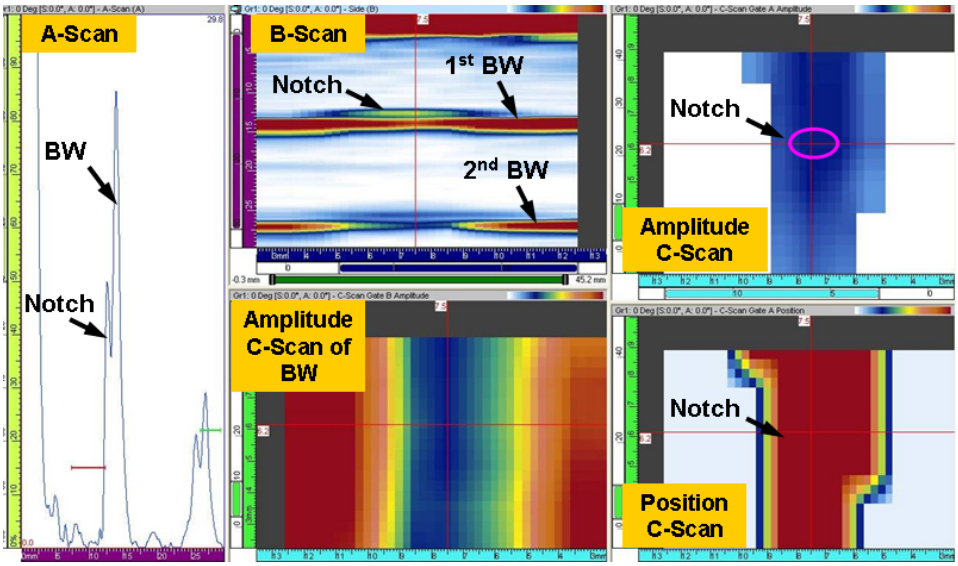

Figure 156. Stationary Electronic Scan Data of 1.2-mm-Deep Notch Using 5-MHz Probe with 6×4 Element Aperture

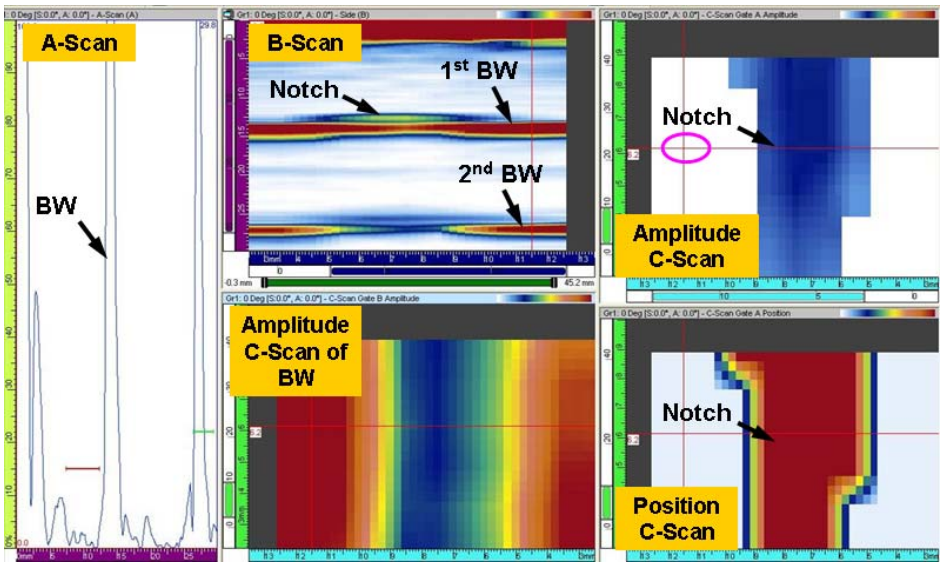

Figure 157. Stationary Electronic Scan Data of Unflawed Base Metal Adjacent to Notch Using 5-MHz Probe with 6×4 Element Aperture

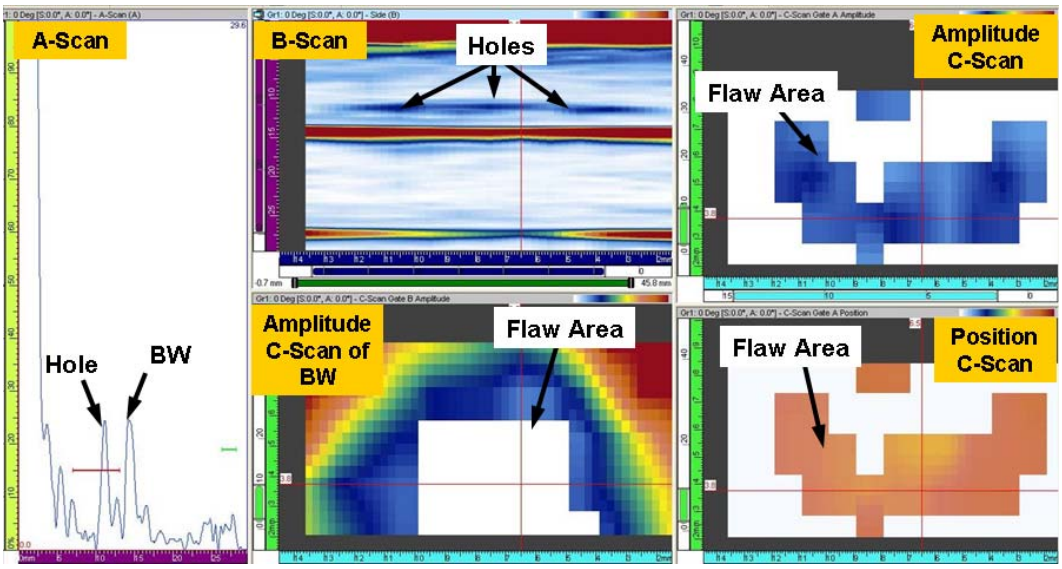

Figure 158. Stationary Electronic Scan Data of Hole Group 1 Using 5-MHz Probe with 4×4 Element Aperture

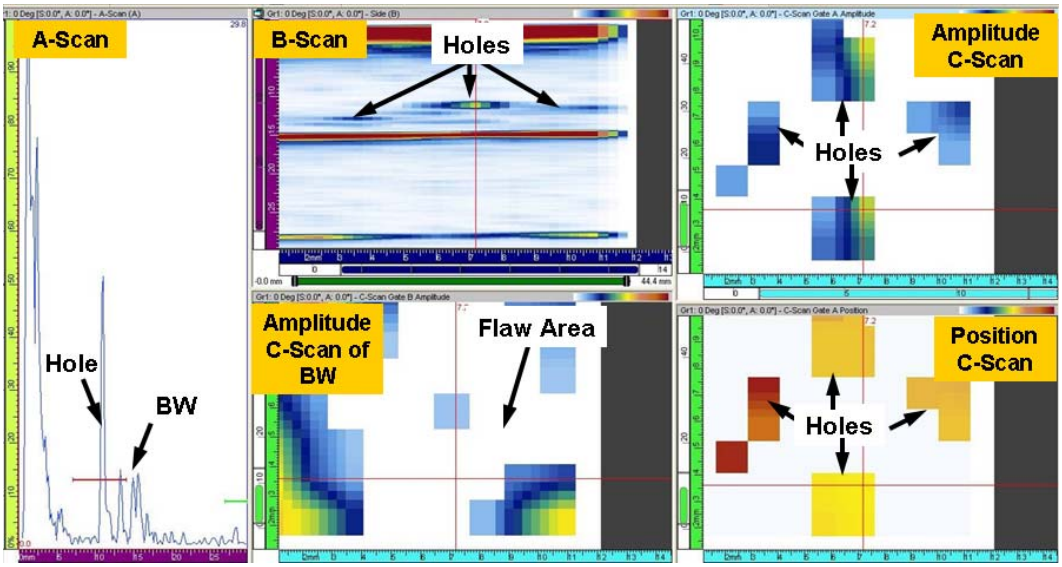

Figure 159. Stationary Electronic Scan Data of Hole Group 1 Using 15-MHz Probe with 3×3 Element Aperture

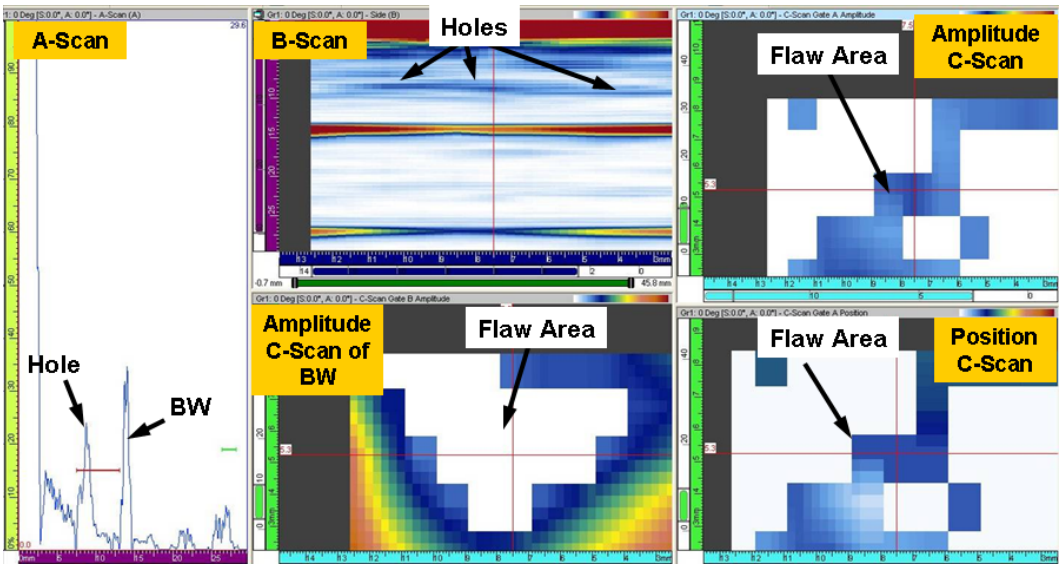

Figure 160. Stationary Electronic Scan Data of Hole Group 3 Using 5-MHz Probe with 4×4 Element Aperture

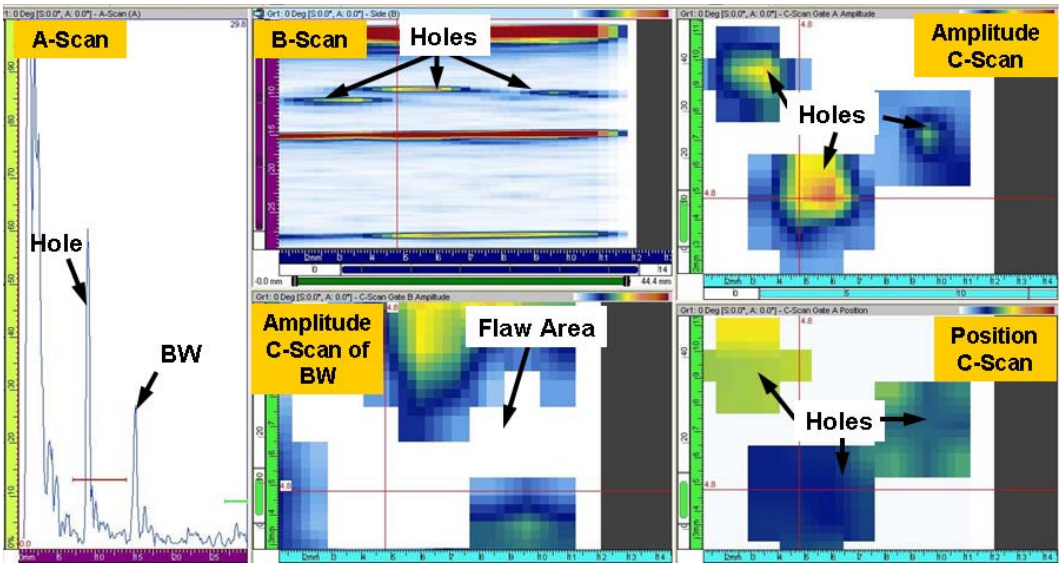

Figure 161. Stationary Electronic Scan Data of Hole Group 3 Using 15-MHz Probe with 3×3 Element Aperture

Evaluations were also conducted with each health monitoring probe on a steel FBH test block having a 2-mm-diameter FBH at a depth of 6.3 mm. Results for the 5-MHz probe are provided in Figures 162 and 163, while results for the 15-MHz probe are shown in Figure 164. Figure 162 shows results obtained using a 4×4 element aperture with the 5-MHz probe. Figure 163 shows results obtained when the aperture was increased to 6×4 elements. Scaling of the C-Scans is different for each screen capture due to the decrease in C-Scan image size as the

aperture is increased. For both aperture selections, the 5-MHz probe oversized the FBH as noted by the measurements in the “Amplitude C-Scan”. By comparison, the 15-MHz probe results shown in Figure 164 still oversized the FBH but were closer to its actual size of 2 mm. The difference is sizing was primarily caused by the slightly larger beam size produced by the 5-MHz probe. Additional images are provided for the 5-MHz probe in Figures 165 through 167. These images show the capability of the probe to detect a 2-mm FBH at greater depths; however, oversizing increased due to the increase in beam spot size. The increase in beam spot size agreed well with modeling predictions for the aperture sizes selected. Selection of a larger aperture would help reduce the beam spot size, but there would be a trade off in the imaging area of the C-Scan window.

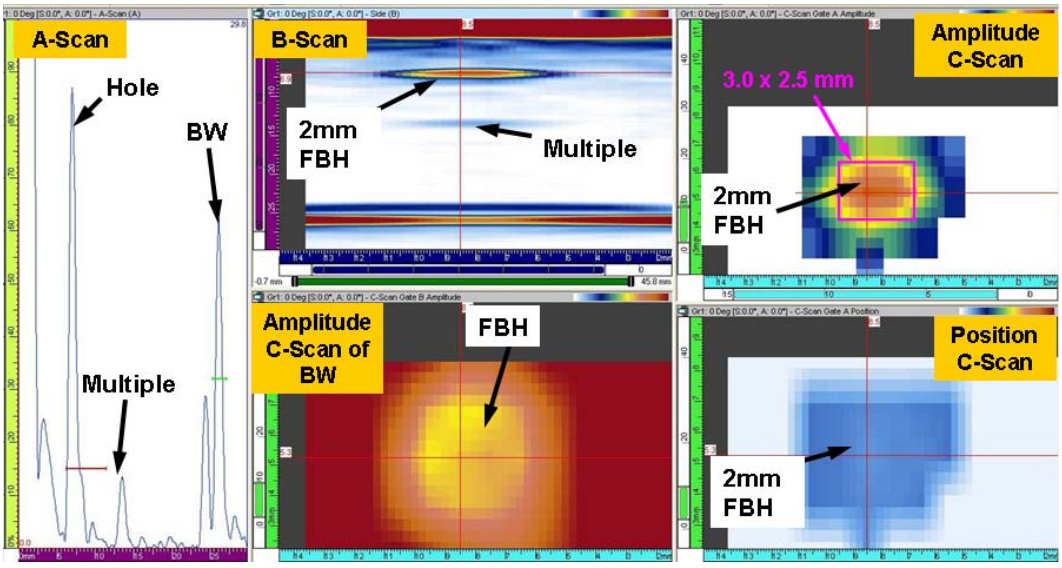

Figure 162. Stationary Electronic Scan Data of 2-mm-Diameter FBH, 6.3-mm Deep Using 5-MHz Probe with 4×4 Element Aperture

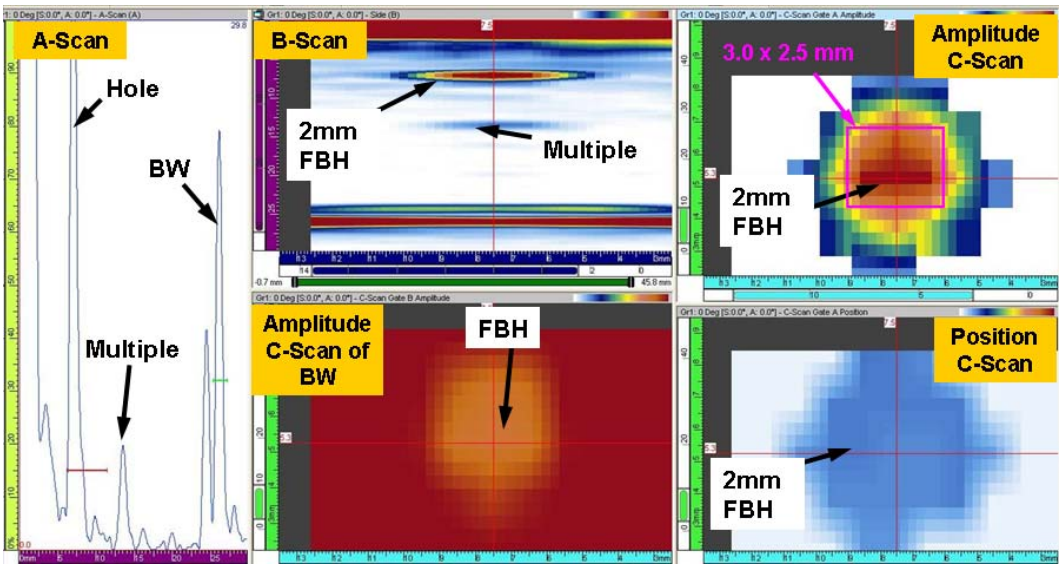

Figure 163. Stationary Electronic Scan Data of 2-mm-Diameter FBH, 6.3-mm Deep Using 5-MHz Probe with 6×4 Element Aperture

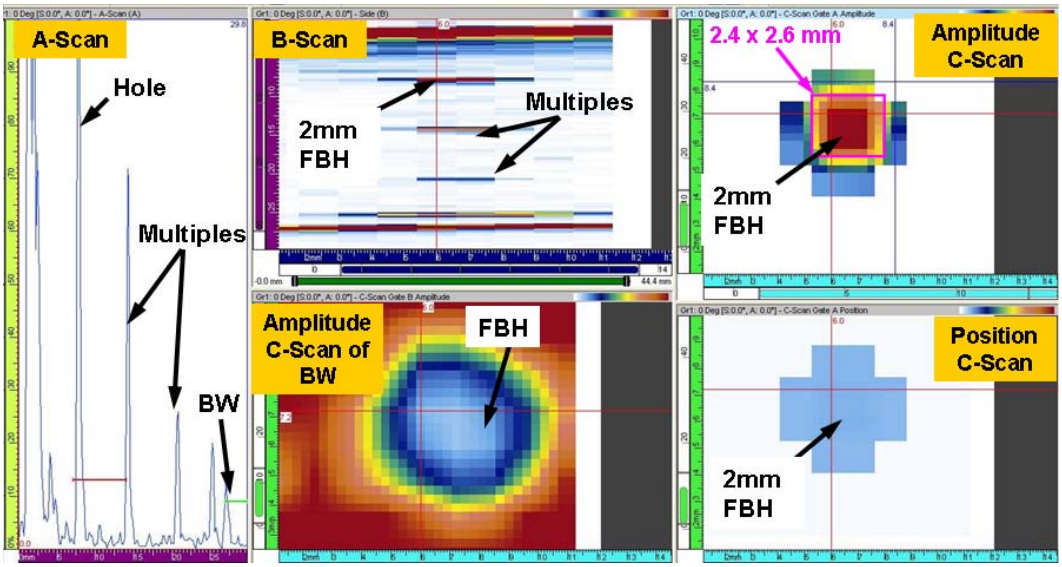

Figure 164. Stationary Electronic Scan Data of 2-mm-Diameter FBH, 6.3-mm Deep Using 15-MHz Probe with 3×3 Element Aperture

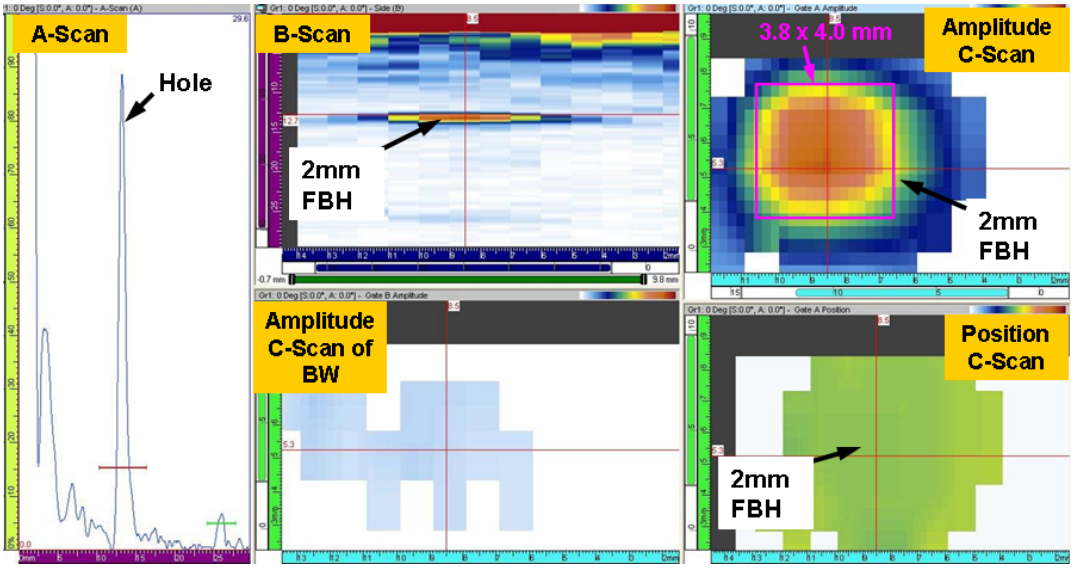

Figure 165. Stationary Electronic Scan Data of 2-mm-Diameter FBH, 12.7-mm Deep Using 5-MHz Probe with 4×4 Element Aperture and 12 mm FD

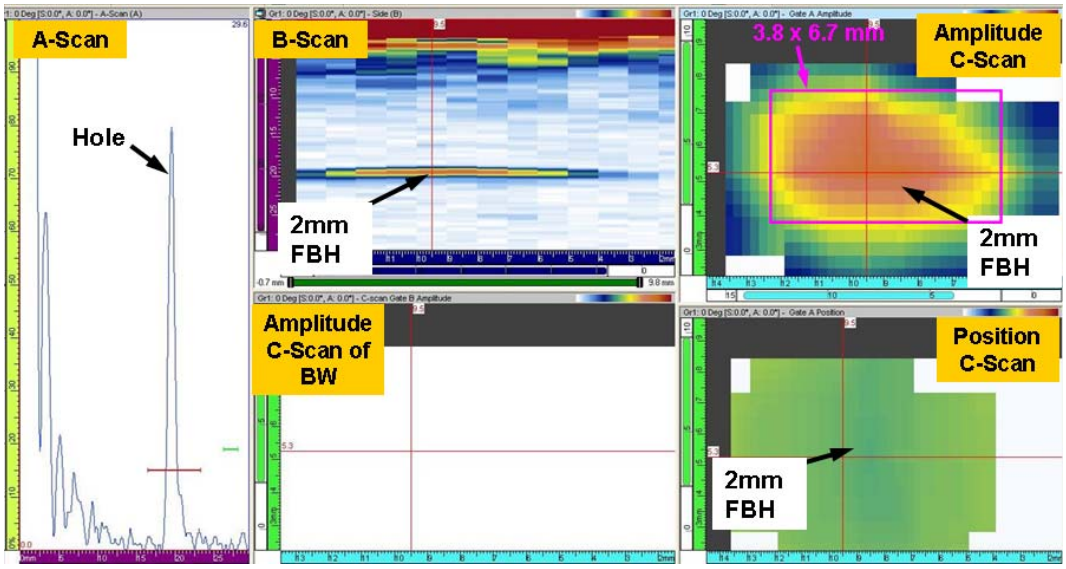

Figure 166. Stationary Electronic Scan Data of 2-mm-Diameter FBH, 19.1-mm Deep Using 5-MHz Probe with 4×4 Element Aperture and 19 mm FD

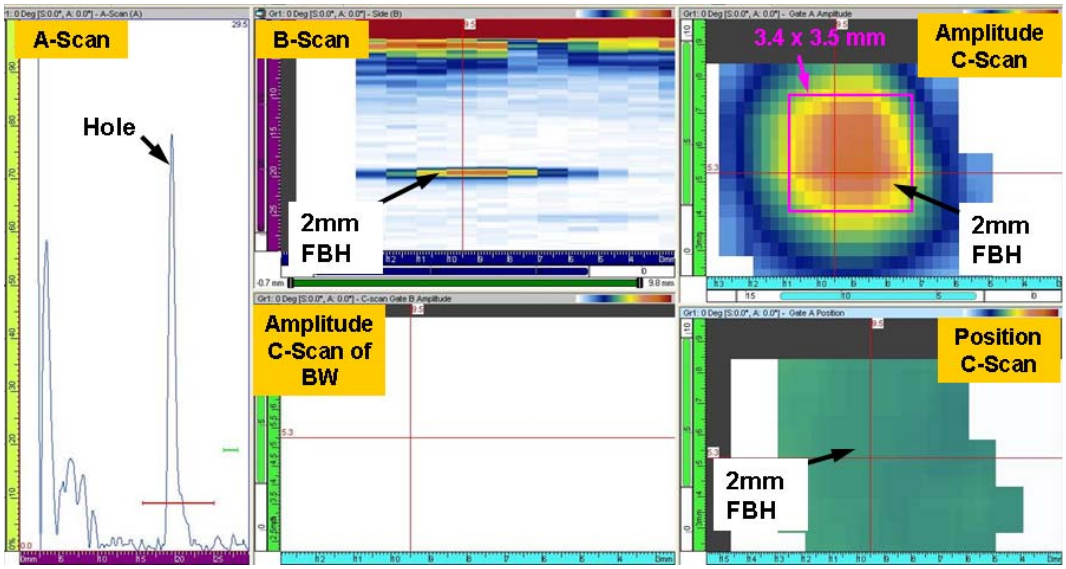

Figure 167. Stationary Electronic Scan Data of 2-mm-Diameter FBH, 19.1-mm Deep Using 5-MHz Probe with 6×4 Element Aperture and 25 mm FD

Additional work was conducted to evaluate the use of the 5-MHz MPA probe for mechanical raster scanning of a pipe section containing SCC. An image of this sample is shown in Figure 168 using magnetic particle inspection to show the extent of the cracks. The 5-MHz probe was mounted on a wedge to allow angle beam shear waves to be used (Figure 169). This inspection technique was similar to the technique used for Concept 1 girth weld inspection where multiple sector scans were used with electronic beam skewing of -7 and +7 degrees (Figure 170). While it is recognized that the mechanical raster technique would not be optimal for stationary health monitoring, it shows the detection and imaging capability that could be used for monitoring of SCC-type flaws. It is envisioned that a larger permanently mounted probe could be used that could permit electronic scanning and produce similar results.

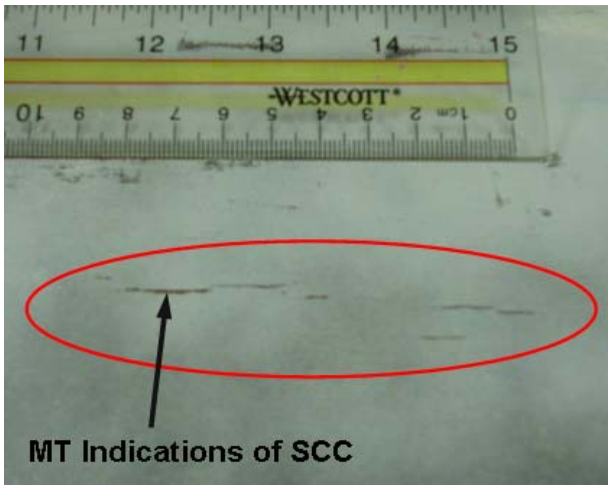

Figure 168. Magnetic Particle Results of SCC in Pipe Sample

Figure 169. 5-MHz MPA Probe Mounted on Shear Wave Wedge

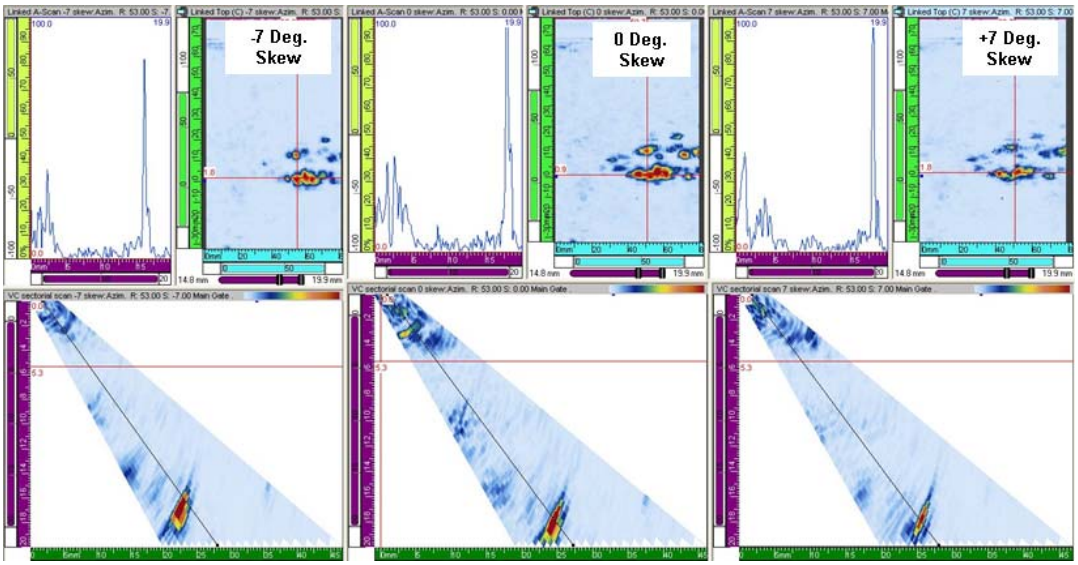

Figure 170. MPA Results of SCC

3.8.1 Task Observations and Conclusions

Element pitch of the 5-MHz MPA probe used during health monitoring performance evaluation was slightly too large in the secondary probe axis. This resulted in poor focusing and limited electronic scanning in the secondary axis. Results from the 15-MHz probe were much better than the 5-MHz probe.

Evaluation results with the 15-MHz probe showed that a 2-mm-diameter FBH at a depth of 6.3 mm could be accurately imaged and sized to within 0.5 mm. In addition, lateral resolution was sufficient to distinguish 3.7-mm-diameter taper bottom holes that were within 1.2-mm edge to edge in a 13.2-mm-thick sample.

MPA probes work well to provide a 2-axis stationary C-Scan. The C-Scan resolution is dependent upon the primary and secondary pitch of the probe elements. Consequently, to obtain a high-resolution scan, a small element pitch is needed; however, a small pitch will result in a shorter focusing range. Therefore, a balance of probe parameters must be made based on the specific health monitoring application.

Unlike single-element probes, a 2D MPA probe provides A-Scan data for each point on the C-Scan. This allows multiple measurements to be made over the entire probe footprint which provides a more comprehensive understanding of test component characteristics. Additionally, electronic beam steering can also be done through the software without changing the probe.

The probe footprint and the aperture sizes selected will determine the size of the C-Scan window. The footprint of the probe is fixed and is determined by the number elements times the

element pitch. In order to cover a larger area, a probe having more elements is required. Aperture size is a variable that can be adjusted. A larger aperture will provide a smaller beam and longer focal depth, but will reduce the C-Scan size. Therefore, a balance between focusing ability, beam steering capabilities, and scan area must be achieved.

A stationary health monitoring probe should be designed for a specific application or range of applications. It is recommended that modeling and simulation software be used to assure that the probe will provide the coverage and focusing capabilities required for the specific application.

4.0 Field Trials

The objective of the field trials was to validate and compare current zonal discrimination PA inspection techniques to MPA non zonal inspection techniques on production pipeline girth welds. EWI developed a MPA field test methodology and quantified the performance of a MPA AUT system under field conditions. As an in-kind cost share, project team member TransCanada Pipelines (TCPL) provided access to a pipeline construction site in Hardisty, Alberta, Canada for field trials from June 5, 2009 through June 18, 2009. The field tests were conducted on a 30-in. OD seam welded, carbon steel pipeline with a 9.8-mm wall thickness. EWI conducted field trials for this project concurrently with DOT project *Advanced Technologies and Methodology for Automated Ultrasonic Testing Systems Quantification* (DTPH56-07-T-000002); EWI Project No. 50454GTH.

4.1 Field Trial Location

EWI performed the field trials on a section of the Keystone pipeline project operated by TCPL located in Hardisty, Alberta, Canada. A photo of the field trial site in Hardisty is shown in Figure 171. The 2,148 mile Keystone Pipeline will transport crude oil from Hardisty, Alberta, Canada to U.S. Midwest markets in Wood River (Patoka, Illinois) and to Cushing, Oklahoma (Figure 172). Throughout its length, the Keystone Pipeline varies in size and WT.

Figure 171. Field Trial Site

Figure 172. Map of Keystone Pipeline Project

4.2 Inspection Procedure

The MPA non zonal inspection procedure used during the field trials was developed by EWI using information gained during other tasks of this project. The procedure is contained in Appendix C and is primarily composed of a 5-MHz, 16×8 element MPA probe carried by a 2-axis mechanical scanner equipped with magnetic wheels (Figure 173). Instead of using tandem zonal techniques for fill passes, the EWI MPA procedure consisted of three sectorial scans (S-Scans) where the beam was electronically steered from 55 to 75 degrees. One S-Scan was at an electronic skew angle of 0 degrees, while the other two were at skew angles of +7 and -7 degrees. The idea was to use the electronic skewing capability of MPA to help detect flaws that may be skewed relative to the weld axis. During the field trial welds were scanned by using a mechanical X-Y raster scan pattern to move the probe over the pipe surface to cover the area of interest. This arrangement provided complete coverage of the weld zone with multiple angles. A screen display showing the output from this technique is shown in Figure 174.

For the MPA non zonal approach, the idea was to identify flaws and determine their through-wall height and length, regardless of signal amplitude. Consequently, the gain setting was set to maintain an acceptable signal-to-noise ratio. The calibration sample was used only as verification that the holes and notches could be detected and correctly measured.

4.3 Calibration Blocks

Early in the project, UT Quality (UTQ) provided a calibration drum for use by all project team members who performed scanning with their equipment at EWI. This drum had a 15.6-mm calibration sample also owned by UTQ that was designed for a single U-groove weld joint with an 8-degree included angle for a 15.6-mm wall pipe (illustrated in Figure 175). The calibration drum itself was designed to mount on a bracket at the rear of a truck; therefore, EWI decided to use the UTQ calibration drum for the field trials. The UTQ calibration block drawings are located in Appendix D.

Figure 173. MPA 2-Axis Scanner

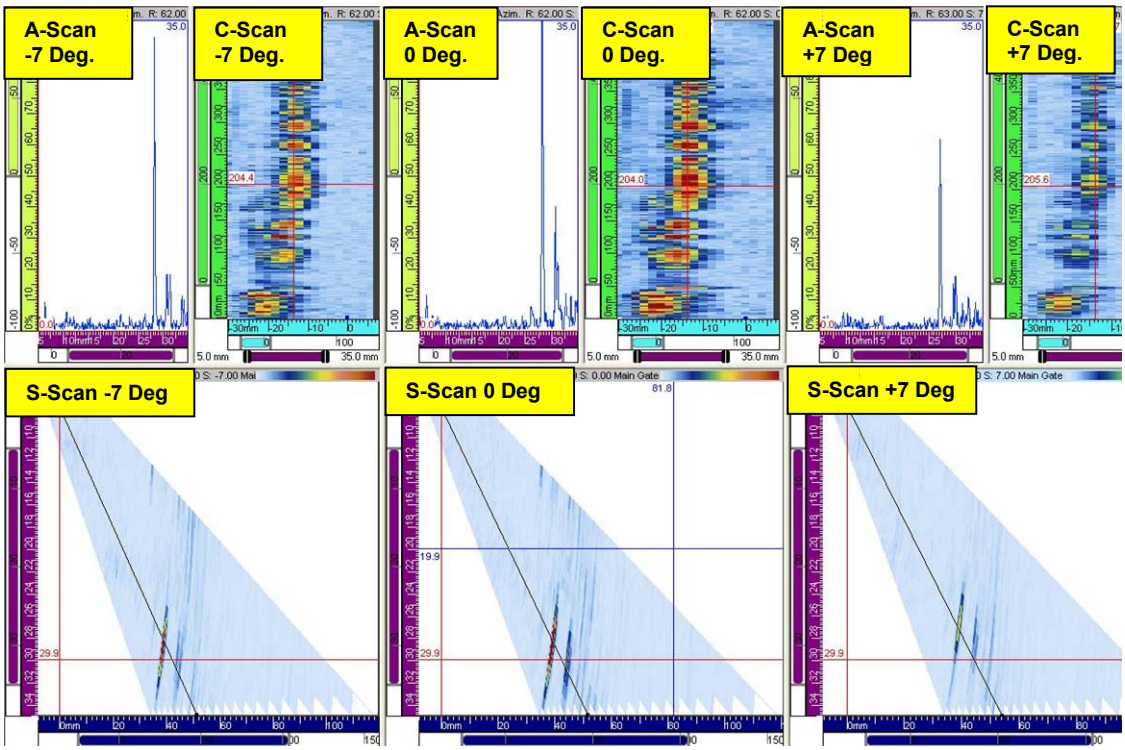

Figure 174. Output Display of MPA Data

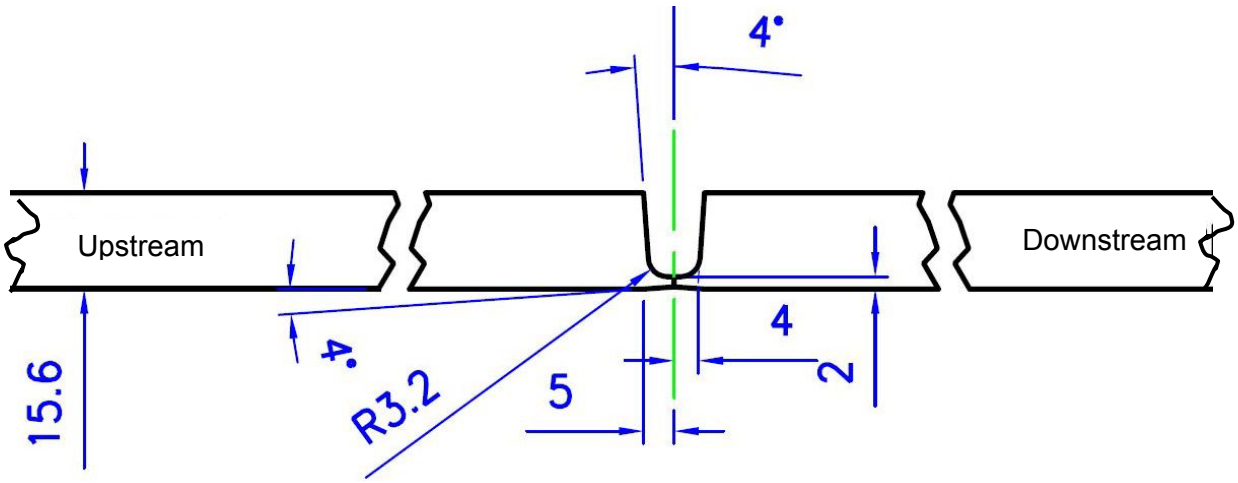

Figure 175. U-Groove Joint for UTQ Calibration Block

When field trial preparations were under way, EWI was informed that the pipe for the field trials would have a 10-degree included angle single U-groove weld preparation geometry with a 15.6-mm pipe WT. The inspection procedure in Appendix C was designed to inspect this joint/material thickness combination.

As mentioned previously, the Keystone Pipeline varies in diameter size and WT. Shortly before the field trials, EWI was informed that the pipeline at the Hardisty site would be a 10-degree included angle single U-groove weld preparation geometry with a 9.8-mm WT. Based on this geometry/material thickness combination, EWI ordered a new calibration block to be delivered to the UTQ facility where the EWI scanning equipment was being delivered and assembled prior to the field trials. The new EWI calibration block drawings are located in Appendix E. Figure 176 shows the new EWI 9.8-mm thick calibration block mounted on the calibration drum attached to the truck provided by UTQ.

Figure 176. UTQ Calibration Drum and 9.8-mm Calibration Sample

When EWI arrived at the field trial site, the weld joints to be inspected consisted of a 20-degree included angle K-groove weld joint geometry for 9.8-mm pipe WT (per TCPL Welding Procedure Specification LD-A-WPS1). Figure 177 is a sketch of this weld joint geometry.

The approach for the field trial was simple. When UTQ discovered a significant weld defect, EWI was to step in and do a LPA scan (for DTPH56-07-T-000002). When that scan was complete, EWI was to change the scanner equipment to do a MPA scan (for DTPH56-08-T-000002). Due to time and data acquisition limitations, only weld sections containing a flaw indication were scanned with MPA. This was anticipated to be the best approach to gather data in the most efficient manner with minimal interruption to the TCPL production schedule. Figure 178 shows the EWI truck (provided by UTQ) following the UTQ truck with the crew that was performing the AUT inspections for TCPL.

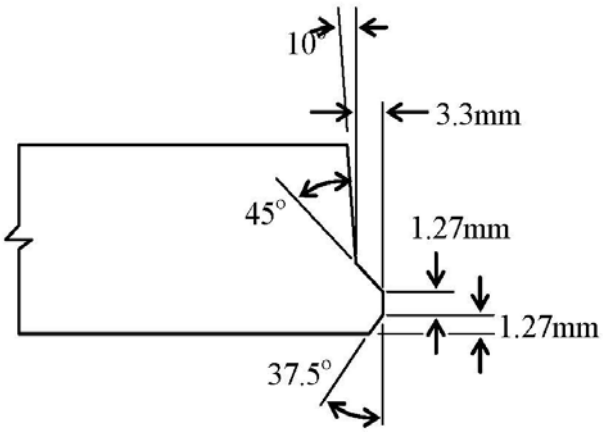

Figure 177. Field Trial Weld Joint Geometry

Figure 178. EWI Truck Following UTQ Truck Performing AUT Scans for TCPL

Using the non zonal technique under field conditions was beneficial from a couple of points. First, the technique could be tested under actual conditions to access the ability to keep up with production, and second, it provided a direct comparison of flaw detection with current LPA zonal techniques. Figures 179 through 184 show example comparisons made during the field trials. Further comparisons and a daily activity log are provided in Appendix F.

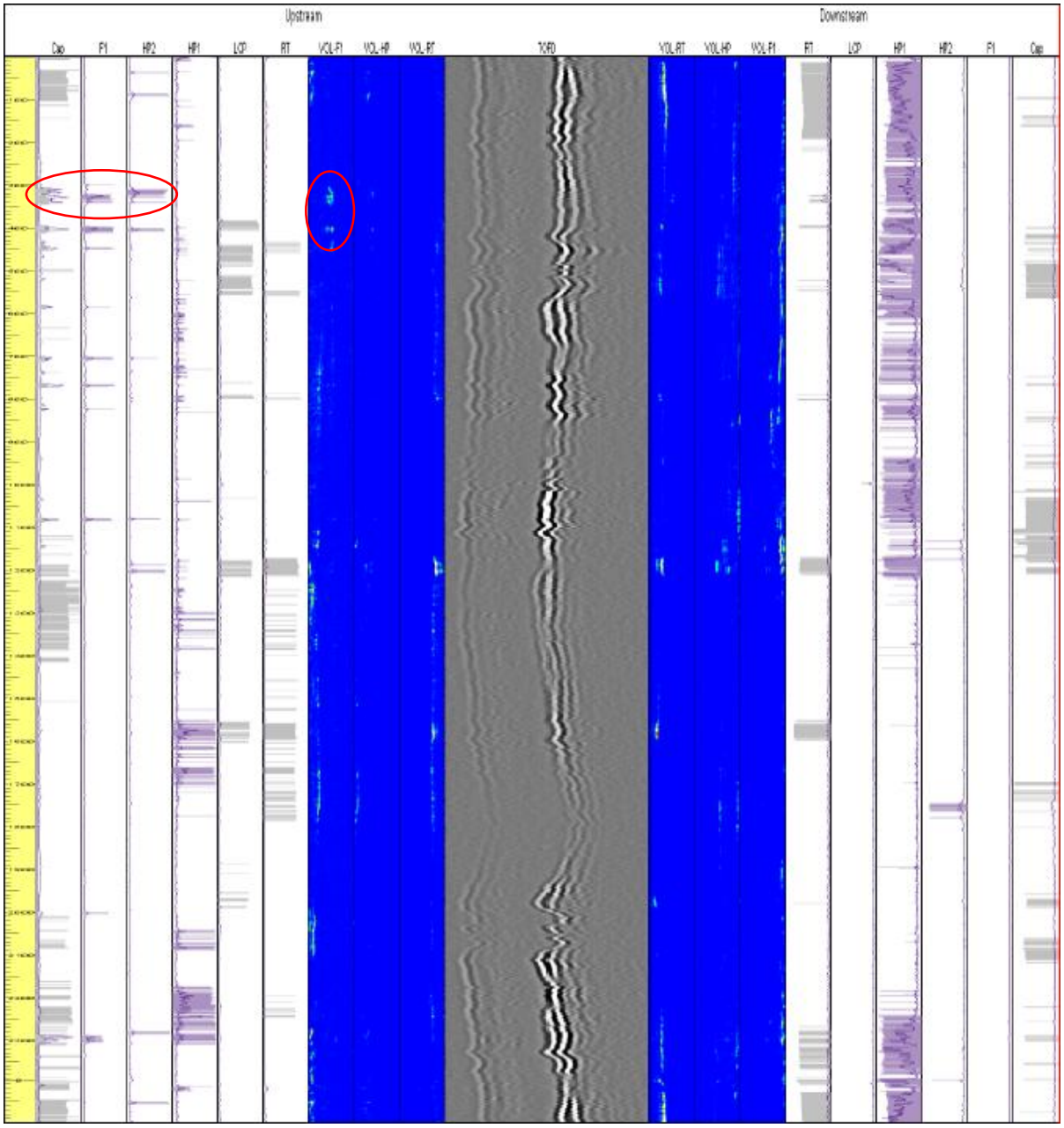

Figure 179. Weld MLA 4681 - UTQ Scan Screen Capture

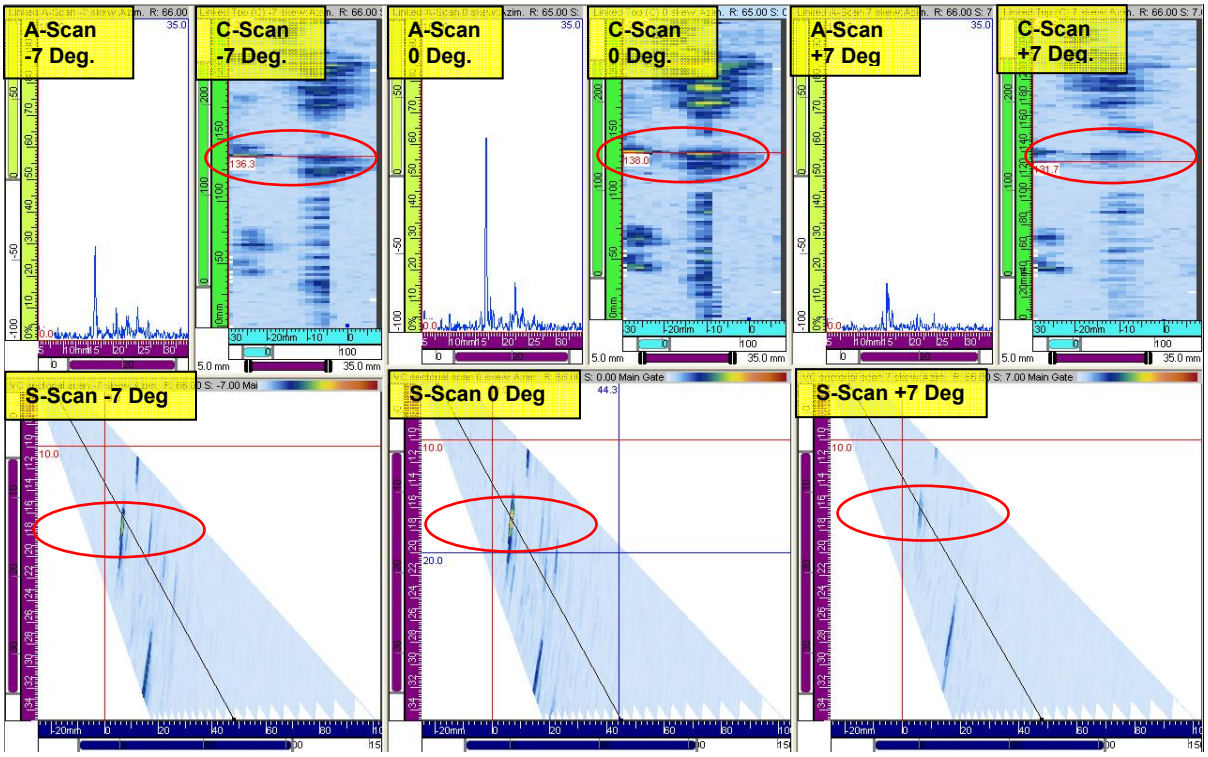

Figure 180. Weld MLA 4681 - EWI MPA Scan Screen Captures (Various Angles)

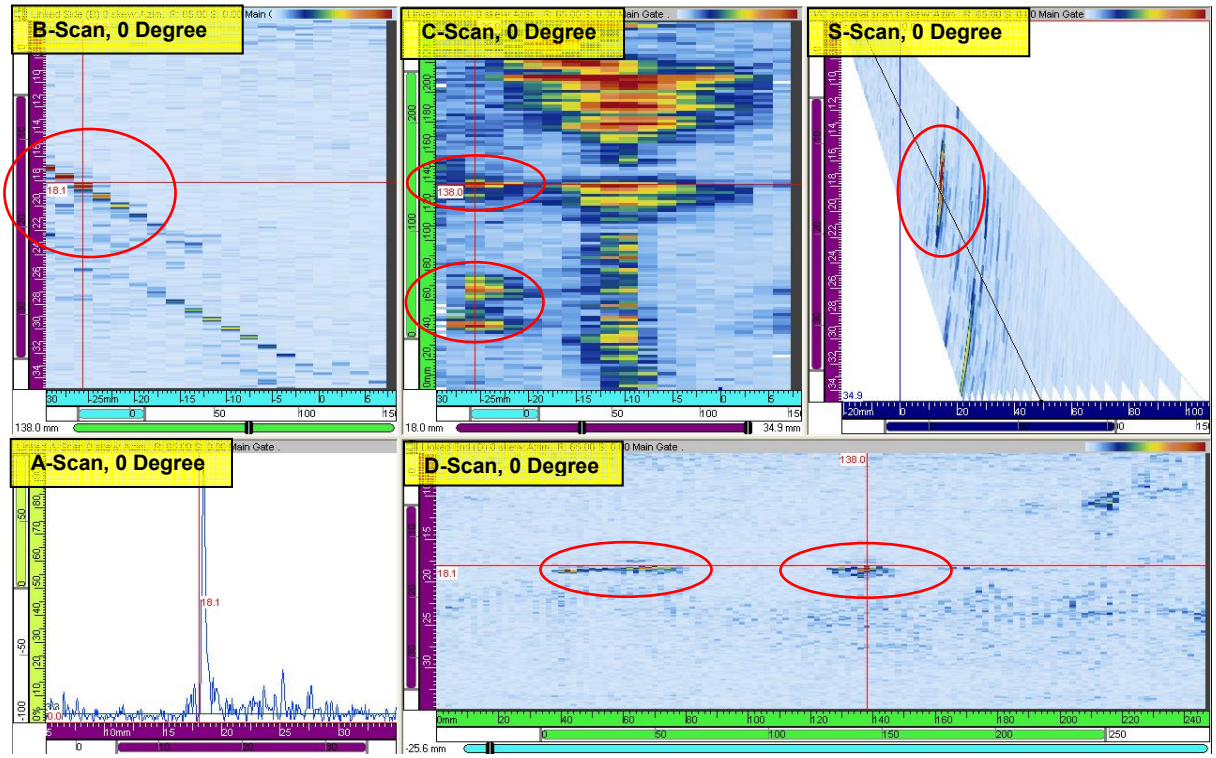

Figure 181. Weld MLA 4681 - EWI MPA Scan Screen Captures (0 Degree Only)

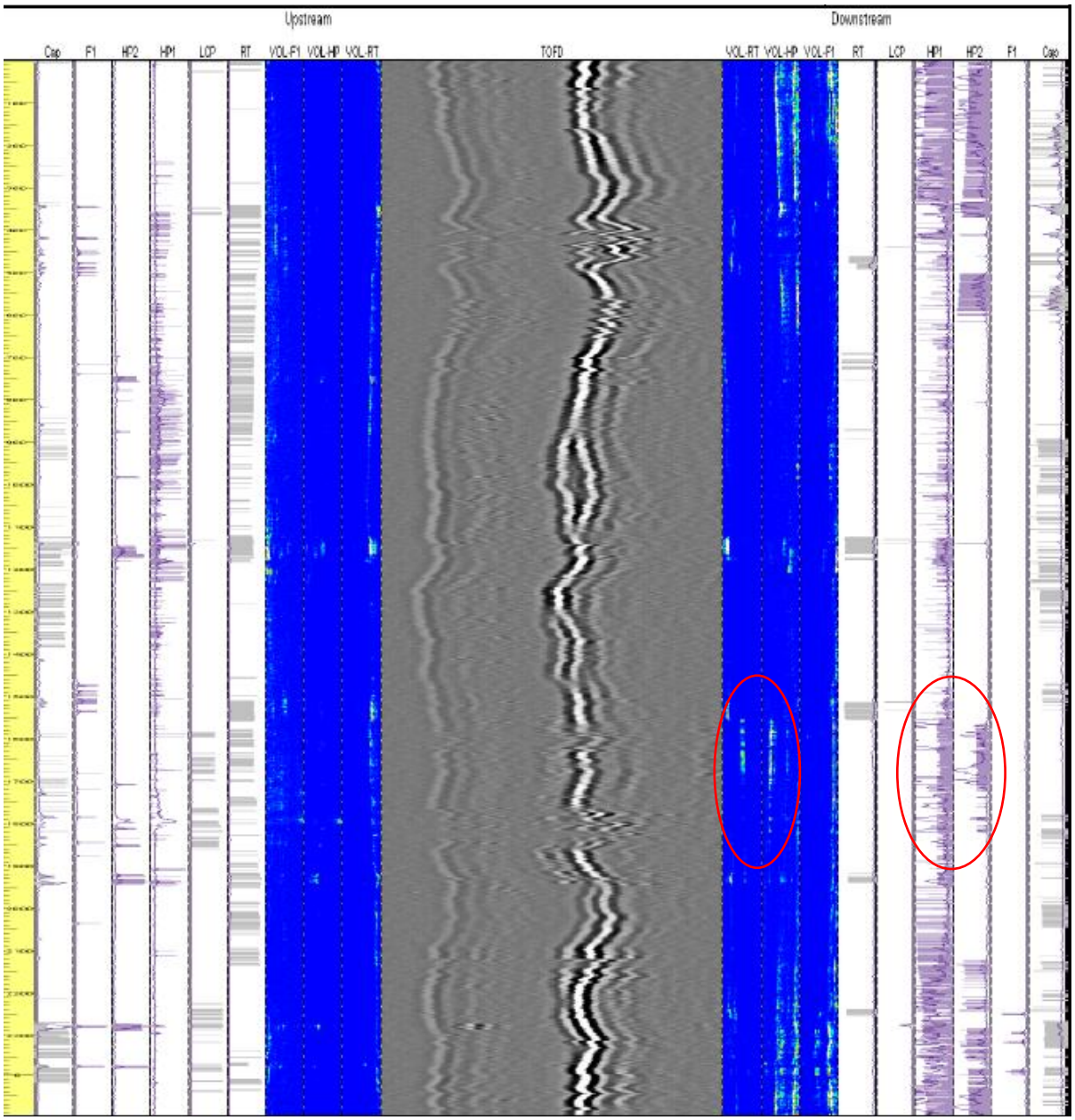

Figure 182. Weld MLA 4925 - UTQ Scan Screen Capture

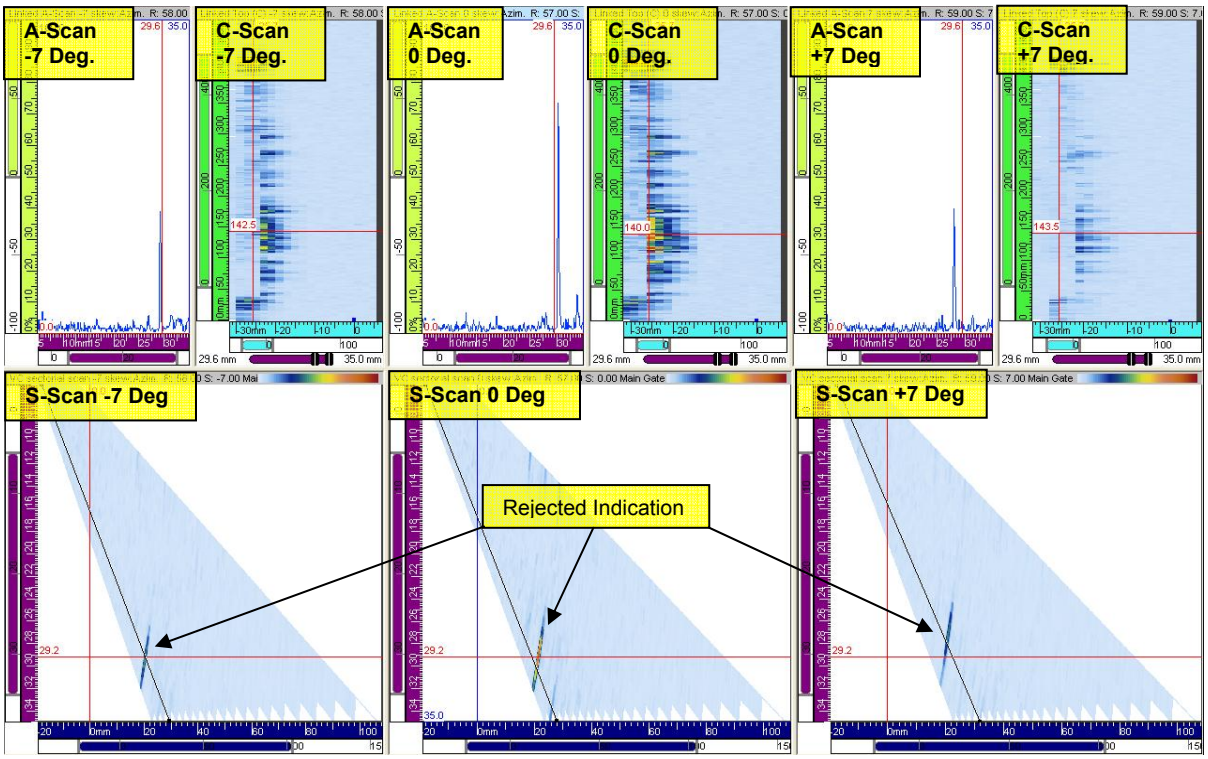

Figure 183. Weld MLA 4925 - EWI MPA Scan Screen Captures (Various Angles)

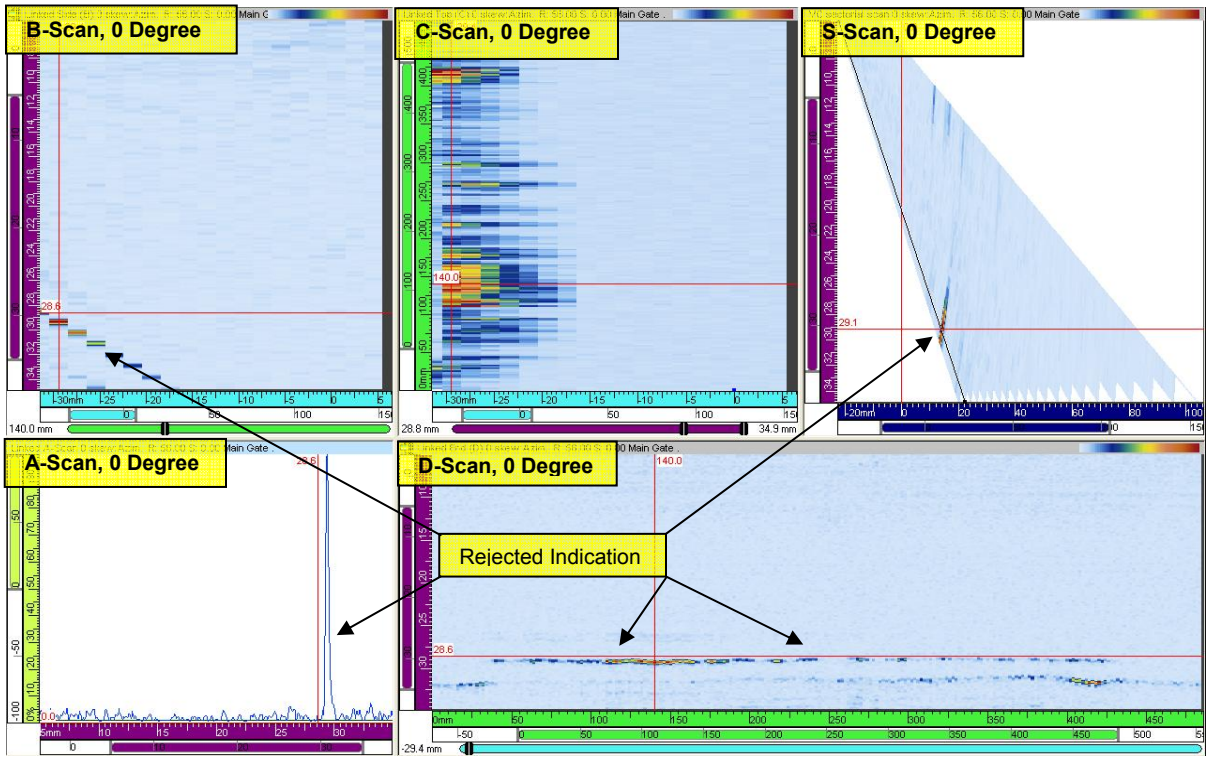

Figure 184. Weld MLA 4925 - EWI MPA Scan Screen Captures (0 Degree Only)

4.4 Task Observations and Conclusions

Although the EWI non zonal MPA procedure was calibrated/optimized for an 8-degree included angle U-groove for 15.6-mm WT, it detected indications on a 20-degree included angle K-groove weld joint geometry for 9.8-mm wall well within the current inspection code criteria.

The MPA probe and wedge used was more suitable for thicker material and was not optimized for the 9.8-mm wall; therefore, the desired distance from the weld centerline could not be achieved. To overcome this, a mechanical raster scanning technique was used with a general purpose magnetic wheel scanner. The magnetic wheel scanner experienced difficulties on the coating and in most cases had to be manually guided to prevent slipping.

The equipment used for zonal discrimination techniques are not capable of inspecting weld joint geometries for which they are not calibrated/optimized. In comparison, the non optimized EWI non zonal MPA procedure was able to detect the same indications that the fully optimized zonal discrimination technique detected, as all field trial scan data shows good agreement between non zonal MPA techniques and zonal discrimination techniques used. The non zonal MPA technique was also able to display flaws in much clearer formats (A-, B-, C-, D-, and S-Scans) as compared to the more limited display formats (strip, and D-Scan) of the zonal discrimination scan.

One of the advantages of using MPA is its ability to more accurately size skewed defects. During the field trials, no skewed flaws were encountered. Therefore, it was not possible to compare the ability of zonal discrimination, LPA or MPA techniques to size skewed flaws in the field.

Current inspection code criteria (e.g., API 1104 and ASTM 1961) only cover LPA zonal discrimination techniques. Based on the results of the field trials, non zonal MPA techniques characterize the types of indications inspected just as well as zonal discrimination techniques. In fact, MPA provides additional scans (A-, B-, C-, D-, and S-Scans) that allow the operator to see more flaw detail. MPA non zonal techniques should be considered for incorporation into current inspection code criteria as an alternate for zonal discrimination techniques.

To obtain more accurate scan data for the weld joint scanned during the field trials, an MPA probe and wedge should be developed with more elements in the primary probe axis. This would allow electronic scanning in the primary axis and permit the use of a band scanner similar to what is currently used for LPA inspection. This new probe/wedge configuration would also require a different PA instrument as compared to the equipment used for the field trials, which was only capable of firing and receiving 64 elements. An improved approach would be to use

PA equipment capable of firing and receiving more elements (to be determined) in combination with the improved probe/wedge.

As compared to zonal discrimination techniques, non zonal MPA techniques have the potential to achieve more accurate results if PA equipment manufacturers develop scanning equipment with faster processing speeds.

Future DOT PHSMA projects should feature field trials as a means to evaluate the applicability of new technologies for the pipeline industry.

5.0 Advanced NDE Training

A training class was developed for representative AUT systems that featured project results and was sponsored by ExxonMobil Development Company (EMDC) as cash cost share for the DOT program. The training course was similar in content to the course conducted in March 2008 as cost share for DOT project DTPH56-07-T-000002; however, it was modified to reflect EMDC's requested syllabus changes. The attendees received an in-depth theoretical and practical overview of the current advanced NDE methods and techniques that are used in oil and gas industry including current project results. The training event was held at EWI in Columbus, Ohio from August 24-28, 2009 and covered the following topics.

- Introduction to conventional [vision testing (VT), penetrant testing (PT), magnetic particle testing (MT), eddy current testing (ET), radiography testing (RT), and ultrasonic testing (UT)] and advanced NDE [acoustic emission (AE), automated ultrasonic testing (AUT), and computed radiography (CR)] of materials and welds with limited PT, MT, CR demonstrations – 8 hours.

- UT and AUT practical demonstrations and training – 8 hours.

- Optimization of UT/AUT procedures using UT modeling and simulation tools with practical demonstrations and training; UT/AUT procedures validation and qualification –
- 8 hours.

- RT practical demonstrations and training – 4 hours.

- Advanced ET practical demonstrations and training; ET/advanced ET procedures validation and qualification – 10 hours.

The first day of the training was mainly theoretical with limited demonstrations. During the last 4 days of the training, EMDC staff were divided into two groups. Parallel training was conducted

with a student to teacher ratio of 4:1 to better expose and involve participants in practical demonstrations and applications related to AUT and ET.

Following is a list of the EMDC staff that participated in the training event:

- Gabriel Rombado
- Germansque Picker
- Pamela Wojtuiewicz
- Amit Kumar
- Andy Shelley
- Timothy Anderson
- Rhys-Sheffer Birthwright
- Gene Settoon
- Troy Widerer
- Benjamin Knight
- Chad Casey
- Rick Noecker

Each attendee was given a CD with PowerPoint presentations for all NDE techniques covered during the training. The training materials contain information that is considered EWI proprietary; therefore, a copy of these materials was not provided as part of this report.

6.0 Technology Demonstration Workshop

On June 23, 2011, EWI hosted a 1-day on-site technology transfer workshop to disseminate the results of the project to DOT PHMSA and the U.S. pipeline industry.

6.1 Workshop Participants

Twenty-nine people registered for the workshop, which was advertised to EWI member companies in the oil and gas industry sector and PHMSA personnel. Registration was administered via the EWI website, where a workshop description and agenda were posted for potential participants. Due to demonstration logistics, workshop size was limited to approximately 40 people. Table 32 contains the list of 24 people who participated in the workshop (excluding EWI staff). 50% of the participants were from the U.S. pipeline industry.

Table 32. Workshop Participants

Last Name	First Name	Company
Agnew	Joe	Zetec
Barber	James	Marathon Pipe Line LLC
Burns	Timothy	Shell Int'l Exploration and Production
Chhabria	Vivek	EWI (High School Intern)
Donnelly	Jeff	Marathon Pipe Line LLC
Huang	Ta-Chieh	UT Technology, Inc.
Kiefer	Joe	ConocoPhillips
Lee	Ken	PHMSA
Ma	Jing	Center for Reliable Energy Systems
Merritt	James	PHMSA
Nestleroth	Bruce	Battelle
O'Neill	Mark	Tennessee Gas Pipeline
Raimondi	Robert	Olympus
Sammons	Bridget	Shell
Sattler	Frank	Diamond Power International, Inc.
Schroeder	Zachary	Marathon Pipe Line LLC
Stechschulte	Donald	Marathon Petroleum Company
Szabo	Tibor	IRISNDT Corp.
Tremblay	Patrick	Zetec
van der Ent	Jan	Applus RTD Group
Vessel	Samuel	Duke Energy
Wahjudi	Thomas	Kiefner and Associates, Inc.
Wasson	Andrew	ExxonMobil Upstream Research Co.
Yellapantula	Sudha	ConocoPhillips

6.2 Workshop Agenda

The workshop began at 8:15 a.m. and ran until 4:30 p.m. Seven speakers from two organizations presented the topics as shown in the following agenda.

8:15 a.m.	**Opening Remarks,** *by Dr. Henry Cialone, CEO and President, EWI*
8:20 a.m.	**Overview − Technical Approach,** *by Nancy Porter, Senior Project Manager, EWI*
8:30 a.m.	**DOT Perspectives,** *by Jim Merritt, R&D Program Manager, DOT PHMSA*
8:45 a.m.	**MPA Probe Concepts,** *by Roger Spencer, Senior NDE Engineer, EWI*
9:15 a.m.	**Modeling and Inspection Simulations,** *by Dr. Evgueni Todorov, Senior NDE Engineer, EWI*
10:15 a.m.	*Break*
10:30 a.m.	**Practical and Field Trials,** *by Perry White, Project Engineer, EWI*
12:00 p.m.	*Lunch*
12:30 p.m.	**Destructive Validation,** *by Roger Spencer, Senior NDE Engineer, EWI*
1:00 p.m.	**POD and Flaw Sizing,** *by Dr. Evgueni Todorov, Senior NDE Engineer, EWI*
1:45 p.m.	*Break*
2:00 p.m.	**Lab Demo A,** *by Perry White* Concept 1 − Girth Weld Inspection
2:45 p.m.	**Lab Demo B,** *by Roger Spencer* Concept 3 − ID Pipe Inspection
3:30 p.m.	**Wrap-up Session,** *by Nancy Porter, Senior Project Manager, EWI*
3:45 p.m.	**One-on-One Discussions with EWI Staff**
3:45 p.m.	**EWI Overview and Tour,** *by Leah Kohr , Membership Development, EWI*

6.3 Workshop Presentations

Located in Appendix G, all workshop presentations are shown in chronological order per the agenda in Section 6.2. Dr. Todorov (EWI) is shown in Figure 185 presenting the Modeling and Inspection Simulations.

Figure 185. Dr. Todorov Presenting Modeling and Inspection Simulations Data

6.4 Workshop Demonstrations

Given the number of workshop participants, it was necessary to divide the attendees into two groups for the laboratory demonstrations. Both 1-hour demonstrations were run simultaneously. After the first hour, participants switched labs and the demonstrations were repeated. This approach gave attendees time to ask detailed questions and to allow hands-on use of the inspection equipment while under the supervision of an experienced PA UT operator.

Demo 1 - MPA Probe Concept 1. Perry White lead the demonstration of MPA probe Concept 1 in the EWI NDE laboratory with the equipment set up shown on a girth weld in Figure 186. Sean Gleeson subsequently showed the participants one of the TomoCar radiography scans. Two large monitors were used to display scan data during the demonstration.

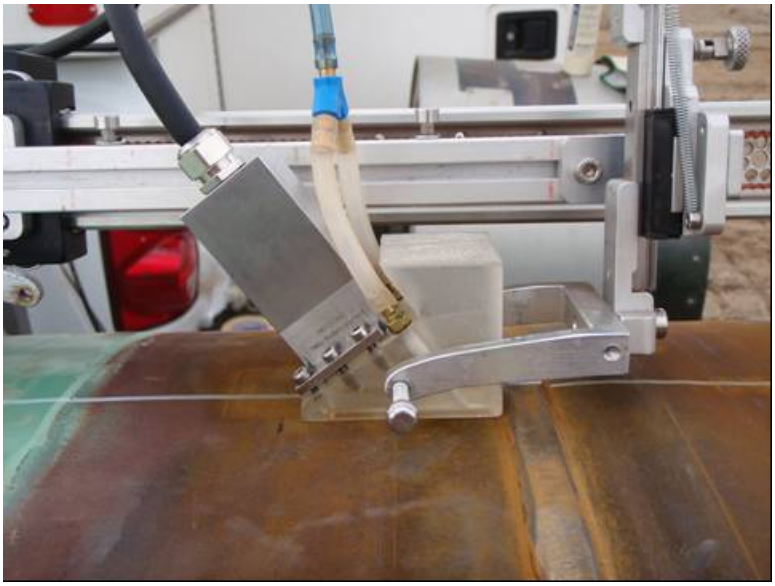

Figure 186. MPA Probe Concept 1 Demonstration Equipment

Demo 2 - MPA Probe Concept 3. Roger Spencer lead the demonstration of MPA probe Concept 3 in the EWI NDE laboratory using the probe carrier (Figure 187) that was mounted on a pipe which was used to manually move the probe through a pipe filled with water. A large monitor was used to display the scans during the demonstration. Dr. Todorov subsequently demonstrated the MPA Concept 4 health monitoring probe.

Figure 187. MPA Concept 3 Probe Mounted in Carrier

6.5 Workshop Survey

At the conclusion of the workshop, a 1-page survey was distributed to the attendees to determine if they found the workshop useful and what they would recommend to improve the next workshop. For the majority of the questions, each participant was asked to rate the usefulness of specific presentations from 1 to 10 (with 10 being the highest). The participants rated the workshop's usefulness from 5 to 10; the average score was 7.8 (Figure 188). The average scores for each presentation are listed in Table 33.

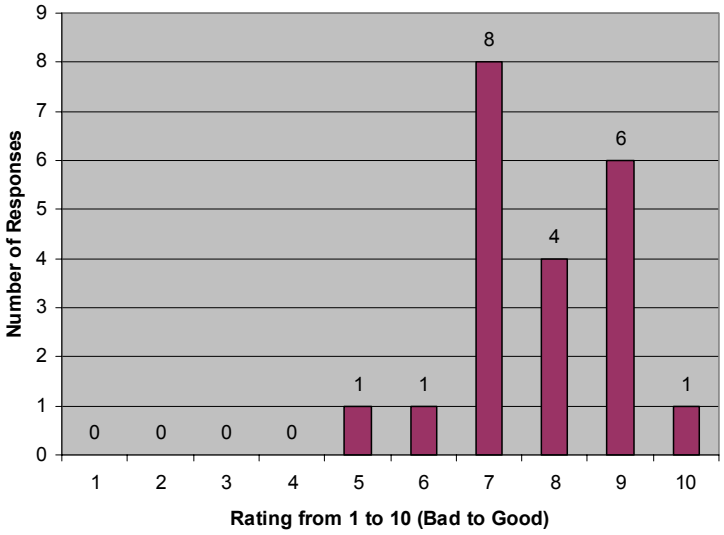

Figure 188. Survey Responses to Question 1

Table 33. Average Score for Each Workshop Presentation

Presentation	Average Score
Overview - Technical Approach presentation by Nancy Porter of EWI	8.3
DOT Perspectives presentation by Jim Merritt of PHMSA	7.6
MPA Probe Concepts presentation by Roger Spencer of EWI	8.3
Modeling & Inspection Simulations presentation by Evgueni Todorov of EWI	8.0
Practical and Field Trials presentation by Perry White of EWI	8.2
Statistical Analysis: POD & Sizing presentation by Evgueni Todorov of EWI	8.0
Concept 1 Girth Weld Demonstration by P. White and S. Gleason of EWI	8.9
Concept 3 ID Pipe Inspection Demonstration by R. Spencer and E. Todorov of EWI	8.6

100% of the workshop attendees indicated that they learned something from the workshop. Twenty survey respondents said that the workshop length was just right; only one person felt that it was too long. The detailed results of the survey are located in Appendix H.

7.0 Pipeline Conference Presentation

During the course of the project, EWI presented project results at a pipeline industry conference as part of Task 8 (Progress Meetings, Pipeline Conference, Annual Panel Peer Review, Reporting and Program Management). A paper was also published as part of the conference proceedings.

The presentation (located in Appendix I) was given at the 2009 Rio Pipeline Conference on September 24, 2009. This is the biggest pipeline event in Brazil and is held every two years. The Conference and Exposition was held at the largest convention center in Rio de Janeiro, Brazil and covered all relevant issues in the pipeline industry sector. The published paper is located in Appendix J.

8.0 Final Financial Section

As required in DOT Agreement DTPH56-08-T-000002, this section contains a final project financial report that summarizes the status of Government and Team contributions for the Project and reconciles any prior discrepancies or variances in contributions.

A high level summary of project funding is shown in Table 34. Slightly less cost share was obtained as compared to the plan ($1,303,678 was obtained; $1,320,000 was planned). Although the planned cost share amount fell short of expectations, total cost sharing contributions were 152%, far exceeding the PHMSA cost share requirement of 50%.

Table 34. Summary of Actual Project Funding

Funding Type	
Government	$ 679,457
Cash Cost Share	$ 520,126
In-kind Cost Share	$ 783,552
Total Funding	**$1,983,135**

8.1 Government Funding

DOT Agreement No. DTPH56-08-T-000002 was fully executed on April 29, 2008; the effective date was May 1, 2008. DOT provided EWI a total of $679,457 for Tasks 2, 5, 6, 7, and 8. At the end of the project, all Quarter 13 activities and deliverables were completed. All payable quarterly milestones/invoices are summarized in Figure 189.

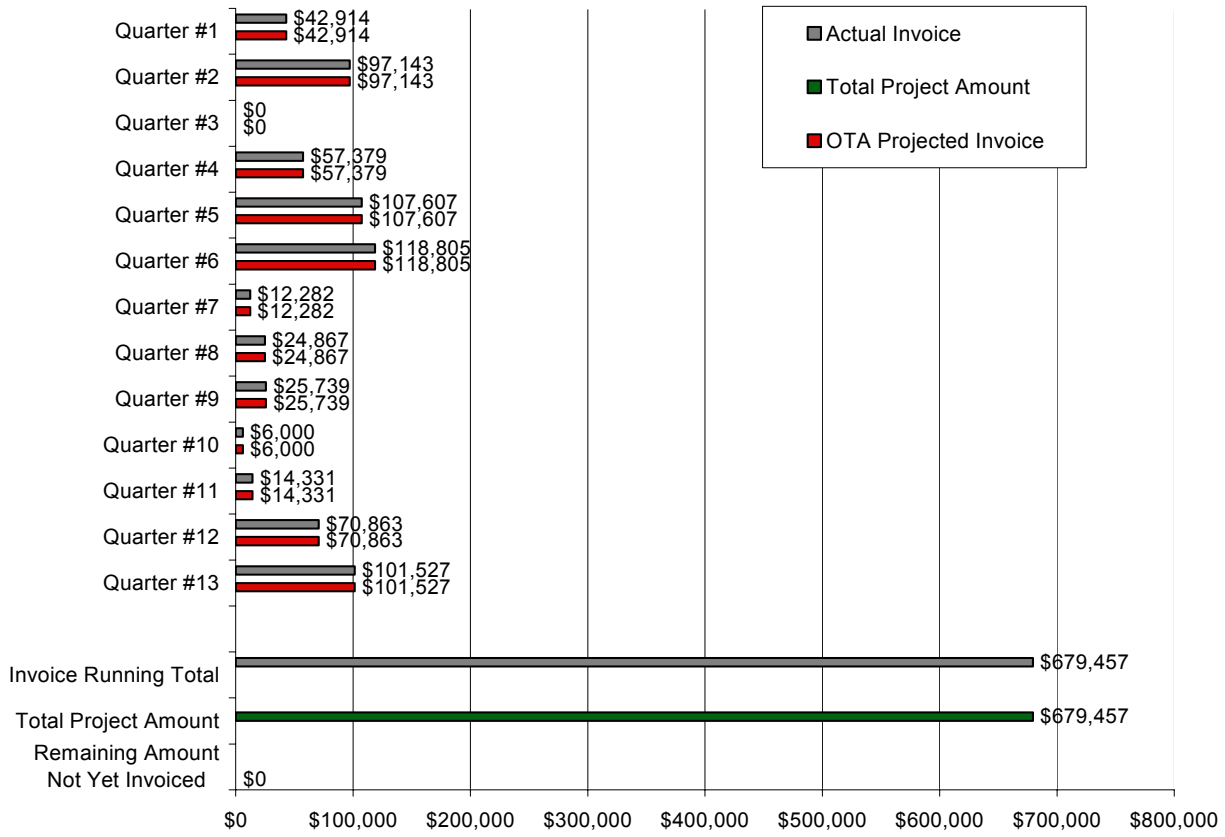

Figure 189. Quarterly Payable Milestones/Invoices - DTPH56-08-T-000002

8.2 Team Cost-Share Funding

As documented in proposal section 2.5 (Program Costs and Schedule), the project was planned to benefit from a minimum industry cost sharing of **$1,145,000**, which was comprised of **$320K** of direct cash funding and **$825K** of in-kind support. As of November 26, 2007, when the proposal was written, EWI, CEA/List, *it*Robotics, Zetec, TCPL, Imasonic, NDT Systems & Services had committed to cost sharing the project. Report section 8.2.1.1 is a description of the planned cash cost-share and section 8.2.1.2 is a description of the planned in-kind support.

Also included in proposal section 2.4.3 was a list of potential "additional" cash/in-kind contributors including ExxonMobil, Development Company (EMDC), ConocoPhillips, ApplusRTD, Mechanical Integrity, INDES/KJTD (USA) Co. Ltd., Fraunhofer Institute of NDE (FNDT), Federal Institute of Materials Research and Testing (a.k.a., BAM), and UT Technology. When the proposal was submitted, these organizations had been invited to join the project team; however, no letter of commitment was yet received. Report section 8.2.2.1 is a description of the additional cash cost-share and section 8.2.2.2 is a description of the additional in-kind support received to date.

Agreement DTPH56-08-T-000002 between DOT and EWI contained a new requirement in section 1.04 *Requirements on Team Participants*. Subsection 2 directed EWI to pass on the relevant provisions of the Agreement to the team participants. Toward this end, EWI created a Terms of the Relationship Agreement (TRA) for all in-kind contributors. Some in-kind contributors refused to sign the TRA, report section 8.2.2.3 *Other Support* was created to track their contributions.

By the time the project ended, the cost share budget had increased (as described below). The final cost-share budget and actual team cost-share expenses (cash and in-kind) are summarized in Table 35.

Table 35. Total Team Cost Share Funding

Budget	Actual
$1,320,000	$1,303,678

Major Deviations: INDES/KJTD, NDT Systems & Services did not provide their in-kind contributions. The itRobotics cost share was reduced by a factor of ten.

Proposed Adjustment Actions: None, as the cost share amount without the above in-kind contributions is 152%, which far exceeds the PHMSA cost share requirement of 50%.

8.2.1 Planned Cost-Sharing (As Quantified in the Original Proposal)

This report section contains a summary of budgeted and actual expenses for planned cost-sharing as quantified in the original proposal.

8.2.1.1 Planned Cash Cost-Share

Planned cash cost-share contributions were provided via a parallel R&D projects funded by EWI and the purchase of MPA probe modules via the EWI capital budget. When the proposal was submitted, a total of **$320K** in cash cost-share was committed. Table 36 contains a summary of all planned cash cost-share contributions (budget and actual).

Table 36. Status of Planned Cash Cost-Share

Team Participant	EWI Project No.	Task	Budget	Actual
EWI	PO #09-0018	4	$120,000	$120,000
EWI	51433GTO	1,2,3	$200,000	$200,126
		Total	***$320,000***	***$320,126***

EWI is an internationally recognized leader in pipeline welding, nondestructive evaluation, and fitness-for-purpose technology and has assisted industry and the United States government agencies in numerous pipeline projects applying advanced NDE and ultrasonic PA technology. EWI provided cash cost-share contributions in two different forms. In support of Tasks 1-3, EWI developed a MPA concept for a MPA module applicable for either outside or inside inspection of the pipe and carried by different inspection tools, platforms, and systems. In collaboration with other partners, EWI also developed improved 3D modeling, simulation, design approach, and tools for detection and virtual visualization of complex flaws, and virtually define and optimize detection and sizing capabilities of the proposed modules. EWI then designed representative MPA modules - rigid/flexible for outside and circumferential for inside inspection of the pipe. EWI also purchased two Imasonic MPA probe modules via the EWI capital equipment budget. **EWI provided a total of $320,126 in cash cost share for this project.**

8.2.1.2 Planned In-Kind Support

When the proposal was written, a total of **$825K** in in-kind cost-share was committed. In-kind cost share was provided to EWI in accordance with as applicable, *49 CFR 18 - Uniform Administrative Requirements for Grants and Cooperative Agreements to State and Local Governments, Section 18.24, Matching or Cost Sharing*, or *49 CFR 19 - Uniform Administrative Requirements for Grants and Agreements with Institutions of Higher Education, Hospitals, and Other Non-Profit Organizations, Section 19.23, Cost Sharing or Matching*. EWI captured and maintained an Excel spreadsheet with a running summary of planned in-kind cost-share contributions as reported by team participants. Budget, current, and cumulative costs are shown in Table 37. ***it*Robotics reduced their in-kind cost share from $300K to $30K due to financial difficulties; the net effect reduced the official planned in-kind support from $825K to $555K.**

Table 37. Status of Planned In-Kind Support

Team Participant	Task	Budget	Actual
CEA/List	2,5,8	$230,000	$230,000
*it*Robotics	1,5,7,8	$30,000*	$30,000
Zetec	5,7,8	$125,000	$128,245
TCPL	1,6,8	$100,000	$100,000
Imasonic	4,8	$50,000	$50,000
NDT Systems & Services	8	$20,000	$0
	Totals	***$555,000***	***$538,245***

Commissariat à l'Energie Atomique (CEA) division of the Laboratory for Integration of Systems and Technologies (LIST) is based in France and is a world leading research organization in the area of NDT, ultrasonic PA technology, advanced ultrasonic modeling and simulation tools integrated in M2M ultrasonic PA instrumentation. CEA/List provided **$230K** in the form of direct in-kind support to attend meetings and reviewing reports (Task 8), a parallel R&D activity to complete developing improved 3D modeling, simulation, design approach, and tools for detection and virtual visualization of fabrication cracks, in-service developed SSC and dents with cracks in carbon steel pipes and welds using rigid and flexible MPA modules (Task 2). CEA/List provided M2M equipment to EWI for several months during the execution of Task 5. **On April 1, 2010, CEA/List reported that they had provided a total of $230K in in-kind support for this project.**

***it*Robotics** is a start-up company based in the U.S. and is a developer of robotics and non-tethered inspection tools for inspection of unpiggable pipes. *it*Robotics planned to provide a total of **$300K** in the form of providing a prototype for inspection of hazardous liquid pipes for up to 6 months and engineering time (Task 5). A prototype robot and engineering time was also promised for the project workshop (Task 7). Direct in-kind support was promised for attending meetings and reviewing reports (Tasks 1 and 8). On January 13, 2010, *it*Robotics informed EWI that they were experiencing financial difficulties that caused significant delays with the availability of the robot for testing. On April 27, 2010, *it*Robotics informed EWI that they will only provide the Concept 3 probe cart, which was delivered in May 2010. **On July 2, 2010, *it*Robotics reported that that their total cost share contribution was reduced from $300K to $30K**.

TransCanada Pipeline Ltd. (TCPL) is one of the largest transmission pipeline companies in Canada. TCPL will provide **$100K** in the form of engineering time and coordination of Field Testing (Task 6), participating in meeting and reviewing reports (Tasks 1 and 8). Field trials

* *it*Robotics reduced their in-kind cost share from $300K to $30K due to financial difficulties, which prevent *it*Robotics from contributing as anticipated. The net effect is to reduce the total industry cost share from $1,590K to $1,320K. Even with this reduction in industry cost share, the project team was well above the 50/50 cost share requirement, as the government funding is $679,457.

were hosted In Hardisty, Alberta (Canada) from June 5-18, 2009. **TCPL reported that they provided a total of $100K cost share in support of this project.**

Zetec is an international company based in the United States, Canada, Germany, and France and is a pioneer of developing PA instrumentation and software for power generation and energy applications (Tasks 5 and 7). Zetec provided **$125K** via the loan of DYNARAY MPA equipment for several months. Zetec also provided on site training for EWI staff when their equipment was delivered. Zetec participated in meetings and reviewed reports (Tasks 7 and 8). Additionally, Zetec provided a system for EWI to using during the June 2011 workshop. **Zetec reported providing a total of $128,245 in cost sharing for this project.**

Imasonic is based in France and is a leading manufacturer of ultrasonic PA probes. Imasonic provided **$50K** via materials, equipment, and engineering time in support of Tasks 4 and 5. **Imasonic reported providing a total of $50K in cost sharing for this project.**

NDT Systems & Services is based in Germany and the United States and is a leading provider of state-of-the-art in-line inspection tools and services utilizing ultrasound technology. NDT Systems committed to providing **$20K** in engineering time to participate in meetings and to review reports (Task 8). **At the end of the project, NDT Systems & Services did not provided any cost share for the program.**

8.2.2 Additional Cost-Sharing (NOT Quantified in the Original Proposal)

In section 2.5 of the proposal to DOT, it was noted that, "EWI remains in active dialogue with numerous additional cost sharing partners. Significant additional industry cost sharing is expected by December 17, 2007." At that time the proposal was submitted, the total of fully committed cash cost-share was $320K to be provided by EWI. These cost-share contributions are not only above and beyond the proposal, they are also above and beyond the 50/50 government/industry cost-share requirement as dictated by law. This report section documents additional cost-share as promised, as delivered and any deviations from the plan.

8.2.2.1 Additional Cash Cost-Share

Additional cash cost-share contributions are typically provided via parallel EWI R&D projects funded by individual cost-share partners. These projects feature a unique agreement between EWI and the cost-share partner and a unique project number against which EWI expenses are charged/tracked. Table 38 contains a summary of all additional cash cost-share contributions (budget and actual).

Table 38. Status of Additional Cash Cost-Share

Team Participant	EWI Project No.	Task	Budget	Actual
ConocoPhillips	51489CSP	5	$200,000	$200,000
		Total	***$200,000***	***$200,000***

ConocoPhillips is a leading U.S. pipeline/offshore operating company. On December 11, 2007, EWI received a letter of support from ConocoPhillips for **$200K** in cash cost-share in support of the Task 5 activities of this project. This funding was used for performance determination of MPA equipment supplied by EWI, CEA/LIST (M2M), and Zetec. The EWI agreement for this cash cost-share was signed by ConocoPhillips in September 26, 2008. **ConocoPhillips provided a total of $200K in cost sharing in support of this project.**

8.2.2.2 Additional In-Kind Support

Additional in-kind cost-share was provided to EWI in accordance with as applicable, *49 CFR 18 - Uniform Administrative Requirements for Grants and Cooperative Agreements to State and Local Governments, Section 18.24, Matching or Cost Sharing*, or *49 CFR 19 - Uniform Administrative Requirements for Grants and Agreements with Institutions of Higher Education, Hospitals, and Other Non-Profit Organizations, Section 19.23, Cost Sharing or Matching*. EWI captured and maintained an Excel spreadsheet with a running summary of additional in-kind cost-share contributions as reported by team participants. Budget and actual costs of additional in-kind are shown in Table Table 39. During Quarter 12, INDES/KJTD withdrew their cost share commitment, bringing the anticipated additional in-kind support to an estimated **$176K**.

Table 39. Status of Additional In-Kind Support

Team Participant	Task	Budget	Actual
ApplusRTD[†] = BAM	5	$100,000[‡]	$100,000[§]
IDES/KJTD	5,7,8	$125,000	$0
ExxonMobil	5	$ 42,449	$ 42,449
ExxonMobil	7	$ 34,200	$ 34,200
	Total	***$176,649***	***$176,649***

[†] Prof. Uwe Ewert (the owner of TomoCAR system) from BAM (Federal Institute for Materials Research and Testing, headquartered in Berlin, Germany) provided the ApplusRTD in kind cost share. Activity is complete.

ApplusRTD is based in the Netherlands, Norway, France, United States, Canada, Australia, and Singapore, and a major part of its business is focus on inspection of pipelines using advanced NDT technologies and tools. ApplusRTD promised 75€ (approximately **$100K** with the current exchange rate) via TomoCAR computed radiography services for fingerprinting of 10 weld specimens of 30-in. diameter, X80 pipe with WT 15.6 mm with up to 120 flaws in support of Task 5. As proposed, the equipment and engineering time was limited to maximum 3 weeks during the 2-year duration of the project. Their commitment letter was received on December 13, 2007. EWI was unable to get ApplusRTD to respond to requests to schedule TomoCAR radiography. Prof. Uwe Ewert (the owner of the TomoCAR system) from the Federal Institute for Materials Research and Testing, headquartered in Berlin, Germany (BAM) provided this cost share for ApplusRTD. **On behalf of Applus RTD, BAM contributed $100K worth of TomoCAR services in support of this project.**

INDES/KJTD (USA) Co., Ltd. is based in Japan and the United States and is a leading provider of state-of-the-art ultrasonic inspection instrumentation and tools. IDES/KJTD promised **$125K** of direct in-kind support providing MPA equipment for up to 6 months (4 times at 1½ months each) and engineering in support of Tasks 5 and 7 (the work load of KJTD engineering was to be limited to 2 months). The INDES/KJTD engineering staff also promised to contribute by participating in meetings and to reviewing reports (Tasks 7 and 8). Their commitment letter that was received on December 19, 2008. **On March 8, 2011, INDES/KJTD informed EWI that they cannot participate in the project. Since 2007, their business conditions changed dramatically. In fact, they no longer have an operation in the United States and their business strategy has been reconsidered.**

ExxonMobil Development Company (EMDC) is one of the leading pipelines and offshore structures U.S. engineering company based in Houston. EMDC promotes the industrial application and advancement of MPA and AUT technology. As part of the program, EMDC funded a 1-week UT training event at EWI for 12 EMDC staff members. The cost of the training event was $34,200. Also as part of the program, EMDC funded ApplusRTD to use a newly EMDC developed MPA system to test implanted flaw samples. The scanning was provided in the quarter ending April 30, 2009. On May 5, 2009, ExxonMobil estimated this portion of their cost share contribution at $42,499. **The total ExxonMobil cost share for this project was $76,699.**

8.2.2.3 Other Support

This section is a summary of the "other" type of support provided by team participants that refused to sign the Terms of the Relationship Agreement (TRA) as required in Agreement DTPH56-08-T-000002 between DOT and EWI. Budget, current, and cumulative costs of all "other" support is shown in Table 40.

Table 40. Status of Other Support

Team Participant	Tasks	Budget	Actual
ConocoPhillips	All	$20,000	$ 9,281
UT Technology	8	$ 4,327	$ 4,327
BP	All	$55,000	$55,000
	Totals	***$79,327***	***$68,608***

ConocoPhillips. In their letter of support, ConocoPhillips stated their intention of providing $20K of "direct in-kind support of engineering time to participate in meetings and review reports. ConocoPhillips' legal department refused to sign the TRA. This contribution was consequently considered "other" support. Mr. Joe Kiefer actively participated in the project. He provided an accounting of his labor and travel expenses related to the project kick-off meeting and the project meeting at EWI on June 15, 2009. Mr. Kiefer also provided EWI with an estimate for the pipe sections that were donated for use on this project and he attended the June 2011 project workshop. **To date, ConocoPhillips has reported $9,281 in other support; however, their contributions are well above that level.**

UT Technology is based in Canada and is a leading provider of state-of-the-art automated ultrasonic PA inspection systems. The UT Technology contribution has not been defined; however, a representative did attend the kick-off meeting at EWI on June 5, 2008. No accounting of his expenses was reported. During the field trials, EWI shipped the scanning equipment to the UT Quality facilities in Edmonton, where it was unpacked and loaded on a truck provided by UT Quality. UT Technology is the parent company of UT Quality. UT Quality also assisted EWI with customs and shipping (both ways) and provided a driver to drive the equipment and EWI staff to and from the dig site every day. Additionally, an engineer from UT Technology attended the June 2011 workshop at EWI. **A value of $4,327 was estimated for this effort.**

BP is a leading U.S. pipeline/offshore operating company, who provided an in-kind contribution in the form of an NDE Expert/Welding Engineer in support of all project tasking; no value was estimated for this contribution. Dr. Mark Lozev provided this in-kind contribution through his active participation in the project and estimated his contribution at $110,000+ over 3 years for both active DOT projects. For this project, the estimated BP cost share is $55K. This BP cost share was not factored into the last contract modification that realigned the cost share budget. **This $55,000 in-kind cost share contribution was provided in full.**

8.3 Subcontracts

There were two subcontractors required for this project: Battelle and CEA/List.

- The subcontract with Battelle was fully executed on June 16, 2008.
- The subcontract with CEA/List was fully executed on July 1, 2008.

9.0 Conclusions

Following are conclusions and observations from the project:

- In general, all four MPA concepts developed during this project showed good potential for pipeline inspection. Concept 4 (health monitoring) could be deployed provided a means for probe attachment to the pipe is addressed. The other three concepts need additional work to make them field ready as explained in the additional comments below.

- When using MPA for girth weld inspection, it was a challenge to manage the large amount of data available through the different MPA tilt and skew channels. It appears that flaw evaluation and sizing algorithms currently used for conventional and LPA may not be sufficient for MPA. For example, algorithms need to address which channel(s) should be used for determining flaw size.

- Despite the challenge of large amounts of data, POD values and flaw sizing accuracy obtained for MPA of girth welds were similar to those obtained for LPA. Given that MPA is an emerging technology for girth weld inspection, the overall results were encouraging.

- TomoCAR radiography results compared well to destructive verification measurements for flaw height and depth. The comparisons were very good and measurements were typically within 0.5 mm. While TomoCAR has limitations, it does open the possibility for an alternative to destructive verification for POD and sizing accuracy studies.

- The flexible MPA probe used on this project provided good results on material approximately 25 mm in thickness where longitudinal and refracted longitudinal beams could be used to detect reflectors on the opposite (back) surface. A possible application for the probe would be to detect ID corrosion damage when inspecting from the OD pipe surface.

- While the ultrasonic part of the flexible MPA probe functioned well, problems were experienced with the LVDT pistons used for surface contour measurements. In three

different instances an LVDT piston stopped functioning resulting in the inability to use the real-time focal law feedback. For field applications, a more robust probe would be required.

- Ultrasonic performance of the ID MPA probe was good; however, a method for transporting the multiple probe segments through a fluid-filled pipe is needed. For optimal performance, the transporting mechanism would need to maintain probe alignment and constant radial distance from the pipe ID surface.

- Modeling and simulations results obtained during this project agreed well with the experimental results and proved valuable for probe design and predicting detection capabilities. This was especially evident from modeling and experimental data for the ID MPA probe.

- MPA probes worked well to provide a 2-axis stationary C-Scan for health monitoring. Unlike single-element probes, the 2D MPA probe provided A-Scan data for each point on the C-Scan. This allowed multiple measurements to be made over the entire probe footprint which provided a more comprehensive understanding of test component characteristics.

10.0 Recommendations

Following are recommendations based on observations and results from this project:

- MPA of girth welds will require further development of data handling and data analysis routines in order to fully use the capabilities of MPA technology. It is recommended that future work concentrate on MPA procedures and software that will provide quick and reliable analysis of MPA data. This should involve the selection of beam tilt and skew angles that are most advantageous, as well as, flaw sizing protocols for tilted and skewed flaws.

- It is recommended that the TomoCAR technology be further developed as a substitute for destructive measurements made during qualification/quantification programs to determine POD and sizing accuracy. This technology could potentially reduce the cost of such programs and allow the validation samples to be re-used.

- It is recommended that flexible MPA technology be further evaluated for inspection of components greater than 15 mm in thickness. In addition, the LVDT plungers should be evaluated for improvements in robustness for field applications.

- While the ID probe segment had good ultrasonic characteristics, additional work should be performed to design a system for transporting the probe through the ID bore. The transporting device would need to maintain good probe alignment and be self contained with power supplies and data acquisition capabilities.

11.0 References

1. http://primis.phmsa.dot.gov/rd/mtg_020707.htm

2. GRI-00/0064 *Sizing Stress Corrosion Cracking in Pipeline Specimens, 2000*.

3. Lozev, M., Spencer, R., Huang T., and Patel P., "Improved Inspection and Assessment Methods for Pipeline Girth Welds and Repair Welds", EWI Final Report, DOT Agreement No. DTRS56-03-T-0012 (2006).

4. DOT Agreement DTPH56-T-000002, "Advanced Technologies and Methodology for AUT Systems Quantification", M. Lozev, Principal Investigator (ongoing 7/07-6/09).

5. Lozev, M. G., Spencer, R. L., and Hodgkinson, D., "Optimized Inspection of Thin-Walled Pipe Welds Using Advanced Ultrasonic Techniques", *Journal of Pressure Vessels Technology*, August 2005, Vol. 127, pp 237-243 (Aug. 2005).

6. ASTM E1961; "Standard Practice for Mechanized Ultrasonic Examination of Girth Welds Using Zonal Discrimination with Focused Search Units"; American Society for Testing and Materials.

7. Ewert, U., Redmer, B., Kannengiesser, T., and Kromm, A., "Mobile Computed Tomography for Inspection of Welded Pipes", BAM, Berlin, Germany.